

On the controlled generation of nonlinear structures in Bose-Einstein condensates

Dissertation
zur Erlangung des Doktorgrades
an der Fakultät für Mathematik, Informatik und Naturwissenschaften
Fachbereich Physik
der Universität Hamburg

vorgelegt von
Alejandro ROMERO ROS

Hamburg
2023

Gutachter/innen der Dissertation:	Prof. Dr. Peter Schmelcher Prof. Dr. Dieter Jaksch
Zusammensetzung der Prüfungskommission:	Prof. Dr. Peter Schmelcher Prof. Dr. Dieter Jaksch Prof. Dr. Henning Moritz Prof. Dr. Andreas Hemmerig Prof. Dr. Daniela Pfannkuche
Vorsitzende/r der Prüfungskommission:	Prof. Dr. Daniela Pfannkuche
Datum der Disputation:	06.02.2024
Vorsitzender Fach-Promotionsausschusses PHYSIK:	Prof. Dr. Markus Drescher
Leiter des Fachbereichs PHYSIK:	Prof. Dr. Wolfgang J. Parak
Dekan der Fakultät MIN:	Prof. Dr.-Ing. Norbert Ritter

To my beloved ones...

Contents

Contents	vii
Zusammenfassung	xi
Abstract	xiii
Preface	xv
Introduction	xix
I Theoretical Framework	1
1 Bose-Einstein condensates	3
1.1 Mean-field approximation	4
1.1.1 Gross-Pitaevskii Equation	5
1.1.2 Healing Length	6
1.1.3 Thomas-Fermi approximation	6
1.1.4 Dimensionality reduction	8
1.2 Multi-component Bose-Einstein Condensates	9
1.2.1 Coupled Gross-Pitaevskii Equation	10
1.2.2 Spinor Gross-Pitaevskii Equation	11
2 Solitons	13
2.1 Inverse Scattering Transform	14
2.2 Nonlinear Schrödinger Equation	15
2.3 Soliton solutions	16
2.3.1 Scalar solitons	16
2.3.2 Vector solitons	17
2.3.3 Matrix Solitons	18
2.4 Solitons in Bose-Einstein Condensates	19
3 Rogue Waves	23
3.1 Soliton Breathers	24
3.2 Modulational Instability	25

II	Outline of the Scientific Contributions	27
4	Controlled generation of soliton trains in BECs	29
5	Soliton gas	35
6	The Peregrine soliton in BECs	37
III	Scientific contributions and Conclusions	41
7	Scientific Contributions	43
7.1	Controlled generation of dark-bright soliton complexes in two-component and spinor Bose-Einstein condensates	45
7.2	On-demand generation of dark soliton trains in Bose-Einstein condensates	63
7.3	On-demand generation of dark-bright soliton trains in Bose-Einstein condensates	77
7.4	Observation of dense collisional soliton complexes in a two-component Bose-Einstein condensate	101
7.5	Theoretical and numerical evidence for the potential realization of the Peregrine soliton in repulsive two-component Bose-Einstein condensates	111
7.6	Experimental realization of the Peregrine soliton in repulsive two-component Bose-Einstein condensates	125
8	Conclusions	137
	Bibliography	141
	Acknowledgements	171
	Eidesstattliche Versicherung / Declaration of oath	173

List of Abbreviations

BEC(s)	Bose-Einstein Condensate(s)
GPE	Gross-Pitaevskii Equation
PDE(s)	Partial Differential Equation(s)
IST	Inverse Scattering Transform
NLS	Non-Linear Schrödinger Equation
VNLS	Vector Non-Linear Schrödinger Equation
MNLS	Matrix Non-Linear Schrödinger Equation
NZBC	Non-Zero Boundary Conditions
DB	Dark-Bright
DDB	Dark-Dark-Bright
DBB	Dark-Bright-Bright
PS(s)	Peregrine Soliton(s)
MI	Modulational Instability
1D	One-Dimensional
3D	Three-Dimensional
OP	Out-of-Phase
IP	In-Phase
GW	Gaussian potential Well

Zusammenfassung

Diese kumulative Dissertation widmet sich der Erforschung zur kontrollierten Erzeugung nichtlinearer Strukturen in Bose-Einstein-Kondensaten (BECs). Insbesondere lassen sich unsere Studien in drei Forschungsrichtungen unterteilen: Solitonenzüge, Solitonengase und Monsterwellen. In der ersten Reihe von Untersuchungen konzentrieren wir uns auf die kontrollierte Erzeugung von Solitonenzügen, d.h. aneinandergereihte, sich bewegende Solitonen. Die Entstehung dieser Solitonenzüge ist die Folge von Interferenzprozessen aus Materiewellen, welcher durch eine kastenförmige Konfiguration (BTC) erzeugt wird. Mit dieser BTC-Anfangsbedingung kann das Anfangswertproblem analytisch unter Zuhilfenahme der inversen Streutransformation gelöst werden. Mit den entsprechenden Lösungen lassen sich dann die Solitonenzüge charakterisieren. Unsere analytischen Herleitungen decken die Erzeugung von Solitonenzügen in ein- und zweikomponentigen BECs ab, während ergänzende numerische Untersuchungen die Ergebnisse auf dreikomponentige und Spinor-BECs erweitern. Im Allgemeinen zeigt sich, dass die Amplitude und die Breite des BTCs die Anzahl der erzeugten Solitonen, ihre Größe und ihre Geschwindigkeit direkt beeinflussen. Die symmetrische Konfiguration der entstehenden Solitonenzüge kann auch durch Änderung der relativen Phase zwischen Regionen innerhalb der BTC verändert werden. In allen Fällen wird, besonders im Hinblick auf mögliche experimentelle Realisierungen, zusätzlich ein externes, harmonisches Potential mit berücksichtigt. Unsere Ergebnisse gelten unter der Annahme, dass die Breite der BTC klein ist im Vergleich zu der Größe des Kondensats. Weitere Ergebnisse sind die Beobachtung von pulsierenden Solitonen in Spinor-BECs und eine analytische Beschreibung der Amplitudenänderung von oszillierenden dark-bright Solitonen in einer harmonischen Falle. Unser zweiter Forschungsschwerpunkt befasst sich mit der experimentellen Erzeugung eines dichten Ensembles von Solitonen in einem zweikomponentigen BEC. Durch den Einsatz von zwei $\pi/2$ -Pulsen in Gegenwart eines Magnetfeldgradienten wird ein periodisches Windungsmuster erzeugt, welches sich dynamisch zu einer Reihe von Solitonenkomplexen entwickelt. Der Abstand zwischen den Windungen kann durch die Dauer zwischen den Impulsen gesteuert werden. Je nach Dichte der Windungen beobachten wir die Bildung von Schockwellen, dark-antidark und dark-bright Solitonen, sowie dynamische Prozesse, bei denen sich die Periodizität des Musters verdreifacht oder die Amplitude abflacht. In den dichtesten Ensembles durchlaufen die entstehenden Solitonen über einen langen Zeitraum hinweg kontinuierliche Kollisionen, wobei jedoch die anfänglichen Merkmale erhalten bleiben. Letzteres eröffnet den Weg für Untersuchungen von Solitongasen in BECs. Schließlich konzentrieren wir uns auf die Realisierung des Peregrine Solitons (PS) in BECs. Das PS ist ein Kandidat für Monsterwellen, d.h. für extreme Wellenereignisse auf dem Meer. Die fokussierende Nichtlinearität von Tiefseewellensystemen führt zu einer modulierenden Instabilität, die als Hauptmechanismus für die Bildung solcher Wellen angesehen wird. Um dieser fokussierenden Nichtlinearität entgegenzuwirken und unerwünschte Instabilitäten zu vermeiden, verwenden wir ein zweikomponentiges BEC, dessen Komponenten sich stark in ihrer Teilchenzahl unterscheiden und sich vermischen lassen. Bei diesem Ansatz stellt die Minoritätskomponente eine effektive fokussierende Nichtlinearität dar. Die Anwendbarkeit

wird theoretisch durch direkte numerische Simulationen der GPE unter den relevanten experimentellen Bedingungen untersucht. In allen Fällen wird eine exzellente Übereinstimmung zwischen den numerisch erhaltenen PS und dessen analytischen Wellenform festgestellt. Dieser Ansatz wird dann zur experimentellen Realisierung des PS verwendet. In dem Versuchsaufbau wird zusätzlich ein kleiner attraktiver Potentialtopf eingefügt, um die Bildung des PS zu stimulieren. Numerische 1D- und 3D-Simulationen untermauern unsere Ergebnisse. Unseres Wissens nach ist dies die erste Realisierung des PS in einem BEC.

Abstract

In this cumulative thesis, we present our investigations on the controlled generation of nonlinear structures in Bose-Einstein condensates (BECs). In particular, our studies can be divided in three lines of research: soliton trains, soliton gases, and rogue waves. In the first set of investigations we focus on the controlled generation of soliton trains, i.e., arrays of moving solitons. The emergence of these structures is a consequence of a matter-wave interference process initialized by a box-type configuration (BTC). This initial condition allows to solve the initial value problem analytically by means of the inverse scattering transform and to obtain expressions which characterize the entities conforming the soliton trains. Our analytical derivations cover the generation of solitons trains in one- and two-component BECs, while further numerical investigations extend our results to three-component and spinor BECs. In general, it is found that the amplitude and width of the BTC directly affects the number of solitons generated, their size, and their velocity. The symmetric configuration of the resulting solitons trains can also be altered by modifying the relative phase between the regions of the BTC. In all cases, and in view of possible experimental realizations, the addition of an external harmonic potential is considered. Our results hold as long as the width of the BTC is way smaller than the size of the condensate. Additional findings include the observation of beating solitons in spinor BECs and an analytical description of the change in amplitude of oscillating dark-bright solitons in a harmonic trap. Our second focus of research deals with the experimental generation of a dense ensemble of solitons in a two-component BEC. By employing two $\pi/2$ -pulses in the presence of a magnetic-field gradient we create a periodic winding pattern that dynamically evolves into an array of soliton complexes. The spacing between windings can be controlled by the duration between the pulses. Depending on the density of windings, we observed the formation of shock-waves, dark-antidark, and dark-bright solitons, as well as dynamical processes where the periodicity of the pattern triples or smooths out. In the densest ensembles, the emerging solitons undergo continuous collisions for a long period of time, preserving the overall initial features. The latter offers a path to the study of soliton gases in BECs. Last, we focus on the realization of the Peregrine soliton (PS) in BECs. The PS is a candidate to rogue waves, i.e., extreme wave events taking place at sea. The focusing nonlinearity of deep-water wave systems leads to a modulational instability considered to be the main mechanism behind the formation of such waves. To address the focusing nonlinearity avoiding undesired instabilities, we employ a highly-imbalanced weakly-immiscible two-component BEC. With this approach, the minority component presents an effective focusing nonlinearity. Its applicability is theoretically investigated by direct numerical simulations of the GPE under relevant experimental conditions. In all cases, an excellent agreement is found between the numerically obtained PS and its analytical waveform. This approach is then employed to experimentally realize the PS. In the experimental setup, an additional small attractive potential well is included to seed the formation of the PS. Numerical 1D and 3D simulations corroborate our findings. To the best of our knowledge, this is the first realization of the PS in a BEC.

Preface

Publications covered by this thesis

- [A1] A. Romero-Ros, G. C. Katsimiga, P. G. Kevrekidis, and P. Schmelcher, “Controlled generation of dark-bright soliton complexes in two-component and spinor Bose-Einstein condensates”, *Phys. Rev. A* **100**, 013626 (2019).
- [A2] A. Romero-Ros, G. C. Katsimiga, P. G. Kevrekidis, B. Prinari, G. Biondini, and P. Schmelcher, “On-demand generation of dark soliton trains in Bose-Einstein condensates”, *Phys. Rev. A* **103**, 023329 (2021).
- [A3] A. Romero-Ros, G. C. Katsimiga, P. G. Kevrekidis, B. Prinari, G. Biondini, and P. Schmelcher, “On-demand generation of dark-bright soliton trains in Bose-Einstein condensates”, *Phys. Rev. A* **105**, 023325 (2022).
- [A4] S. Mossman, G. C. Katsimiga, S. I. Mistakidis, A. Romero-Ros, T. M. Bersano, P. Schmelcher, P. G. Kevrekidis, and P. Engels, *Observation of dense collisional soliton complexes in a two-component Bose-Einstein condensate*, Mar. 2023, [arXiv:2208.10585](https://arxiv.org/abs/2208.10585) [[cond-mat](#), [physics:nlin](#)].
- [A5] A. Romero-Ros, G. C. Katsimiga, S. I. Mistakidis, B. Prinari, G. Biondini, P. Schmelcher, and P. G. Kevrekidis, “Theoretical and numerical evidence for the potential realization of the Peregrine soliton in repulsive two-component Bose-Einstein condensates”, *Phys. Rev. A* **105**, 053306 (2022).
- [A6] A. Romero-Ros, G. C. Katsimiga, S. I. Mistakidis, S. Mossman, G. Biondini, P. Schmelcher, P. Engels, and P. G. Kevrekidis, “Experimental Realization of the Peregrine Soliton in Repulsive Two-Component Bose-Einstein Condensates”, *Phys. Rev. Lett.* **132**, 033402 (2024).

This cumulative thesis is based on the publications listed above. Throughout this thesis, they will be cited with the reference index [A. . .].

Further publications

- [A7] D. Ledesma, A. Romero-Ros, A. Polls, and B. Juliá-Díaz, “Dynamic structure function of two interacting atoms in 1D”, *EPL* **127**, 56001 (2019).

[A4] is submitted to *Communication Physics*.

Declaration of personal contributions to the publications [A1–A6]

[A1] was initially proposed by Prof. Dr. Peter Schmelcher and Dr. Garyfallia Katsimiga and, in a later stage, discussed and shaped in collaboration with Prof. Dr. Panayotis Kevrekidis. I performed all the numerical simulations and analysis, and wrote the manuscript myself.

[A2, A3] are a collaboration with Prof. Dr. Barbara Prinari and Prof. Dr. Gino Biondini, as a complement to [A1]. I performed all the numerical calculations and analysis, and wrote the manuscript myself. The spectrum of analytical solutions was partially obtained using a modified code from Prof. Dr. Gino Biondini. The analytical analysis in the manuscripts are based on notes provided by Prof. Dr. Barbara Prinari.

[A4] is a collaboration with the experimental group of Prof. Dr. Peter Engels in an effort to apply the tools developed in [A3] to recently obtained experimental data by Dr. Thomas Bersano. Posterior experiments were done and analyzed by Dr. Sean Mossman, who also wrote the main body of the manuscript and the supplemental material. In this project, I contributed with the initial one-dimensional simulations that led to the three-dimensional results computed and added to the texts by Dr. Garyfallia Katsimiga and Dr. Simeon Mistakidis. I also created the multimedia files and Figure 6(b) from the one-dimensional data, and Figure 1(a) from the three-dimensional data.

[A5] was proposed by Prof. Dr. Panayotis Kevrekidis. I performed all the one-dimensional simulations and analysis thereof, and wrote most of the manuscript. Dr. Simeon Mistakidis and Dr. Garyfallia Katsimiga performed the three-dimensional simulations and wrote the corresponding section of the manuscript.

[A6] is the experimental realization of [A5] done in collaboration with Dr. Sean Mossman and Prof. Dr. Peter Engels, who provided the experimental data. I performed the one-dimensional numerical simulations, and Dr. Garyfallia Katsimiga and Dr. Simeon Mistakidis performed the three-dimensional ones. Prof. Dr. Panayotis Kevrekidis wrote the introduction and conclusions, and the rest of us wrote the corresponding sections of our results in both the manuscript and the supplemental material.

In all cases, the progress of the investigations was supervised by Prof. Dr. Peter Schmelcher, and the manuscripts were revised and improved by all the authors in a set of continuous iterations.

Outline

In Part **I** we provide a theoretical background in three chapters, summarizing the basic necessary concepts employed in our works, together with some historical contextualization on the topic. Chapter **1** is dedicated to the mean-field description of BECs. In particular, we derive the GPE and its multi-component forms. We also discuss the characteristic length scales of the system and the role of the trapping potential employed to address the 1D nature of the solitonic structures. In Chapter **2** we first discuss the concept of solitons as solutions of the NLS. We start with a simplified description of the IST formalism. Then, we introduce the NLS and its multi-component forms, in analogy with the GPE in the previous chapter. The soliton solutions are provided subsequently. In particular, we analyze soliton solutions of the bright and dark type, and multi-component soliton solutions of the dark-bright type. Last, we discuss solitons in the context of BECs and some relevant aspects to consider in experiments. Chapter **3** is devoted to rogue waves. More specifically, we present three soliton solutions candidates to rogue waves known as breathers. Additionally, we also comment on the main mechanism proposed for the formation of rogue waves, i.e., the modulational instability.

In Part **II** we motivate our works within the current state of the art, describe the methods employed, and outline our scientific contributions. In Chapter **4** we discuss three different works in which we generate multi-component arrays of moving solitons, i.e., soliton trains, of the dark-bright type starting from box-type configurations. In the first work [A1], we numerically investigate how tuning the initial size of the box-type configuration we can control the number, size, and velocity of the generated soliton trains. This study extends to two-component, three-component, and spinor-BECs. In the following two works [A2, A3], we employ the IST formalism to characterize, this time analytically, the emerging soliton trains in one- and two-component BECs. In Chapter **5** we present an experimental work [A4] where we generate dense soliton ensembles in a two-component BEC employing a near-resonant microwave pulse in the presence of a small magnetic-field gradient. In this case, the solitons form from a periodic phase-winding pattern between the two components of the BEC. Last, in Chapter **6** we dedicate two works to the realization of the Peregrine soliton in BECs. More specifically, the first work is a theoretical proposal [A5]. Here, we leverage the effective single-component description of a highly-imbalanced weakly-immiscible two-component BEC in the semiclassical limit to realize the Peregrine soliton. In the second work [A6], we additionally introduce to our setup a potential well to *seed* the emergence of the Peregrine soliton and, for the first time, experimentally realize the Peregrine soliton in a BEC.

Part **III** closes our thesis. Chapter **7** consists of the publications of our scientific contributions. Finally, in Chapter **8**, we conclude our work and discuss some future perspectives.

Introduction

Solitons are one of the most renowned nonlinear excitations in nonlinear media. They are solitary waves stemming from the balance between dispersion and nonlinearity. Interestingly, these objects present particle-like properties that grant them the name of *solitons*. In a nutshell, solitons can be defined as localized waves of permanent form, which retain shape after interacting with one another. Since the early water-tank experiments of J.S. Russell in 1840s [1], solitons have been found in a large variety of physical nonlinear media, e.g., from water-waves systems [2–5], nonlinear optics [6–8], and Bose-Einstein condensates (BECs) [9–12], to plasmas [13], atmospheric dynamics [14], and molecular chains [15], such as DNA [16].

On one hand, some of the most interesting technological applications come from the field of nonlinear optics involving high-speed communications [17]. For instance, already in 1973, it was proposed to employ solitons as bits of information in light transmitted devices, namely optical fibers [18, 19]. On the other hand, recent theoretical proposals went beyond the usual scope of soliton theory and suggested to employ them as qubit states for quantum metrology [20, 21], as mechanisms to study Hawking radiation [22] from an analog event horizon in BECs [23–28], or even as the positive-energy solution to the Alcubierre warp drive [29] to hyper-fast travel within general relativity [30]. These are only some peculiar examples to showcase the broad audience and interest that these structures evoke in the scientific community.

A natural question to ask at this point is: Why do solitons appear in so many different physical systems? The answer is simple. It resides in the evolution equations describing each one of the nonlinear systems where solitons are found. Basically, under the adequate assumptions, these equations reduce to the same nonlinear partial differential equations (PDEs), which admit soliton solutions. Over the last half century, a rigorous mathematical formalism, known as the inverse scattering transform (IST) [31–40], has been developed to solve these nonlinear PDEs.

One relevant nonlinear PDE with soliton solutions is the nonlinear Schrödinger equation (NLS) [41–47]. This equation is one-dimensional (1D), and so are its soliton solutions. The most renowned ones are the so-called *bright* [48] and *dark* [49] solitons. Bright solitons are solutions of the NLS with a focusing (attractive) nonlinearity, and consist of a local hump in the absence of a background. On the contrary, dark solitons are solutions of the NLS with a defocusing (repulsive) nonlinearity, and consist of a local depletion living atop of a constant background.

Among the different aforementioned nonlinear systems where solitons can emerge, we are particularly interested in BECs. BECs can be described by the Gross-Pitaevskii equation

(GPE) [50–54], a NLS-type equation which can admit soliton solutions [55]. Hence, since their first experimental realization in 1995 [56–58], BECs have become a fruitful platform in which to investigate solitons [9–12]. In BECs, the nonlinearity arises from the interactions between the atoms, which can be easily controlled by means of Feshbach resonances [59–66]. These interactions can be attractive or repulsive, and thus give rise to either bright [67, 68] or dark [69–72] solitons, respectively. Interestingly, BECs can consist of mixtures of the same [73–76] or different [77–81] atomic species, which opens the door to a more exotic spectrum of solitonic structures, where solitons of the same or different type can coexist in symbiosis [82–84].

Notwithstanding, solitons are not the only interesting wave phenomena arising in nonlinear media. For instance, in open sea waters, extreme oceanic wave events, several times higher than the average sea state, emerge and vanish without a trace. These freak, enormous waves are known as rogue waves, and they are of great concern to the maritime community [85, 86]. In particular, rogue waves put at risk vessels and other maritime structures, as well as those onboard. This motivates the need to study and understand them. Fortunately, deep water-wave phenomena can be modeled by the NLS [87]. Therefore, similar to solitons, the study of rogue waves is not restricted solely to oceanic water-wave [88–91] and water-tank experiments [92, 93], but it also extends to nonlinear optics [94–105], BECs [106–109], plasmas [110–114], phononic lattices and crystals [115–117], superfluid helium [118], and even to atmospherics [119] and finance [120, 121].

The aim of this thesis is to provide to the nonlinear community robust, consistent, and controllable mechanisms to generate and study nonlinear structures in multi-component BECs. In particular, we investigate the generation of three different complexes. The first one is a soliton train [A1–A3]. This complex consists of an array of moving solitons. As we shall see, from a simple and accessible box-type configuration, we can generate trains of solitons in one-, two- and three-component BECs, the latter also with spin interactions. Additionally, we can control the properties of the solitons by modifying the parameters of the box-type configuration. The second complex consists of a two-component BEC densely packed with solitons [A4]. Employing two microwave-pulses and a small magnetic-field gradient we generate periodic modulations which evolve into solitons. The number of modulations is directly proportional to the time interval between pulses and can be easily controlled to modify the amount of solitonic entities in the condensate. This puts at reach the study of soliton gases in BECs. The third complex is a solution of the NLS candidate to rogue wave: the Peregrine soliton [A5, A6]. It is a wave localized in time and space, which fits the definition of rogue wave. The Peregrine soliton is experimentally realized in a two-component BEC employing a highly particle-imbalanced weakly-immiscible mixture and, in the presence of a small potential well, we can control where and when the Peregrine soliton forms.

Part I

Theoretical Framework

Chapter 1

Bose-Einstein condensates

“From a certain temperature on, the molecules ‘condense’ without attractive forces, that is, they accumulate at zero velocity. The theory is pretty, but is there also some truth to it?”

*letter to P. Ehrenfest (November 1924)*¹

Albert Einstein

Bose-Einstein condensation is an outstanding quantum phenomenon occurring at a *macroscopic* level. Its theoretical prediction dates back to 1925 when, in his paper [122], Albert Einstein extended the work of S. N. Bose on the statistical properties of photons [123] to a gas of non-interacting massive particles. He found that when a bosonic gas is cooled down below a certain critical temperature, T_c , a large fraction of the bosons² conforming the gas fall (condense) into the lowest-energy single-particle state. Interestingly, the condensed gas shows coherence. This allows to treat the whole ensemble as a single entity, and describe it employing a classical field (see below).

Due to its unprecedented properties, it had no application to physical systems until in 1938 it was proposed as the main mechanism behind superfluidity [125], after its discovery in liquid Helium [126, 127]. In the 1970s, magnetic and optical trapping mechanisms started to be developed to confine atomic gases [128, 129] and, since T_c solely depends on the mass and the density of the bosonic ensemble, hydrogen was initially thought to be the most adequate candidate for condensation [130, 131]. Later on, experiments started to work with alkali atoms, whose properties were easier to access and whose interactions could be externally controlled [132–134]. This, together with more advanced laser- and evaporative-cooling techniques, made possible to reach the low temperatures and densities needed to undergo condensation [135, 136]. Then, in 1995, the first experimental realizations of Bose-Einstein condensates (BECs) were achieved with alkali atoms [56–58] and recognized with the Nobel Prize in Physics in 2001 [137].

In the last decades, BECs have become versatile platforms to study quantum phenomena due to their high degree of controllability. For instance, depending on the atomic species of a BEC, the interactions between two colliding atoms can be attractive (e.g., ⁸⁵Rb or ⁷Li) or repulsive (e.g. ⁸⁷Rb or ²³Na) [57, 138, 139]. These depend on the scattering length, whose

¹A. Pais, *Subtle Is the Lord: The Science and the Life of Albert Einstein*, (Oxford University Press, New York, 2005), p. 432.

²Bosons are particles of integer spin described by symmetric wave functions named after S. N. Bose [124].

magnitude and sign can be tuned by means of Fano-Feshbach resonances [59–66]. Moreover, the possibility to confine them in arbitrary potential landscapes [140] provides us with the tools to study condensation in lower dimensions [141–145].

Some applications of BECs include high precision inertial measurements as atom lasers [146, 147] and atomic clocks [148–150], or mater-wave interferometers [151–154] with which to detect gravitational waves [155]. More recently, condensation of heavier, dipolar atoms, such as ^{162}Dy [156] or ^{166}Er [157], have been found to be an ideal platform to study supersolids [158–162]. Nevertheless, our interest in BECs is that they are one of the most widely used platforms for studying solitons [9, 11, 84, 163]. These structures and their dynamics are well described by the Gross-Pitaevskii equation (GPE), an equation derived in 1961 by Gross [50] and Pitaevskii [51] to describe oscillations of a Bose gas at zero temperature.

In this chapter, we introduce the mean-field approximation from which the GPE is derived. Then, we discuss the characteristic length scales of a BEC and how to reduce its dimensionality to access the 1D nature of solitons. Last, we generalize the GPE to describe multi-component BECs in which more exotic soliton structures can emerge. A description of the solitons and other emerging structures is provided in Chapter 2 and Chapter 3.

1.1 Mean-field approximation

It has been shown that the properties and dynamics of a dilute, weakly-interacting, Bose gas close to zero temperature can be modeled by mean-field theories [52–54, 164]. In simple terms, the mean-field approach can be thought as averaging the interactions that all bosons in the condensate exert on one another, instead of solving the complex many-body problem.

In second quantization, the Hamiltonian of an interacting gas of N bosons of mass m confined in an external potential $V(\mathbf{r})$ is given by

$$\begin{aligned} \hat{\mathcal{H}} = & \int d\mathbf{r} \hat{\Psi}^\dagger(\mathbf{r}) \left[-\frac{\hbar^2}{2m} \nabla^2 + V(\mathbf{r}) \right] \hat{\Psi}(\mathbf{r}) \\ & + \frac{1}{2} \int d\mathbf{r} d\mathbf{r}' \hat{\Psi}^\dagger(\mathbf{r}) \hat{\Psi}^\dagger(\mathbf{r}') U(\mathbf{r} - \mathbf{r}') \hat{\Psi}(\mathbf{r}') \hat{\Psi}(\mathbf{r}), \end{aligned} \quad (1.1)$$

where $\hat{\Psi}^\dagger(\mathbf{r})$ and $\hat{\Psi}(\mathbf{r})$ are the bosonic creation and annihilation field operators, respectively, satisfying the canonical commutation relations,

$$[\hat{\Psi}(\mathbf{r}), \hat{\Psi}^\dagger(\mathbf{r}')] = \delta(\mathbf{r} - \mathbf{r}'), \quad [\hat{\Psi}(\mathbf{r}), \hat{\Psi}(\mathbf{r}')] = 0, \quad [\hat{\Psi}^\dagger(\mathbf{r}), \hat{\Psi}^\dagger(\mathbf{r}')] = 0, \quad (1.2)$$

and $U(\mathbf{r} - \mathbf{r}')$ is the potential describing the interatomic two-body interactions.

Following the description proposed by Bogoliubov [165], the idea behind the mean-field approximation consists of decomposing the field operator, $\hat{\Psi} = \Psi + \delta\hat{\Psi}$, into a condensed contribution, $\Psi \equiv \langle \hat{\Psi} \rangle$, and a non-condensed one, $\delta\hat{\Psi}$. At zeroth-order, and for sufficiently low temperatures ($T < T_c$), one can neglect the non-condensed contribution, which accounts for thermal and quantum fluctuations. Then, the field operator $\hat{\Psi}$ coincides with the classical field Ψ and the system behaves like a classical object. Here, Ψ has the meaning of an order

parameter [9, 52, 166]. It is referred to as the macroscopic wave function of the condensate and normalized to the number of condensed particles $\int |\Psi(\mathbf{r})|^2 d\mathbf{r} = \int n(\mathbf{r}) d\mathbf{r} = N_0$. In order for this approximation to be valid, we need to assume that in the thermodynamic limit ($N \rightarrow \infty$) the condensed fraction of the bosonic gas (N_0/N) remains finite. Under this assumption, the condensate can be seen as a reservoir, with $N_0 \gg 1$. Thus, states with N or $N \pm 1$ bosons are physically equivalent and the expectation value of the time-dependent field operator

$$\langle \hat{\Psi}(\mathbf{r}, t) \rangle = \langle N-1 | e^{i\hat{\mathcal{H}}t/\hbar} \hat{\Psi}(\mathbf{r}) e^{-i\hat{\mathcal{H}}t/\hbar} | N \rangle. \quad (1.3)$$

yields

$$\Psi(\mathbf{r}, t) = \Psi(\mathbf{r}) e^{-i\mu t/\hbar}, \quad (1.4)$$

where we employed the Schrödinger equation, $\hat{\mathcal{H}} |N\rangle = E_N |N\rangle$. Importantly, the chemical potential $\mu = \partial E_N / \partial N \sim E_N - E_{N-1}$ has appeared as the parameter governing the time evolution of the macroscopic wave function of a BEC [52–54].

1.1.1 Gross-Pitaevskii Equation

The governing equation for the classical field Ψ can be obtained from the Heisenberg equation of the Hamiltonian (1.1),

$$\begin{aligned} i\hbar \frac{\partial}{\partial t} \hat{\Psi}(\mathbf{r}, t) &= [\hat{\Psi}, \hat{\mathcal{H}}] \\ &= \left[-\frac{\hbar^2}{2m} \nabla^2 + V(\mathbf{r}) + \int d\mathbf{r}' \hat{\Psi}^\dagger(\mathbf{r}', t) U(\mathbf{r} - \mathbf{r}') \hat{\Psi}(\mathbf{r}', t) \right] \hat{\Psi}(\mathbf{r}, t). \end{aligned} \quad (1.5)$$

Low-energy short-range elastic collisions between neutral atoms are characterized by the s -wave scattering length, a_s . In ultracold gases, for which the diluteness condition, $a_s \ll n^{-1/3}$, is assumed, particle interactions can be modeled via s -wave interactions [54]. Under this consideration, one can approximate the interaction potential by a delta pseudopotential [167],

$$U(\mathbf{r} - \mathbf{r}') = \frac{4\pi\hbar^2 a_s}{m} \delta(\mathbf{r} - \mathbf{r}'). \quad (1.6)$$

Inserting Eq. (1.6) in Eq. (1.5) and replacing the field operator $\hat{\Psi}$ with the classical field Ψ , we obtain the well-known Gross-Pitaevskii equation (GPE) [50, 51]:

$$i\hbar \frac{\partial}{\partial t} \Psi(\mathbf{r}, t) = \left[-\frac{\hbar^2}{2m} \nabla^2 + V(\mathbf{r}) + \frac{4\pi\hbar^2 a_s}{m} |\Psi(\mathbf{r}, t)|^2 \right] \Psi(\mathbf{r}, t). \quad (1.7)$$

It is important to keep in mind that the GPE is only strictly valid at zero temperature [166]. In finite-temperature systems, additional corrections to the GPE are needed in order to account for the interactions with the thermal cloud, i.e., the non-condensed part of the Bose gas [168–173]. In this regard, one could include a dissipative term D_T describing the coupling between the condensate fraction and the thermal reservoir at temperature T . Additionally, one can also include a noise term η accounting for incoherent collisions of random nature within the

system [174]. Inserting these terms into Eq. (1.7), we obtain the dissipative GPE [175],

$$i\hbar \frac{\partial}{\partial t} \Psi(\mathbf{r}, t) = \left[-\frac{\hbar^2}{2m} \nabla^2 + V(\mathbf{r}) - iD_T(\mathbf{r}, t) + \frac{4\pi\hbar^2 a_s}{m} |\Psi(\mathbf{r}, t)|^2 \right] \Psi(\mathbf{r}, t) + \eta(\mathbf{r}, t), \quad (1.8)$$

which is a simplified form of the so-called stochastic GPE [176].

Similarly, Eq. (1.6) is a zeroth-order approximation to the interaction potential [177]. For instance, the first beyond mean-field correction, i.e., the Lee-Huan-Yang term ($\propto a_s^{5/2} n^{3/2}$) [178], accounts for quantum fluctuations stemming from the zero-point motion of Bogoliubov excitations, which can stabilize an attractive condensate against collapse, leading to the formation of liquid-like states known as quantum droplets [179–185].

1.1.2 Healing Length

From Eq. (1.4), the time independent GPE follows,

$$\left[-\frac{\hbar^2}{2m} \nabla^2 + V(\mathbf{r}) + \frac{4\pi\hbar^2 a_s}{m} |\Psi(\mathbf{r}, t)|^2 \right] \Psi(\mathbf{r}) = \mu \Psi(\mathbf{r}). \quad (1.9)$$

The characteristic length scale of a BEC is defined as the equilibrium distance between the zero-point kinetic energy ($\hbar^2/2m\xi$) and the mean-field interaction energy ($4\pi\hbar^2 a_s n/m$),

$$\xi = \frac{1}{\sqrt{8\pi a_s n}} = \frac{\hbar}{\sqrt{2mgn}}, \quad (1.10)$$

Equation (1.10) is the healing length, where we defined $g = 4\pi\hbar^2 a_s/m$. It provides a sense for the distance over which a localized density defect returns to its bulk value, i.e., it *heals* itself. To illustrate it, we simplify our system to a one-dimensional BEC (see Section 1.1.4) in a half-box potential with $V(x) = 0$ for $x > 0$, and $V(x) = \infty$ elsewhere. Under this assumption, the GPE is analytically solvable satisfying the boundary conditions $\Psi(0) = 0$ and $\Psi(x \rightarrow \infty) = \psi_0$. In this case, the solution reads

$$\Psi(x) = \psi_0 \tanh\left(\frac{x}{\sqrt{2}\xi}\right). \quad (1.11)$$

In Fig. 1.1(a) we depict Eq. (1.11). It clearly shows how the wave function, near $x = 0$, varies within a distance of the order $\mathcal{O}(\xi)$ [52, 53]. Interestingly enough, the healing length also defines the size of fundamental nonlinear excitations [9], such as vortices or solitons (see Section 2.3). Hence, the validity of the GPE is restricted to scales larger than the healing length (see below).

1.1.3 Thomas-Fermi approximation

In the presence of repulsive interactions ($a_s > 0$), when the size of the condensate is large compared to the healing length ($R \gg \xi$) and the density varies smoothly over space, the kinetic term in Eq. (1.9) becomes negligible compared to the other energy terms. Under this approximation, known as the Thomas-Fermi regime, the GPE (1.9) takes a compact form for

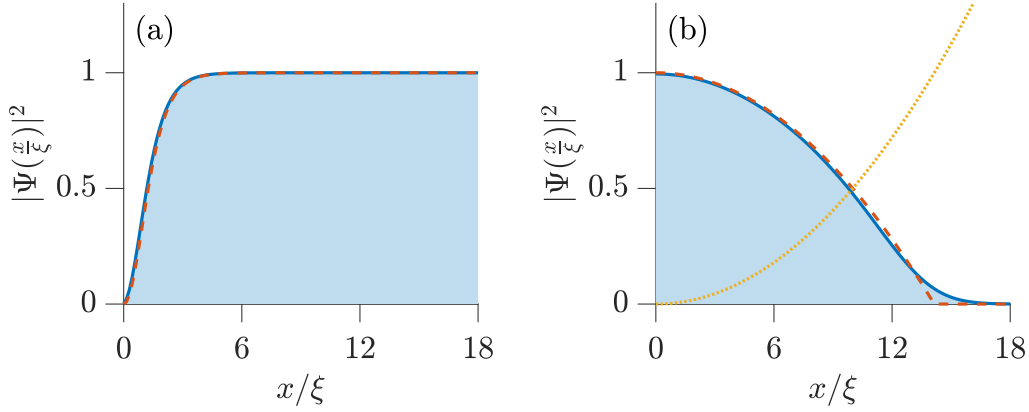


FIGURE 1.1: (a) Blue area depicts the density profile of a 1D BEC in a half-box potential. Around $x = 0$, the density varies on the order of the healing length, $\mathcal{O}(\xi)$. Red dashed line corresponds to Eq. (1.11). (b) Blue area depicts the density profile of a 1D BEC in a harmonic potential for $x > 0$. Red dashed line corresponds to the Thomas-Fermi profile, $|\Psi_{\text{TF}}(x/\xi)|^2$ (1.12). Yellow dotted line depicts the 1D harmonic potential, $V(x)$ (1.16).

which the ground-state wave function can easily be found³,

$$\Psi_{\text{TF}}(\mathbf{r}) = \sqrt{\frac{\mu - V(\mathbf{r})}{g}} \Theta(\mu - V(\mathbf{r})), \quad (1.12)$$

where $\Theta(\cdot)$ is the Heaviside step function [52, 54]. An example is provided in Fig. 1.1(b) for a 1D BEC trapped in a harmonic confinement (see below).

In a uniform system ($V = 0$), it is easy to see that $\Psi(\mathbf{r})$ is constant, and the chemical potential is given by $\mu = gn$. In this system, the speed of sound $c = \sqrt{\mu/m}$ is also easily derived from thermodynamic relations⁴. On the other hand, in trapped systems, the chemical potential reads $\mu = gn + V(\mathbf{r})$. As an example, in the presence of a harmonic confinement, $V(\mathbf{r}) = m\omega^2 \mathbf{r}^2/2$, it can be shown that [187]

$$\mu_{\text{TF}} = \frac{\hbar\omega}{2} \left(\frac{15N_0 a_s}{a} \right)^{2/5}. \quad (1.13)$$

Here, $a = \sqrt{\hbar/m\omega}$ and $\hbar\omega$ are the characteristic length and energy scales of the harmonic trap, respectively. Additionally, the size of the condensate is given by the Thomas-Fermi radius [188],

$$R_{\text{TF}} = \sqrt{\frac{2\mu_{\text{TF}} a^2}{\hbar\omega}}. \quad (1.14)$$

To this end, we can classify the length scales of an isotropically trapped BEC as follows:

$$R \gg a \gg \xi \gg n^{-1/3} \gg a_s. \quad (1.15)$$

³A rigorous derivation of the exact ground-state wave function of a trapped weakly interacting Bose gas can be found in the work by Lieb [186].

⁴The speed of sound is given by $c = \sqrt{\frac{\mathcal{V}}{m} \frac{\partial P_0}{\partial N}}$, where $P_0 = -\frac{\partial E_N}{\partial \mathcal{V}}$, \mathcal{V} is the volume of the system, and we used $\mu = \partial E_N / \partial N$.

1.1.4 Dimensionality reduction

To reduce the dimensionality of a condensate, it is necessary to modify its confinement. In general, most experiments employ harmonic trapping potentials to confine BECs [166, 189]. These can be written as

$$V(\mathbf{r}) = V(x) + V(y) + V(z) = \frac{1}{2}m(\omega_x^2 x^2 + \omega_y^2 y^2 + \omega_z^2 z^2). \quad (1.16)$$

Experimentally, the three different trapping frequencies can be modified independently from each other. In what follows, we assume $\omega_y = \omega_z = \omega_\perp$. In an isotropic trap, i.e., $\omega_x \approx \omega_\perp$, the condensate is almost spherical, while in an anisotropic one the condensate can be either disc-shaped ($\omega_x > \omega_\perp$) or cigar-shaped ($\omega_x < \omega_\perp$). The latter cases are particularly interesting when the trap is highly anisotropic and the condensates can be assumed to be quasi-2D ($\omega_x \gg \omega_\perp$) and quasi-1D ($\omega_x \ll \omega_\perp$).

In light of this thesis, we focus on quasi-1D cigar-shaped BECs, and hereafter we define the characteristic length scale of the condensate in terms of the transverse harmonic oscillator length as $a_\perp = \sqrt{\hbar/m\omega_\perp}$. In order to obtain an effective 1D system we need to avoid excitations in the transverse dimensions, which requires a tight confinement, i.e., $a_\perp < \xi$, $\hbar\omega_\perp > \mu$. The latter is equivalent to $\omega_x/\omega_\perp \ll 1$, with typical values ranging between 0.1 and 0.01 [9, 10, 54]. This allows to decompose the macroscopic wave function Ψ into longitudinal and transverse degrees of freedom.

$$\Psi(\mathbf{r}, t) = \psi(x, t)\chi(y, z)e^{-i\mu t/\hbar} \quad (1.17)$$

with $\int \chi(y, z)dydz = 1$.

Inserting Eq. (1.17) in Eq. (1.7), we can then integrate out the transverse degrees of freedom by multiplying the expression from the left with $\chi^*(y, z)$ and solve the auxiliary problem

$$\left[-\frac{\hbar^2}{2m}\nabla_\perp^2 + V(y) + V(z) \right] \chi(y, z) = 0 \quad (1.18)$$

with $\nabla_\perp^2 = \partial_y^2 + \partial_z^2$, so that

$$\chi(y, z) = \frac{1}{\sqrt{\pi}a_\perp} \exp\left(-\frac{y^2 + z^2}{2a_\perp^2}\right). \quad (1.19)$$

As a result we obtain the one-dimensional GPE,

$$i\hbar\frac{\partial}{\partial t}\Psi(x, t) = \left[-\frac{\hbar^2}{2m}\frac{\partial^2}{\partial x^2} + V(x) + g|\Psi(x, t)|^2 \right] \Psi(x, t). \quad (1.20)$$

Here, g is now the effective one-dimensional interaction strength of the form

$$g = \frac{4\pi\hbar a_s}{m} \int dydz |\chi(y, z)|^4 = 2\hbar\omega_\perp a_s. \quad (1.21)$$

It is important to have in mind that the dimensionality reduction presented above should be

considered as the 1D limit of the 3D mean-field theory, rather than a genuine 1D model [190]. In a more rigorous derivation the contribution of the transverse degrees of freedom should also be taken into account [191–193]. Besides, if $a_{\perp} \sim a_s$, then Eq. (1.21) needs a correction term to account for the so-called confined induced resonance [194].

The 1D GPE (1.20) is the equation that describes solitons and captures soliton dynamics in one-dimensional BECs. More precisely, under the following change of variables, $x \rightarrow \sqrt{2}a_{\perp}x'$, $t \rightarrow t'\omega_{\perp}^{-1}$ and $|\psi|^2 \rightarrow |\Psi|^2a_s^{-1}$, and by setting $V(x) = 0$, we obtain the nonlinear Schrödinger equation (NLS),

$$i\partial_t\Psi = -\partial_x^2\Psi + 2\nu|\Psi|^2\Psi, \quad (1.22)$$

where we dropped the primes, and the spatial and time dependency. The NLS is a nonlinear partial differential equation admitting soliton solutions [35]. The NLS and its vector forms as analogs of the GPE and its multi-component variants (see below) will be further discussed in Chapter 2.

1.2 Multi-component Bose-Einstein Condensates

With the constant improvement of magneto-optical trapping and cooling techniques, it did not take long until the first realization of condensates consisting of bosonic mixtures was achieved, either of the same [73, 74] or different [77, 78] atomic species. When a BEC is trapped in a magnetic field, its internal (spin) degrees of freedom are virtually frozen. Condensates composed of two magnetically trapped hyperfine states of the same atomic species are usually referred to as a *pseudo*-spinor BEC. On the other hand, in an optical trap the potential exerts the same force independently of the magnetic sublevel, thence making it possible to realize a condensate with different Zeeman spin sublevels of the same hyperfine state in what is called a spinor BEC [74–76].

The $2F + 1$ governing equations of motion for a multi-component BEC can be derived in a similar manner as the GPE (1.7) from the Hamiltonian (1.1) for bosons with spin F ⁵ [54],

$$\begin{aligned} \hat{\mathcal{H}} = & \int d\mathbf{r} \sum_{m_F=-F}^F \hat{\Psi}_{m_F}^{\dagger}(\mathbf{r}) \left[-\frac{\hbar^2}{2m} \nabla^2 + V(\mathbf{r}) - pm_F + qm_F^2 \right] \hat{\Psi}_{m_F}(\mathbf{r}) \\ & + \frac{1}{2} \int d\mathbf{r}d\mathbf{r}' \sum_{\mathcal{F}} \sum_{\mathcal{M}=-\mathcal{F}}^{\mathcal{F}} A_{\mathcal{F},\mathcal{M}}^{\dagger}(\mathbf{r},\mathbf{r}') U^{(\mathcal{F})}(\mathbf{r}-\mathbf{r}') A_{\mathcal{F},\mathcal{M}}(\mathbf{r},\mathbf{r}'). \end{aligned} \quad (1.23)$$

Here, $\hat{\Psi}_{m_F}^{\dagger}$ and $\hat{\Psi}_{m_F}$ are the creation and annihilation field operators of a boson with magnetic quantum number $m_F = F, F-1, \dots, -F$. Additionally, p and q are the linear and quadratic Zeeman terms, respectively, accounting for the hyperfine interaction between the nuclear and electronic magnetic moments. Moreover, $U^{(\mathcal{F})}(\mathbf{r}-\mathbf{r}')$ describes the interatomic interactions

⁵Here, we refer to the hyperfine spin of the atoms $F = |S \pm I|$, where S and I denote the electronic and nuclear spins, respectively.

for the total spin- \mathcal{F} channel ,

$$U^{(\mathcal{F})}(\mathbf{r} - \mathbf{r}') = \frac{4\pi\hbar^2 a_{\mathcal{F}}}{m} \delta(\mathbf{r} - \mathbf{r}'). \quad (1.24)$$

with $a_{\mathcal{F}}$ denoting the scattering length of the spin- \mathcal{F} channel,

$$A_{\mathcal{F},\mathcal{M}}(\mathbf{r}, \mathbf{r}') = \sum_{m_F, m_{F'} = -F}^F \langle \mathcal{F}, \mathcal{M} | F, m_F; F, m_{F'} \rangle \hat{\Psi}_{m_F}(\mathbf{r}) \hat{\Psi}_{m_{F'}}(\mathbf{r}'), \quad (1.25)$$

is an operator that annihilates a pair of bosons with total spin $\mathcal{F} = 0, 2, \dots, 2F$ and total magnetic number $\mathcal{M} = \mathcal{F}, \mathcal{F} - 1, \dots, -\mathcal{F}$ at positions \mathbf{r} and \mathbf{r}' , $\langle \mathcal{F}, \mathcal{M} | F, m_F; F, m_{F'} \rangle$ are the Clebsch-Gordan coefficients, and

$$\sum_{\mathcal{F}} \sum_{\mathcal{M} = -\mathcal{F}}^{\mathcal{F}} |\mathcal{F}, \mathcal{M}\rangle \langle \mathcal{F}, \mathcal{M}| = \hat{\mathbb{1}}, \quad (1.26)$$

with $\hat{\mathbb{1}}$ being the identity operator.

1.2.1 Coupled Gross-Pitaevskii Equation

Assuming $F = 1/2$ and ignoring the Zeeman terms in Eq. (1.23), we obtain a pair of coupled Gross-Pitaevskii equations (CGPE) for a two-component or pseudo-spinor BEC of the form [53, 195]

$$i\hbar \frac{\partial}{\partial t} \Psi_j(\mathbf{r}, t) = \left[-\frac{\hbar^2}{2m} \nabla^2 + V(\mathbf{r}) + \sum_{k=1}^{\mathcal{N}=2} g_{jk} |\Psi_k(\mathbf{r}, t)|^2 \right] \Psi_j(\mathbf{r}, t), \quad (1.27)$$

where $j = \{1, 2\}$ denotes each component and $g_{jk} = 4\pi\hbar^2 a_{jk}/m$ stands for the inter- ($j \neq k$) and intra- ($j = k$) component interaction strength given by the scattering length a_{jk} .

A common protocol to prepare a pseudo-spinor BEC is a two-photon transition driven between two hyperfine states of the atomic species [196, 197]. A pulse of microwave radiation with a frequency slightly detuned from the Zeeman splitting between the two states connects them, transferring atoms from one to the other. For this fast process, the latter can be written in a time-independent form as

$$\begin{pmatrix} \Psi'_1 \\ \Psi'_2 \end{pmatrix} = \exp \left[-i \frac{p_0}{2} \begin{pmatrix} 0 & 1 \\ 1 & 0 \end{pmatrix} \right] \begin{pmatrix} \Psi_1 \\ \Psi_2 \end{pmatrix}, \quad (1.28)$$

where the primes denote the new states and p_0 determines the amount of particles transferred, e.g., $p_0 = \pi/2$ results in a 50% transfer. Of course, this protocol can be used for both mixing and demixing of components [198, 199]. In the presence of an external magnetic-field gradient, a different additional phase accumulates at each point of the condensate, which, after applying a $\pi/2$ -pulse, describes a periodic magnetization pattern [A4, 200].

In the absence of a trapping potential ($V = 0$), the competition between the inter- and intracomponent interactions in Eq. (1.27) of purely repulsive systems ($g_{jk} > 0$) defines the

immiscibility of the condensate [201],

$$\Delta \equiv (g_{12}g_{21} - g_{11}g_{22})/g_{11}^2 > 0. \quad (1.29)$$

When this condition is fulfilled, the repulsion between components dominates over the self-repulsion and the ground state is not mixed, but rather phase separated [202–206], either as a shell or domain walls. The phase transition from the miscible ($\Delta < 0$) to the immiscible ($\Delta > 0$) regime is of second order [207] and its properties and dynamics [208–217] can be explored by tuning the interaction strengths by means of Feshbach resonances [59–66]. Such a level of control has further allowed the study of two-component solitons of different kind [82, 84].

In these setups, it is also common to study mixtures of different atomic species [A5, 218–220], specially in the realization of quantum droplets [179, 184, 185, 221] and dipolar supersolids [162, 222, 223]. Currently, experiments have already produced ^{41}K - ^{87}Rb [80], ^{23}Na - ^{133}Cs [81], and highly mass-imbalanced ^{174}Yb - ^7Li bosonic mixtures [79]. In this heteronuclear mixtures, it is important to account for the different masses of the atoms, m_j , in the kinetic, potential and interaction terms of the CGPE (1.27). In the latter, the interaction strength reads now $g_{jk} = 2\pi\hbar^2 a_{jk}/M_{jk}$, where $M_{jk} = m_j m_k / (m_j + m_k)$ is the reduced mass.

Interestingly, the CGPE can be easily generalized to any number of (non-spinor) components \mathcal{N} [224]. For instance, it has been used to describe the properties of three-component BECs [225]. These triple mixtures present new phenomena not found in two-component systems, such as surfactant behaviour [226] or Borromean supercounterfluidity [227], as well as generalizations of soliton complexes [A1, 228–231] and rogue waves [232–234].

1.2.2 Spinor Gross-Pitaevskii Equation

Considering now an $F = 1$ spinor BEC, the spinor GPE reads [54, 235, 236]

$$\begin{aligned} i\hbar \frac{\partial}{\partial t} \Psi_{m_F}(\mathbf{r}, t) = & \left[-\frac{\hbar^2}{2m} \nabla^2 + V(\mathbf{r}) - pm_F + qm_F^2 \right] \Psi_{m_F}(\mathbf{r}, t) \\ & + g_n \sum_{m'_F=-1}^{+1} |\Psi_{m'_F}|^2 \Psi_{m_F}(\mathbf{r}, t) \\ & + g_s \sum_{m'_F=-1}^{+1} \langle \hat{\mathbf{f}} \rangle \cdot \mathbf{f}_{m_F, m'_F} \Psi_{m_F}(\mathbf{r}, t), \end{aligned} \quad (1.30)$$

where

$$g_n = \frac{4\pi\hbar^2}{m} (2a_2 + a_0), \quad g_s = \frac{4\pi\hbar^2}{m} (a_2 - a_0), \quad (1.31)$$

are the mean-field and spinor interaction strength, respectively, defined through the scattering lengths $a_{\mathcal{F}}$ of the $\mathcal{F} = 0$ and $\mathcal{F} = 2$ spin channels. For example, in ^{87}Rb BECs these values are $a_0 = 101.78 a_B$ and $a_2 = 100.4 a_B$ [236, 237], in units of the Bohr radius a_B .

Additionally, $\langle \hat{\mathbf{f}} \rangle = (\langle \hat{f}_x \rangle, \langle \hat{f}_y \rangle, \langle \hat{f}_z \rangle)$,

$$\langle \hat{f}_\alpha \rangle = \sum_{m_F, m'_F=-1}^{+1} \Psi_{m'_F}^* (f_\alpha)_{m_F, m'_F} \Psi_{m_F} \quad (\alpha = x, y, z), \quad (1.32)$$

with

$$f_x = \frac{1}{\sqrt{2}} \begin{pmatrix} 0 & 1 & 0 \\ 1 & 0 & 1 \\ 0 & 1 & 0 \end{pmatrix}, \quad f_y = \frac{i}{\sqrt{2}} \begin{pmatrix} 0 & -1 & 0 \\ 1 & 0 & -1 \\ 0 & 1 & 0 \end{pmatrix}, \quad f_z = \begin{pmatrix} 1 & 0 & 0 \\ 0 & 0 & 0 \\ 0 & 0 & -1 \end{pmatrix}, \quad (1.33)$$

being the spin-1 matrices. The last term of Eq. (1.30) accounts for the spin interactions among the three components, whose energy contribution contains the term

$$g_s \int d\mathbf{r} (\Psi_0^\dagger \Psi_0^\dagger \Psi_+ \Psi_- + \Psi_+^\dagger \Psi_-^\dagger \Psi_0 \Psi_0) \quad (1.34)$$

describing spin-mixing dynamics [76, 238–240]. Note that for simplicity, we employed $m_{m_F} = \{+, 0, -\}$. These stem from collisions between two atoms in the Ψ_0 state and two atoms in the Ψ_\pm states (one each), and vice versa. Consequently, the number of atoms in each component is not constant, but the total, $N = N_+ + N_0 + N_-$, is. Besides, spin-1 BECs possess an additional conserved quantity

$$M = |\Psi_+|^2 - |\Psi_-|^2, \quad (1.35)$$

referred to as the total magnetization of the system.

Depending on the sign of g_s , the ground state of the condensate can be ferromagnetic ($g_s < 0$) or anti-ferromagnetic ($g_s > 0$). In ferromagnetic BECs the energy is minimized by maximizing the average spin. On the other hand, in anti-ferromagnetic BECs the energy is minimized by minimizing the average spin. Together with the possibility to tune the linear, p , and quadratic, q , Zeeman terms, spinor BECs offer a wide range of different phases and spin domains [74], polarized states and domain walls [241], multicomponent vortices [242, 243], and solitons of all kinds, from bright [244–247], dark [248] and gap [249] solitons to more complex dark-bright structures [250, 251], as well as generalizations thereof in 2D [252] and $F = 2$ spin BECs [253]. Interestingly, and only in the anti-ferromagnetic regime, a new family of *magnetic* solitons was found [254, 255]. These solitons consist only of the Ψ_\pm states and, contrary to classic dark-bright solitons (see Section 2.3.2), they must have a non-zero velocity [256–258]. Moreover, in the presence of spin-mixing dynamics, an intrinsic beating is induced in the motion of spinor solitons [A1], which in two-component systems can only be achieved by means of an external Rabi coupling [259–261].

Chapter 2

Solitons

“I was observing the motion of a boat which was rapidly drawn along a narrow channel by a pair of horses, when the boat suddenly stopped - not so the mass of water in the channel which it had put in motion; it accumulated round the prow of the vessel in a state of violent agitation, then suddenly leaving it behind, rolled forward with great velocity, assuming the form of a large solitary elevation, a rounded, smooth and well-defined heap of water, which continued its course along the channel apparently without change of form or diminution of speed. I followed it on horseback, and overtook it still rolling on at a rate of some eight or nine miles an hour, preserving its original figure some thirty feet long and a foot to a foot and a half in height. Its height gradually diminished, and after a chase of one or two miles I lost it in the windings of the channel. Such, in the month of August 1834, was my first chance interview with that singular and beautiful phenomenon which I have called the Wave of Translation.”

Report on Waves (1844)

John Scott Russell

A solitary wave, or soliton, is a nonlinear excitation stemming from the balance between dispersion and nonlinearity. The study of solitary waves started with the water-tank wave experiments of John Scott Russell in his backyard, after his encounter with one of such waves in 1834 at the Union Canal (Edinburgh). In his work, *Report on Waves* [1], Russell describes the *Wave of Translation* as a long-lived traveling wave that does not merge with others, whose velocity is given by its size and its width by the depth of the water. Unfortunately for Russell, his *Wave of Translation* did not fit into the Newtonian wave theory of the time and he would have to wait more than three decades before J. V. Boussinesq [262] and Lord Rayleigh [263] theoretically supported Russell’s experiments by introducing the equation governing those waves, later known as the Korteweg-de Vries equation (KdV) [264]. Solitary waves were studied from a purely hydrodynamic perspective until the 1960s, when the KdV started to appear in other physical systems — such as plasma physics, internal waves, lattice dynamics, etc. [3]. Then, in 1965, Zabusky and Kruskal found that, surprisingly, the solitary waves described by the KdV had particle-like elastic interactions [265], which granted these waves the name of *solitons*. This interesting discovery set the starting point for a series of studies in soliton theory that still continue to this day [7, 12, 31, 35, 36, 41, 47, 84, 266].

In this chapter we introduce the concept of solitons from a general perspective. As we shall see, solitons are solutions of nonlinear partial differential equations (PDEs) integrable by the inverse scattering transform (IST). First, we provide a simple description of the IST formalism. Then, we introduce the nonlinear Schrödinger equation (NLS). This nonlinear PDE is the analog of the GPE introduced in Section 1.2 and possesses the soliton solutions studied in BECs. These solutions are presented subsequently. In the last section, we finalize the chapter discussing some of the considerations to bear in mind when studying solitons in BECs.

2.1 Inverse Scattering Transform

After Zabusky and Kruskal discovered the particle-like properties of solitons [265], the growing interest on these wave forms led to the development of a powerful mathematical formalism known as the IST [33]. The IST allows to solve certain nonlinear PDEs for a particular initial value problem. Typically, these nonlinear PDEs are governing equations of physical systems describing the propagation of waves in nonlinear media. If a nonlinear PDE is solvable by the IST, it is said that it is integrable, and thus admits soliton solutions. The IST is an extensive and complex formalism [34–40, 42–46], and a detailed description of the methodology is beyond the scope of this thesis¹. Nonetheless, in this section, we bring forward the basic concepts behind the IST.

The idea behind the IST — also referred to as the nonlinear Fourier transform [33]— is to linearize a nonlinear PDE,

$$q_t = F[x, t, q, q_x, q_{xx}, \dots], \quad (2.1)$$

by a nontrivial change of variables from the physical space to a scattering space and obtain global information about the structure of the solution. Therefore, the first requisite of the IST is to find a pair of linear problems associated to the nonlinear PDE, i.e.,

$$\phi_x = \mathbf{X}\phi, \quad \phi_t = \mathbf{T}\phi, \quad (2.2)$$

so that their compatibility condition results in the nonlinear PDE. These linear problems (2.2) are known as a Lax pair [32]. They are constructed by a pair of linear operators, \mathbf{X} and \mathbf{T} , and ϕ is a matrix eigenvector. Generally, \mathbf{X} and \mathbf{T} are matrix functions of the complex field $q(x, t)$, its spatial derivatives, and a time-independent complex parameter k . Also, they must satisfy the compatibility condition $\mathbf{X}_t - \mathbf{T}_x = \mathbf{X}\mathbf{T} - \mathbf{T}\mathbf{X}$ for any solution $q(x, t)$ of the nonlinear PDE.

The first equation of the Lax pair (2.2) is the scattering problem. Its associated eigenvalues and eigenfunctions depend on the scattering parameter k and $q(x, 0)$, which contains the initial physical data. These eigenfunctions are then employed to construct a set of solutions ϕ satisfying the initial value problem. Such solutions are related to each other through

¹For those interested in a complete description of the IST, we recommend the works of Ablowitz and Prinari [41, 47] and references therein.

the scattering matrix $\mathbf{S}(k, 0)$, which contains the scattering data. Importantly here, \mathbf{S} is independent of the initial physical parameters. The second equation of the Lax pair is associated to the time evolution of the scattering data and it can be explicitly solved. This way, one can obtain the time-evolved scattering data $\mathbf{S}(x, t)$ from which to reconstruct the eigenfunctions, and thus recover the original (evolved) physical data $q(x, t)$.

In short, the IST formalism can be summarized as follows [36]:

1. the direct problem:
transforming the initial physical data $q(x, 0)$ into scattering data $\mathbf{S}(k, 0)$.
2. time evolution:
obtaining the time-evolved scattering data $\mathbf{S}(k, t)$ from the initial scattering data $\mathbf{S}(k, 0)$ by solving simple evolution equations.
3. the inverse problem:
recovering the time-evolved physical data $q(x, t)$ from the time-evolved scattering data $\mathbf{S}(k, t)$.

In some cases, instead of solving an initial value problem, the IST also allows to obtain solutions by directly solving the inverse problem, if the form of the scattering space is known. For example, soliton and multisoliton solutions of the NLS can be constructed employing this approach [41, 47].

2.2 Nonlinear Schrödinger Equation

Among the different integrable nonlinear PDEs admitting soliton solutions [35], we are particularly interested in the NLS,

$$iq_t + q_{xx} - 2\nu|q|^2q = 0. \quad (2.3)$$

Here, the subscripts t and x denote partial derivation with respect to time and space, respectively. The NLS is a dimensionless nonlinear PDE which describes the evolution of complex field envelopes $q = q(x, t)$ in nonlinear media [9], with either a focusing ($\nu = -1$) or defocusing ($\nu = +1$) nonlinearity. Additionally, it possesses an infinite number of conserved quantities and it is integrable via the inverse scattering transform [41, 47]. Originally, the NLS was derived in the context of superconductivity [267, 268] and superfluidity [269]. Later on, it was also derived in the context of Bose gases [50, 51], but became physically relevant when it was related to the self-focusing phenomena of electromagnetic beams in nonlinear media [270–272]. From that point onward, the NLS has also appeared in a wide range of physical systems, e.g., water-waves [273, 274], plasma physics [275], and nonlinear optics [18, 19], among others.

Equation (2.3) is also referred to as the scalar NLS, as it is describing only one complex field. However, in some physical systems, it arises the necessity to describe multiple fields. The vector NLS (VNLS),

$$i\mathbf{q}_t + \mathbf{q}_{xx} - 2\nu\|\mathbf{q}\|^2\mathbf{q} = 0, \quad (2.4)$$

also referred to as the coupled NLS, is the generalization of Eq. (2.3) to a system with \mathcal{N} complex fields [44, 276]. Here, $\|\cdot\|$ is the Euclidian norm and \mathbf{q} is an \mathcal{N} -component vector. The VNLS was first introduced in 1973 by Manakov [277], in the context of nonlinear optics, to describe two light beams with different polarizations. Hence, a binary system is also referred to as a Manakov system. As for bosonic gases, the VNLS is the CGPE (1.27) analog used to describe two- and three-component systems [9, 84].

In multi-component BECs composed of different hyperfine states of the same atomic species, it is also important to take into account spin interactions [236, 278]. For spin-1 BECs, another form of the NLS was proposed [244, 245]. Due to the SU(2) symmetry of the spin exchange interactions present in the nonlinear terms of the SGPE (1.30), its NLS analog can be expressed in the following matrix form

$$iQ_t + Q_{xx} - 2\nu QQ^\dagger Q = 0, \quad (2.5)$$

where

$$Q(x, t) = \begin{pmatrix} q_+(x, t) & q_0(x, t) \\ q_0(x, t) & q_-(x, t) \end{pmatrix}, \quad (2.6)$$

is a 2×2 matrix-valued function, Q^\dagger is the Hermitian conjugate, and the subscripts $\{+, 0, -\}$ denote each of the three hyperfine states of the atomic species conforming the condensate. In this case, Eq. (2.5) is referred to as the matrix NLS (MNLS) [46].

2.3 Soliton solutions

2.3.1 Scalar solitons

The scalar NLS (2.3) possesses two of the most renown soliton solutions: the *bright* soliton and the *dark* soliton. While the bright soliton consists of a simple hump, the dark soliton consists of a dip on top of a constant background.

In 1972 Zakharov and Shabat solved the focusing NLS ($\nu = -1$) with zero boundary conditions, i.e., $q(x, t) \rightarrow 0$ as $x \rightarrow \pm\infty$, and obtained the bright soliton solution [48] given by

$$q_b(x, t) = 2i\eta \operatorname{sech}[2\eta(x - 2\xi t - x_0)] e^{-2i\xi x - 4i(\xi^2 - \eta^2)t}, \quad (2.7)$$

where 2η denotes the amplitude and inverse width of the soliton, $v = 2\xi$ is the soliton velocity, and x_0 is an arbitrary parameter. This solution depends on two independent variables, η and ξ , which implies that it is possible to have bright solitons of different amplitudes moving at the same speed, and vice versa. An example is depicted in Fig. 2.1(a).

One year later, in 1973, Zakharov and Shabat solved the defocusing NLS ($\nu = +1$) under non-zero boundary conditions, i.e., $q(x, t) \rightarrow q_0$ as $x \rightarrow \pm\infty$, and obtained the dark soliton solution [49], given by

$$q_d(x, t) = q_0(\cos \beta + i \sin \beta \tanh[q_0 \sin \beta(x + 2q_0 \cos \beta t - x_0)]) e^{-2iq_0^2 t}, \quad (2.8)$$

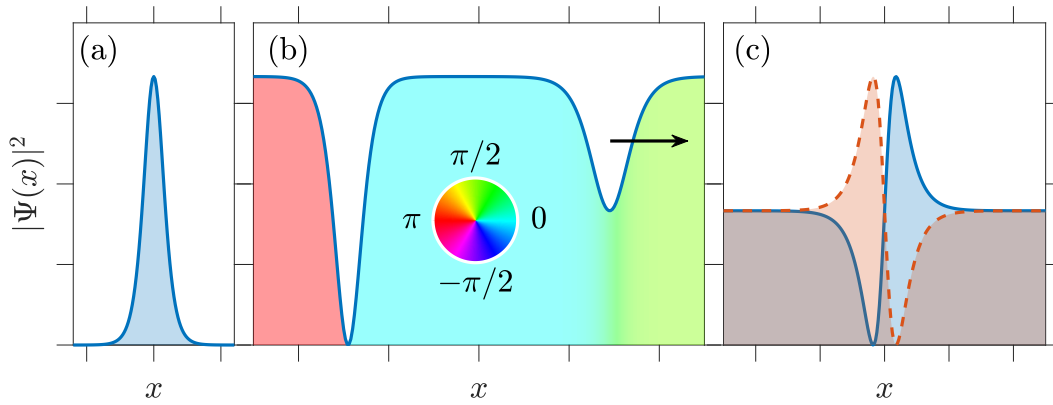


FIGURE 2.1: (a) Density profile of a bright soliton (2.7). (b) Density profile of two dark solitons (2.8). Left soliton is a static *black* soliton ($\beta = \pi/2$). Right soliton is a moving *gray* soliton ($\beta = 3\pi/4$). The colormap illustrates the characteristic phase-jump at their minima. (c) Density profile of a two-component beating DB soliton (1.28). The *beating* is a result from the exchange of waveforms between the red and blue components, with a characteristic frequency ω_b .

where q_0 is the amplitude of the background, and β is the phase angle. The latter is the only free parameter of the dark soliton solution. It determines its velocity, $v = -2q_0 \cos \beta$, inverse width² and amplitude, $q_0 \sin \beta$, and constrains the dark soliton solutions to $0 < \beta \leq \pi$. When $\beta = \pi/2$, the dark soliton solution is static ($v = 0$) and its amplitude is maximal. This particular solution is called a *black* soliton, and presents a characteristic phase-jump of π at its minima. On the contrary, if $\beta \neq \pi/2$, dark solitons have a finite velocity ($v \neq 0$) and are usually referred to as *gray* solitons. Opposite to bright solitons, the amplitude of a dark soliton decreases with its velocity. In the limit $\beta \rightarrow 0$, or $\beta \rightarrow \pi$, moving dark solitons approach their maximum velocity ($|v| \rightarrow q_0$), which coincides with the speed of sound (or light, depending on the physical system) in the medium ($c = q_0$). At the same time, its amplitude approaches zero. Hence, gray solitons are limited by their speed. Examples of a *black* and a *gray* soliton are provided in Fig. 2.1(b).

2.3.2 Vector solitons

In a binary or Manakov system, bright (2.7) and dark (2.8) solitons conform the building blocks of more exotic structures [82]. For instance, the focusing VNLS admits soliton solutions of the bright-bright type (BB) [253], while the defocusing VNLS admits soliton solutions of the dark-dark (DD) [259–261, 279], and dark-bright (DB) type [280–282]

Among them, DB solitons present interesting applications as quantum switches or splitters under the concept of waveguiding [7, 283, 284], with the dark soliton acting as an effective potential for the bright one. Interestingly, this solution was initially found by construction [285–289], as the development of the IST formalism for the VNLS remained an

²In the context of BECs, the width of a dark soliton is of the order of the healing length (see Section 1.1.2).

open problem until recently [38, 42]. The DB soliton solution has the form [42]

$$q_d(x, t) = q_0(\cos \beta + i \sin \beta \tanh[\eta(x + 2\xi t - x_0)])e^{i\beta + 2iq_0^2 t}, \quad (2.9a)$$

$$q_b(x, t) = i \sin \beta \sqrt{q_0^2 - |z|^2} \operatorname{sech}[\eta(x + 2\xi t - x_0)]e^{i\xi x - i(\xi^2 - \eta^2)t + 2iq_0^2 t}. \quad (2.9b)$$

where $q_d(x, t)$ is the dark component and $q_b(x, t)$ is the bright one. In this case, the DB soliton is uniquely characterized by the uniformization variable $z = |z|e^{i\beta} = \xi + i\eta$, which is associated to the discrete eigenvalues of the scattering problem of the IST (see Chapter 4) with the caveat $|z| < q_0$. Additionally, it provides the amplitudes $A_d = q_0 \sin \beta$ and $A_b = \sin \beta \sqrt{q_0^2 - |z|^2}$ of the dark and the bright solitons, respectively, as well as their common inverse width, η , and velocity, $v = -2\xi$.

Interestingly, the defocusing VNLS admits a dynamical soliton solution, consisting of SU(2)-rotated solutions of dark (2.9a) and bright (2.9b) solitons, which can be written as [259–261]

$$\mathbf{q}(x, t) = \begin{pmatrix} A & -B^* \\ B & A^* \end{pmatrix} \begin{pmatrix} q_d(x, t) \\ q_b(x, t) \end{pmatrix}, \quad (2.10)$$

with $A, B \in \mathbb{C}$ and $|A|^2 + |B|^2 = 1$. In this solution, both components present a dip next to a hump on top of a non-zero background, and each component's dip is located at the same position as the other component's hump, and vice versa [see Fig. 2.1(c)]. In the literature, this structure is known as a beating soliton because the dips and the humps of each component exchange positions over time with a characteristic intrinsic oscillation frequency, $\omega_b = \xi^2 + \eta^2$.

Exact solutions of the three-component VNLS have also been found by means of the IST [228, 290]. In [A1] we derived soliton solutions of the dark-dark-bright and dark-bright-bright type by employing Eqs. (2.9) as an ansatz to the three-component VNLS. In this case, the soliton solutions are also given by Eqs. (2.9), but choosing β and A_b as the free soliton parameters. Therefore, its inverse width and velocity are given by

$$\eta^2 = \sum_d A_d^2 - \sum_b A_b^2 > 0, \quad \text{and} \quad v = 2\xi = 2\eta \frac{\cos(\beta)}{\sin(\beta)}, \quad (2.11)$$

respectively, where the summations are performed over all the dark (d) and bright (b) solitons in the system. Note also that q_0 and A_b can be different for each component. More importantly, the above generalization can be extended to any \mathcal{N} -component VNLS [224, 291].

2.3.3 Matrix Solitons

The MNLS (2.5) was derived to describe spinor BECs, in analogy to the SGPE (1.30). It is also integrable by the IST and admits soliton solutions [43, 46, 244, 245, 248, 253, 292]. Spinor solitons are unique. Due to the SU(2) symmetry of the spin-exchange interactions (see Section 1.2.2), they have no analog in other systems, as compared to the scalar or vector solitons which are easily found in both BECs and nonlinear optics [6–8]. Moreover, the

interplay between the mean-field and spin interactions, as well as the magnetization of the system (1.35), results in a vast amount of solutions, too large to be covered in this section. Hence, we refer the interested reader to the references provided above.

Here, we would like to point out that, albeit being employed in analogy to the SGPE, the MNLS solutions impose an impractical physical condition of equal mean-field and spin interaction strengths, $\nu = g_n = g_s$ (1.31). Note that in actual spin-1 BECs $g_s/g_n \sim 10^{-3}$ [236, 237]. Nevertheless, physically relevant experimental [293] and theoretical works [249, 294–297] have found classic as well as new families of solitons, such as magnetic solitons [254–258], and ways to excite beating solitons [A1].

2.4 Solitons in Bose-Einstein Condensates

So far in this chapter, we have introduced the concept of soliton as the mathematical solution of a particular nonlinear PDE integrable by the IST. More precisely, we have focused on the soliton solutions of the NLS. However, as we pointed out in Section 2.3.3, in some cases the NLS might not truly capture the nature of the physical system under study. Hence, in this section we aim to put into perspective the study of solitons in BECs.

BECs are described by the GPE (1.7) within the mean-field approximation (see Section 1.1). In general, the GPE is not integrable and does not possess exact soliton solutions. Not to mention, genuine soliton solutions are purely 1D objects. As discussed in Section 1.1.4, it is possible to realize quasi-1D cigar-shaped BECs employing adequate confinement techniques. Regardless, the transverse degrees of freedom are a relevant factor to take into account when considering the stability of dark solitons. For instance, they can suffer from the so-called *snake* instability [298] and decay into vortices [71, 72, 299–303]. Moreover, the GPE, and by extension the NLS and its soliton solutions, are only valid at zero temperature (see Section 1.1.1). Dynamics in finite-temperature systems have shown that moving dark solitons radiate sound waves [304, 305] due to the finite transverse confinement, and thus they dissipate over time [306–309]. Interestingly enough, soliton diffusion has been proposed as a signature analog of Hawking radiation [22].

In multi-component BECs, the different interaction strengths between components play a fundamental role in their stability and interactions [310–312]. In spite of that, the possibility to address the intensity of the interactions by means of Feshbach resonances [59–66] allows one to drive the system between the miscible and immiscible regimes (1.29), and even to effectively modify the nonlinearity of one of the components (see Chapter 6). It is in these regimes, i.e., outside of the integrable limit, where exotic structures like the dark-antidark soliton³ can emerge [83, 84, 294, 313, 314]. These structures have also been observed during DB soliton collisions beyond the mean-field approximation [315].

An additional factor present in BEC experiments is the external confinement, typically a harmonic trapping potential (1.16). Even in quasi-1D systems, the trapping potential in the longitudinal direction, although weak, is finite. This implies that the density decays as it reaches the extremes of the condensate. At the same time, it impedes the possibility to

³An antidark soliton consists of a bright soliton on top of a non-zero background.

create the constant background in which dark solitons live. In particular, unless it finds itself at the minima of the harmonic potential, a soliton oscillates and its motion can be described classically. In the case of bright solitons, their oscillations are given by the trapping frequency, $\omega_0 = \omega_x$ [68, 163, 316]. On the other hand, the frequency of a dark soliton oscillating in a harmonic trap is $\omega_0 = \omega_x/\sqrt{2}$ [317]. Similarly, the oscillating frequency of a DB soliton reads [318, 319]

$$\omega_0^2 = \frac{\omega_x^2}{2} \left(1 - \frac{N_b}{\sqrt{16 + N_b^2}} \right), \quad (2.12)$$

where $N_b = \int |q_b|^2 dx$ is the number of atoms conforming the bright soliton (2.9b). Note that in the limit $N_b \rightarrow 0$, the oscillation frequency of a dark soliton is recovered. In this regard, it has also been shown that, contrary to single dark or bright solitons, the symbiotic relation between the two in a DB soliton induces a change in their amplitudes during oscillations according to [A3]

$$\cos^2 \beta(t) = \cos^2 \beta \cos^2(\omega_0 t) + \frac{1}{2q_0^2} \omega_x^2 \left(\frac{v}{\omega_0} \right)^2 \sin^2(\omega_0 t), \quad (2.13)$$

where the parameter $\beta(t)$ defining the amplitudes [see Eq. (2.9)] is now time-dependent.

Nonetheless, the motion induced by the harmonic confinement is ideal to induce collisions between solitons. Solitons are well known for their particle-like properties [265]. The quality of preserving shape after collision, with only a change on their phase, allows to put their interactions under test [230, 320, 321]. Already from early works in nonlinear optics [7, 322, 323], it is known that the interaction between a pair of dark solitons is always repulsive [321, 324], while bright solitons repel each other if they are out-of-phase (OP), and attract if in-phase (IP) [316, 325, 326]. Yet, it has also been found that if quantum fluctuations are to be taken into account, the interaction is always repulsive independently of the relative phase [327]. On the contrary, in repulsive media, OP bright solitons attract each other [328]. This is relevant in the context of DB solitons, as the interplay between the repulsion of the dark solitons and the attraction of IP bright solitons allows for the formation of bound, or molecular, states of DB solitons in multi-component BECs [281, 310, 329].

In the presence of a harmonic confinement, the equilibrium position of two dark solitons is given by [324]

$$x_{\pm} = \pm \frac{1}{4q_0} w \left(\frac{32q_0^4}{\omega_0^2} \right), \quad (2.14)$$

where $w(u)$ is the Lambert's w function defined as the inverse of $u(w) = we^w$. When perturbed, they undergo harmonic oscillations. If the oscillations are IP, the oscillation frequency coincides with that of a single soliton, $\omega_{\text{IP}} = \omega_x/\sqrt{2}$. If they are OP, the frequency is given by

$$\omega_{\text{OP}}^2 = \omega_0^2 + 32q_0^2 e^{-4q_0|x_{\pm}|}. \quad (2.15)$$

In the case of DB solitons, the equilibrium position, as well as their motion, can not be easily characterized, as one needs to solve the equations of motion, $\ddot{x} = -\omega_0^2 x - F_{\text{DD}}(x) - F_{\text{BB}}(x) - 2F_{\text{DB}}(x)$, accounting for the interactions between the different components [315].

On a different side, ballistic head-on collisions between pairs of solitons can be derived within the IST formalism [224, 228, 276, 290, 330, 331]. While collisions between pairs of dark [332] or bright [333] solitons may seem rather trivial, when it comes to multi-component solitons, new scattering effects take place [224, 330]. For instance, depending on the incident velocity during DB soliton collisions, the scattered solitons can maintain shape, exchange shape, or experience mass-transfer [311].

In some cases, instead of a pair of soliton individuals, one can consider a system densely packed with solitons. If so, the interactions between them need to be understood from a statistical perspective. This ensemble is known as a soliton gas [334], and we further discuss it in Chapter 5.

Chapter 3

Rogue Waves

“Far from ridiculing the old sailors’ stories about enormous waves, modern research has confirmed that such monsters can occur, and that wave heights can exceed by an appreciable amount the maximum values which have been accepted in responsible circles.”

Severe Wave Conditions at Sea (1967)

Laurence Draper

The sighting of monstrous waves can be traced back in time to the stories of sailors who embarked to explore the oceans and in illustrations such as the famous *The Great Wave off Kanagawa* (1831). But stories of rogue waves — walls of water appearing out of nowhere — seemed to be mere exaggerations until the first scientific report on rogue waves appeared in 1964 [335]. In his report, Laurence Draper documented the records of the heights of waves gathered by the National Institute of Oceanography in the North Atlantic ocean, and described *freak* wave events, as he called them, with the highest recorded reaching around 20 meters. The 1st of January of 1995, the first official measurement of a rogue wave was recorded at the Draupner oil-drilling platform, 100 miles off shore from Norway, with a height of 26 meters [336].

The *Draupner* wave, or *New Year’s* wave, set the starting point in rogue-waves studies, coinciding with the launch of the first specialized satellites to survey the surface of the oceans — ERS-1 (1991), ERS-2 (1995) and ENVISAT (2002) —, which revealed that the appearance of these extreme events is much more frequent than it was expected [337–339]. For instance, between 1969 and 1994, at least 22 super-carriers were lost due to encounters with rogue waves [340], and in the last two decades more than 500 encounters have been reported [341, 342]. An encounter with a rogue wave is a threat to the integrity of vessels, offshore maritime structures, and to the lives of those onboard. Hence the interest of the scientific community in describing and understanding the formation of rogue waves.

Although there is no universal definition for a rogue wave [343], according to the maritime and oceanographic statistical definition, they are extreme wave events that *appear and disappear without a trace*, and at least twice as large as the significant wave height [340, 344]. Many of these phenomena are modeled by nonlinear PDEs [87]. In particular, rogue waves in deep waters are described by the focusing NLS with non-zero boundary conditions (NZBC) [345–351] and modifications thereof [352–355]. In general, the focusing NLS with

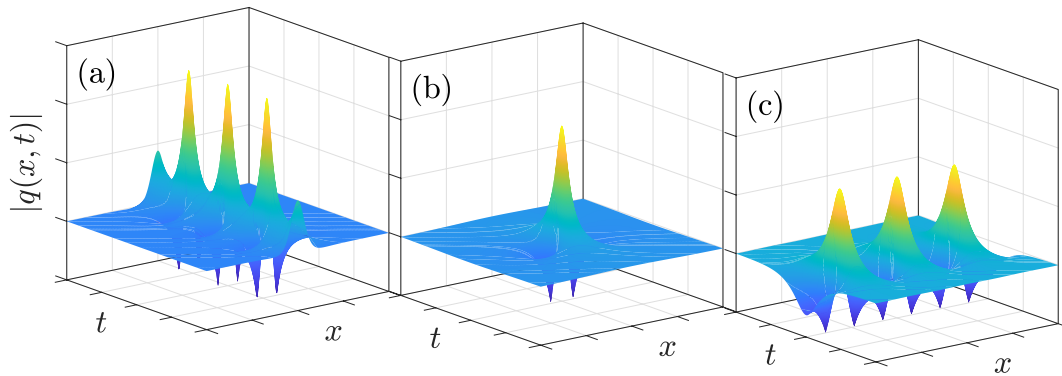


FIGURE 3.1: Family of solutions of the focusing NLS with NZBC candidates to rogue waves. (a) Kuznetsov-Ma breather; (b) Peregrine soliton; (c) Akhmediev breather.

NZBC is integrable by the IST [37, 356] and possesses a rich spectrum of soliton solutions, none of which is stationary [357]. Yet, under certain limits, they all reduce to a family of solutions known as the soliton breathers [358].

In this brief chapter, we present the family of soliton breathers and introduce the modulational instability (MI). The latter is an ubiquitous phenomenon in focusing nonlinear media [106, 108, 246, 260, 359–362] and one of the main mechanisms to explain the formation of rogue waves [90, 345, 363–365].

3.1 Soliton Breathers

Under adequate assumptions, deep-water waves can be described by the NLS [87]. In 1972, Zakharov and Shabat [48] solved the IST for the focusing NLS with zero boundary conditions, i.e., with the complex field $q(x, t) \rightarrow 0$ as $x \rightarrow \pm\infty$, and found the bright soliton solution (see Section 2.3.1). Then, Ma [366] extended the IST for the focusing NLS to the case with NZBC, i.e., $q(x, t) \rightarrow q_0 e^{2iq_0^2 t}$ as $x \rightarrow \pm\infty$. He found a solution, also previously found by Kuznetsov [367] in the context of unstable plasma, which can be written as

$$q_M(x, t) = \left[1 + \frac{2\mu^2 \cos(4\mu\eta q_0^2 t) + 2i\mu\eta \sin(4\mu\eta q_0^2 t)}{\eta \cosh(2\mu q_0 x) + \cos(4\mu\eta q_0^2 t)} \right] q_0 e^{2iq_0^2 t}, \quad (3.1)$$

with $\eta^2 = 1 + \mu^2$, and μ being a free parameter. Equation (3.1) is the Kuznetsov-Ma breather, a periodic solution in time and localized in space [see Fig. 3.1(a)]. Following from the Kuznetsov-Ma solution, Peregrine employed a double Taylor-series expansion around the amplitude peak [34] and found a new rational solution for the focusing NLS with NZBC, which reads [368]

$$q_P(x, t) = \left[1 - \frac{4(1 + 4iq_0^2 t)}{1 + 4q_0^2 x^2 + 16q_0^4 t^2} \right] q_0 e^{2iq_0^2 t}. \quad (3.2)$$

This solution is known as the Peregrine soliton. The particularity of this solution is that it is localized in time and space [see Fig. 3.1(b)]. The last solution of this family was found by Akhmediev and Korneev [369] employing an ansatz with time-dependent coefficients. It reads

$$q_A(x, t) = \left[1 + \frac{\gamma^2 \cosh(2\beta q_0^2 t) + i\beta \sinh(2\beta q_0^2 t)}{\sqrt{2\alpha} \cos(\gamma q_0 x) - \cosh(2\beta q_0^2 t)} \right] q_0 e^{2iq_0^2 t}, \quad (3.3)$$

with $\beta^2 = 8a(1 - 2\alpha)$, $\gamma^2 = 2(1 - 2\alpha)$, and $\alpha < 1/2$. The above is the Akhmediev breather which, contrary to the Kuznetsov-Ma solution, is localized in time and periodic in space [see Fig. 3.1(c)].

Equations (3.1)–(3.3) are the soliton breathers, and they constitute the family of solutions candidates to rogue waves [346]. Interestingly, all three are related to each other¹. For instance, in Eq. (3.3), if $\alpha > 1/2$ we recover the Kuznetsov-Ma breather (3.1), and in the limit $\alpha \rightarrow 1/2$ we retrieve the Peregrine soliton (3.2) [96, 97, 370]. Hence, it is not rare in the literature to present Eq. (3.3) as the compact form of this family.

Yet, the Peregrine soliton is the most exceptional among the three [371]. With its spatiotemporal localization and a peak amplitude three times that of its background, it perfectly matches the general definition of a rogue wave, i.e., a wave that appears and disappears without a trace with a crest-to-trough height at least twice the size of the average sea state [340, 344]. Recently, this solution has gained a lot of interest in the nonlinear community, specially after its first observations in nonlinear optics [94, 96, 102], where it was proposed for supercontinuum generation [95, 99, 372] or pulse compression [105, 373, 374], in water-tank experiments [92, 375–380], where the Draupner wave has been successfully recreated [93], in plasmas [111], and very recently in BECs [A6] (see Chapter 6).

3.2 Modulational Instability

Until now, many mechanisms have been proposed to explain the formation of rogue waves in deep waters [90, 381], e.g., strong currents [382], gravity waves [88, 383], or wind waves [384], among others [385, 386]. In optics, it has also been proposed as a result of soliton collisions [349]. However, the Benjamin-Feir instability [387, 388], also known in the nonlinear community as MI [389], seems to be the most prolific mechanism for rogue wave generation [90, 345, 363–365].

The MI is the instability of a uniform background to long wavelength perturbations [390–392]. In a media with a focusing nonlinearity, the speed of sound becomes imaginary and long wavelength perturbations grow or decay exponentially in time [10, 393]. When the perturbation is enhanced by the nonlinearity, it builds up sidebands in the Fourier spectra. This translates into the formation and growth of spatial modulations, in what is known as the linear state of MI. In this linear stage, MI can lead to the formation of localized solitonic structures [68, 106, 333] and rogue waves [379, 394, 395].

When perturbations become large relative to the uniform background, the MI is said to enter a nonlinear stage. Initially, it was thought that the nonlinear stage of MI was induced

¹Eq. (3.1) and Eq. (3.3) are equivalent under the change of variables $2\alpha = \eta^2$, $\gamma^2 = -2\mu^2$, and $\beta^2 = -4\eta^2\mu^2$.

by solitons [396, 397]. However, it was later shown that all generic perturbations of the uniform background leading to the nonlinear stage of MI are linearly unstable [390], and thus solitons could not entail it. Instead, the contribution to the nonlinear stage comes from the continuous spectrum of the scattering problem associated with the NLS [392]. Interestingly, the asymptotic nonlinear stage of MI is universal, and it is characterized by a modulated elliptic wave confined in a region defined by $x = \pm 4\sqrt{2}q_0t$ [391].

Part II

Outline of the Scientific Contributions

Chapter 4

Controlled generation of soliton trains in BECs

A first step in the study of solitons in BECs is to develop tools and techniques to generate them in a controlled fashion. A lot of work regarding the experimental realization of solitons in BECs was done in the early 2000s. For instance, owing to the modulational instability of focusing media (see Section 3.2), trains of bright solitons were realized [68, 163, 316, 333, 398] by quenching the system interactions from repulsive to attractive by means of Feshbach resonances [59–66]. The same method can be used on smaller condensates to realize single solitons [67], as well as excitations thereof [399], although techniques such as evaporation [400] or wave-guiding [401] can provide more control.

Regarding dark solitons, some of the first experimental works relied on the collision of two BECs [321, 324, 402–405]. The principle behind this method is based on the matter-wave interference process. The wave character of a BEC leads to the formation of interference fringes during collision, some of which further develop into dark solitons. In a similar manner, dark solitons have been produced by perturbing the condensate with impurities [406]. More controllable processes are those employing density engineering techniques [72, 302, 406, 407], where only a couple of solitons are generated. The number of solitons emerging from the aforementioned processes has been studied under the Bohr-Sommerfeld quantization [408, 409]. Besides, it is also possible to generate single dark solitons employing phase imprinting techniques [69–71, 319].

In multi-component BECs, methods to create DB solitons involve phase imprinting together with Raman transfer processes [230, 280, 319]. This methodology allows for a high control on the creation of a single DB soliton. In order to generate trains of DB solitons, a common method is the counter flow process, which is analogous to the concept of matter-wave interference. However, in this case two different components are involved in the process [260, 261, 281, 410]. Some other methods with more control on the number of DB solitons generated in the condensate involve a winding process [A4, 200] (see Chapter 5).

Yet, the possibility to tune at hand the number of solitons and, more importantly, their characteristics is still an open challenge. In this chapter, we address to this problem and present three works dedicated to the controlled generation of soliton trains in 1D repulsive multi-component BECs [A1–A3]. In particular, we employ the concept of matter-wave

interference to generate a train of solitons through an initial condition consisting of a box-type configuration (BTC). Employing the notation from Section 2.2, the BTC reads

$$q(x, 0) = \begin{cases} q_0 e^{-i\theta} & x < -L, \\ h e^{i\alpha} & |x| \leq L, \\ q_0 e^{i\theta} & x > L. \end{cases} \quad (4.1)$$

Equation (4.1) splits the initial complex field $q(x, 0)$ into three regions. The outer regions ($|x| > L$) have the same amplitude q_0 but differ in phase by $\Delta\theta = 2\theta$, while the central region has an independent amplitude h and phase α . The matter-wave interference process takes place in the box region ($|x| < L$). During the dynamics, the two sides of the box interfere with each other generating trains of dark solitons. These consist of identical pairs of solitons moving away from each other with equal but opposite velocities. If a second component is found in the box, then the dark solitons act as an effective potential and wave-guide the other component, which develops into bright solitons (see Fig. 1 in Section 7.3). In our investigations, we also considered the presence of an external harmonic confinement, with $\omega_x/\omega_\perp = 0.01$ (see Section 1.1.4). In this case, the BTC is imprinted on top of the ground state. The reason we have chosen a BTC is because all its parameters can be easily accessed experimentally in BECs [324, 405], and even in other nonlinear systems, such as nonlinear optics [328, 411].

In our first work presented below, we extended the previous knowledge from single-component BECs [408, 409, 412] to two-component, three-component, and spinor BECs. In these more complex setups, we performed a systematic numerical study on the dynamical formation of soliton trains upon considering different initial conditions of the BTC [A1]. In the other two works, we solved the direct scattering problem of the IST (see Section 2.1) for the BTC. Recall that the IST allows us to linearize the initial value problem and reduce it to a linear eigenvalue problem, which allows us to fully characterize the emerging soliton trains analytically. More specifically, we solved the asymptotic scattering problem, i.e., in the limit $x \rightarrow \pm\infty$. The choice of solving the asymptotic problem simplifies the mathematical treatment but, at the same time, it implies that the dark soliton solutions are expected to be valid at $x \gg 1$ or, equivalently, at $t \gg 1$, as we indeed verified. Employing this approximation, the scattering matrix $\mathbf{S}(k)$ is independent of time. Consequently, the problem can be solved at $t = 0$, for which the form of the complex field, $q(x, 0)$, is known. Moreover, the first element of the scattering matrix contains the eigenvalue problem we need to solve, i.e., $S_{1,1}(k_0) = 0$. The zeros k_0 are the discrete eigenvalues of the scattering problem, each of which describes a different soliton solution of the soliton train. Subsequently, in [A2] we derived the soliton train solutions for the single-component scenario. Then, in [A3] we extended our derivation to the two-component case. It is important to mention that the results presented in [A2, A3] are not limited to BECs, but are generally valid for any system described by the NLS (see Section 2.2).

Outline: Controlled generation of dark-bright soliton complexes in two-component and spinor Bose-Einstein condensates [A1]

In this work, we performed a systematic numerical investigation to tailor the dynamical generation of dark-bright soliton trains. In particular, we studied three different 1D repulsive multi-component BEC setups: a two-component, a three-component, and a genuine spinor BEC. In all cases, we employed an in-phase ($\Delta\theta = 0$) BTC (4.1) with a zero-amplitude central region ($h = 0$) as initial condition for the component(s) that will host dark solitons. For the one(s) hosting bright solitons, we employed a Gaussian pulse instead, localized in the central region of the BTC.

In the two component setup, we found that the number of DB soliton trains generated in the two-component system increases linearly with the width of the BTC, L , as well as with the amplitude of the density background, q_0 . Additionally, different parametric variations of the BTC allowed us to monitor the changes of the soliton characteristics by direct comparison with their analytical expressions (see Sections 2.3.2). For instance, for a fixed L , increasing q_0 resulted in faster solitons, while employing a larger Gaussian pulse resulted in slower ones.

The addition of a third component to the system allows the emergence of more complex structures, either being a dark-bright-bright (DBB) or a dark-dark-bright (DDB) soliton. For the former, two Gaussian pulses are employed to form the bright counterparts, while for the latter two identical BTC are employed to host the dark solitons. In this three-component setup, we found the same trend as in the two-component setup regarding the generation of soliton trains. The only major difference was that the DDB case developed trains with one additional pair of solitons.

In the spinor system, we considered again DBB and DDB soliton configurations. Recall that in this system, spin interactions allow for the exchange of particles between components (see Section 1.2.2). On the one hand, the DBB case showcased the same dynamics as the non-spinor scenario. This is because the overall overlap between the ψ_{\pm} and ψ_0 components is low, and thus the spin-mixing dynamics (1.34) are highly suppressed. On the other hand, we found that in the DDB configuration the spin-mixing dynamics play a crucial role. In this case, the overall overlap was considerable, specially between the ψ_+ and ψ_0 components hosting the dark solitons. Consequently, the spin-mixing dynamics led to an increase of particles in the ψ_- component hosting bright solitons. At the same time, this increase in particles gave rise to a finite background which resulted in the formation of beating DDB solitons (2.10). Interestingly, similar structures are described in Ref. [413].

Last, we repeated our simulations in the presence of an experimentally relevant harmonic potential. Surprisingly, we found that as long as the width of the BTC is way smaller than the size of the condensate in the trap, the overall results from the homogeneous setup also apply. Of course, the presence of the trap modifies the trajectories of the resulting soliton trains, which undergo oscillations. Therefore, in order to verify the DB character of the generated solitons, we compared the numerical trajectories with the analytical ones (2.12). Our results showed an excellent agreement between the two, with discrepancies below a 5%.

Outline: On-demand generation of dark soliton trains in Bose-Einstein condensates [A2]

In the past, there were several attempts to characterize the formation of dark soliton trains from density engineering and matter-wave interference processes [72, 402–405, 408, 409]. However, a generalized solution to the problem remained absent. In this work, we provide the generalized characterization of the soliton trains generated from an initial BTC (4.1). Employing the tools provided by the IST formalism (see Chapter 2), we solved the defocusing NLS (2.3) with NZBC. More specifically, we solved analytically the asymptotic direct scattering problem for the BTC. Subsequently, we obtained the eigenvalue problem and the discrete eigenvalues $k_0 \in \mathbb{R}$ form the scattering data $\mathbf{S}(k)$, which characterize the dark solitons of the soliton trains through the relation $k_0 = q_0 \cos \beta$ [see Eq. (2.8)].

Having the eigenvalue problem at hand, we proved that the spectrum of eigenvalues is symmetric when the BTC is in-phase ($\Delta\theta = 0$), independently of the parameters describing the central region. This implies that the resulting train of dark solitons is composed by pairs of moving solitons with equal but opposite velocities. On the other hand, an out-of-phase BTC ($\Delta\theta \neq 0$) presents a symmetric spectrum of eigenvalues only if $\alpha = \pi/2$ or $h = 0$. In the latter case, an additional single *black* soliton is generated at the center of the BTC. Otherwise, the spectrum is asymmetric and all the dark solitons formed have different velocities, i.e., no pairs are formed.

Then, in order to showcase the versatility of the BTC, we solved the eigenvalue problem for a particular set of initial conditions, in analogy to different experimental realizations. To mimic methods employing the collision of condensates to generate dark solitons [321, 324, 402, 404], we set $h = 0$. In this case, the outer regions of the BTC correspond to the colliding condensates separated by a distance of $2L$. With this configuration, we were able to derive a general expression for the number of dark solitons analogous to those found in previous works [49, 414]. Methods employing phase-imprinting techniques were also analyzed. For instance, with $L = 0$, the BTC is reduced to two regions. The imprinting of a phase difference between the two regions creates a single dark soliton, whose size and velocity depends on the magnitude of the phase-jump [69–71, 319]. On the contrary, if the phase difference is imprinted on the central region, corresponding to a BTC with $L \neq 0$ and $h = q_0$, two identical dark solitons are created [320]. In all cases, we obtained expressions describing solutions in line with the previous experimental findings.

For other methods, such as density-engineering techniques, the BTC needs to be designed particularly for each case. In this regard, we performed an exhaustive analysis of the eigenvalue spectra corresponding to different BTCs. For selected cases, we solved the time-dependent GPE (1.20) and compared the analytical solutions with the numerically obtained dynamics at $t \gg 1$, which showcased an excellent agreement. These same cases were then investigated in the presence of a harmonic trapping potential, where the solitons perform in-trap oscillations. Surprisingly, the in-trap trajectories were completely characterized by the dark soliton frequency [317, 324] and the eigenvalues, k_0 , with no more than a 3% discrepancy.

Outline: On-demand generation of dark-bright soliton trains in Bose-Einstein condensates [A3]

The generation of DB solitons in two-component BECs has been an active line of investigation during the last decade [A4, 200, 230, 260, 261, 280, 281, 319, 410]. The generation of a single DB soliton can be achieved by means of phase imprinting and particle transfer between components [280, 319]. On the other hand, the generation of multiple of these structures in a controlled manner has been a challenge. Most techniques employ counter-flow dynamics among both constituents of the BEC [260, 281, 410], or phase-winding protocols [A4, 200].

In this work, we complemented our previous investigations on DB soliton generation [A1] by generalizing the findings from our previous work [A2]. Similarly, we were able to completely characterize analytically the formation of DB soliton trains by employing the IST formalism (see Section 2.1) for the defocusing VNLS (2.3) with NZBC [38, 42, 44, 47]. To do so, we solved again the asymptotic direct scattering problem and the eigenvalue problem at $t = 0$. Contrary to the scalar case, now the initial complex field $\mathbf{q}(x, 0)$ is a vector. The first component corresponds to a BTC, while the second component corresponds only to the central region of a BTC, i.e., $q(x, 0) = 0$ for $|x| > L$ [see Eq. (4.1)]. Hence, the dark solitons will form in the first component, while the bright solitons will form in the second one. Despite employing different BTCs for each component, we will still refer to our initial condition as BTC.

In this case, the DB soliton solutions (2.9) are characterized by the spectral parameter $z = k_0 + \sqrt{k_0^2 - q_0^2}$ with $|z| < q_0$, which depends on the discrete eigenvalues $k_0 \in \mathbb{C}$. The spectra of eigenvalues k_0 was obtained through an exhaustive parametric exploration of different BTCs. We found that in the case when only the *bright* component is present in the central region of the BTC ($h = 0$), the emergence of solitonic structures occurs as expected and in line with our results reported in [A1]. For instance, the number of DB solitons increases with the width of the central region, L , while their velocities decrease with the amplitude of the second component in the central region of the BTC, H . Moreover, if the external regions of the BTC are out-of-phase ($\Delta\theta = \pi$), the spectra also become antisymmetric and the DB solitons are not generated in pairs. On the other hand, if both components are present in the central region of the BTC ($h \neq 0$) the emergence of DB soliton structures is hindered, and the amount of solitons is highly reduced.

In order to test the validity of our analytical findings, we compared selected cases with direct numerical simulations of the CGPE (1.27). For those cases where only the bright component is in the central region of the BTC, the numerically obtained DB solitons and the analytical ones showcased an excellent agreement, especially at $t \gg 1$. For these particular cases, we could extrapolate the analytical results to the presence of an external harmonic trapping potential in which their oscillatory trajectories could be described by the eigenvalues k_0 characterizing each soliton and the characteristic DB soliton frequency [318].

By contrast, in the case when both components were initially mixed in the central region of the BTC, the numerical DB solitons only agree with the analytically obtained waveforms in the limit $t \rightarrow \infty$. This was confirmed by measuring their amplitudes and velocities, which approach asymptotically to the analytical values. Consequently, in the presence of an external

potential, the emergence of these concrete DB solitons is prevented. More precisely, the oscillatory motion taking over during the dynamics due to the presence of the trap interrupts the development of the expected DB solitons. As a result, the train of oscillatory DB solitons differs from that in the homogeneous case.

Interestingly, we noted that the symbiotic relation between the dark and bright counterparts prevents a DB soliton to maintain shape while oscillating in the presence of a harmonic potential. This behavior is unexpected, since one of the main properties of solitons is that they preserve shape. Hence, in an effort to characterize this change in shape, we derived an analytic expression (2.13) and successfully managed to capture the change in the amplitudes with deviations not larger than a 1%.

Chapter 5

Soliton gas

Assume a BEC densely packed with equidistant solitons. This type of chain formation is known as a Toda lattice [415]. Under this setup, entities that run over all the others without disturbing the chain, in the same spirit as a Newton cradle, have been identified as hypersolitons [416]. However, when the ensemble of solitons is irregular, the non-equilibrium dynamics within the system need to be interpreted statistically. This is usually referred to as soliton turbulence¹ or soliton gas [334]. The concept of a soliton gas was already introduced in 1971 in the context of dilute solitonic ensembles [420], and some works in plasmas [421], solid-state physics [422], and nonlinear optics [423–426] followed. While collisions in dilute systems occur between pairs of solitons (see Section 2.4), in dense ensembles the individual particle-like character of solitons is blurrier, and collisions need a thermodynamic treatment as the collective dynamics take over [427].

In the last years, soliton gases have grown in interest within the nonlinear community [428–430], specially for their generalized hydrodynamic properties [431] and recent experiments with shallow-water [432], deep-water [433], and oceanic [434–436] waves, the latter also in the scope of rogue waves [437] (see Chapter 3). In the upcoming work, we explore the generation of a dense soliton ensemble to put the experimental study of soliton gases within reach in the context of BECs.

Outline: Observation of dense collisional soliton complexes in a two-component Bose-Einstein condensate [A4]

In this work, we presented a consistent experimental method to produce solitonic arrays from an initial periodic pattern to study dense soliton ensembles in two-component BECs. To support our findings, direct numerical simulations of the CGPE (1.27) in one and three dimensions have also been realized.

Initially, we prepared a condensate of around 9×10^5 ⁸⁷Rb atoms in the $|F = 1, m_F = -1\rangle$ hyperfine state, confined in a highly elongated, cigar-shaped, harmonic trap with $\omega = 2\pi \times \{2.5, 245, 258\}$ Hz, of roughly $500\mu\text{m}$. Then, with a near-resonant microwave $\pi/2$ -pulse protocol (1.28), we transferred half of the atoms into the $|F = 2, m_F = -2\rangle$ state. Afterwards, the mixture was allowed to naturally evolve in the presence of a magnetic gradient along the longitudinal direction. During this period of *winding* time, τ , the phase of each component evolves differently at each point along the condensate. Eventually, a second

¹This term has also been employed in the context of nonintegrable wave dynamics [417–419]

$\pi/2$ -pulse was applied to the condensate and, depending on the acquired phase, the atoms either remained in their current state, or changed to the other one. This method produces a periodic sinusoidal pattern, complementary between components, whose wavelength is determined by the duration of the winding time, i.e., longer winding times produce shorter wavelength patterns, and vice versa. Moreover, the windings² of each pattern within a component are out-of-phase with their neighboring ones, a key ingredient in the formation of dark solitons [69–71, 319].

In our experiments we let the system freely evolve in the trap after different winding times. For short winding times ($\tau \sim 10$ ms), we found that few, wide windings are formed. During the dynamics, these windings steepened, approaching the gradient catastrophe. In the context of dispersive hydrodynamics, the gradient catastrophe is regularized by the emission of shock waves [438]. In our case, the latter led to the formation of persisting dark notches that spread over the condensate, in the spirit of dark solitons. Employing longer winding times ($\tau \sim 20$ ms), we generated periodic patterns consisting of about a dozen windings. In this case, the windings evolved into dark-antidark solitons during the early dynamics. These structures are similar to a DB soliton (2.9) but with the bright component also on top of a finite background, hence antidark. With this configuration, we found that the number of windings tripled over time, which restricted the space against the formation of more solitonic structures.

Interestingly enough, the maximum number of structures in the condensate was found to be limited by the characteristic size of DB solitons in our system. The latter was further demonstrated with tighter winding patterns. For instance, employing $\tau = 60$ ms, we reached winding sizes close to that of a soliton. This configuration, saturated with more or less 30 windings, remained stable for nearly 70 ms before the dynamics gradually set in. Interestingly, we came across a reproducible stage in the dynamics in which the winding pattern smoothed out to a Thomas-Fermi profile (1.12). But more surprisingly, after this *fuzzy* stage, a revival of the initial pattern was always observed.

Last, we pushed the winding pattern to the limit. With $\tau = 100$ ms, we prepared a dense pattern with over 55 windings. In this case, we observed dense soliton complexes undergoing collisions. Despite the initial pattern becoming irregular due to the constant soliton interactions, we observed that its characteristic initial features remained qualitatively unchanged, namely the number and size of the solitons. The latter puts forward our protocol as a mechanism to study dense soliton ensembles, specially aimed at the hydrodynamic properties and thermalization aspects of soliton gases [439].

²We refer to each of the modulations of the sinusoidal pattern as a *winding*.

Chapter 6

The Peregrine soliton in BECs

The Peregrine soliton (PS) is a solution of the focusing NLS and a possible candidate for rogue waves — extreme wave events which appear and disappear without a trace (see Chapter 3). Although it has been realized in other fields, namely in water tank experiments [92, 375–378, 380], plasmas [111], and optical fibers [96, 102], in BECs it has remained elusive [A5, 107, 109, 440] until recently [A6]. Some of the difficulties to overcome in realizing the PS in BECs include: (i) the instability in the face of collapse of attractive (focusing) BECs above a certain number of particles [441–445], (ii) the modulationally unstable background from where the PS forms [390–392], and (iii) its spatiotemporal-localized and 1D nature [368]. In this chapter we present two of our works dedicated to the realization of the PS in two-component 1D repulsive BECs.

While the 1D nature of the PS can be explored in quasi-1D trapping potentials (see Section 1.1.4), the key behind our methodology leverages the effective single-component description of a minority component immersed in a bath of a majority component [446, 447]. This approach allows us to prepare an effective focusing medium from a purely repulsive BEC, and thus avoid the instabilities of attractive condensates and focusing media. In particular, it is assumed that the majority component is way larger than the minority component everywhere in the condensate. Also, that the majority extends to infinity, while the minority does not. Then, if the scattering lengths of the components are similar to each other, i.e., in the limit $|g_{22} - g_{11}| \ll g_{11}$ and $|g_{12} - g_{11}| \ll g_{11}$, the majority species can adjust to the minority one with a negligible cost to the kinetic energy (see Section 1.2.1),

$$\mu \approx 0 + g_{11}n_1(x) + g_{12}n_2(x) \rightarrow n_1(x) \approx n_{1,\infty} - \frac{g_{12}}{g_{11}}n_2(x). \quad (6.1)$$

Therefore, it is expected that the total density remains constant and only weakly perturbed. Inserting Eq. (6.1) into the CGPE (1.27) for the minority component, we obtain an effective single-component GPE (1.20). The important element of the effective GPE is that the effective nonlinear interaction strength,

$$g_{\text{eff}} = g_{22} - \frac{g_{12}^2}{g_{11}}, \quad (6.2)$$

depends on the intra- (g_{11}, g_{22}) and intercomponent (g_{12}) interaction strengths. Employing the adequate atomic species, e.g., ^{87}Rb [208, 211, 215], or by fine tuning the interactions by means of Feshbach resonances [59–66], it is possible to obtain the effective attractive interaction, i.e., $g_{\text{eff}} < 0$, needed for the emergence of the PS.

Additionally, we rely on the semiclassical (dispersionless) limit of the focusing NLS. Within this limit, a sufficiently wide pulse undergoes a gradient catastrophe [438], i.e., the divergence of the derivatives of the wave function describing the pulse. Importantly, near this point the regularized field is described by the same waveform as the PS [105, 448]. The universality of this mechanism implies that the PS can emerge from any pulse, independently of its shape as long as it is wide enough. Hence, this second approach circumvents the necessity of a constant density background promoter to MI (see Section 3.2).

In our first work outlined below [A5], we theoretically and numerically investigated the emergence of the PS in BECs utilizing the approaches described above. Then, in our second work [A6], we applied the concepts developed in [A5] to realize, for the first time, the PS in a BEC.

Theoretical and numerical evidence for the potential realization of the Peregrine soliton in repulsive two-component Bose-Einstein condensates [A5]

In this work, we proposed an experimentally accessible setup to realize the PS in a 1D repulsive two-component BEC. The setup consists of a highly imbalanced mixture of two hyperfine states of the same atomic species of ^{87}Rb atoms, namely a majority component in the $|F = 1, m_F = -1\rangle$ state and a minority component in the $|F = 2, m_F = 1\rangle$ state. For this particular choice of hyperfine states, the mixture is weakly immiscible (1.29), leading already to an effective attractive interaction ($g_{\text{eff}} < 0$) for the minority component. In addition, we always prepared the initial state so that the total density adds up to a constant background, or to a Thomas-Fermi profile (1.12) in the presence of an external trapping potential.

First, in the absence of the trapping potential and as a proof of principle, we imprinted the PS waveform (3.2) on the minority component and compared the time evolution of the mixture with that of the effective single-component description. For the former, we employed the 1D CGPE (1.27), while the 1D GPE (1.20) was employed for the latter. What we found was an excellent agreement between the two, evidencing the validity of the effective focusing dynamics of the minority component. Interestingly, in the long-time dynamics of the minority component in the mixture, we encountered the nonlinear stage of MI, which is a purely focusing phenomenon (see Section 3.2). We corroborated its formation by characterizing its shape. However, instead of consisting of a modulated wave, it presented periodic revivals of the PS in both time and space.

Then, in favor of an experimental approach and willing to capture the semiclassical limit, we investigated the emergence of the PS by employing wide, generic, experimentally accessible Gaussian pulses as the initial condition for the minority component. More precisely, we examined the dynamical evolution of two representative Gaussian pulses of different widths in the absence of an external trapping potential. It was found that the dynamics of the narrower pulse showcases a recursive pattern with revivals of the PS over time, while the wider one leads to the gradient catastrophe and the formation of a cascade of PSs. The latter resembles a branching pattern, and thus it is usually referred to as a Christmas tree [109, 116]. Nevertheless, once again we compared the emerging structures with those of the effective

single-component description and the analytical PS waveform (3.2). The results showcased a really good agreement in both cases, in particular around the core of the PS.

Having the validity of the semiclassical limit at hand, we subsequently investigated the emergence of the PS in the presence of a wide parabolic trap, with a ratio $\omega_x/\omega_\perp = 0.002$ (see Section 1.1.4). The choice of a wide trapping potential was made to reduce its impact in the early-time dynamics prior to the formation of the PS. In this case, the total density is well described by a Thomas-Fermi profile (see Section 1.1.3). As a result, for both the narrower and wider Gaussian pulses, we obtained similar dynamics to those in the homogeneous setup discussed above. However, we found unexpected results in the late-time dynamics of the wide Gaussian pulse. In particular, the outermost branches of the Christmas tree underwent in-trap oscillations, but with unprecedented convex trajectories as compared to the classical concave oscillations of DB solitons (see Section 2.4). Here, we additionally considered the possibility of a mass-imbalanced mixture (see Section 1.2.1). We concluded that a lighter minority component allows for the emergence of the PS only below a particular threshold of the width of the Gaussian pulse. Above this threshold, wider pulses only disperse and no PS is found. On the other hand, with a heavier minority component, we found the same overall phenomenology as per the mass-balanced case.

In view of a possible experimental realization, we included in our model dissipative effects to account for finite temperatures (1.8). Interestingly, it turns out that in the interval of temperatures considered, $T \in [10, 100]$ nK, the early dynamics did not present qualitatively major changes. This means that the formation of the PS was still present in the dynamics. However, the emergence of later structures, such as the Christmas tree, was totally suppressed due to the accumulated loss of particles over time. Finally, we tested if our methodology holds in 3D BECs, more faithful to experiments. Not only that, but also if the 1D PS could manifest beyond 1D systems [449]. Hence, we extended our model and performed quasi-1D simulations of the 3D CGPE (1.27). Remarkably, we were able to verify the emergence of robust PSs by direct comparison with its analytical waveform (3.2). In this case, we also employed narrow and wide Gaussian pulses. With the former, the characteristic revival of the PS described in the 1D simulations was also present. Whilst, with the latter, we found the emergence of the Christmas tree.

Experimental realization of the Peregrine soliton in repulsive two-component Bose-Einstein condensates [A6]

Following the proposal from [A5], in this work we presented the first experimental realization of the PS in ultracold atoms. Initially, a BEC consisting of 9×10^5 ^{87}Rb atoms in the $|F = 1, m_F = -1\rangle$ hyperfine state was prepared in a quasi-1D cigar-shaped harmonic trapping potential, with $\omega = 2\pi \times \{2.5, 245, 258\}$ Hz. Here, we additionally superimposed a Gaussian potential well (GW) at the center of the trap, with Gaussian widths $s = \{25, 13, 13\}$ μm and 40 nK depth. The presence of the GW was found to be a key ingredient in the experimental realization of the PS. It brings more control to the spatial location and time scales in which the PS emerges, making the experiment highly reproducible.

Then, by means of a $\pi/2$ -pulse (1.28), a small percentage of atoms ($\sim 15\%$) was transferred to the $|F = 2, m_F = 0\rangle$ state, while the majority of them ended up in the $|F = 1, m_F = 0\rangle$ state ($\sim 85\%$). This mixture is weakly immiscible (1.29), providing an effective focusing (weak) nonlinearity to the minority component ($a_{\text{eff}} = -2.41a_B < 0$), required for the emergence of the PS. After the transfer of atoms, the system was allowed to evolve.

Absorption images of the minority component at different times allowed us to compare the dynamics with direct numerical simulations of the 3D CGPE (1.27), showcasing an excellent agreement. More importantly, we found that the emergence of the PS is not restricted to a specific set of parameters, but emerges for a rather general setup, namely different sizes of the GW and even different nonlinearities. For instance, we have observed the PS emerging in a mixture of ^{87}Rb atoms in the states $|F = 1, m_F = -1\rangle$ and $|F = 2, m_F = 0\rangle$, as initially proposed in [A5], despite presenting a weaker nonlinearity ($a_{\text{eff}} = -1.34a_B$).

The important role of the intercomponent interactions became apparent when repeated experiments with a single-component BEC showed no evidence of PS formation nor dynamics of any kind. Similarly, two-component experiments in the absence of the GW did not exhibit PS in the timescales sampled. Interestingly, the PS still emerges if the GW is turned off shortly after the dynamics starts. In fact, the earlier the well was turned off, the later the PS emerged. The latter results put forward the fact that the role of the GW is none other than to *seed* the dynamics leading to the emergence of the Peregrine soliton. Furthermore, we found out that the time instant at which the PS emerges can also be tuned, mainly by changing the width of the GW. This is an important consideration to have in mind, as a GW too wide can delay the emergence of the PS to the point that thermal effects take over the dynamics and can obstruct its formation. In this regard, we performed an extensive 1D numerical investigation, accounting for different amplitudes and widths of the GW, to optimize the emergence of the PS. As a result, we determined that the best choice for the width of the GW, independently of its amplitude, corresponds to the characteristic length scale of the PS. In addition, in some of our 1D simulations we have also encountered the nonlinear stage of MI (see Section 3.2). Yet, in these cases, the nonlinear MI is found at very early stages of the dynamics, as compared to the one previously reported in [A5]. The latter suggests that employing a GW can provide experimental access to the nonlinear stage of MI for its study in BECs.

Part III

Scientific contributions and Conclusions

Chapter 7

Scientific Contributions

Controlled generation of dark-bright soliton complexes in two-component and spinor Bose-Einstein condensates

A. Romero-Ros,¹ G. C. Katsimiga,¹ P. G. Kevrekidis,² and P. Schmelcher^{1,3}

¹*Center for Optical Quantum Technologies, Department of Physics, University of Hamburg, Luruper Chaussee 149, 22761 Hamburg, Germany*

²*Department of Mathematics and Statistics, University of Massachusetts Amherst, Amherst, Massachusetts 01003-4515, USA*

³*The Hamburg Centre for Ultrafast Imaging, University of Hamburg, Luruper Chaussee 149, 22761 Hamburg, Germany*



(Received 7 March 2019; revised manuscript received 18 June 2019; published 22 July 2019)

We report on the controlled creation of multiple soliton complexes of the dark-bright type in one-dimensional two-component, three-component, and spinor Bose-Einstein condensates. The formation of solitonic entities of the dark-bright type is based on the so-called matter-wave interference of spatially separated condensates. In all three cases, a systematic numerical study is carried out upon considering different variations of each system's parameters both in the absence and in the presence of a harmonic trap. It is found that manipulating the initial separation or the chemical potential of the participating components allows us to tailor the number of nucleated dark-bright states. Particularly, the number of solitons generated increases upon increasing either the initial separation or the chemical potential of the participating components. Similarities and differences of the distinct models considered herein are showcased, while the robustness of the emerging states is illustrated via direct numerical integration, demonstrating their long time propagation. Importantly, for the spinorial system, we unravel the existence of beating dark soliton arrays that are formed due to the spin-mixing dynamics. These states persist in the presence of a parabolic trap, often relevant for associated experimental realizations.

DOI: [10.1103/PhysRevA.100.013626](https://doi.org/10.1103/PhysRevA.100.013626)

I. INTRODUCTION

Among the nonlinear excitations that arise in Bose-Einstein condensates (BECs) [1,2], matter-wave dark [3] and bright [4] solitons constitute, arguably, some of the fundamental signatures. These structures stem from the balance between dispersion and nonlinearity and exist in single-component BECs with repulsive and attractive interparticle interactions respectively [5,6]. Also, more complex structures consisting of dark solitons in one component and bright solitons hosted in the second component of a binary BEC have been experimentally realized [7–12]. The existence and robustness of a single dark-bright (DB) soliton as well as interactions between multiple DB states both with each other or with impurities have been exhaustively studied in such settings [10,13–21]. In contrast to single-component setups, DB solitons are the building blocks that emerge in repulsively interacting two-component BECs [22]. In such a repulsive environment (where bright solitonic states cannot exist on their own), DB states owe their existence to the effective potential created by each of the participating dark solitons into which each of the bright solitons is trapped and consequently waveguided [23–25]. This waveguiding notion was originally introduced in the context of nonlinear optics [26–34]. Besides the aforementioned two-component BECs, the experimental realization of spinor BECs [35–39] offers possibilities of investigating the different soliton entities that arise in them [38–52]. In this context, more complex compounds in the form of dark-dark-bright (DDB) and dark-bright-bright (DBB) solitons have been theoretically predicted [53,54] and very recently experimentally observed [55].

There are multiple ways of generating single and multiple dark solitons [56] (with the latter sometimes referred to as the dark soliton train [57]) in single-component BECs. Common techniques consist of density engineering [58–60], phase engineering [7,61–63], and collision of two spatially separated condensates [64,65] (see also Ref. [66] for an interesting geometric higher dimensional implementation of the latter process so as to produce vortices). This latter generation process can be thought of as a consequence of matter-wave interference of the two condensates [64,67–69]. Additionally, also known are the conditions under which the controllable formation of dark soliton trains can be achieved [57,64,67–69]. In particular, it has been demonstrated that the number of generated dark solitons depends on the phase and momentum of the colliding condensates [64,69]. On the contrary, in multicomponent settings such as two-component and spinor BECs, the dynamics is much more involved. In this context, large-scale counterflow experiments exist according to which also DB soliton trains can be created [9]. However, to the best of our knowledge, a systematic study regarding the controllable formation of these more complex solitonic structures and their relevant extensions in spinorial BECs is absent in the current literature. Such a controlled formation process represents the core of the present investigation.

Motivated by recent experimental advances in one-dimensional (1D) two-component [8–12], and more importantly spinor BECs [55], here we report on the controllable generation of multiple soliton complexes. These include DB solitons in two-component BECs, and variants of these structures, i.e., DDB and DBB soliton arrays, in three-component and spinor BECs. For all models under consideration, the

creation process of the relevant states is based on the so-called matter-wave interference of separated condensates being generalized to multicomponent systems. In all cases, the homogeneous setting is initially discussed and subsequently we generalize our findings to the case where an experimentally motivated parabolic confinement, i.e., trap, is present.

Specifically, for the homogeneous settings investigated herein, the creation process is as follows. To set up the interference dynamics, an initial inverted rectangular pulse (IRP) is considered [6] for the component(s) that will host later on the dark solitons. The counterflow process relies on the collision of the two sides of the pulse. For the remaining component(s) that will host later on the bright solitons, a Gaussian pulse initial condition is introduced. It is shown that such a process ensures the formation of dark soliton arrays, and that the number of solitons can be manipulated by properly adjusting the width of the initial IRP. Additionally, the dispersive behavior of the Gaussian used, due to the defocusing nature of each system, allows its confinement in the effective potential created by each of the formed dark solitons and thus leads to the formation of the desired localized humps. The latter are trapped and subsequently waveguided by the corresponding dark solitons. In this way, arrays of robustly propagating DB, DDB, and DBB solitons in two-component, three-component, and spinor systems are showcased. Indeed, and as far as the two-component system is concerned, we verify among others that during evolution the trajectory of each of the nucleated pairs follows the analytical predictions stemming from the exact single DB state. Also, for the three-component scenario, generalized expressions for the soliton characteristics are extracted and deviations from the latter when different initializations are considered are discussed in detail. In the spinor setting, the controlled nucleation of arrays consisting of multiple DBB and DDB solitons is demonstrated, a result that can be tested in current state-of-the-art experiments [55]. Remarkably enough, in the DDB nucleation process, the originally formed DDB arrays soon after their formation transition into beating dark solitons that gradually arise in all three hyperfine components [11,12,34,70]. This transition stems, as we will explain in more detail below, from the spin-mixing dynamics that allows for particle exchange among the hyperfine components.

After the proof of principle in the spatially homogeneous case, we turn to the harmonically trapped models, where once again in order to induce the dynamics, counterflow techniques are utilized [9,64,69]. Now, the background on top of which the spatially separated BECs are initially set up asymptotes to a Thomas-Fermi (TF) profile for all the participating components. The counterflowing components are initially relaxed in a double-well potential, while the other component encounters a tight harmonic trap. The system is then released and evolves in a common parabolic potential. It is found that properly adjusting the initial separation of the condensates or the chemical potential in each of the participating components leads to the controlled nucleation of a desired number of soliton structures in this case too, with similar functional dependences of the soliton number on the system characteristics as above. For the two- and three-component systems, it is found that the generated soliton arrays travel within the parabolic trap oscillating and interacting with one another for large evolution

times. Finally, in the genuine spinor case and for a DDB formation process again, arrays of oscillating and interacting beating dark solitons emerge in all hyperfine components. We find that these states occur earlier in time when compared to the homogeneous scenario. The spin-mixing dynamics is explained via monitoring the population of the three hyperfine states. Damping oscillations of the latter are observed, in line with the predictions in spinor $F = 1$ BECs [37,71].

The workflow of this presentation proceeds as follows. In Sec. II, we present the different models under consideration. In particular, the spinor $F = 1$ BEC system is initially introduced and the complexity of the model is reduced all the way down to the single-component setting. Subsequently, a brief discussion summarizing prior results regarding the controllable generation of dark soliton trains emerging in single-component systems is provided. Finally, here we comment on the initial-state preparation utilized herein in order to controllably generate multiple soliton complexes of the DB type in multicomponent BECs. Section III contains our numerical findings ranging from two-component to spinor BEC systems. In all the cases presented, the homogeneous setting is initially investigated, and we next elaborate on the relevant findings in the presence of traps. To conclude this work, in Sec. IV we summarize our findings and we also discuss future directions.

II. MODELS AND SETUPS

A. Equations of motion

We consider a one-dimensional (1D) harmonically confined spinor $F = 1$ BEC. Such a system can be described by three coupled Gross-Pitaevskii equations (CGPEs), one for each of the three hyperfine states $m_F = -1, 0, +1$ of, e.g., a ^{87}Rb gas. In the mean-field framework, the wave functions $\Psi(x, t) = [\Psi_{+1}(x, t), \Psi_0(x, t), \Psi_{-1}(x, t)]^T$ of the aforementioned hyperfine components are known to obey the following GPEs (see, e.g., Refs. [39,55]):

$$i\partial_t \Psi_{\pm 1} = \mathcal{H}_0 \Psi_{\pm 1} + g_n(|\Psi_{+1}|^2 + |\Psi_0|^2 + |\Psi_{-1}|^2) \Psi_{\pm 1} + g_s(|\Psi_{\pm 1}|^2 + |\Psi_0|^2 - |\Psi_{\mp 1}|^2) \Psi_{\pm 1} + g_s \Psi_0^2 \Psi_{\mp 1}^*, \quad (1a)$$

$$i\partial_t \Psi_0 = \mathcal{H}_0 \Psi_0 + g_n(|\Psi_{+1}|^2 + |\Psi_0|^2 + |\Psi_{-1}|^2) \Psi_0 + g_s(|\Psi_{+1}|^2 + |\Psi_{-1}|^2) \Psi_0 + 2g_s \Psi_{+1} \Psi_0^* \Psi_{-1}. \quad (1b)$$

In the above expressions, the asterisk denotes the complex conjugate and $\mathcal{H}_0 = -\frac{1}{2}\partial_x^2 + V(x)$ is the single-particle Hamiltonian. Here, $V(x) = (1/2)\Omega^2 x^2$ denotes (unless indicated otherwise) the external harmonic potential with frequency $\Omega = \omega_x/\omega_{\perp}$ and ω_{\perp} is the trapping frequency in the transverse direction. Equations (1a) and (1b) were made dimensionless by measuring length, time, and energy in units $a_{\perp} = \sqrt{\hbar/(M\omega_{\perp})}$, ω_{\perp}^{-1} , and $\hbar\omega_{\perp}$, respectively. Here, a_{\perp} is the transverse oscillator length. In this work, we consider condensates consisting of ^{87}Rb atoms of mass M , and we assume strongly anisotropic clouds having a transverse trapping frequency $\omega_{\perp} = 2\pi \times 175 \text{ Hz} \gg \omega_x$ that is typically used in experiments with spinor $F = 1$ BECs of ^{87}Rb atoms [55].

In general, spinor BECs exhibit both symmetric or spin-independent and asymmetric or spin-dependent interatomic

interactions. In particular, g_n is the so-called spin-independent interaction strength being positive (negative) for repulsive (attractive) interatomic interactions. g_s denotes the so-called spin-dependent interaction strength being in turn positive (negative) for antiferromagnetic (ferromagnetic) interactions [72]. Specifically, for a 1D spin-1 BEC, $g_n = \frac{2(a_0+2a_2)}{3a_1}$ and $g_s = \frac{2(a_2-a_0)}{3a_1}$. Here, a_0 and a_2 are the corresponding s -wave scattering lengths of two atoms in the scattering channels with total spin $F = 0$ and $F = 2$, respectively. The measured values of the aforementioned scattering lengths for ^{87}Rb are $a_0 = 101.8a_B$ and $a_2 = 100.4a_B$, where a_B is the Bohr radius, resulting in a ferromagnetic spinor BEC [73,74].

Finally, the total number of particles and the total magnetization for the system of Eqs. (1a) and (1b) are defined as $N = \sum_{m_F} \int |\Psi_{m_F}|^2 dx$ and $M_z = \int (|\Psi_{+1}|^2 - |\Psi_{-1}|^2) dx$, respectively.

Simplified BEC models can be easily obtained from Eqs. (1a) and (1b). In particular, when the spin degrees of freedom are frozen, namely for $g_s = 0$, the aforementioned system reduces to the following three-component one:

$$i\partial_t \Psi_j = \mathcal{H}_0 \Psi_j + g_n (|\Psi_j|^2 + |\Psi_k|^2 + |\Psi_l|^2) \Psi_j. \quad (2)$$

The indices j, k, l here refer to each of the three $m_F = +1, 0, -1$ components, with $j \neq k \neq l$. This three-component system, in the absence of an external confinement [i.e., for $V(x) = 0$] and for constant g_n which, without loss of generality, can be set to $g_n = 1$, is said to be integrable and reduces to the so-called Manakov model [41,49,75]. As such, it admits exact soliton solutions of the DDB and DBB types [76]. Accounting for repulsive inter- and intraspecies interactions (up to a rescaling), we will set $g_n = 1$ in our subsequent results discussion. Additionally, the two-component BEC can be retrieved by setting, e.g., $\Psi_l = 0$ in Eq. (2). Note that such a binary mixture consists of two different spin states, e.g., one with $|F = 1\rangle$ and one with $|F = 2\rangle$, of the same atomic species and is theoretically described by the following GPEs [77]:

$$i\partial_t \Psi_j = \mathcal{H}_0 \Psi_j + g_n (|\Psi_j|^2 + |\Psi_k|^2) \Psi_j. \quad (3)$$

Here, the indices j, k refer to each of the two participating species. Finally, the single-component case is retrieved by setting in Eq. (3) $\Psi_k = 0$. The corresponding GPE reads [78,79]

$$i\partial_t \Psi = \mathcal{H}_0 \Psi + g_n |\Psi|^2 \Psi. \quad (4)$$

In the forthcoming section, we will first focus on the integrable version of Eq. (4) and the exact arrays of dark soliton solutions that it admits.

B. Prior analytical considerations and initial-state preparation

It is well known and experimentally confirmed that multiple dark solitons can be systematically generated in single-component BECs, via the so-called matter-wave interference of two initially separated condensates [64,67–69]. Aiming to generalize this mechanism to multicomponent systems, below we briefly discuss previous studies on this topic.

In particular, the problem of determining the parameters of a dark soliton formed by an initial excitation on a uniform

background has been analytically solved by the inverse scattering method [6]. In this framework, Eq. (4) [with $V(x) = 0$] is associated with the Zakharov-Shabat (ZS) [6,80] linear spectral problem. The corresponding soliton parameters are related to the eigenvalues of this spectral problem, calculated for a given initial condensate wave function $\Psi(x, 0)$. Specifically, let us assume that $\Psi(x, 0)$ has the form corresponding to an IRP

$$\begin{aligned} \Psi(x, 0) &= u_0 & \text{at } x < -a, \\ \Psi(x, 0) &= 0 & \text{at } -a < x < a, \\ \Psi(x, 0) &= u_1 e^{i\Delta\phi} & \text{at } x > a, \end{aligned} \quad (5)$$

with $a, u_0, u_1, \Delta\phi$ denoting respectively the half-width, the two amplitudes, and the phase difference between the two sides of the IRP. Subsequently, for the case of $|u_0| = |u_1| = |u|$, it has been shown [6] that the number of dark soliton pairs depends on the amplitude, $|u|$, and the phase difference $\Delta\phi$ of the initial IRP. Namely, for $\Delta\phi = 0$, which corresponds to a symmetric or in-phase (IP) IRP [see Eq. (5)], there exist n -symmetrical pairs of dark soliton solutions that are given by the solutions of the (transcendental) eigenvalue equations

$$|u| \cos(2a_n \lambda_n) = \pm \lambda_n. \quad (6)$$

Here, λ_n are the corresponding eigenvalues being bounded within the interval $[0, |u|]$. Importantly, solutions of Eq. (6) exist only within the intervals $2a_n \lambda_n \in [(n-1)\pi, (n-\frac{1}{2})\pi]$ with $n = 1, 2, 3, \dots$. Notice also that for $n = 1$ Eq. (6) has at least one root within the interval $0 < 2a_n \lambda_n < \frac{\pi}{2}$. Thus, there exists at least one pair of coherent structures. Multiple roots of Eq. (6) can be found but for appropriate values of the half-width, a_n , that lie within the aforementioned interval. Therefore, there exists a threshold for a_n above which solitons can be created. It has been demonstrated that the lower bound for the width of the IP-IRP in order to obtain n -symmetrical pairs of soliton solutions has the form

$$W_{\text{IP}} = 2a_n = \frac{(n-1)\pi}{|u|}. \quad (7)$$

In the above expression, we have defined $W_{\text{IP}} \equiv 2a_n$. Moreover, as dictated by Eq. (6), the total number of solitons is always even. Additionally, in order to obtain at least one pair of soliton solutions, i.e., for $n = 1$, then $W_{\text{IP}} > 0$ according to Eq. (7).

On the other hand, for $\Delta\phi = \pi$ [see Eq. (5)], i.e., for an asymmetric IRP or out-of-phase (OP) initial conditions, the n pairs of soliton solutions are given by the following eigenvalue equations:

$$|u| \sin(2a_n \lambda_n) = \pm \lambda_n. \quad (8)$$

Here, $2a_n \lambda_n \in [(n-\frac{1}{2})\pi, n\pi]$ with $n = 1, 2, 3, \dots$. In the OP case, the corresponding threshold for the width $2a_n$ reads [see Eq. (8)]

$$W_{\text{OP}} = 2a_n = \frac{(n-\frac{1}{2})\pi}{|u|}, \quad (9)$$

where $W_{\text{OP}} \equiv 2a_n$ is introduced. For both IP- and OP-IRPs, the amplitude, v_n , of each dark soliton pair is defined by the eigenvalues $0 \leq |\lambda_n| \leq |u|$ through the relation $v_n = \sqrt{|u|^2 - \lambda_n^2}$. Also each soliton's velocity is given by $v_n =$

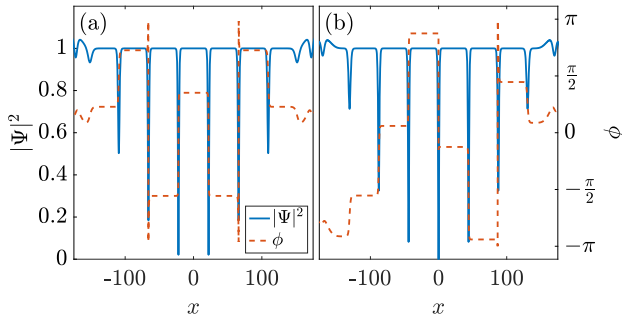


FIG. 1. Left axes: Profile snapshots of the density, $|\Psi|^2$, at $t = 150$ showcasing the generated dark solitons for (a) IP-IRP and (b) OP-IRP initial conditions. In both cases $|u| = 1$ and $a = 5$, resulting in three pairs of dark solitons being formed in panel (a) and three pairs and a central black soliton in panel (b). Right axes: Snapshots of the corresponding phase, ϕ (see legend) for (a) an IP-IRP and (b) an OP-IRP, illustrating the characteristic phase jump occurring at each of the dark soliton minima. Phase shifts $0 < \Delta\phi < \pi$ correspond to moving (gray) solitons, and the maximum phase shift $\Delta\phi = \pi$ belongs to the black soliton centered at $x = 0$ in the OP case (b). Note that the quantities shown are measured in transverse oscillator units (see text).

$\pm\lambda_n$. From Eq. (9) and for $n = 1$, we can again obtain the minimum width to assure the existence of at least a one-pair solution. The latter reads $W_{\text{OP}} = \pi/(2|u|)$. Although Eq. (8) gives the solutions for n pairs of solitons, there exists also an isolated wave for $\lambda = 0$ corresponding to a black soliton with $v = |u|$ and $v = 0$. In summary, an odd number of dark solitons is expected to be generated for OP initial conditions. We should remark at this point that Eqs. (7) and (9) dictate the dependence of the generated number of dark solitons not only on the phase but also on the momenta of the colliding condensates [64,69]. In particular, for larger initial widths the number of dark solitons generated increases since the two sides of the IRP acquire, during the counterflow, larger momenta (see also here the works of Refs. [33,81] and references therein for relevant studies in nonlinear optics). Importantly, also, the effective intuition of the number of solitons filling in the space between the two sides in “units” of the healing length, namely in dark solitons, is a relevant one to qualitatively bear in mind. Finally, we must also note that in the BEC context an initial-state preparation having the form of Eq. (5) can, in principle, be achieved by standard phase-imprinting methods and the use of phase masks [7,62,66].

Figures 1(a) and 1(b) illustrate profile snapshots (at $t = 150$) of the density, $|\Psi|^2$, for IP- and OP-IRPs, respectively. As per our discussion above, an even number of dark solitons is expected and indeed observed for an IP-IRP [see Fig. 1(a)]. In particular, for an initial amplitude $|u| = 1$ and half-width $a = 5$, three pairs of dark solitons symmetrically placed around the origin ($x = 0$) are clearly generated. On the other hand, for an OP-IRP, an odd number of solitons occurs, consisting of three pairs of dark states formed symmetrically around $x = 0$ and an isolated black soliton residing at $x = 0$ [see Fig. 1(b)]. In both cases, by inspecting the relevant phase, ϕ , the characteristic phase jump, $\Delta\phi$, located right at the dark density minima, expected for each of the nucleated dark states

can be clearly inferred [see dashed lines in Figs. 1(a) and 1(b)]. Notice that all the solitons formed for both IP- and OP-IRPs are gray (moving) ones since $0 < \Delta\phi < \pi$, except for the black one shown in Fig. 1(b), which has a phase shift $\Delta\phi = \pi$.

Up to this point, we have briefly reviewed the well-known results regarding the controllable generation of multiple dark solitons in homogeneous single-component settings. Below, we focus on the controllable formation of more complex solitonic entities that appear in multicomponent BECs. In this latter context, analytical expressions like the ones provided by Eqs. (7) and (9) are, to the best of our knowledge, currently unavailable in the literature for the initial waveforms considered herein. Thus, in the following we resort to a systematic numerical investigation aiming at controlling the emergence of more complex solitonic structures consisting of multiple solitons of the DB type. In particular, we initially focus on the simplest case scenario, i.e., a two-component BEC [see Eq. (3)]. Next, in our systematic progression, we consider a three-component mixture [see Eq. (2)]; finally, we turn our attention to the true spinorial BEC system [see Eqs. (1a) and (1b)]. Additionally, and also in all cases that will be examined herein, in order to initialize the dynamics, we use as initial condition for the component(s) that during the evolution will host multiple dark solitons the IRP wave function given by Eq. (5). Furthermore, for the component(s) that during the evolution will host multiple bright states, a Gaussian pulse is used. The latter ansatz is given by

$$\Psi(x, 0) = \sqrt{A} \exp\left[-\frac{1}{2}\kappa^2(x - X_0)^2\right], \quad (10)$$

with A , κ , and X_0 denoting respectively the amplitude, the inverse width, and the center of the Gaussian pulse. To minimize the emitted radiation during the counterflow process, in the trapped scenarios the following procedure is used. The multicomponent system is initially relaxed to its ground-state configuration. For the relaxation process, we use as an initial guess Thomas-Fermi (TF) profiles for all the participating components, i.e., $\Psi(x) = \sqrt{\mu - V_i(x)}$. Here, μ denotes the common chemical potential assumed throughout this work for all models under consideration. It is relevant to mention in passing here that the selection of a common μ is a necessity (due to the spin-dependent interaction) in the spinor system, but not in the Manakov case (where it constitutes a simplification in order to reduce the large number of parameters in the problem). Additionally, $i = d, b$ indicates the different traps used for the participating species. In particular, the component(s) that will host during evolution dark solitons is (are) confined in a double-well potential that reads [67,69]

$$V_d(x) = V(x) + G \exp(-x^2/w^2). \quad (11)$$

In Eq. (11), $V(x)$ is the standard harmonic potential, while G and w are the amplitude and width of the Gaussian barrier used. Tuning G and w allows us to control the spatial separation of the two condensates. We also note in passing that the choice of Eq. (11) is based on the standard way to induce the counterflow dynamics in single-component BEC experiments [64,65]. The remaining component(s) that during evolution will host bright solitons are trapped solely in a harmonic potential $V_b(x) = \frac{1}{2}\Omega_b^2 x^2$, with $\Omega_b > \Omega$. The latter

choice is made in order to reduce the initial spatial overlap between the components which, in turn, facilitates soliton generation during the dynamics. After the above-discussed relaxation process, the system is left to dynamically evolve in the common harmonic potential $V(x)$ by switching off the barrier in Eq. (11), i.e., setting $G = 0$, and also removing V_b by setting $\Omega_b = 0$.

In all cases under investigation, in order to simulate the counterflow dynamics of the relevant mixture, a fourth-order Runge-Kutta integrator is employed, and a second-order finite-differences method is used for the spatial derivatives. The spatial and time discretizations are $dx = 0.1$ and $dt = 0.001$, respectively. Moreover, unless stated otherwise, throughout this work we fix $|\mu| = 1$, $\Delta\phi = 0$ [see Eq. (5)] and $A = 1$, $\kappa = 1$, $X_0 = 0$ [see Eq. (10)]. The default parameters for the trapped scenarios are $\mu_j = \mu = 1$ (with j denoting the participating components) $G = 5\mu$, $w^2 = 5$, $\Omega = 0.05$, and $\Omega_b = 30\Omega$. We have checked that slight deviations from these parametric selections do not significantly affect our qualitative observations reported below. Additionally, for the spinor BEC system, we also fix $g_s = -4.6 \times 10^{-3}$. Notice that the chosen value is exactly the ratio $\frac{a_2 - a_0}{a_0 + 2a_2}$ that is (in the range) typically used in ferromagnetic spinor $F = 1$ BEC of ^{87}Rb atoms [73,74]. However, we note that the numerical findings to be presented below are not altered significantly even upon considering a spinor $F = 1$ BEC of ^{23}Na atoms.

Finally, focusing on ^{87}Rb BEC systems, our dimensionless parameters can be expressed in dimensional form by assuming a transversal trapping frequency $\omega_\perp = 2\pi \times 175$ Hz. Then, all timescales must be rescaled by 8.1 s and all length scales by $100 \mu\text{m}$. This yields an axial trapping frequency $\omega_x \approx 2\pi \times 1.1$ Hz, which is accessible by current state-of-the-art experiments [55]. The corresponding aspect ratio is $\omega_x/\omega_\perp = 5 \times 10^{-3}$ and as such lies within the range of applicability of the 1D GP theory according to the criterion $Na_\perp^4/a^2a_z^2 \gg 1$ [82]. Here, a_\perp and a_z denote respectively the oscillator length in the transversal and axial direction, while a is the three-dimensional s -wave scattering length.

III. NUMERICAL RESULTS AND DISCUSSION

A. Two-component BEC

In this section, we present our findings regarding the controlled generation of arrays of DB solitons and their robust evolution in two-component BECs [7–12]. To induce the counterflow dynamics, we utilize the methods introduced in Sec. II B. Before delving into the associated dynamics, we should first recall that in the integrable limit, i.e., $g_n = 1$ and $V(x) = 0$, the system of Eqs. (3) admits an exact DB soliton solution. The corresponding DB waveforms read [10, 19–21,76]

$$\Psi_d(x, t) = [v \tanh[\mathcal{D}(x - x_0(t))] + i\lambda]e^{-it}, \quad (12)$$

$$\Psi_b(x, t) = \eta \operatorname{sech}[\mathcal{D}(x - x_0(t))]e^{[ikx + i\varphi(t)]}, \quad (13)$$

and are subject to the boundary conditions $|\Psi_d|^2 \rightarrow 1$ and $|\Psi_b|^2 \rightarrow 0$ as $|x| \rightarrow \infty$, in the dimensionless units adopted herein. In Eqs. (12) and (13), Ψ_d (Ψ_b) is the wave function of the dark (bright) soliton component. In the aforementioned

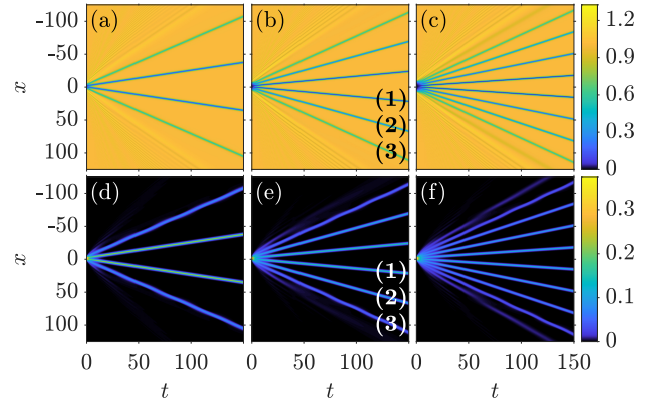


FIG. 2. Spatiotemporal evolution of the density $|\Psi_1|^2$ ($|\Psi_2|^2$) of the first (second) component upon varying the half-width a of the initial IRP. From left to right, $a = 3$, $a = 5$, and $a = 7$, allowing the generation of four [(a)–(d)], six [(b)–(e)], and ten [(c)–(f)] DB solitons, respectively. In all cases, top (bottom) panels illustrate the formation of dark (bright) solitons in the first (second) component of the two-component system. Labels (1)–(3) introduced in panels (b) and (e) number the DB solitons discussed in Table I. Note that the quantities shown are measured in transverse oscillator units (see text).

solutions, v and η are the amplitudes of the dark and the bright solitons, respectively, while λ sets the velocity of the dark soliton. Furthermore, \mathcal{D} denotes the common—across components—inverse width parameter, and $x_0(t)$, which will be traced numerically later on, refers to the center position of the DB soliton (see also our discussion below). Additionally, in the above expressions, $k = \mathcal{D}(\lambda/v)$ is the constant wave number of the bright soliton associated with the DB soliton’s velocity and $\varphi(t)$ is its phase. Inserting the solutions of Eqs. (12) and (13) in the system of Eqs. (3) leads to the following conditions that the DB soliton parameters must satisfy for the above solution to exist:

$$\mathcal{D}^2 = v^2 - \eta^2, \quad (14)$$

$$\dot{x}_0 = \mathcal{D} \frac{\lambda}{v}, \quad (15)$$

where \dot{x}_0 is the DB soliton velocity. Through the normalization of Ψ_b , we can connect the number of particles of the bright component, N_b , with η and \mathcal{D} :

$$N_b = \int |\Psi_b(x, t)|^2 dx = \frac{2\eta^2}{\mathcal{D}}. \quad (16)$$

In the following, we will use the aforementioned conditions, namely Eqs. (14) and (15), not only to verify the nature of the emergent states but also to compare the trajectories of the evolved DBs to the analytical prediction provided by Eq. (15). Moreover, by making use of Eq. (16), we will further estimate the number of particles hosted in the bright soliton component of the mixture.

The outcome of the counterflow process for different variations of the half-width a of the initial IP-IRP is illustrated in Figs. 2(a)–2(f). In particular, in all cases depicted in this figure, the spatiotemporal evolution of the densities, $|\Psi_j|^2$ (with

$j = 1, 2$), of both components for propagation times up to $t = 150$ is presented. It is found that from the very early stages of the dynamics the interference fringes in the first component evolve into several dark soliton states being generated in this component. For example, four dark solitons can be readily seen in Fig. 2(a) for $a = 3$. The nucleation of these dark states leads in turn to the emergence, via the confinement of the spreading Gaussian pulse, also of four bright solitons in the second component of the binary mixture [Fig. 2(d)]. The latter bright wave forms are created in each of the corresponding dark minima and are subsequently waveguided by their dark counterparts. The robust propagation of the newly formed array of DB solitons is illustrated for times up to $t = 150$. Importantly, here we were able to showcase that by tuning the half-width of the initial IRP a controllable formation of arrays of DB solitons can be achieved. In particular, it is found that increasing the initial half-width of the IP-IRP leads to a larger number of DB solitons being generated. Indeed, as shown in Figs. 2(b) and 2(e), six DB states are formed for $a = 5$, while for $a = 7$ the resulting array consists of ten DB solitons as illustrated in Figs. 2(c) and 2(f). We should remark also here that since an IP-IRP is utilized only an even number of DB solitons is expected and indeed observed in all of the aforementioned cases. This result is in line with the analytical predictions discussed in the single-component scenario [see also Eq. (7)].

Moreover, to verify that indeed the entities formed are DB solitons we proceed as follows. First, upon fitting it is confirmed that the evolved dark and bright states have the standard tanh- and sech-shaped wave forms, respectively [see Eqs. (12) and (13)]. Then, by monitoring during evolution a selected DB pair, we measure the amplitudes ν and η of the dark and the bright constituents, respectively. Having at hand the numerically obtained amplitudes, we then use the analytical expressions stemming from the single DB soliton solution, namely Eqs. (14)–(16). In this way, estimates of the corresponding DB trajectory as well as the number of particles, N_b , hosted in the selected bright soliton are extracted. Via the aforementioned procedure and, e.g., for the closest to the origin ($x = 0$) right-moving DB solitary wave labeled as (1) and shown in Figs. 2(b)–2(e), it is found that $N_b = 0.3611$ while the numerically obtained value is $N_b^{\text{num}} = 0.3607$. Notice that the deviation between the semianalytical calculation and the numerical one is less than 1%. To have access to N_b^{num} , we simply integrated $|\Psi_2|^2$ within a small region around the center of the bright part of the selected DB pair. Additionally, for the same DB pair $\dot{x}_0 = 0.1467$ while $\dot{x}_0^{\text{num}} = 0.1495$.

After confirming that all entities illustrated in Figs. 2(a)–2(f) are indeed DB solitons, with each of the resulting DBs following the analytical predictions of Eqs. (14)–(16), we next consider different parametric variations. In particular, we will investigate modifications in the DB soliton characteristics when the number of the nucleated DB states is held fixed. To this end, below we fix $a = 5$ and we then vary within the interval $[0.5, 2]$ one of the following parameters at a time: $|u|$, A , κ .

Before proceeding, two important remarks are of relevance at this point. (i) Fixing $a = 5$ is not by itself sufficient to *a priori* ensure that a fixed number of DB solitons will be

TABLE I. Changes in the DB soliton characteristics upon considering different variations of the systems' parameters for fixed $a = 5$. Here, (1) [(3)] refers to the innermost [outermost] DB solitons [see Figs. 2(b) and 2(e)]. The top row indicates the distinct variations, namely of each $|u|$, A , and κ , performed separately within the interval $[0.5, 2]$. The second row contains the soliton characteristics such as the dark, ν , and bright, η , amplitudes. Also shown are the inverse width, \mathcal{D} , the normalized number of particles, n_b , hosted in each of the bright solitons formed in the second component of the mixture, and the velocity, \dot{x}_0 , of the DB pair. \uparrow (\downarrow) arrows indicate an increase (decrease) of the corresponding quantity.

[0.5, 2]	$ u \uparrow$					$A \uparrow$					$\kappa \uparrow$				
	DB	ν	η	\mathcal{D}	n_b	\dot{x}_0	ν	η	\mathcal{D}	n_b	\dot{x}_0	ν	η	\mathcal{D}	n_b
(1)	\uparrow	\uparrow	\uparrow	\uparrow	\uparrow	\downarrow	\uparrow	\downarrow	\downarrow	\downarrow	\uparrow	\downarrow	\uparrow	\downarrow	\downarrow
(2)	\uparrow	\uparrow	\uparrow	\uparrow	\uparrow	\downarrow	\uparrow	\downarrow	\downarrow	\downarrow	\uparrow	\downarrow	\uparrow	\downarrow	\downarrow
(3)	\uparrow	\uparrow	\uparrow	\downarrow	\uparrow	\downarrow	\uparrow	\downarrow	\uparrow	\downarrow	\uparrow	\downarrow	\uparrow	\uparrow	\downarrow

generated via the interference process. This is because the number of solitons formed is proportional to a and $|u|$ as detected by Eq. (7). This is the reason for restricting ourselves to the aforementioned interval in terms of $|u|$ ($|u| \in [0.5, 2]$). This selection leads to the formation of an array consisting of only six DB solitons like the ones shown in Figs. 2(b) and 2(e) for $A = \kappa = 1$. (ii) Additionally, here variations of either A or κ could in principle affect the bright soliton formation; however, we have not found this to be the case in our intervals of consideration.

Taking advantage of the symmetric formation of these six DB structures in the analysis that follows, we will focus our attention to the three, i.e., (1), (2), and (3), right-moving with respect to $x = 0$ DB solitons shown in Figs. 2(b) and 2(e). The effect that different parametric variations have on the characteristics of these three DB solitons are summarized in Table I. In particular, in this table, the arrow \uparrow (\downarrow) indicates an increase (decrease) of the corresponding soliton characteristics as one of the parameters $|u|$, A , or κ is increased within the chosen interval. In general, it is found that as the amplitude, $|u|$, of the initial IP-IRP increases, the amplitudes, ν and η , of all three DB structures increase as well (see the second column in Table I). Also, the resulting DB states are found to be narrower (larger inverse width \mathcal{D}) and faster (larger \dot{x}_0). However, the normalized number of particles, n_b , hosted in each of the bright soliton constituents is found to increase for the two innermost DB states [i.e., (1) and (2)] while it decreases for the outer one [i.e., (3)]. For instance, for the inner DB wave labeled (1) shown in the first column of Table I, n_b is found to be $n_b = 0.196$ for $|u| = 0.5$, while $n_b = 0.204$ for $|u| = 1$. Thus, the symbol \uparrow is used to describe the increasing tendency of n_b (see the second column of Table I). We defined n_b according to $n_b = N_b^{\text{num}}/N_2$ with $N_2 = \int |\Psi_2|^2 dx$ being the total number of particles in the second component of the binary mixture. For comparison here, for the outer DB soliton labeled (3), $n_b = 0.092$ for $|u| = 0.5$, while $n_b = 0.075$ for $|u| = 1$, and thus a symbol \downarrow is introduced (see again the second column in Table I).

On the contrary, upon increasing the amplitude, A , of the initial Gaussian pulse [see Eq. (10)] the amplitudes of all dark

(bright) solitons for all three DB pairs decrease (increase); thus a decrease of the corresponding inverse width results in wider and slower soliton pairs (see the third column in Table I). Moreover, n_b is found to decrease for the two inner DB pairs while it increases for the outer one. Variations of the inverse width, κ , of the Gaussian pulse have more or less the opposite of the above-described effect. As κ increases, the resulting dark (bright) states have larger (smaller) amplitudes for all three DB pairs but the solitons are narrower and slower (see the fourth column in Table I). Recall that narrower does not directly imply faster states since the amplitude of the generated dark solitons is also involved [see Eqs. (14) and (15)]. Also, in this case n_b increases for the outer DB pair (see the fourth column in Table I). Finally, we also considered different displacements, X_0 , of the initial Gaussian pulse within the interval $[0, 7.5]$. A behavior similar to the aforementioned κ variation is observed. However, the produced solitons are found to be asymmetric for $X_0 \neq 0$ due to the asymmetric positioning of the two components. On the other hand, for $X_0 \geq a$ ($a = 5$), we never observe DB soliton generation.

Having discussed in detail the homogeneous system, we next turn our attention to the harmonically confined one [see Eq. (3)]. Recall that in this case the initial guesses used for both components of the binary mixture are TF profiles. The first component is initially confined in the double-well potential $V_d(x)$ with the width w of the barrier controlling the spatial separation of the two parts of the condensate [see Eq. (11)]. The corresponding second component is in turn trapped in the harmonic potential $V_b(x)$ (see Sec. II B). After relaxation, the two-component system is left to dynamically evolve in the common parabolic trap $V(x)$.

In line with our findings for the homogeneous setting, also here a desirable number of DB solitons can be achieved by properly adjusting either w or the chemical potentials μ_i (with $i = 1, 2$) of the binary mixture. Note that in this latter case, the amplitude of the system is directly related to μ [see Eq. (7)]. In both cases, it is found that an increase of w or μ results in more DB solitons being generated. In particular, Figs. 3(a)–3(c) [Figs. 3(d)–3(f)] illustrate the dynamical evolution of the density, $|\Psi_1|^2$ ($|\Psi_2|^2$), of the first (second) component of the mixture upon increasing w . An array consisting of two, four, and six DB soliton pairs can be observed for $w^2 = 1$, $w^2 = 5$, and $w^2 = 10$, respectively. In all cases depicted in this figure, the DB states are formed from the very early stages of the dynamics. After their formation, the states begin to oscillate within the parabolic trap. Monitoring their propagation for evolution times up to $t = 450$, it is found that while coherent oscillations are observed for the two DB case [see Figs. 3(a) and 3(d)], this picture is altered for larger DB soliton arrays. In the former case, measurements of the oscillation frequency, ω_{osc} , verify that it closely follows the analytical predictions for the single DB soliton. Namely, $\omega_{\text{osc}}^2 = \Omega^2(\frac{1}{2} - \frac{\chi}{\chi_0})$, with $\chi = N_b/\sqrt{\mu}$ and $\chi_0 = 8\sqrt{1 + (\frac{\chi}{4})^2}$ [10,83]. For instance, our semianalytical calculation stemming from the aforementioned theoretical prediction gives $\omega_{\text{osc}} = 34.3 \times 10^{-3}$, while direct measurements from our numerical simulations provide $\omega_{\text{osc}}^{\text{num}} = 35.3 \times 10^{-3}$. This represents a 3% discrepancy, which can be attributed to the interaction of the solitons both with one another but also with the background excitations,

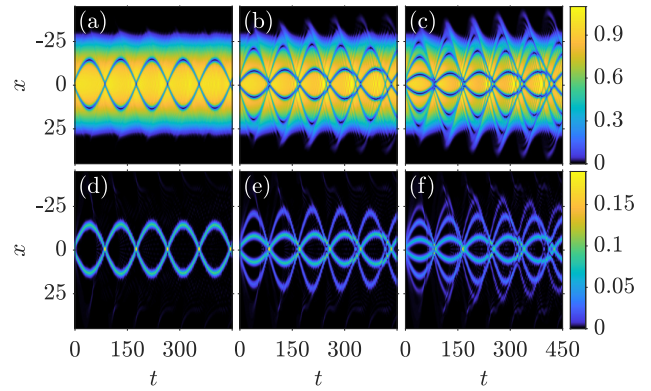


FIG. 3. Spatiotemporal evolution of the density $|\Psi_1|^2$ ($|\Psi_2|^2$) of the first (second) component in the trapped scenario upon varying the width of the double-well barrier w used for the preparation of the initial state. From left to right, $w^2 = 1$, $w^2 = 5$, and $w^2 = 10$, allowing the generation of two [(a)–(d)], four [(b)–(e)], and six [(c)–(f)] DB solitons respectively. In all cases, top (bottom) panels illustrate the formation of dark (bright) solitons in the first (second) component of the two-component system. Note that the quantities shown are measured in transverse oscillator units (see text).

with the latter having the form of sound waves. Additionally, it should be noted that the theoretical prediction is valid in the large μ limit (which may be partially responsible for the relevant discrepancy). However, for larger DB soliton arrays, the number of collisions is higher and the background density is more excited, as can be deduced by comparing Figs. 3(a) and 3(d) to Figs. 3(b) and 3(e), and Figs. 3(c) and 3(f). Importantly, here the generated DB states are of different masses and thus each DB soliton oscillates with its own ω_{osc} . It is this mass difference that results in the progressive “dephasing” observed during evolution. Notice also that in all cases illustrated in the aforementioned figures, the outer (faster) DB solitons are the ones that are affected the most. The above effect is enhanced for larger initial separations w [compare Figs. 3(b) and 3(e) to Figs. 3(c) and 3(f)], leading to discrepancies up to 11.6% between ω_{osc} and $\omega_{\text{osc}}^{\text{num}}$ observed for the outermost DB pair shown in Figs. 3(c) and 3(f).

As mentioned above, besides w also the chemical potential, μ , serves as a controlling parameter. Indeed, by inspecting the spatiotemporal evolution of the densities, $|\Psi_j|^2$ (with $j = 1, 2$), shown in Figs. 4(a) and 4(f) for fixed $w^2 = 5$, it becomes apparent that increasing μ leads to an increased number of DB solitons being generated. Four, six, and eight DB solitons are seen to be nucleated for $\mu = 1$, $\mu = 3$, and $\mu = 5$, respectively, and to propagate within the BEC medium for long evolution times. Notice that Figs. 4(a) and 4(b) are the same as Figs. 3(b) and 3(e). Increasing the system size reduces the impact that the radiation expelled (when matter-wave interference takes place) has on the resulting DB states, as can be deduced by comparing Figs. 4(c) and 4(d) to Figs. 3(c) and 3(f). Indeed, further measurements of ω_{osc} reveal that the maximum discrepancy observed for the outermost DB solitons when $\mu = 1$ [see Figs. 4(a) and 4(b)] is of about 8.5%, while upon increasing μ the discrepancy is significantly reduced. The latter reduction is attributed to

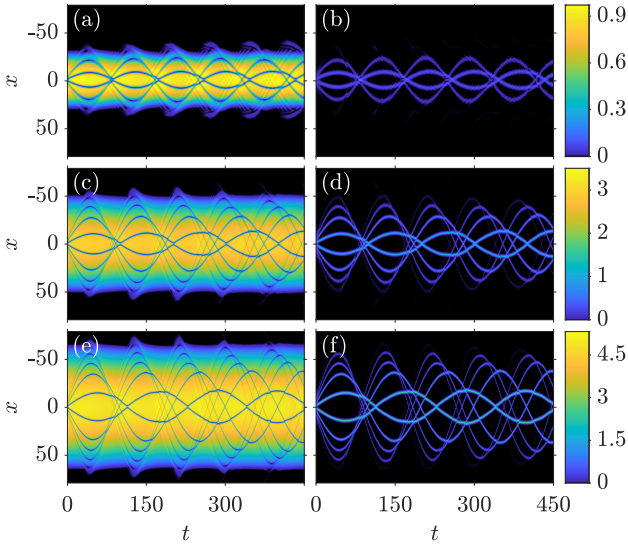


FIG. 4. Spatiotemporal evolution of the density $|\Psi_1|^2$ ($|\Psi_2|^2$) of the first (second) component in the trapped scenario upon varying the chemical potential μ while fixing $w^2 = 5$. From top to bottom $\mu = 1$, $\mu = 3$, and $\mu = 5$, leading to the emergence of four [(a), (b)], six [(c), (d)], and eight [(e), (f)] DB solitons, respectively. In all cases, left (right) panels illustrate the formation of dark (bright) solitons in the first (second) component of the two-component system. Note that the quantities shown are measured in transverse oscillator units (see text).

the fact that for larger μ the asymptotic prediction of ω_{osc} is progressively more accurate. More specifically, for $\mu = 5$ we obtain a discrepancy of only 0.3% for the third, with respect to $x = 0$, DB soliton pair shown in Figs. 4(e) and 4(f). Yet still, the emergent DB states have different periods of oscillation, leading in turn to several collision events taking place during evolution. Nevertheless, in all cases presented above, a common feature of the solitary waves is that they survive throughout our computational horizon.

B. Three-component BEC

Now, we increase the complexity of the system by adding yet another component to the previously discussed two-component mixture. Namely we consider a three-component mixture consisting of three different hyperfine states of the same alkali isotope such as ^{87}Rb . We aim at revealing the DB soliton complexes that arise in such a system and their controllable formation via the interference processes introduced in Sec. II B. From a theoretical point of view, such a three-component BEC mixture is described by a system of three coupled GPEs [see Eqs. (2) in Sec. II A], i.e., one for each of the participating $m_F = +1, 0, -1$ components.

To begin our analysis, we start with the integrable version of the problem at hand. Namely, we fix $g_n = 1$ and we set $V(x) = 0$ in the corresponding Eqs. (2). This homogeneous mixture admits exact solutions in the form of DDB and DBB solitons as it was rigorously proven via the inverse scattering method [76]. In the following, we will attempt to produce in a controlled fashion arrays consisting of these types of

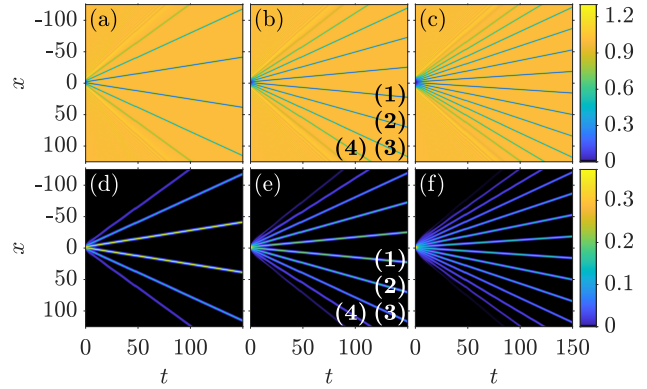


FIG. 5. Spatiotemporal evolution of the density $|\Psi_{+1}|^2$ ($|\Psi_{-1}|^2$) of the $m_F = +1$ ($m_F = -1$) component upon varying the half-width a of the initial IRP. From left to right, $a_{+1} = a_0 = 3$, $a_{+1} = a_0 = 5$, and $a_{+1} = a_0 = 7$, resulting in the nucleation of six [(a), (d)], eight [(b), (e)], and twelve [(c), (f)] DDB solitons, respectively. In all cases, top (bottom) panels illustrate the formation of dark (bright) solitons in the $m_F = +1$ ($m_F = -1$) component of the three-component system. Since the evolution of the $m_F = 0$ component is the same as the one depicted for the $m_F = +1$, only the two components that differ from one another are illustrated. The labels (1)–(4) introduced in panels (b) and (e) number the DDB solitons that are discussed in Table II. Note that the quantities shown are measured in transverse oscillator units (see text).

soliton compounds. We further note that in the numerical findings to be presented below the abbreviations in the form XYZ (with $X, Y, Z = \text{D or B}$) reflect the $m_F = +1, 0, -1$ order. For example, a DDB abbreviation indicates that dark solitons are generated in the $m_F = +1, 0$ components while bright solitons are generated in the $m_F = -1$ component of the mixture.

As was done in the two-component setting, in order to generate a DDB configuration, the counterflow dynamics is performed by two of the participating hyperfine components. Recall that dark solitons in each hyperfine state emerge via the destructive interference that takes place at the origin where the two spatially separated sides of the initial IP-IRP collide. Specifically, the initial ansatz used for the $m_F = +1, 0$ states is provided by Eq. (5) and the corresponding ansatz for the $m_F = -1$ component is the Gaussian of Eq. (10). It turns out that we can again tailor the number of nucleated DDB solitons by manipulating the half-width, a_{m_F} (with $m_F = +1, 0$), of the initial IP-IRP. To showcase the latter, in Figs. 5(a)–5(f) we present the outcome of the distinct variations of a_{m_F} . Notice that as a_{m_F} increases arrays consisting of a progressively larger number of DDB solitons are formed. Namely, $a_{+1} = a_0 = 3$ results in an array of six DDB solitons [Figs. 5(a) and 5(d)]. Accordingly, when $a_{+1} = a_0 = 5$ the nucleation of eight DDB wave forms is observed [see Figs. 5(b) and 5(e)], while twelve such states occur for $a_{+1} = a_0 = 7$ [Figs. 5(c) and 5(f)]. In all of the above cases, the spatiotemporal evolution of the densities $|\Psi_{+1}|^2$ and $|\Psi_{-1}|^2$ is shown in the top and bottom panels of Fig. 5, respectively. The resulting propagation of the ensuing DDB states is monitored for evolution times up to $t = 150$. Moreover, only the $m_F = \pm 1$ components are depicted in the aforementioned figure. This is

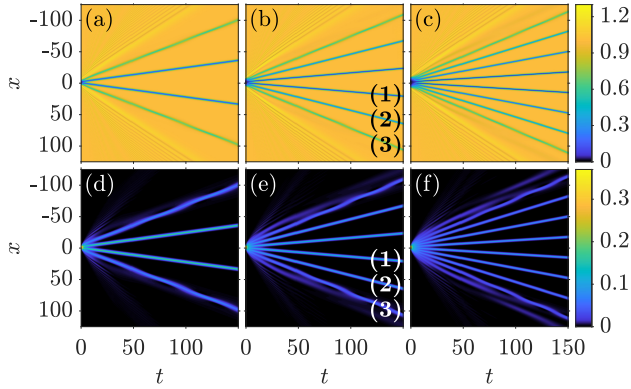


FIG. 6. Same as in Fig. 5 but showcasing the generation of DBB solitons. In this case, from left to right $a_{+1} = 3$, $a_{+1} = 5$, and $a_{+1} = 7$, allowing the generation of four [(a), (d)], six [(b), (e)], and eight [(c), (f)] DBB solitons respectively. The labels (1)–(3) introduced in panels (b) and (e) number the DBB solitons that are discussed in Table III. Note that the quantities shown are measured in transverse oscillator units (see text).

because the evolution of the $m_F = 0$ component is essentially identical to the one shown for the $m_F = +1$ component.

The same overall picture is qualitatively valid for the corresponding DBB soliton formation. Note that in contrast to the DDB nucleation, to generate DBB soliton arrays the counterflow dynamics is featured solely by one of the hyperfine components, which as per our choice is the $m_F = +1$ one. The remaining two hyperfine components, namely $m_F = 0, -1$, share the same Gaussian-shaped initial profile. In Figs. 6(a)–6(f), the formation of four, six, and eight DBB soliton complexes is shown for $a_{+1} = 3$, $a_{+1} = 5$, and $a_{+1} = 7$, respectively. Notice that the number of the generated DBB states appears to be lower when compared to the DDB solitons formed for the same value of a_{+1} . For instance, four DBB solitons are formed for $a_{+1} = 3$ [Figs. 6(a) and 6(d)] while the corresponding DDB soliton count is six [Figs. 5(a) and 5(d)]. The observed difference between the number of nucleated DBB and DDB states can be intuitively understood as follows. For a DDB production, the total number of particles is $N = 2990$, while for a DBB one, it is $N = 1498$, e.g., for the case examples presented in Figs. 5(a) and 5(d), and in Figs. 6(a) and 6(d), respectively. Recall that in our simulations we fix the chemical potential and thus N is a free parameter. The significantly lower number of particles in a DBB nucleation process stems from the fact that two of the participating components have a Gaussian initial profile and as such host fewer particles. This decrease of the system size for a DBB realization when compared to a DDB one may be partially responsible for the observed decreased DBB soliton count. Moreover, in the DDB case, the presence of two components (namely $m_F = +1, 0$ components, each one characterized by an amplitude $|u|$ with a finite background leads to a total amplitude $|u_{\text{eff}}| \approx 2|u|$. Thus, as dictated by Eq. (7), the number of solitons is expected to be higher as well. Further adding to the above, for a DBB formation only one component develops, via interference, dark solitons. These dark solitons are, in turn, responsible for the trapping of bright solitons in the other two hyperfine

TABLE II. Changes in the DDB soliton characteristics upon considering different variations of the systems' parameters and monitoring the four right-moving DDB solitons generated for fixed $|u_{+1}| = 1$ and $a_{+1} = a_0 = 5$. Here, (1) [(4)] refers to the innermost [outermost] DDB state [see Figs. 5(b) and 5(e)]. The top row indicates the distinct variations, namely $|u_0|$, A_{-1} , and κ_{-1} , performed within the interval $[0.5, 2]$. The second row contains the soliton characteristics, i.e., the dark, $v_{+1,0}$, and bright, η_{-1} , amplitudes, the common inverse width, \mathcal{D} , the normalized number of particles, n_b , hosted in the bright soliton component and the velocity, \dot{x}_0 , of the DDB pair. \uparrow arrows (\downarrow) indicate an increase (decrease) of the corresponding quantity. \updownarrow arrows indicate that within the above interval a nonmonotonic tendency of the respective quantity is observed.

[0.5, 2]	$ u_0 \uparrow$				$A_{-1} \uparrow$				$\kappa_{-1} \uparrow$									
DDB	v_{+1}	v_0	η_{-1}	\mathcal{D}	n_b	\dot{x}_0	v_{+1}	v_0	η_{-1}	\mathcal{D}	n_b	\dot{x}_0	v_{+1}	v_0	η_{-1}	\mathcal{D}	n_b	\dot{x}_0
(1)	\uparrow	\uparrow	\uparrow	\uparrow	\uparrow	\uparrow	\downarrow	\downarrow	\uparrow	\downarrow	\downarrow	\updownarrow	\uparrow	\uparrow	\downarrow	\uparrow	\downarrow	\downarrow
(2)	\uparrow	\uparrow	\uparrow	\uparrow	\uparrow	\uparrow	\downarrow	\downarrow	\uparrow	\downarrow	\downarrow	\updownarrow	\uparrow	\uparrow	\downarrow	\uparrow	\downarrow	\downarrow
(3)	\uparrow	\uparrow	\uparrow	\uparrow	\downarrow	\uparrow	\downarrow	\downarrow	\uparrow	\downarrow	\downarrow	\updownarrow	\uparrow	\uparrow	\downarrow	\uparrow	\downarrow	\downarrow
(4)	\uparrow	\uparrow	\uparrow	\uparrow	\downarrow	\uparrow	\downarrow	\downarrow	\uparrow	\downarrow	\downarrow	\updownarrow	\uparrow	\uparrow	\uparrow	\uparrow	\uparrow	\downarrow

components. However, since two components develop bright solitons effectively, the number of particles that have to be sustained by each effective dark well increases. As such in the DBB case, the system prefers to develop fewer but also wider and deeper dark solitons than in the DDB process; this is also inter-related with the smaller counterflow-induced momentum in the DBB case. These deeper dark solitons can in turn efficiently trap and waveguide the resulting (also fewer) bright solitons. The above intuitive explanation is fairly supported by our findings. Indeed, both the dark and the bright solitons illustrated in Figs. 6(a) and 6(d) appear to be wider, having also larger amplitudes when compared to the ones formed in the DDB interference process shown in Figs. 5(a) and 5(d).

In all cases presented in Figs. 5(a)–5(f) and Figs. 6(a)–6(f), we were able to showcase upon fitting that the evolved dark and bright states have the standard tanh- and sech-shaped wave forms, respectively [see Eqs. (12) and (13)]. Moreover, following the procedure described in the two-component setting (see Sec. III A), we verified that the number of particles hosted in each of the bright solitons formed follows Eq. (16), with the common inverse width, \mathcal{D} , satisfying the generalized conditions

$$\mathcal{D}^2 = v_j^2 + v_k^2 - \eta_l^2, \quad (17)$$

$$\mathcal{D}^2 = v_j^2 - \eta_k^2 - \eta_l^2, \quad (18)$$

for the DDB and the DBB cases, respectively. The indices j, k, l in the above expressions denote the three (distinct) hyperfine components. As a case example, for one of the DDB states shown in Figs. 5(b) and 5(e), $N_b^{\text{num}} = 0.3715$, while the semianalytical prediction gives $N_b = 0.3721$. Notice that the deviation is again smaller than 1%.

As a next step, we attempt to appreciate the effects that different initial configurations have on the characteristics of the resulting DDB and DBB soliton compounds. Our findings are summarized in Tables II and III, respectively. Specifically, for a DDB nucleation process, $|u_{+1}| = 1$ and $a_{+1} = a_0 = 5$

TABLE III. Same as Table II but for the three right-moving DBB solitons generated for fixed $a_{+1} = 5$. (1) [(3)] denotes the innermost [outermost] DBB structure shown in Figs. 6(b) and 6(e). Other parameters used are $A_{-1} = \kappa_{-1} = 1$.

[0.5, 2]	$ u_{+1} \uparrow$							$A_0 \uparrow$							$\kappa_0 \uparrow$							
	DBB	v_{+1}	η_0	η_{-1}	\mathcal{D}	n_0	n_{-1}	\dot{x}_0	v_{+1}	η_0	η_{-1}	\mathcal{D}	n_0	n_{-1}	\dot{x}_0	v_{+1}	η_0	η_{-1}	\mathcal{D}	n_0	n_{-1}	\dot{x}_0
(1)	↑	↑	↑	↑	↑	↑	↑	↓	↑	↓	↓	↓	↓	↓	↑	↓	↑	↑	↓	↓	↓	↓
(2)	↑	↑	↑	↑	↑	↑	↑	↓	↑	↓	↓	↓	↓	↓	↑	↓	↑	↑	↓	↓	↑	↓
(3)	↑	↑	↑	↑	↓	↓	↑	↓	↑	↓	↓	↑	↑	↓	↑	↓	↑	↑	↓	↓	↓	↓

are held fixed. The remaining parameters are varied (one of them at a time) within the interval $[0.5, 2]$. The above selection leads to the appearance of eight DDB solitons symmetrically formed around the origin as already illustrated in Figs. 5(d) and 5(e). Exploiting this symmetric formation only the four, i.e., (1)–(4), right-moving DDB solitons indicated in Figs. 5(d) and 5(e) are monitored and shown in Table II.

It becomes apparent, by comparing the DDB results of Table II with the ones found in the two-component scenario (see Table I), that the inclusion of an extra $m_F = +1$ component prone to host dark solitons leads to the following comparison of the resulting soliton characteristics. As $|u_0|$ is increased within the interval $[0.5, 2]$, all the generated DDB states appear to be faster and narrower (see second column in Table II). Additionally, larger amplitudes are observed for all the solitons in all the three hyperfine components. The same qualitative results were also found in the relevant variation but for the two-component system (see second column in Table I). It is important to stress at this point that further increase of $|u_0|$ and/or different initial values of $|u_{+1}|$ can lead to a change in the number of states generated as suggested also by Eq. (7). This is the reason for limiting our variations to the aforementioned interval. However, our findings for choices of $|u_{+1}| \neq |u_0|$ suggest that, given the same half-width $a_{+1} = a_0$, the number of nucleated DDB solitons will be determined by the larger $|u_{m_F}|$ value.

On the contrary, upon varying the amplitude, A_{-1} , of the initial Gaussian pulse the impact of the additional $m_F = +1$ component is imprinted on the velocity outcome of the resulting DDB solitons (see third column in Table II). Indeed, as A_{-1} increases, a uniquely defined tendency of the velocity of the resulting states cannot be inferred at least within the interval of interest here. This result differs from the systematic overall decrease of the DB soliton velocity observed in the two-component scenario (see third column in Table I). Notice also that all the remaining soliton characteristics here are similar to the ones found in the two-component scenario (compare the third column in Tables II and I, respectively). Additionally, the presence of the extra $m_F = +1$ component leads to no modification on the observed DDB soliton characteristics when considering variations of the inverse width, κ_{-1} , of the Gaussian pulse (see fourth column in Table II). Namely, for increasing κ_{-1} all the resulting DDB states are narrower and slower. This is an outcome that was also found in this type of variation but in the two-component setting (see fourth column in Table I).

Next, we will check the same diagnostics but for the DBB nucleation process. Along the same lines, the initial parameters used for a DBB realization are $A_0 = \kappa_0 = 1$ and

$a_{+1} = 5$ [as per Eqs. (10) and (5), respectively]. This choice results in the six DBB solitons illustrated in Figs. 6(d) and 6(e). Again due to symmetry, only the three, i.e. (1)–(3), right-moving states indicated in Figs. 6(d) and 6(e) are monitored in Table III. When comparing the relevant findings presented in Table III to those shown in Table I, the following conclusions can be drawn. For increasing $|u_{+1}|$, the generated DBB solitons are found to be narrower and faster, similar to the evolved DB states observed in the two-component scenario (see second column in Table I). Alterations occur only upon varying the characteristics of the initial Gaussian pulse. In particular, the effect of adding an extra bright component upon increasing the amplitude, A_0 , of the initial Gaussian pulse is the observed increased amplitude of all bright solitons formed in this component (see third column in Table III). Yet, all the resulting DBB states are found to be wider and slower for increasing A_0 , an outcome which is similar to that found in the two-component setting (see third column in Table I). Lastly, upon increasing κ_0 , the impact that the extra $m_F = 0$ component has on the resulting DBB solitons is the following (see fourth column in Table III). Besides the observed decreased amplitude of all bright solitons formed in this component, the outermost DBB states, i.e., (2) and (3), are the ones that are affected the most. Notice that a nonmonotonic response of the normalized number of particles, n_0 , hosted in this $m_F = 0$ component is found as κ_0 increases within the interval $[0.5, 2]$. Additionally, the velocity of all three DBB solitons shows a nonmonotonic tendency as κ_0 is increased. It is relevant to note that this result is in contrast to the decrease observed in the two-component scenario (see fourth column in Table I).

It is worth commenting at this point that in both of the above-discussed processes we also considered variations of the relevant in each case a_{m_F} . Recall that $a_{+1,0}$ and a_{+1} are the associated half-widths of the initial IP-IRP for a DDB and DBB nucleation process, respectively. In particular, by fixing all parameters to their default values (see here Sec. II B), we varied the relevant a_{m_F} within the interval $[1, 10]$. The general conclusion for such a variation, in both processes, is that increasing a_{m_F} results in more states which become narrower and slower as their number is increased. Differences here mostly refer to the relevant amplitudes of the resulting solitons and the normalized number of particles hosted in each bright soliton constituent. Importantly, and referring solely to the DDB process, it is found that given the same initial amplitude, $|u_{m_F}|$, the number of solitons generated depends on the smallest initial a_{m_F} . For this latter case ($a_{+1} \neq a_0$), a spatially modulated density background occurs for the components hosting the dark states. Finally, and also in both processes, we were able to verify that for displacements, X_0 ,

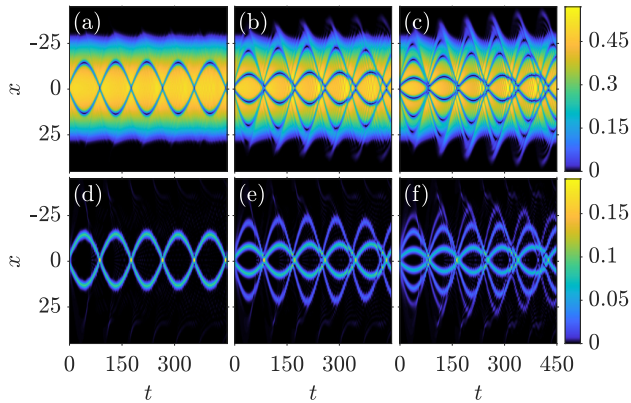


FIG. 7. Evolution of the densities $|\Psi_{+1}|^2$, $|\Psi_{-1}|^2$ showcasing the generated DDB solitons in a harmonic trap with $\Omega = 0.05$. Increasing the width w of the double-well barrier allows the generation of DDB soliton arrays consisting of two [(a), (b)], four [(c), (d)], and six [(e), (f)] DDB solitons respectively for $w^2 = 1$, $w^2 = 5$, and $w^2 = 10$. In all cases, top (bottom) panels illustrate the formation of dark (bright) solitons in the $m_F = +1$ ($m_F = -1$) component. Since the evolution of the $m_F = 0$ component is identical to the one shown for the $m_F = +1$ component, it is omitted. Note that the quantities shown are measured in transverse oscillator units (see text).

of the initial Gaussian pulse $X_0 \geq a$ generation of DDB and DBB solitons is absent. This is in line with our findings in the two-component system.

We now turn to the trapped three-component DDB and DBB case, in analogy with the corresponding two-component one. As in the latter, for the systematic production of multiple DDB and DBB solitons, we use as a control parameter the width, w , of the double-well potential [see Eq. (11)]. Figures 7(a)–7(f) illustrate the formation of two, four, and six DDB solitons for $w^2 = 1$, $w^2 = 5$, and $w^2 = 10$, respectively. In all cases presented in this figure, top (bottom) panels depict the evolution of the density, $|\Psi_{+1}|^2$ ($|\Psi_{-1}|^2$), of the $m_F = +1$ ($m_F = -1$) component. Notice the close resemblance of the dynamical evolution of the DDB states when compared to the relevant evolution of the DB soliton arrays shown in Figs. 3(a)–3(f). We remark here that the above-observed evolution holds equally for the corresponding DBB states (results not shown here for brevity).

Furthermore, below we briefly report on the systematic production of the desired number of DDB and DBB solitons upon varying the common chemical potential μ of the confined three-component system. In Figs. 8(a)–8(f), a direct comparison of the resulting DDB and DBB soliton compounds is provided for three different values of μ . Evidently, the number of DDB and DBB soliton complexes generated in each different initialization is exactly the same, and as expected, it increases for increasing μ . For example, for $\mu = 3$ illustrated in Figs. 8(c) and 8(d) for the DDB and DBB processes, respectively, the nucleated states at $t = 45$ are six. Note also that in all cases the $m_F = 0$ component overlaps either with $m_F = +1$ component (DDB nucleation process) or with the $m_F = -1$ (DBB nucleation process) and as such it is not shown in the relevant profiles. In conclusion, the dynamical evolution of both types of soliton arrays is

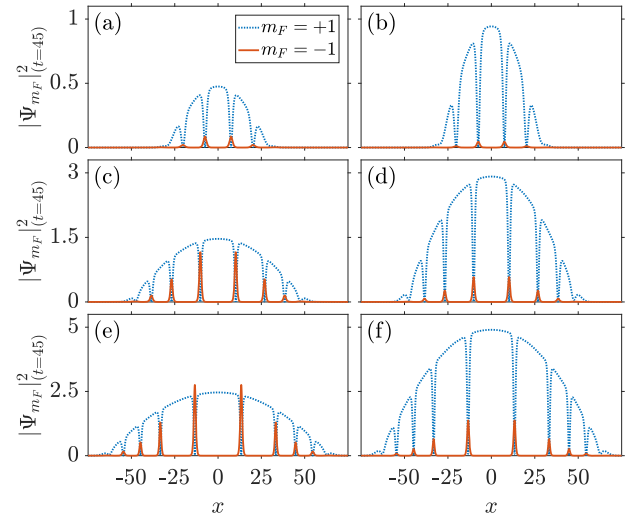


FIG. 8. Profile snapshots of the density $|\Psi_{m_F}|^2$ with $m_F = \pm 1$ at $t = 45$, illustrating the generated DDB (left) and DBB (right) solitons in the trapped scenario. In all cases, $w^2 = 5$ and we vary the corresponding chemical potential. From top to bottom, $\mu = 1$, $\mu = 3$, and $\mu = 5$, resulting in four [(a), (b)], six [(c), (d)], and eight [(e), (f)] DDB-DBB solitons, respectively. The $m_F = 0$ component is omitted since it shows the same profile as the $m_F = +1$ ($m_F = -1$) for the DDB (DBB) nucleation process. Note that the quantities shown are measured in transverse oscillator units (see text).

qualitatively the same and closely resembles the one observed in the two-component setting. Also, in all the different parametric variations and for both nucleation processes studied above, the resulting arrays of DDB and DBB solitons remain robust, while oscillating and colliding with one another, for evolution times up to $t = 450$ that we have checked.

C. Spinor BEC

Up to now, the controlled formation of multiple soliton complexes of the DB type in two- and three-component BECs has been established. In what follows, we turn our attention to the spinor $F = 1$ BEC [55]. In this way, we will be able to address the fate of the generated DDB and DBB soliton arrays when spin degrees of freedom are taken into account. Recall that the evolution of this system is dictated by Eqs. (1a) and (1b). In order to induce the dynamics, we will utilize once more the counterflow processes introduced in Sec. II B.

As usual, we start our analysis by considering the homogeneous system. As in the previous section, for a DDB generation process the initial ansatz used for the $m_F = +1$, 0 [$m_F = -1$] components is given by Eq. (5) [Eq. (10)]. Accordingly, to dynamically produce DBB soliton arrays, the corresponding initial conditions are provided by Eq. (10) [Eq. (5)] for the $m_F = 0$, -1 [$m_F = +1$] hyperfine components. Figures 9(a)–9(j) and Figs. 10(a)–10(j) summarize our numerical findings. In particular, Figs. 9(a)–9(i) illustrate the evolution of the density, $|\Psi_{m_F}|^2$, of all three $m_F = +1$, 0, -1 components. The controlled generation of four, six, and eight DBB soliton arrays can be readily seen as a_{+1} is increased from $a_{+1} = 3$ to $a_{+1} = 7$ [see Figs. 9(a), 9(d), 9(g); Figs. 9(b), 9(e), 9(h); and Figs. 9(c), 9(f), 9(i), respectively]. Comparing

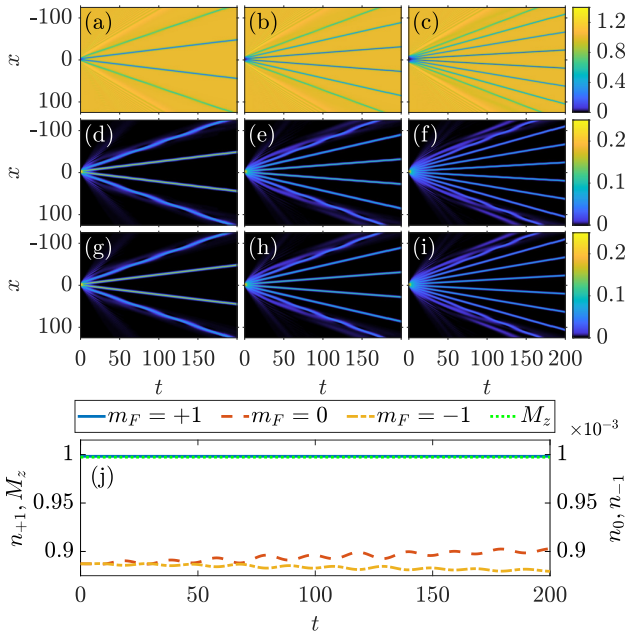


FIG. 9. Spatiotemporal evolution of the density $|\Psi_{m_F}|^2$ of the (a)–(c) $m_F = +1$, (d)–(f) $m_F = 0$, and (g)–(i) $m_F = -1$ components, respectively, for varying a_{+1} . From left to right, $a_{+1} = 3$, $a_{+1} = 5$, and $a_{+1} = 7$, allowing the generation of four [(a), (d), (g)], six [(b), (e), (h)], and eight [(c), (f), (i)] DBB solitons respectively for the homogeneous spinor setting. In all cases, (a)–(c) illustrate the formation of dark solitons in the $m_F = +1$ component and (d)–(f) [(g)–(i)] depict the formation of bright solitons in the $m_F = 0$ [$m_F = -1$] component of the spinor system. (j) Evolution of the population, n_{m_F} , of each hyperfine component, and of the total magnetization, $M_z(t)$ for $a_{+1} = 5$. Notice that n_0 and n_{-1} are three orders of magnitude smaller than n_{+1} , which is why a second axis is introduced. Note that the quantities shown are measured in transverse oscillator units (see text).

the dynamical evolution of the spinor system to the one observed in the corresponding three-component setting [see Figs. 6(a)–6(f)], it becomes apparent that the inclusion of the spin interaction has a minuscule effect on both the nucleation and the long-time evolution of the DBB states. To appreciate the latter, in Fig. 9(j) we monitor the temporal evolution of the population, i.e., $n_{m_F}(t) = \frac{1}{N} \int |\Psi_{m_F}(x, t)|^2 dx$, of each hyperfine component, as well as the total magnetization $M_z(t) = \int (|\Psi_{+1}(x, t)|^2 - |\Psi_{-1}(x, t)|^2) dx$ of the spinor system for $a_{+1} = 5$ (see also Sec. II A). Note that $n_0(t)$, $n_{-1}(t)$ have their own axis in order to be visible and that the same picture holds equally for all the distinct variations of a_{+1} presented in Fig. 9. As can be deduced, oscillations of $n_{+1}(t)$, $n_0(t)$, and $n_{-1}(t)$ occur during the evolution. Recall now that a spinor condensate is subject to the so-called spin relaxation process. The latter allows for collisions of two $m_F = 0$ atoms that can in turn produce a pair of particles in the $m_F = +1$ and $m_F = -1$ component and vice versa [37]. It is this continuous exchange of particles that leads to the oscillatory trajectories observed for the bright soliton constituents of the resulting DBB arrays. Notice that $n_{+1}(t)$ is significantly larger when compared to $n_{0,-1}(t) \sim 10^{-3}$ and due to the rescaling used appears almost constant [$n_{+1}(t) \approx 1$] during evolution.

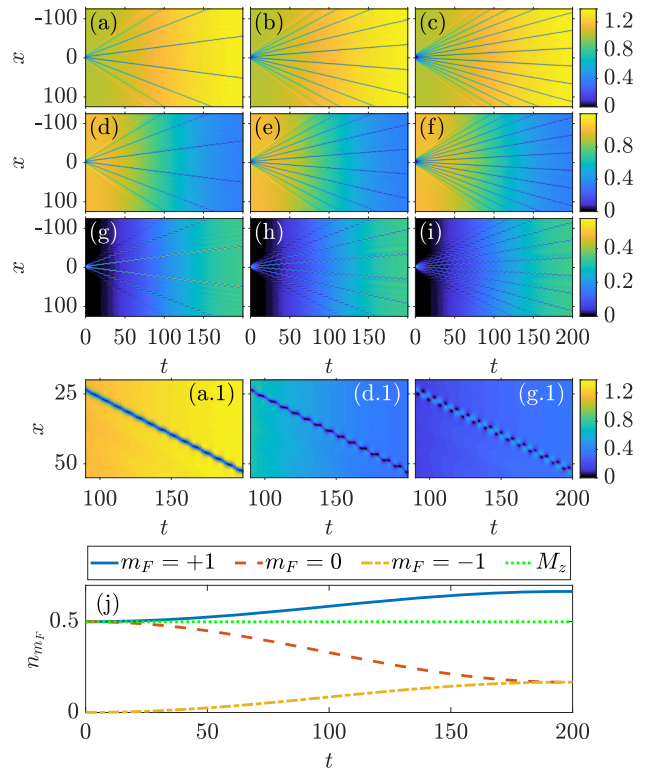


FIG. 10. Same as in Fig. 9 but showcasing the generation of DBB solitons. In all cases, panels (a)–(c) [(d)–(f)] illustrate the formation of dark solitons in the $m_F = +1$, 0 components and panels (g)–(i) illustrate the formation of bright solitons in the $m_F = -1$ component of the spinor system. [(a.1), (d.1), (g.1)] Trajectory of the closest to the origin right moving originally formed DBB soliton shown in panels (a), (d), and (g) transitioning during evolution into beating dark states. (j) Evolution of the population, n_{m_F} , of each hyperfine component, as well as of the total magnetization, $M_z(t)$, for $a_{+1} = a_0 = 5$. Note that the quantities shown are measured in transverse oscillator units (see text).

However, we must stress that also not discernible oscillations of the population of this hyperfine component are present and are similar to the ones observed for the $n_{-1}(t)$ component. Therefore, $M_z(t)$ remains constant during the evolution while being of order unity.

Contrary to the DBB nucleation process investigated above, for a DBB realization the spin-mixing dynamics plays a crucial role. As in the previous scenario, Figs. 10(a)–10(i) show the spatiotemporal evolution of the densities, $|\Psi_{m_F}|^2$, of all three m_F components. Also here, by manipulating $a_{+1} = a_0 = a$, we were able to controllably generate arrays of DBB solitons in this homogeneous spinor setting. From left to right in this figure, six, eight, and twelve solitons are formed, corresponding to $a = 3$, $a = 5$, and $a = 7$, respectively. In particular, Figs. 10(a)–10(c) [Figs. 10(d)–10(f)] depict the dark solitons formed in the $m_F = +1$ [$m_F = 0$] component. Additionally, Figs. 10(g)–10(i) illustrate the bright states formed in the respective $m_F = -1$ component. Strikingly enough, as it is observed in all of the aforementioned figures, as time evolves, the background density gradually changes (notice the change in the color gradient). This result, as we

will show later on, is attributed to the spin-mixing dynamics that significantly alters the evolution of the DDB soliton arrays formed. To shed light on the observed dynamics, below let us focus our attention on Figs. 10(a), 10(d), and 10(g) for $a = 3$. Here, also an enlargement is provided in Figs. 10(a.1), 10(d.1), and 10(g.1) to elucidate our analysis. In the latter figures, the closest to the origin DDB pair is monitored. As time evolves, the background density of the $m_F = +1$ component increases, which suggests that transfer of particles from the lower hyperfine components takes place. The latter can indeed be confirmed by inspecting the evolution of the $m_F = 0$ component. Evidently, the background density of this component gradually decreases. The corresponding density of the $m_F = -1$ component is also seen to increase. Monitoring the evolution of the respective populations, $n_{m_F}(t)$, shown in Fig. 10(j), delineates the above trend. Indeed, at $t = 0$, $n_{+1}(0) = n_0(0) = 0.5$ while $n_{-1}(0) \sim 10^{-3}$. However, during evolution $n_{+1}(t)$ increases, reaching the value of $n_{+1}(t = 200) \approx 0.66$. Accordingly, $n_0(t)$ decreases drastically during propagation, acquiring a similar value with $n_{-1}(t)$ at later evolution times, i.e., $n_0(t = 200) \approx n_{-1}(t = 200) \approx 0.16$. Note also that the total magnetization of the system is preserved with $M_z(t) = 0.5$ throughout the evolution. Returning now to the relevant densities, since the background density of the $m_F = 0$ component decreases, the dark states formed in this component begin to deform. At later times ($t > 150$), the solitonic states developed in this hyperfine component have both a dark and a bright component [see Fig. 10(d.1)]. Similarly, at early times, the $m_F = -1$ component hosts bright solitons. Since the number of particles in this case increases, a finite background slowly appears [45,51]. As such, also the bright solitons of this component begin to deform. The latter deformation leads in turn to the formation of solitonic structures that again have both bright and dark parts, involving a beating between the two, and are formed also faster in this $m_F = -1$ component when compared to the $m_F = 0$ one [see Fig. 10(g.1)]. The same deformation occurs also in the $m_F = +1$ component but at propagation times even larger than the ones depicted in Fig. 10(a). Indeed, by inspecting the evolution of the closest to the origin dark soliton of the originally formed DDB state shown in Fig. 10(a.1), the dark soliton is also deformed in this case, yet the beating pattern of Fig. 10(g.1) [and even that of Fig. 10(d.1)] is not as straightforwardly discernible. Nevertheless, close inspection indicates that the evolved states in all three m_F components bear similar characteristics to the so-called beating dark solitons that were experimentally observed in two-component systems [12]. As such, these states can be thought of as the generalization of the beating dark solitons in spinor BECs.

Before proceeding to the harmonically confined spinor BEC system, a final comment is of relevance here. Investigating the current setting, we also considered different initializations in which the symmetric, with respect to the $m_F = 0$, hyperfine states have the same initial conditions. In this way, we were able to generate symmetric variants of the DDB and DBB states discussed above, namely, DBD and BDB soliton arrays. In these cases, our simulations indicate that the resulting states show all features found in the three-component setting. Although the spin interaction is present, the conversion of particles from one component

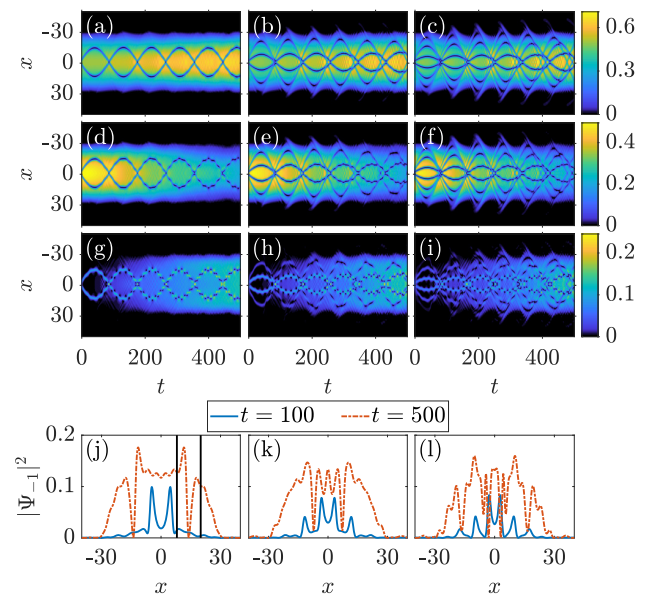


FIG. 11. Spatiotemporal evolution of the densities $|\Psi_{m_F}|^2$ of the (a)–(c) $m_F = +1$, (d)–(f) $m_F = 0$, and (g)–(i) $m_F = -1$ components upon varying the width, w , of the double-well barrier. From left to right, $w^2 = 1$, $w^2 = 5$, and $w^2 = 10$, allowing the generation of two [(a), (d), (g)], four [(b), (e), (h)], and six [(c), (f), (i)] DDB solitons respectively in the spinor system. In all cases, panels (a)–(c) [(d)–(f)] illustrate the formation of dark solitons in the $m_F = +1$ [$m_F = 0$] component and (g)–(i) the generated bright solitons, transitioning into beating dark states, in the $m_F = -1$ component. (j)–(l) Vertical cuts of $|\Psi_{-1}|^2$ for the three distinct values of w (see legend). In panel (j), solid rectangle indicates a beating dark soliton. Note that the quantities shown are measured in transverse oscillator units (see text).

to another is six orders of magnitude smaller than the total number of particles. As such, the spin interaction is negligible. For these systems, also the total magnetization is zero, in contrast to the finite one observed for the asymmetric, in the above sense, DDB and DBB soliton arrays addressed herein. In that light, it appears as if the drastic effect of the spin-interaction contribution in the previous realization is able to excite the beating dark soliton generalizations. On the other hand, following the approach of Ref. [12] in the three-component Manakov case, it is also possible to excite beating solitons in the latter (spin-independent) case. However, a more systematic theoretical analysis of the beating states is deferred for a separated work. In the trapped scenario, we exclusively present our findings for a DDB generation process. This is because only this nucleation process entails new features stemming from the spin-mixing dynamics. The initial-state preparation used herein is the one described in the confined three-component setting (see Sec. III B). Once more, by properly adjusting the initial width, w , of the double-well potential [see Eq. (11)], the controlled formation of multiple DDB soliton complexes is achieved in this harmonically trapped spinor system. From top to bottom, Figs. 11(a)–11(i) show the evolution of $|\Psi_{m_F}|^2$ (with $m_F = +1, 0, -1$). As w^2 is increased from $w^2 = 1$ to $w^2 = 10$, two, four, and six such solitons are formed [e.g., see Figs. 11(a)–11(c)]. Dark solitons

emerge in the $m_F = +1, 0$ components [see Figs. 11(a)–11(c), 11(d)–11(f)] while bright states are generated in the $m_F = -1$ component [see Figs. 11(g)–11(i)]. However, as in the homogeneous scenario, soon after their formation all states formed and also in all hyperfine components begin to deform. This deformation occurs more quickly in the less populated $m_F = -1$ component and later on in the other two hyperfine states. This phenomenon is yet again attributed to the spin-mixing dynamics that allows for particle exchange between the components. Focusing on Figs. 11(a), 11(d) and 11(g), the background densities of both the $m_F = \pm 1$ components increase while the density of the $m_F = 0$ one decreases. This exchange in population leads in turn during evolution to a transition of the soliton states in each component into states that bear both dark and bright parts. Thus, in line with our findings in the homogeneous case, beating dark solitons are progressively formed in all three hyperfine components. Since these beating structures are more pronounced in the $m_F = -1$ component, in Fig. 11(j) profile snapshots of the density of this component are illustrated. In particular, $|\Psi_{-1}|^2$ is depicted for two different time instants, namely $t = 100$ and $t = 500$, during the evolution and for $w^2 = 1$. At initial times, the two bright solitons originally formed in this component are now on top of a still small yet finite background. Namely, they are already deformed into states that are reminiscent of the so-called antidark solitons [84–86]. At larger evolution times, instead of the aforementioned antidark solitons, two beating dark states are seen to propagate. One of them is indicated in Fig. 11(j) by a black rectangle. Notice that this beating state has a density dip followed by a density hump.

The above-discussed dynamical evolution of the spinor system holds equally for all the different variations illustrated in Figs. 11(a)–11(i). However, the deformation of the DDB states is found to be delayed as w^2 is increased. The latter result can be deduced by comparing at earlier evolution times the density profile shown in Fig. 11(l) to the relevant ones illustrated in Figs. 11(j) and 11(k). Additionally, and also in all cases depicted in Figs. 11(a)–11(i), the initially formed DDB structures that evolve later on into beating dark solitons are seen to oscillate and interact within the parabolic trap. However, while coherent oscillations are observed in Figs. 11(a), 11(d) and 11(g), incoherent ones occur when the number of states is increased (i.e., for increasing w^2). In these latter cases, as shown in Figs. 11(b), 11(e) and 11(h), several collision events between the outer and the inner beating states take place. Despite the much more involved dynamical evolution of the spinor system in such cases, these beating states remain robust for all the evolution examples that we have checked. Furthermore, we also explored the dynamical evolution of the spinorial BEC system for different values of the chemical potential, μ . Similarly to the aforementioned w variation, a controlled formation of larger DDB arrays as μ increases can be once more verified. The resulting states in increasing order, in terms of μ , are presented in Figs. 12(a)–12(i) for fixed $w^2 = 5$. Notice that since $w^2 = 5$ Figs. 12(a)–12(c) are respectively identical to Figs. 11(b), 11(e), and 11(h). However, increasing μ increases the system's size. As such, arrays consisting of a larger number of DDB solitons are formed. Indeed, six and eight DDB states are generated for $\mu = 3$ and $\mu = 5$, respectively. Importantly, here it is

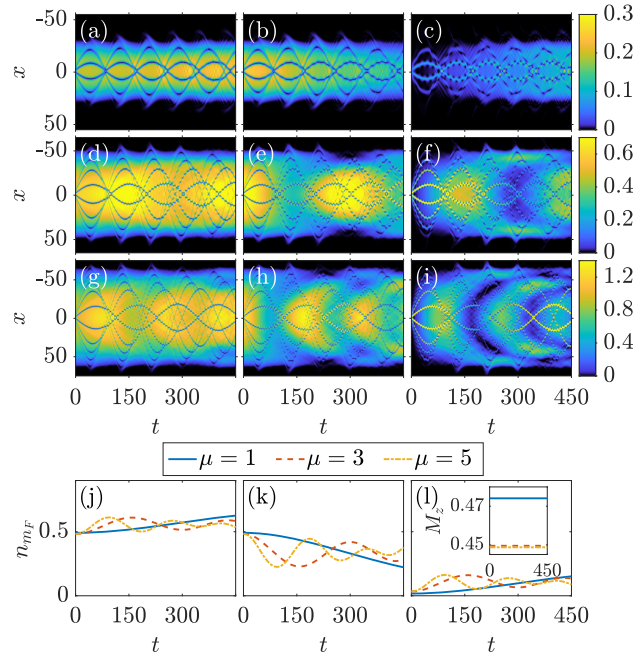


FIG. 12. Same as Fig. 11 but upon varying the chemical potential μ . From top to bottom, $\mu = 1$, $\mu = 3$, and $\mu = 5$, allowing the generation of four [(a)–(c)], six [(d)–(f)], and eight [(g)–(i)] DDB solitons respectively. In all cases, panels (a), (d), and (g) [(b), (e), and (h)] illustrate the formation of dark solitons in the $m_F = +1$ [$m_F = 0$] component and panels (c), (f), and (i) show the generated bright solitons in the $m_F = -1$ component of the spinor system. Notice that the colormap has a 2.5 : 2 : 1 ratio between the columns. [(j)–(l)] Evolution of the normalized number of particles, $n_{m_F}(t)$, for each value of μ . The inset in panel (l) shows the total magnetization, $M_z(t)$, for each value of μ . Note that the quantities shown are measured in transverse oscillator units (see text).

found that the presence of the spin interaction has a more dramatic effect on the resulting states when compared to the previous variation. Namely, the originally formed DDB structures transition into beating dark ones much faster when compared to the w variation. A case example can be seen in Fig. 12(g), corresponding to $\mu = 5$, where the dark solitons of the $m_F = +1$ component evolve into beating ones already at $t = 150$. Even for the largest $w^2 = 10$ value considered above, such a transition occurs for this hyperfine component at evolution times larger than the ones depicted herein [see Fig. 11(c)]. To appreciate the effect of the spin interaction, we monitor during evolution the population, $n_{m_F}(t)$ ($m_F = +1, 0, -1$), of each hyperfine component and for all the different values of μ considered herein. In particular, from left to right Figs. 12(j)–12(l) illustrate $n_{+1}(t)$, $n_0(t)$, and $n_{-1}(t)$ respectively. Notice that the population of each hyperfine component is affected more and the value of $n_0(t)$ evidently, the monotonic increase [$n_{+1}(t)$] or decrease [$n_0(t)$] for $\mu = 1$ turns into damping oscillations as μ increases. Such a coherent spin-mixing dynamics is in line with earlier predictions in spinor $F = 1$ BECs [37,71]. Finally, we verified that the total magnetization, $M_z(t)$, remains constant during evolution, acquiring a slightly smaller value as μ is increased [see the inset in Fig. 12(l)].

IV. CONCLUSIONS AND FUTURE PERSPECTIVES

In this work, the controlled creation of multiple soliton complexes of the DB type that appear in one-dimensional two-component, three-component, and spinor BECs has been investigated. Direct numerical simulations of each system's dynamical evolution have been performed both in the absence and in the presence of a parabolic trap. In all models considered herein, the nucleation process is based on the so-called matter-wave interference of separated condensates being utilized to study multicomponent systems. In this sense, this work offers a generalization of earlier findings in single-component setups to the much more involved multicomponent ones, enabling the identification of dark-bright solitons in two-component gases and dark-dark-bright and dark-bright-bright solitons in three-component (and spinorial) gases. To achieve control over each system's dynamical evolution, different parametric variations have been considered.

In particular, for the homogeneous systems addressed in this effort, inverse rectangular pulses were employed for the components featuring interference, and Gaussian ones for the remaining participating components. Destructive interference of the two sides of the former pulse leads to the nucleation of an array of dark solitons. Additionally, the dispersion of the Gaussian pulse and its subsequent confinement in the effective potential created by each of the nucleated dark solitons results in the formation of bright solitons that are subsequently trapped and waveguided by their corresponding dark counterparts. It is found that manipulating the width of the IRP is sufficient to ensure the desired nucleation of multiple soliton compounds of the DB type. This way, arrays of DB, DDB, and DBB solitons are dynamically produced in the two-component and spinor cases, respectively. Moreover, for the two-component system, it is showcased that each of the generated DB solitons follows the analytical expressions stemming from the integrable theory of the Manakov system. The same holds true also for the DBB and DDB states nucleated in the three-component system. In the latter, generalized expressions that connect the soliton parameters are extracted and used to appreciate modifications of the soliton characteristics under different parametric variations. While the same overall dynamical evolution is observed for the two- and three-component systems, a significantly different picture can be drawn for the spinorial case. Strikingly, and for a DDB nucleation process, it is found that during evolution the originally formed DDB soliton arrays begin to deform due to the spin-mixing dynamics. The latter allows for exchange of particles between the hyperfine components. The aforementioned deformation leads in turn to the gradual formation of arrays of beating dark states. The latter, once formed, are seen to robustly propagate for large evolution times. The existence of beating dark states in spinor systems has not, to the best of our knowledge, been reported previously and it is an interesting topic for further exploration.

For the harmonically trapped scenarios, our numerical findings suggest similar characteristics as in the homogeneous cases in terms of the nucleation process, although naturally the dynamics is rendered more complex due to the confinement and the induced interactions between the produced solitary waves. In all cases, it is found that by adjusting the

width of the rectangular pulse or the chemical potential of the participating components, the desirable number of DB, DDB, and DBB soliton complexes can be generated. This provides a sense of dynamical control and design of desired configurations in our system. The number of the resulting coherent structures is found to increase upon increasing each of the above parameters. In the trapped case, the resulting multisoliton arrays, irrespective of their type, are found to oscillate and interact within the parabolic trap being robust for large evolution times. Contrary to the above findings, for the spinorial BEC system a departure of the initially formed DDB states to the beating dark ones is showcased. Here, coherent spin-mixing dynamics is observed when monitoring the population of each hyperfine component. Damping oscillations of the latter occur, that are found to be enhanced upon increasing, for example, the chemical potential of each component. Additionally, and also in comparison to the homogeneous case, the beating dark states are formed faster in the trapped setting. This formation is further enhanced as the chemical potential increases. It is found that the beating dark solitons persist while oscillating and interacting with one another. The existence of these spinorial beating states can be tested in current state-of-the-art experiments [55], and it is clearly a direction of interest in its own right for future studies. More specifically, it would be particularly interesting to generalize the findings associated with the two-component beating dark solitons [12] to the spinor case and study in a detailed manner the formation and interactions of the spinor beating dark states identified herein.

Yet another interesting perspective would be to compare and contrast the numerically identified DDB and DBB states of the three-component system to the analytical expressions that are available, at least for the integrable version of this model [76]. More specifically, one could generalize the criteria of the single-component IRP scenario obtained in the earlier works of Ref. [6] to the formation of both DB and also DDB or DBB solitons from similar initial data in the multicomponent case and compare these predictions against the corresponding numerical computations. Then, one could depart from the above Manakov limit and also study the fate of these structures in nonintegrable systems [21], including the spinor one. The breaking of integrability would allow in turn for effects such as the miscibility or immiscibility of the involved components to come into play [87]. The interplay of the resulting density variations with the potential persistence of the solitary wave structures is an interesting topic for future study. Also, in the same context, it would be interesting to systematically examine interactions between multiple DDB and DBB states. The role of other effects such as the potential Rabi coupling between the components could also be of interest in its own right [82,83].

Lastly, as has been discussed in relevant reviews such as Ref. [22], many of these ideas, such as the DB solitons (generalizing to vortex-bright ones), the beating dark solitons, etc., naturally generalize to corresponding higher dimensional states. Examining the potential for such states as a result of interference or possibly other methods more concretely associated with higher dimensions such as the transverse instability would be of particular interest in its own right.

ACKNOWLEDGMENTS

A.R.-R. thanks M. Pyzh and K. Keiler for helpful discussions. This material is based upon work supported by the U.S. National Science Foundation under Grant No.

PHY-1602994 and under Grant No. DMS-1809074 (P.G.K.). P.G.K. is also grateful to the Alexander von Humboldt Foundation for support and to Kevin Geier (University of Heidelberg) for preliminary iterations on the subject of the present work.

-
- [1] M. H. Anderson, J. R. Ensher, M. R. Matthews, C. E. Wieman, and E. A. Cornell, *Science* **269**, 198 (1995).
- [2] K. B. Davis, M. O. Mewes, M. R. Andrews, N. J. van Druten, D. S. Durfee, D. M. Kurn, and W. Ketterle, *Phys. Rev. Lett.* **75**, 3969 (1995).
- [3] D. J. Frantzeskakis, *J. Phys. A* **43**, 213001 (2010).
- [4] F. Abdullaev, A. Gammal, A. Kamchatnov, and L. Tomio, *Int. J. Mod. Phys. B* **19**, 3415 (2005).
- [5] V. E. Zakharov and A. B. Shabat, *Zh. Eksp. Teor. Fiz.* **61**, 118 (1971) [*Sov. J. Exp. Theor. Phys.* **34**, 62 (1972)].
- [6] V. E. Zakharov and A. B. Shabat, *Zh. Eksp. Teor. Fiz.* **64**, 1627 (1973) [*Sov. J. Exp. Theor. Phys.* **37**, 823 (1973)].
- [7] C. Becker, S. Stellmer, P. Soltan-Panahi, S. Dörscher, M. Baumert, E.-M. Richter, J. Kronjäger, K. Bongs, and K. Sengstock, *Nat. Phys.* **4**, 496 (2008).
- [8] S. Middelkamp, J. Chang, C. Hamner, R. Carretero-González, P. Kevrekidis, V. Achilleos, D. Frantzeskakis, P. Schmelcher, and P. Engels, *Phys. Lett. A* **375**, 642 (2011).
- [9] C. Hamner, J. J. Chang, P. Engels, and M. A. Hoefer, *Phys. Rev. Lett.* **106**, 065302 (2011).
- [10] D. Yan, J. J. Chang, C. Hamner, P. G. Kevrekidis, P. Engels, V. Achilleos, D. J. Frantzeskakis, R. Carretero-González, and P. Schmelcher, *Phys. Rev. A* **84**, 053630 (2011).
- [11] M. A. Hoefer, J. J. Chang, C. Hamner, and P. Engels, *Phys. Rev. A* **84**, 041605(R) (2011).
- [12] D. Yan, J. J. Chang, C. Hamner, M. Hoefer, P. G. Kevrekidis, P. Engels, V. Achilleos, D. J. Frantzeskakis, and J. Cuevas, *J. Phys. B: At. Mol. Opt. Phys.* **45**, 115301 (2012).
- [13] V. A. Brazhnyi and V. M. Pérez-García, *Chaos, Solitons Fractals* **44**, 381 (2011).
- [14] C. Yin, N. G. Berloff, V. M. Pérez-García, D. Novoa, A. V. Carpentier, and H. Michinel, *Phys. Rev. A* **83**, 051605(R) (2011).
- [15] V. Achilleos, P. G. Kevrekidis, V. M. Rothos, and D. J. Frantzeskakis, *Phys. Rev. A* **84**, 053626 (2011).
- [16] A. Álvarez, J. Cuevas, F. R. Romero, C. Hamner, J. J. Chang, P. Engels, P. G. Kevrekidis, and D. J. Frantzeskakis, *J. Phys. B: At. Mol. Opt. Phys.* **46**, 065302 (2013).
- [17] D. Yan, F. Tsitoura, P. G. Kevrekidis, and D. J. Frantzeskakis, *Phys. Rev. A* **91**, 023619 (2015).
- [18] E. T. Karamatskos, J. Stockhofe, P. G. Kevrekidis, and P. Schmelcher, *Phys. Rev. A* **91**, 043637 (2015).
- [19] G. C. Katsimiga, J. Stockhofe, P. G. Kevrekidis, and P. Schmelcher, *Phys. Rev. A* **95**, 013621 (2017).
- [20] G. C. Katsimiga, J. Stockhofe, P. G. Kevrekidis, and P. Schmelcher, *Appl. Sci.* **7**, 388 (2017).
- [21] G. C. Katsimiga, P. G. Kevrekidis, B. Prinari, G. Biondini, and P. Schmelcher, *Phys. Rev. A* **97**, 043623 (2018).
- [22] P. Kevrekidis and D. Frantzeskakis, *Rev. Phys.* **1**, 140 (2016).
- [23] S. Trillo, S. Wabnitz, E. M. Wright, and G. I. Stegeman, *Opt. Lett.* **13**, 871 (1988).
- [24] D. N. Christodoulides, *Phys. Lett. A* **132**, 451 (1988).
- [25] E. A. Ostrovskaya and Y. S. Kivshar, *Opt. Lett.* **23**, 1268 (1998).
- [26] V. V. Afanasyev, Y. S. Kivshar, V. V. Konotop, and V. N. Serkin, *Opt. Lett.* **14**, 805 (1989).
- [27] Y. S. Kivshar and S. K. Turitsyn, *Opt. Lett.* **18**, 337 (1993).
- [28] D. N. Christodoulides, S. R. Singh, M. I. Carvalho, and M. Segev, *Appl. Phys. Lett.* **68**, 1763 (1996).
- [29] A. V. Buryak, Y. S. Kivshar, and D. F. Parker, *Phys. Lett. A* **215**, 57 (1996).
- [30] A. P. Sheppard and Y. S. Kivshar, *Phys. Rev. E* **55**, 4773 (1997).
- [31] Z. Chen, M. Segev, T. H. Coskun, D. N. Christodoulides, and Y. S. Kivshar, *J. Opt. Soc. Am. B* **14**, 3066 (1997).
- [32] Y. S. Kivshar and B. Luther-Davies, *Phys. Rep.* **298**, 81 (1998).
- [33] E. A. Ostrovskaya, Y. S. Kivshar, Z. Chen, and M. Segev, *Opt. Lett.* **24**, 327 (1999).
- [34] Q.-H. Park and H. J. Shin, *Phys. Rev. E* **61**, 3093 (2000).
- [35] D. M. Stamper-Kurn and W. Ketterle, in *Coherent Atomic Matter Waves*, edited by R. Kaiser, C. Westbrook, and F. David, Les Houches-Ecole d'Ete de Physique Theorique (Springer, Berlin, 2001), pp. 139–217.
- [36] M.-S. Chang, C. D. Hamley, M. D. Barrett, J. A. Sauer, K. M. Fortier, W. Zhang, L. You, and M. S. Chapman, *Phys. Rev. Lett.* **92**, 140403 (2004).
- [37] M.-S. Chang, Q. Qin, W. Zhang, L. You, and M. S. Chapman, *Nat. Phys.* **1**, 111 (2005).
- [38] Y. Kawaguchi and M. Ueda, *Phys. Rep.* **520**, 253 (2012).
- [39] D. M. Stamper-Kurn and M. Ueda, *Rev. Mod. Phys.* **85**, 1191 (2013).
- [40] T. Ohmi and K. Machida, *J. Phys. Soc. Jpn.* **67**, 1822 (1998).
- [41] T. Tsuchida and M. Wadati, *J. Phys. Soc. Jpn.* **67**, 1175 (1998).
- [42] J. Ieda, T. Miyakawa, and M. Wadati, *Phys. Rev. Lett.* **93**, 194102 (2004).
- [43] J. Ieda, T. Miyakawa, and M. Wadati, *J. Phys. Soc. Jpn.* **73**, 2996 (2004).
- [44] J. Ieda, Study of matter-wave solitons in spinor Bose-Einstein condensates, Ph.D. thesis, Tokyo University, Tokyo, 2005 (unpublished).
- [45] L. Li, Z. Li, B. A. Malomed, D. Mihalache, and W. M. Liu, *Phys. Rev. A* **72**, 033611 (2005).
- [46] M. Wadati and N. Tsuchida, *J. Phys. Soc. Jpn.* **75**, 014301 (2005).
- [47] J. Ieda, T. Miyakawa, and M. Wadati, *Laser Phys.* **16**, 678 (2006).
- [48] M. Uchiyama, J. Ieda, and M. Wadati, *J. Phys. Soc. Jpn.* **75**, 064002 (2006).
- [49] J. Ieda, M. Uchiyama, and M. Wadati, *J. Math. Phys.* **48**, 013507 (2007).
- [50] W. Zhang, O. E. Müstecaplıoğlu, and L. You, *Phys. Rev. A* **75**, 043601 (2007).
- [51] T. Kurosaki and M. Wadati, *J. Phys. Soc. Jpn.* **76**, 084002 (2007).

- [52] B. J. Dabrowska-Wüster, E. A. Ostrovskaya, T. J. Alexander, and Y. S. Kivshar, *Phys. Rev. A* **75**, 023617 (2007).
- [53] H. E. Nistazakis, D. J. Frantzeskakis, P. G. Kevrekidis, B. A. Malomed, and R. Carretero-González, *Phys. Rev. A* **77**, 033612 (2008).
- [54] B. Xiong and J. Gong, *Phys. Rev. A* **81**, 033618 (2010).
- [55] T. M. Bersano, V. Gokhroo, M. A. Khamehchi, J. D'Ambrose, D. J. Frantzeskakis, P. Engels, and P. G. Kevrekidis, *Phys. Rev. Lett.* **120**, 063202 (2018).
- [56] G. C. Katsimiga, S. I. Mistakidis, G. M. Koutentakis, P. G. Kevrekidis, and P. Schmelcher, *Phys. Rev. A* **98**, 013632 (2018).
- [57] V. A. Brazhnyi and A. M. Kamchatnov, *Phys. Rev. A* **68**, 043614 (2003).
- [58] Z. Dutton, M. Budde, C. Slowe, and L. V. Hau, *Science* **293**, 663 (2001).
- [59] P. Engels and C. Atherton, *Phys. Rev. Lett.* **99**, 160405 (2007).
- [60] I. Shomroni, E. Lahoud, S. Levy, and J. Steinhauer, *Nat. Phys.* **5**, 193 (2009).
- [61] S. Burger, K. Bongs, S. Dettmer, W. Ertmer, K. Sengstock, A. Sanpera, G. V. Shlyapnikov, and M. Lewenstein, *Phys. Rev. Lett.* **83**, 5198 (1999).
- [62] J. Denschlag, J. E. Simsarian, D. L. Feder, C. W. Clark, L. A. Collins, J. Cubizolles, L. Deng, E. W. Hagley, K. Helmerson, W. P. Reinhardt, S. L. Rolston, B. I. Schneider, and W. D. Phillips, *Science* **287**, 97 (2000).
- [63] B. P. Anderson, P. C. Haljan, C. A. Regal, D. L. Feder, L. A. Collins, C. W. Clark, and E. A. Cornell, *Phys. Rev. Lett.* **86**, 2926 (2001).
- [64] A. Weller, J. P. Ronzheimer, C. Gross, J. Esteve, M. K. Oberthaler, D. J. Frantzeskakis, G. Theocharis, and P. G. Kevrekidis, *Phys. Rev. Lett.* **101**, 130401 (2008).
- [65] M. A. Hofer, P. Engels, and J. J. Chang, *Physica D (Amsterdam, Neth.)* **238**, 1311 (2009).
- [66] D. R. Scherer, C. N. Weiler, T. W. Neely, and B. P. Anderson, *Phys. Rev. Lett.* **98**, 110402 (2007).
- [67] W. P. Reinhardt and C. W. Clark, *J. Phys. B: At. Mol. Opt. Phys.* **30**, L785 (1997).
- [68] T. F. Scott, R. J. Ballagh, and K. Burnett, *J. Phys. B: At. Mol. Opt. Phys.* **31**, L329 (1998).
- [69] G. Theocharis, A. Weller, J. P. Ronzheimer, C. Gross, M. K. Oberthaler, P. G. Kevrekidis, and D. J. Frantzeskakis, *Phys. Rev. A* **81**, 063604 (2010).
- [70] P. Öhberg and L. Santos, *Phys. Rev. Lett.* **86**, 2918 (2001).
- [71] H. Pu, C. K. Law, S. Raghavan, J. H. Eberly, and N. P. Bigelow, *Phys. Rev. A* **60**, 1463 (1999).
- [72] T.-L. Ho, *Phys. Rev. Lett.* **81**, 742 (1998).
- [73] N. N. Klausen, J. L. Bohn, and C. H. Greene, *Phys. Rev. A* **64**, 053602 (2001).
- [74] E. G. M. van Kempen, S. J. J. M. F. Kokkelmans, D. J. Heinzen, and B. J. Verhaar, *Phys. Rev. Lett.* **88**, 093201 (2002).
- [75] S. V. Manakov, *Zh. Eksp. Teor. Fiz.* **65**, 505 (1973) [*Sov. Phys. JETP* **3**, 248 (1974)].
- [76] G. Biondini, D. K. Kraus, and B. Prinari, *Comm. Math. Phys.* **348**, 475 (2016).
- [77] P. G. Kevrekidis, D. J. Frantzeskakis, and R. Carretero-González, *The Defocusing Nonlinear Schrödinger Equation: From Dark Solitons to Vortices and Vortex Rings* (SIAM, Philadelphia, 2015).
- [78] E. P. Gross, *Nuovo Cim* **20**, 454 (1961).
- [79] L. P. Pitaevskii, *J. Exptl. Theoret. Phys. (U.S.S.R.)* **40**, 646 (1961) [*Sov. J. Exp. Theor. Phys.* **13**, 451 (1961)].
- [80] J. A. Espínola-Rocha and P. Kevrekidis, *Math. Comput. Simul.* **80**, 693 (2009).
- [81] N. I. Nikolov, D. Neshev, W. Królikowski, O. Bang, J. J. Rasmussen, and P. L. Christiansen, *Opt. Lett.* **29**, 286 (2004).
- [82] L. Pitaevskii and S. Stringari, *Bose-Einstein Condensation and Superfluidity*, International Series of Monographs in Physics Vol. 164 (Oxford University Press, Oxford, UK, 2016).
- [83] T. Busch and J. R. Anglin, *Phys. Rev. Lett.* **87**, 010401 (2001).
- [84] I. Danaila, M. A. Khamehchi, V. Gokhroo, P. Engels, and P. G. Kevrekidis, *Phys. Rev. A* **94**, 053617 (2016).
- [85] P. G. Kevrekidis, H. E. Nistazakis, D. J. Frantzeskakis, B. A. Malomed, and R. Carretero-González, *Eur. Phys. J. D* **28**, 181 (2004).
- [86] G. C. Katsimiga, G. M. Koutentakis, S. I. Mistakidis, P. G. Kevrekidis, and P. Schmelcher, *New J. Phys.* **19**, 073004 (2017).
- [87] H. Kiehn, S. I. Mistakidis, G. Katsimiga, and P. Schmelcher, [arXiv:1902.09316](https://arxiv.org/abs/1902.09316).

On-demand generation of dark soliton trains in Bose-Einstein condensates

A. Romero-Ros,¹ G. C. Katsimiga,¹ P. G. Kevrekidis,² B. Prinari,³ G. Biondini,^{3,4} and P. Schmelcher^{1,5}


¹*Center for Optical Quantum Technologies, Department of Physics, University of Hamburg, Luruper Chaussee 149, 22761 Hamburg, Germany*

²*Department of Mathematics and Statistics, University of Massachusetts Amherst, Amherst, Massachusetts 01003-4515, USA*

³*Department of Mathematics, State University of New York, Buffalo, New York 14260, USA*

⁴*Department of Physics, State University of New York, Buffalo, New York 14260, USA*

⁵*The Hamburg Centre for Ultrafast Imaging, University of Hamburg, Luruper Chaussee 149, 22761 Hamburg, Germany*

 (Received 4 September 2020; revised 15 January 2021; accepted 21 January 2021; published 24 February 2021)

Matter-wave interference mechanisms in one-dimensional Bose-Einstein condensates that allow for the controlled generation of dark soliton trains upon choosing suitable box-type initial configurations are described. First, the direct scattering problem for the defocusing nonlinear Schrödinger equation with nonzero boundary conditions and general box-type initial configurations is discussed, and expressions for the discrete spectrum corresponding to the dark soliton excitations generated by the dynamics are obtained. It is found that the size of the initial box directly affects the number, size and velocity of the solitons, while the initial phase determines the parity of the solutions. The analytical results obtained for the untrapped system are compared to those of numerical simulations of the Gross-Pitaevskii equation, both in the absence and in the presence of a harmonic trap. The numerical results bear out the analytical results with excellent agreement.

DOI: [10.1103/PhysRevA.103.023329](https://doi.org/10.1103/PhysRevA.103.023329)

I. INTRODUCTION

Dark solitons are fundamental nonlinear excitations stemming from the balance between dispersion and suitable kinds of nonlinearity. They are found to arise in diverse physical systems ranging from water waves [1] and magnetic materials [2] to nonlinear optics [3–5] and Bose-Einstein condensates (BECs) [6–9]. For instance, in nonlinear optics dark solitons emerge in media with positive dispersion and defocusing nonlinearity whose evolution is described by the so-called defocusing nonlinear Schrödinger (NLS) equation [10]. On the other hand, in the BEC context dark solitons form in systems with repulsive interatomic interactions [11] obeying the so-called Gross-Pitaevskii equation (GPE).

BECs, due to their high degree of controllability and isolation from the environment [12], constitute fertile physical platforms for investigating the existence, dynamics and interactions [13–16] of these matter waves or multicomponent [17–19] and multidimensional variants thereof [20–22]. Additionally, several powerful techniques have been utilized in order to generate such waves. These include, among others, phase imprinting [8,20,23] and density engineering [22], perturbing the BEC with localized impurities [24,25] and interference experiments [26–29].

Among the aforementioned methods, the latter is based on the matter-wave interference of two colliding condensates, a process via which dark soliton trains can be produced. Several experimental and theoretical works have been devoted to studying the controllable creation of such dark soliton arrays [26–28,30,31]. They revealed, among other things, that the momenta of the colliding BEC parts and their relative phase

play an important role in the number of generated solitonic entities. This result has been derived analytically for the defocusing NLS equation by means of the inverse scattering transform (IST) in the seminal work of Ref. [3]. Recent theoretical attempts have exploited the integrable nature of the above scalar NLS model and further developed an IST formalism accounting for both symmetric [32,33] and fully asymmetric non-zero-boundary conditions (NZBC) [34].

In the present work we exploit the unprecedented level of control that the ultracold environment offers along with the exact analytical tools provided by both direct scattering methods and the IST with NZBC, and we report the on-demand generation of dark soliton arrays. In particular, we consider a one-dimensional (1D), harmonically trapped scalar BEC composed of repulsively interacting atoms, and we study the response of such a system to box-type initial configurations [3,31,33,35] (see also Refs. [36–38] in nonlinear optics) whose shape is controlled by five distinct parameters. Limiting cases of the latter directly mimic interference and density or phase engineering processes suggesting the experimental relevance of our findings. The closest analog to this in the context of trapped BECs that we are familiar with appears in Ref. [30]; however, that work is based on the (approximate) Bohr-Sommerfeld quantization rule for hyperbolic function based perturbations of the initial density or phase profile. Here, on the other hand, we leverage both the pioneering work of Ref. [3] and the recent developments of Refs. [32,33] to obtain explicit analytical results based on IST.

More specifically, first we consider the integrable version of the problem, i.e., the defocusing NLS equation with NZBC. The direct scattering problem for this equation with the above

box-type initial condition is solved analytically. Expressions for the discrete eigenvalues of the scattering problem, which as usual determine the amplitudes and the velocities of the ensuing dark solitons, are found, and the exact soliton waveforms and the center of each of them can be extracted within the IST. Having at hand the exact analytical expressions, a systematic study of the dynamical evolution of the scalar system is then put forth. Distinct parameter explorations are conducted including, for instance, in-phase (IP) and out-of-phase (OP) initial configurations. In all cases investigated herein, remarkable agreement between the analytical predictions and our numerical findings is observed. This agreement in turn means that, for example, the number of dark solitons that are expected to nucleate via interference is *a priori* predicted by our initial condition, along with the amplitudes and velocities of the emergent matter waves. It is also found that the size of the initial box directly affects the number, amplitude, and velocity of the emitted dark solitons. Additionally, its phase, which can be now manipulated with the analytical tools discussed in this work, along with its depth can determine not only the even or odd number of nucleated dark solitons, but can also lead to an asymmetrical distribution thereof. Remarkably, the analytical solutions of the homogeneous setting (where by ‘‘homogeneous’’ we mean the case without confinement) can be suitably extended to the presence of a harmonic confinement. Specifically, it is found that in each scenario the number of in-trap emitted dark solitons and their amplitudes coincide with that of the homogeneous setting, while their trajectories closely follow those of a particle in a harmonic oscillator [9]. Additionally here, by monitoring during evolution the center of mass of each nucleated dark soliton, estimations of the oscillation frequency of individual waves are obtained. Excellent agreement with the analytical expressions is exposed for the soliton amplitudes and velocities, while deviations smaller than 4% are identified for the oscillation frequency when compared to the analytical predictions.

The flow of this paper is as follows. In Sec. II we introduce the model and discuss the direct scattering problem for the NLS with a general box-type initial condition. Additionally, we comment on limiting cases, in terms of the involved box parameters, and thus establish connections with interference and density or phase engineering processes used in contemporary BEC experiments. In Sec. III we present our findings. First, we extract the eigenvalues of the scattering problem over a wide range of different initial configurations. Then we perform a comparison of the analytical predictions with direct numerical simulations of the GPE both in the absence and in the presence of the trap. Finally, in Sec. IV we summarize our results and discuss possible directions for future study.

II. MODEL SETUP, SCATTERING PROBLEM, AND DISCRETE EIGENVALUES

A. The Gross-Pitaevskii and nonlinear Schrödinger equation setup

The system of interest is a scalar 1D BEC consisting of repulsively interacting atoms being confined in a highly anisotropic trap with longitudinal and transverse trapping fre-

quencies chosen such that $\omega_x \ll \omega_\perp$. In such a cigar shaped geometry [8,17], the condensate wave function along the transverse direction, being the ground state of the respective harmonic oscillator, can be integrated out. Then, in the mean-field framework, the BEC dynamics for the longitudinal part of the wave function $\Psi(x, t)$ is governed by the following 1D GPE [6,7]:

$$i\hbar \frac{\partial \Psi}{\partial t} = -\frac{\hbar^2}{2m} \frac{\partial^2 \Psi}{\partial x^2} + V(x)\Psi + g|\Psi|^2\Psi. \quad (1)$$

Moreover, in the above expression $V(x) = m\omega_x^2 x^2/2$ denotes the external harmonic potential. Additionally, m denotes the atomic mass, while $g = 2\hbar\omega_\perp a_s$ is the effective 1D coupling constant expressed in terms of the s -wave scattering length, a_s . The latter accounts for two-atom collisions and can be tuned by means of Feshbach resonances [39,40]. In the present work we consider $g = 1$ and our setup can be realized experimentally by considering, e.g., a gas of ^{87}Rb atoms [6,7]. By performing the transformations: $|q|^2 = 2a_s|\Psi|^2$, $x' = a_\perp^{-1}x$, with $a_\perp = \sqrt{\hbar/m\omega_\perp}$ being the transverse oscillator length, and $t' = \omega_\perp t$, we cast the aforementioned scalar GPE in the dimensionless form

$$i \frac{\partial q}{\partial t} = -\frac{1}{2} \frac{\partial^2 q}{\partial x^2} + \frac{1}{2} \Omega^2 x^2 q + |q|^2 q, \quad (2)$$

where $\Omega \equiv \omega_x/\omega_\perp$. For convenience we dropped the primes. In the absence of a trapping potential (i.e., for $\Omega = 0$), Eq. (2) reduces to the well-known defocusing NLS equation [10].

The latter integrable model can be solved analytically via IST and it is known to possess dark soliton solutions that have NZBC at infinity [33]. To this end for the analytical considerations to be carried out below, we further perform the rescaling $\tilde{q}(x, t) = q(\sqrt{2}x, t) \exp(-2iq_o^2 t)$ in the integrable version of Eq. (2) and by omitting the tildes we end up with

$$iq_t + q_{xx} - 2(|q|^2 - q_o^2)q = 0. \quad (3)$$

Notice that with the aforementioned transformation Eq. (3) satisfies the following time-independent NZBC at infinity:

$$\lim_{x \rightarrow \pm\infty} q(x, t) = q_\pm = q_o e^{i\theta_\pm}. \quad (4)$$

Henceforth, $q_o = |q_\pm| > 0$ (without loss of generality), θ_\pm are real numbers, and the subscripts t and x introduced in Eq. (3) denote here and throughout this work partial differentiation with respect to time and space, respectively.

Motivated by our recent work of Ref. [31], but also by the earlier works of Refs. [3,36,38,41–44] regarding the controllable nucleation of soliton arrays, for our analytical and numerical investigations below, we consider the following box-type initial configurations for the condensate wave function:

$$q(x, 0) = \begin{cases} q_o e^{i\theta_-}, & x < -L \\ h e^{i\alpha}, & |x| < L \\ q_o e^{i\theta_+}, & x > L \end{cases} \quad (5)$$

Here $h \geq 0$ refers to the depth ($h < q_o$) or height ($h > q_o$) of the box. Additionally, L corresponds to the half width of the box, q_o is the background amplitude, θ_\pm are the asymptotic phases at either side of the box, and α is the phase inside the

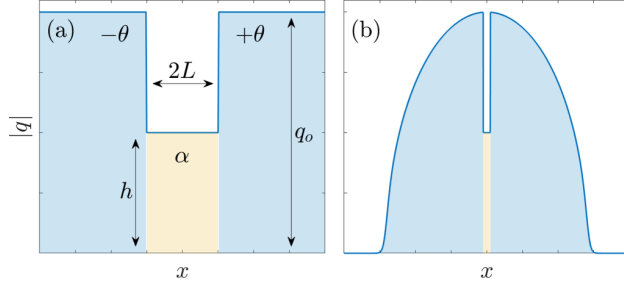


FIG. 1. Schematic illustration of the box-type initial configuration (5), for generic wave function parameters, i.e., L , q_0 , θ , h and α (a) in the absence and (b) in the presence of a harmonic trapping potential. Note that the quantities shown are measured in transverse oscillator units.

box. It will be convenient to introduce the quantities

$$\Delta\theta = \theta_+ - \theta_-, \quad \Delta\theta_+ = \theta_+ - \alpha, \quad \Delta\theta_- = \alpha - \theta_- \quad (6)$$

to denote the distinct phase differences in each of the different regions of the box. Owing to the phase invariance of the NLS equation, we can take $\theta_+ = -\theta_- = \theta$ without loss of generality, and we will do so hereafter so that $\Delta\theta = 2\theta$ and $\Delta\theta_{\pm} = \theta \mp \alpha$. Note, however, that the phase inside the box, α , remains as an additional, independent parameter. We will refer to the cases $\Delta\theta = 0$ and $\Delta\theta = \pi$ as in-phase (IP) and out-of-phase (OP) condensates, respectively, and to the special case $h = 0$ (which describes the complete absence of atoms inside the box) as that of a “zero box.” A schematic illustration of the initial configuration (5) is provided in Fig. 1(a).

B. Direct scattering of box-type configurations

Here we follow the presentation of Ref. [33]. As noted earlier, the defocusing NLS equation [Eq. (3)] is an integrable nonlinear partial differential equation, whose initial value problem can be solved by means of the IST via its Lax pair. The 2×2 Lax pair associated with Eq. (3) is

$$\phi_x = \mathbf{X}\phi, \quad \phi_t = \mathbf{T}\phi, \quad (7)$$

where ϕ is a 2×2 matrix eigenvector,

$$\mathbf{X}(x, t, k) = ik\mathbf{J} + \mathbf{Q}, \quad (8)$$

$$\mathbf{T}(x, t, k) = 2ik^2\mathbf{J} - i\mathbf{J}(\mathbf{Q}_x - \mathbf{Q} + q_0^2) - 2k\mathbf{Q}, \quad (9)$$

and

$$\mathbf{J} = \begin{pmatrix} -1 & 0 \\ 0 & 1 \end{pmatrix}, \quad \mathbf{Q}(x, t) = \begin{pmatrix} 0 & q \\ q^* & 0 \end{pmatrix}. \quad (10)$$

The first equation in (7) is referred to as the scattering problem, $k \in \mathbb{C}$ as the scattering parameter, and $q(x, t)$ as the scattering potential. One can expect that, as $x \rightarrow \pm\infty$, the solutions of the direct scattering problem are approximated by those of the asymptotic scattering problem $\phi_x = \mathbf{X}_{\pm}\phi$, where $\mathbf{X}_{\pm} = ik\mathbf{J} + \mathbf{Q}_{\pm}$ and $\mathbf{Q}_{\pm} = \lim_{x \rightarrow \pm\infty} \mathbf{Q}(x, t)$.

The eigenvalues of \mathbf{X}_{\pm} are $\pm i\lambda$, where

$$\lambda(k) = \sqrt{k^2 - q_0^2}. \quad (11)$$

As in Refs. [33,45–47], we take the branch cut along the semilines $(\infty, -q_0)$ and (q_0, ∞) , and we define uniquely $\lambda(k)$ by requiring that $\text{Im}\lambda(k) \geq 0$. (This corresponds to working on one sheet of the two-sheeted Riemann surface defined by $\lambda(k)$ [33,45–47]).

Here we define the Jost solutions $\phi_{\pm}(x, t, k)$ as the simultaneous solutions of both parts of the Lax pair satisfying the boundary conditions

$$\phi_{\pm}(x, t, k) \equiv \mathbf{Y}_{\pm}(k)e^{i\Theta(x,t,k)} + o(1) \quad \text{as } x \rightarrow \pm\infty, \quad (12)$$

where $\Theta(x, t, k) = \Lambda x - \Omega t$, $\Lambda = \text{diag}(-\lambda, \lambda)$, $\Omega = \text{diag}(2k\lambda, -2k\lambda)$, and $\mathbf{Y}_{\pm}(k)$ are the simultaneous eigenvector matrices of \mathbf{X}_{\pm} and \mathbf{T}_{\pm} . Both Jost solutions are related to each other through the scattering relation

$$\phi_-(x, t, k) = \phi_+(x, t, k)\mathbf{S}(k), \quad (13)$$

and the scattering coefficients [the entries of the 2×2 scattering matrix $\mathbf{S}(k)$] are time independent on account of the fact that the Jost eigenfunctions are chosen to be simultaneous solutions of the Lax pair.

As we are concerned with only the discrete eigenvalues of the scattering operator, which are time independent, hereafter we will consider the scattering problem at $t = 0$ and omit the time dependence from the eigenfunctions. At $t = 0$ the scattering problem in each of the three regions $x < -L$, $|x| < L$, and $x > L$ takes the form $v_x = (-ik\mathbf{J} + \mathbf{Q}_j)v$ with the index $j = c, \pm$ with constant potentials \mathbf{Q}_{\pm} and \mathbf{Q}_c ,

$$\mathbf{Q}_{\pm} = \begin{pmatrix} 0 & q_0 e^{\pm i\theta} \\ q_0 e^{\mp i\theta} & 0 \end{pmatrix}, \quad \mathbf{Q}_c = \begin{pmatrix} 0 & h e^{i\alpha} \\ h e^{-i\alpha} & 0 \end{pmatrix}, \quad (14)$$

where again we set $\theta_+ = -\theta_- = \theta$ without loss of generality. One can then easily find explicit solutions for the scattering problem in each of the three regions:

$$\phi_l(x, k) = \mathbf{Y}_-(k)e^{i\Lambda x} \quad x \leq -L, \quad (15a)$$

$$\phi_c(x, k) = \mathbf{Y}_c(k)e^{i\mathbf{M}x} \quad |x| \leq L, \quad (15b)$$

$$\phi_r(x, k) = \mathbf{Y}_+(k)e^{i\Lambda x} \quad x \geq L, \quad (15c)$$

where $\mathbf{M} = \text{diag}(-\mu, \mu)$, with $\mu = \sqrt{k^2 - h^2}$, and

$$\mathbf{Y}_{\pm}(k) = \begin{pmatrix} k + \lambda & -iq_0 e^{\pm i\theta} \\ iq_0 e^{\mp i\theta} & k + \lambda \end{pmatrix}, \quad (16)$$

$$\mathbf{Y}_c(k) = \begin{pmatrix} k + \mu & -ih e^{i\alpha} \\ ih e^{-i\alpha} & k + \mu \end{pmatrix}. \quad (17)$$

We then have explicit representations for the Jost solutions $\phi_{\pm}(x, 0, k)$ in their respective regions, i.e., $\phi_-(x, 0, k) \equiv \phi_l(x, k)$ for $x \leq -L$, and $\phi_+(x, 0, k) \equiv \phi_r(x, k)$ for $x \geq L$. At the boundary of each region one can express the fundamental solution on the left as a linear combination of the fundamental solution on the right, and vice versa. In particular, we can introduce scattering matrices $\mathbf{S}_-(k)$ and $\mathbf{S}_+(k)$ such that

$$\phi_-(-L, k) = \phi_c(-L, k)\mathbf{S}_-(k), \quad (18a)$$

$$\phi_c(L, k) = \phi_+(L, k)\mathbf{S}_+(k). \quad (18b)$$

As a consequence, we can express the scattering matrix $S(k)$ relating the Jost solutions $\phi_{\pm}(x, k)$ as

$$\begin{aligned} \mathbf{S}(k) &= \mathbf{S}_+(k)\mathbf{S}_-(k) \\ &= e^{-i\lambda L}\mathbf{Y}_+^{-1}\mathbf{Y}_c e^{2i\mu L}\mathbf{Y}_c^{-1}\mathbf{Y}_- e^{-i\lambda L}. \end{aligned} \quad (19)$$

Computing the right-hand side of Eq. (19), we obtain the following expression for the first element $s_{11}(k)$ of the scattering matrix $\mathbf{S}(k)$:

$$\begin{aligned} \lambda\mu e^{-i(2\lambda L+\theta)}s_{11}(k) \\ = \mu \cos(2\mu L)(\lambda \cos \theta - ik \sin \theta) \\ + i \sin(2\mu L)[hq_o \cos \alpha - k(k \cos \theta - i\lambda \sin \theta)]. \end{aligned} \quad (20)$$

The discrete eigenvalues of the scattering problem are the zeros of $s_{11}(k)$. Each of them contributes a dark soliton to the solution. For the scalar defocusing NLS equation the zeros are real and simple, and there is a finite number of them, belonging to the spectral gap $k \in (-q_o, q_o)$ [48]. In the case of a single zero k_o , the dark soliton solution of Eq. (3) reads

$$q_d(x, t) = q_o \cos \beta_o - iq_o \sin \beta_o \tanh[\sin \beta_o(x - \kappa_o(t))], \quad (21)$$

where $k_o = q_o \cos \beta_o$ and $\lambda_o = iq_o \sin \beta_o$ provide the velocity and the amplitude of the soliton,

$$v = -q_o \cos \beta_o \equiv -k_o, \quad (22a)$$

$$A_d = q_o \sin \beta_o \equiv \sqrt{q_o^2 - k_o^2}, \quad (22b)$$

respectively, and $\kappa_o(t) = x_o - q_o \cos \beta_o t$ stands for the center of the soliton.

We point out that the maximum soliton speed $|v_{\max}| = q_o$, which coincides with the speed of sound of the condensate, $c = q_o$ (note that $c = \sqrt{gn}$ [49,50] in the dimensionless units adopted herein, with n being the density of the BEC). Recall [cf. Eqs. (22)] that a true soliton can never reach such speed ($v = k_o < q_o$). On the other hand, the maximum amplitude of a soliton is $A_d^{\max} = q_o$, and it is attained by solitons with $v = k_o = 0$, also known as black solitons. In what follows, we will use the variable k_o to refer to a generic zero or to a set of zeros.

C. Special cases, symmetries, interference, and phase-density engineering

Some of the most popular methods to generate dark solitons in 1D BECs are phase imprinting, density engineering, and colliding condensates, as discussed in the introduction. In this section we show how box-type initial configurations can be analogous to most setups used in the aforementioned methods for the generation of dark solitons in 1D BECs, and we obtain analytical results in the corresponding cases.

Before discussing each case, it is worth noting that, regardless of the method of creation, configurations with a phase difference $\Delta\theta = \pi$ allow the emergence of black solitons. Recall that black solitons are static solitons, i.e., $v = k_o = 0$ [see Eqs. (22)]. We can establish straightforward necessary and sufficient conditions to ensure that $k = 0$ is a discrete eigenvalue, i.e., a zero of $s_{11}(k)$. Since we are looking for zeros, from now on it is convenient to work with only the right-hand side of Eq. (20). When $k = 0$ both λ and μ are

purely imaginary, i.e., $\lambda = iq_o$ and $\mu = ih$, and Eq. (20) yields

$$\cosh(2hL) \cos \theta + \sinh(2hL) \cos \alpha = 0. \quad (23)$$

Thus, $k = 0$ is a discrete eigenvalue if and only if either (i) $\cos \theta = \cos \alpha = 0$, for any choice of h, L, q_o or (ii) $\tanh(2hL) = -\cos \theta \sec \alpha$. The former is in line with the previous statement regarding black solitons, i.e., $\theta = \pi/2$. The latter obviously requires $\cos \theta \sec \alpha > -1$.

Equation (23) is a special case of the symmetries possessed by the discrete spectrum in certain configurations. Since λ and μ are both even functions of k , when $\theta = 0$ (corresponding to an in-phase background, i.e., $\Delta\theta = 0$), the right-hand side of Eq. (20) is also an even function of k . Thus, independently of the value of h and α , to each discrete eigenvalue $k_o \neq 0$ there corresponds a symmetric discrete eigenvalue $-k_o$, yielding a pair of symmetric solitons with the same amplitude and opposite velocity. The same symmetry also arises when $\theta = \pi/2$ (i.e., $\Delta\theta = \pi$) if either $h = 0$ or $\alpha = \pi/2$, since in this case the right-hand side of Eq. (20) becomes an odd function of k .

We now discuss how the box-type configurations (5) relate to two of the aforementioned methods, associated with the interference process. Such a setup in principle consists of two condensates, e.g., of the same atomic species, being separated from each other by some distance. The emergence of dark solitons in this setting relies on matter-wave interference phenomena occurring during the collision of the condensates [26–29]. Basically, when the condensates collide an interference pattern appears. Then, depending on the initial momenta and phase of the colliding condensates, some of the interference fringes formed might develop into dark solitons. Specifically, the number of the latter is known to be proportional to the momenta of the colliding condensates [27,28] and can be increased by placing them farther apart. Additionally, also known is that the parity of the number of solitons depends on the phase difference between the condensates. Namely, an even (odd) number of them is going to emerge if the initial condensates are IP (OP). A box-type initial configuration that can mimic such an interference process is that with $h = 0$. In this case the two sides of the box represent the two independent colliding condensates, being separated by a distance $2L$ and having a phase difference $\Delta\theta = 2\theta$. Taking $h = 0$, Eq. (20) reduces to

$$\begin{aligned} 0 &= k \cos(2kL)[\lambda \cos \theta - ik \sin \theta] \\ &\quad - ik \sin(2kL)[k \cos \theta - i\lambda \sin \theta], \end{aligned} \quad (24)$$

which can be rewritten as

$$\sqrt{k^2 - q_o^2} k \cos(2kL + \theta) - ik^2 \sin(2kL + \theta) = 0. \quad (25)$$

Apart from the trivial solution $k = 0$, the other solutions k_n are given by

$$2k_n L + \theta = \arctan\left(\frac{\sqrt{q_o^2 - k_n^2}}{k_n}\right) + \pi n, \quad (26)$$

with $n \in \mathbb{Z}$ (note: in Sec. III the subscript n is replaced by o). This sets all the solutions in the interval $-q_o < k_n < q_o$, as expected. Moreover, the limiting case of $k_n \rightarrow q_o$ provides the

number of zeros \mathcal{N} for a given L and $0 \leq \theta \leq \pi$ as

$$\mathcal{N} = \left\lceil \frac{2q_o L + \theta}{\pi} \right\rceil. \quad (27)$$

In the above expression $\lceil \cdot \rceil$ denotes the ceiling function [Eq. (27) was already derived in Refs. [3,35]]. From the above equation, it is then clear that the number of solitons (zeros) is proportional to the distance between the colliding condensates, and its parity depends on their phase difference.

We now discuss the second methodology, namely, phase imprinting [8,23,51]. This technique imprints a phase jump on the condensate, by exposing part of it to a far-detuned laser beam, which can dynamically develop into dark solitons. This setting can be reproduced by box-type initial configurations even with $L = 0$. This extreme case represents the setting of a highly localized in space phase imprinting. Notice that such a choice indeed leads to a condensate that has two regions with different phases. Then Eq. (20) directly reduces to

$$\lambda \cos \theta - ik \sin \theta = 0, \quad (28)$$

which yields a single zero

$$k = q_o \cos \theta = q_o \cos \left(\frac{\Delta\theta}{2} \right). \quad (29)$$

Notice also that a black soliton solution occurs when $\Delta\theta = \pi$, as expected from condition (i) of Eq. (23). Even though Eq. (29), having a single phase jump, does not produce soliton trains, it nevertheless assures the controlled generation of a single soliton given a particular θ . Moreover it correctly captures earlier findings [8,14,52,53] according to which the generated solitons are faster, shallower and wider, the smaller the phase difference is [see also Eqs. (22)].

We can consider other cases as well. For instance a case in which a phase is imprinted on a finite region of the BEC, resulting in a three-section condensate with two phase jumps [8,14,52,53]. To reproduce such a setup with the box-type initial configuration of Eq. (5) we consider a homogeneous condensate ($h = q_o$) having an extent $2L$ and to which we impose a phase (α). In this case, if $L \approx q_o$ then Eq. (20) needs to be numerically solved. Yet, in the limit $L \gg q_o$, we can treat both phase jumps as being sufficiently far apart from each other to treat them locally. Thereby, we can make use again of Eq. (29) with the appropriate phase difference

$$k_{\pm} = q_o \cos \left(\frac{\Delta\theta_{\pm}}{2} \right) = q_o \cos \left(\frac{\theta \mp \alpha}{2} \right). \quad (30)$$

Recall that \pm denotes the right or the left phase jump [see Eq. (5)]. Here we want to point out that we assume $0 \leq \Delta\theta_{\pm} \leq \pi$, otherwise it needs to be transformed accordingly with a π shift. Yet, another case example consists of a box-type initial configuration corresponding to a barrier on top of a background, i.e., $h > q_o$. Considering $h \gg q_o$ and imposing a phase α at the location of the barrier, Eq. (20) can be expressed as

$$\tanh(2hL) = \frac{k \sin \theta - \sqrt{q_o^2 - k^2} \cos \theta}{q_o \cos \alpha}. \quad (31)$$

Since the left-hand side is always positive, Eq. (31) provides zeros if and only if θ and α are such that they produce

a positive right-hand side. For example, if we look for zeros corresponding to black solitons, i.e., $k_o = 0$, we recover condition (ii) from Eq. (23). Additionally, in the limit $L, h \rightarrow \infty$, Eq. (31) reduces to

$$k_{\pm} = q_o \sin \Delta\theta_{\pm}. \quad (32)$$

Last, we briefly comment on the analogy of density engineering methods with our box-type initial configurations. These methods are typically used to create density defects on a condensate, which can be small [24] or substantial [25] depletions of the latter. To mimic such techniques with our box-type initial configurations, each case needs to be considered individually and the zeros must be found numerically by solving Eq. (20). Specific case examples of the zeros and their parametric dependencies for distinct box-type initial configurations are presented in the next section.

III. DARK SOLITON GENERATION AND DYNAMICS

A. Analytical results for the discrete spectrum

Here we analytically characterize the dark solitons produced by the box-type initial configurations (5) by studying the zeros of the first element, $s_{11}(k)$, of the scattering matrix, $\mathbf{S}(k)$ [Eq. (20)], upon considering different selections of the system parameters. Specifically, we utilize the wave function of Eq. (5) which is characterized by the following five parameters: the half width, L , the amplitude, q_o , the side phase, $\pm\theta$, the depth (or height) of the box, h , and its phase, α [see also Fig. 1(a)]. To sort out all the spectra, we choose a set defined by two main variables, which will be varied while the remaining system parameters are held fixed. Since L and h can be thought of as the main parameters of the scalar system under consideration, the following discussion will be mainly focused on the set of values of L and h . The corresponding exploration, in terms of parametric variations, is performed for the following selection of the configuration parameters:

$$L \in [1, 9], \quad \theta = \left\{ 0, \frac{\pi}{2} \right\}, \quad h \in [0, q_o], \quad \alpha = \{0, \pi\}, \quad (33)$$

together with $q_o = 1$. However, we will also briefly comment on other selections too whose results are not included herein for brevity.

In what follows, we present the spectra of zeros of the first element $s_{11}(k)$ of the scattering matrix for three different sets of values of L and h . Each distinct exploration is shown in a figure consisting of 10 panels (a) to (i) that range from $L = 1$ to $L = 9$, respectively. Each panel contains different zeros, k_o , as h is varied, with each of which corresponding to a particular dark soliton solution.

1. All in-phase

The first selection we investigate is the case $q_o = 1, \theta = 0$ and $\alpha = 0$. Here $\Delta\theta = 0$ implying an IP configuration [see Fig. 1(a)], and $\alpha = 0$ implies that the box is also in-phase with the background. The corresponding spectra of zeros is presented in Fig. 2. Due to the parity of the zeros, only $k_o > 0$ are shown in the figure. As can be directly seen, increasing L increases the number of solitons (i.e., the number of k_o). Particularly, when $L = 1$ only one pair of zeros, $\pm k_1$, appears

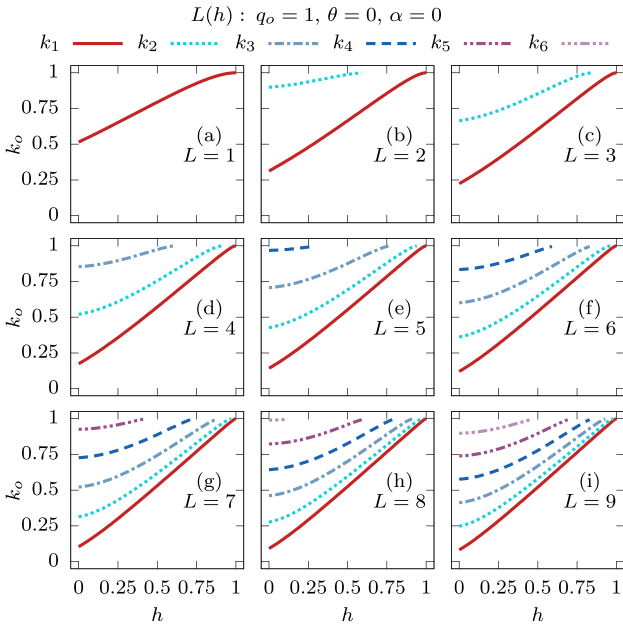


FIG. 2. Zeros of $s_{11}(k)$ as a function of h for different values of L . The parameters $q_o = 1$, $\theta = 0$, and $\alpha = 0$ remain fixed. Only $k_o > 0$ are shown due to the parity of the zeros. Note that the quantities shown are measured in transverse oscillator units.

(one pair of soliton solutions) while $L = 5$ ($L = 9$) allows up to four (six) pairs of them, $\pm k_1, \dots, \pm k_4$ ($\pm k_1, \dots, \pm k_6$), to occur. This is in agreement with the analytical expression of Eq. (27) and correctly captures the $h = 0$ case. Recall that $h = 0$ is referred to as a “zero box” and is physically associated with a setting of independent condensates colliding. Note also that even though Eq. (27) is not a general expression but rather a limiting case, the number of solitons still increases with L and q_o even when $h \neq 0$. Also by inspecting Fig. 2, it becomes apparent that for fixed h , increasing L decreases the value of k_o . This implies that the resulting solitons are slower as L increases [see Eqs. (22)], which can be understood as the momenta available in the system being distributed among a larger number of solitons. This trend can be easily discerned by monitoring, e.g., $k_1(h = 0)$ as L increases [see also Eq. (26)]. Indeed, initially, i.e., for $L = 1$, $k_1(h = 0) = 0.515$ [Fig. 2(a)]. Then, for $L = 2$, k_1 decreases to $k_1(h = 0) = 0.313$ [Fig. 2(b)] and already for $L = 9$ $k_1(h = 0) = 0.083$ [Fig. 2(i)]. On the other hand, for a fixed L it is found that the value of k_o increases, i.e., the solitons become faster, upon increasing h . Moreover, since $k \in (-q_o, q_o)$ (see also Sec. II), this increasing tendency of k_o for increasing h holds as such until $k_o = q_o$, a threshold above which solitons cease to exist [see Eqs. (22)]. Recalling now that increasing h implies that the initial jump in the configuration becomes progressively shallower, then when $h = q_o$ there is no box configuration that can lead to the creation of solitonic excitations. Such an outcome also persists for $h > q_o$.

2. Out-of-phase box

Next we turn to the second selection of parameters, in which $q_o = 1$, $\theta = 0$ as before, but where now $\alpha = \pi$. This

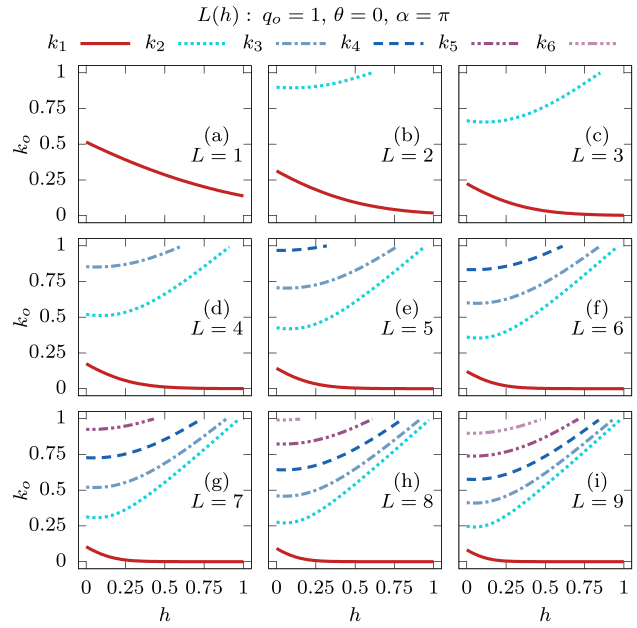


FIG. 3. Zeros of $s_{11}(k)$ as a function of h for different values of L . The parameters $q_o = 1$, $\theta = 0$, and $\alpha = \pi$ remain fixed. Only $k_o > 0$ are shown due to the parity of the zeros. Note that the quantities shown are measured in transverse oscillator units.

is also an IP configuration, but the box is now out-of-phase with the background. The analytical solutions, given by the zeros of the first scattering element, are illustrated in Fig. 3. Since $\Delta\theta = 0$ here as well, we show only the range $k_o > 0$, as before. Below we solely focus on k_1 since it is the only zero having a distinct trend when compared to those shown in Fig. 2. Notice that contrary to the aforementioned zeros, and also to the previous parameter selection, as h increases k_1 decreases with the associated soliton thus becoming slower and, in fact, $k_1 \rightarrow 0$ as $h \rightarrow \infty$. This decreasing tendency of k_1 is in agreement with Eq. (23) and specifically with condition (ii).

Additionally, it is also evident from Figs. 3(b)–3(i) that $k_1 \rightarrow 0$ as $L \rightarrow \infty$ independently of h . A discrete eigenvalue $k_1 = 0$ would in theory correspond to a pair of black solitons, each generated as a consequence of the phase jump $\Delta\theta_{\pm} = \mp\pi$ at $x = \pm L$. In turn, this would correspond to $k_1 = 0$ being a degenerate eigenvalue with degeneracy two. However, it is well known that, for the scalar defocusing NLS, all discrete eigenvalues are simple [48], and no coalescence of zeros is possible, in contrast to the focusing case. What is happening is that, as $L \rightarrow \infty$, one reaches an approximate degeneracy: when the phase jumps at $x = \pm L$ are sufficiently far apart from each other, one can approximately treat them as independent scattering problems. Then the solution to each problem is simply given by Eq. (29), which indeed coincides with the observed result. Nonetheless, it is important to realize that the discrete eigenvalues of the overall system are only approximately given by those of the individual scattering problems, and a careful analytical treatment shows that in practice the symmetric pair of discrete eigenvalues is always at a nonzero

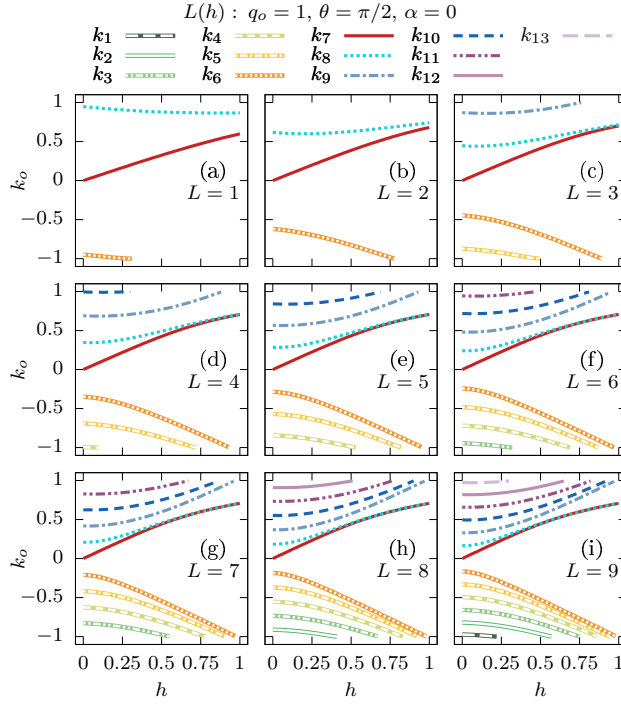


FIG. 4. Zeros of $s_{11}(k)$ as a function of h for different values of L . The parameters $q_o = 1$, $\theta = \pi/2$, and $\alpha = 0$ remain fixed. Note that the quantities shown are measured in transverse oscillator units.

distance from $k = 0$, although this distance vanishes in the limit $L \rightarrow \infty$.

Finally, we note in passing that cases corresponding to different choices of α have also been explored, for which upon increasing h , $k_1 \rightarrow k_{\pm}$ [Eq. (30)]. To be precise, it is found that if $0 \leq \alpha \leq \pi/2$ then k_1 increases and eventually reaches $k_1 = q_o$. On the other hand, if $\pi/2 < \alpha \leq \pi$, then k_1 asymptotically tends to a different yet again finite value, as h is increased. Indeed, taking the limit $h \gg q_o$ and for $\theta = 0$, Eq. (31) yields

$$\tanh(2hL) = -\sec \alpha \sqrt{1 - \left(\frac{k}{q_o}\right)^2}, \quad (34)$$

which directly implies that $\sec \alpha < 0$ explaining this way that there exist values of α for which $k_1 = q_o$ is reached. Past this point, and for $L \rightarrow \infty$ or $h \rightarrow \infty$, $k_1 \rightarrow q_o \sin \alpha$ asymptotically slow [see Eq. (32)].

3. Asymptotic phase difference

Our last parametric exploration, shown in Fig. 4, consists of various choices of L and h as before, but with the remaining system parameters as $q_o = 1$, $\theta = \pi/2$, and $\alpha = 0$. This initial state preparation corresponds to an OP box-type configuration, with $\Delta\theta = \pi$. In contrast to the previous cases, this choice produces an asymmetric distribution of discrete eigenvalues. This outcome is evident by looking at the zeros as h is varied, as illustrated in Fig. 4. Exceptionally, for $h = 0$ all zeros are paired, i.e., $k_o = \pm k$, except for the k_7 one. For instance, for $L = 9$ and $h = 0$, 13 soliton so-

lutions are identified, corresponding to the thirteen distinct zeros, k_1, \dots, k_{13} , shown in Fig. 4(i). From these, solutions $k_1, \dots, k_6 = -k_{13}, \dots, -k_8$, respectively. As in the preceding scenarios, it is clear that in the present case the number of solitons also increases as L increases, and increasing L while keeping h fixed results in zeros that have smaller $|k_o|$ value and are thus slower. Additionally, for fixed L the number of expected soliton solutions decreases as we increase h . For example, for $L = 3$ all five solutions k_5, \dots, k_9 occur, e.g., at $h = 0$, but only four of them, i.e., k_6, \dots, k_9 , are left for $h = 0.6$, further reducing to three (k_6, k_7 and k_8) for $h = 0.8$ [Fig. 4(c)]. Moreover, increasing h produces also an increase in the magnitude of each zero ($|k_o|$) until eventually $|k_o| = q_o$ is reached, leading in turn to the absence of soliton solutions.

Exceptions to the aforementioned general behavior of the solutions are the zeros k_7 and k_8 that never reach the threshold $|k_o| = q_o$ for $h \leq q_o$. Instead, these two solutions are seen to merge asymptotically as h increases, a merging that occurs faster for larger L values. This merging can in turn be translated into two (asymptotically) identical solitons, having the same velocity and amplitude, but different soliton centers, x_0 [see Eqs. (22)]. To understand further the aforementioned behavior, we considered also different values of θ which in turn unraveled that if $h = q_o$ then $k_7 = k_8 \rightarrow q_o \cos(\theta/2)$ as $L \rightarrow \infty$ [see Eq. (30)]. This is also in line with our interpretation for the existence of approximate degenerate zeros in the scalar NLS (see also our previous discussion). On the other hand, if $h \rightarrow \infty$ then $k_7 = k_8 \rightarrow q_o \sin(\Delta\theta_{\pm})$ independently of L [see Eq. (32)]. Note here that the subscripts referring to the solutions k_7, k_8 are such for the specific case example addressed herein. However, different values of θ might change the number of solutions and thus their relevant labeling.

B. Nucleation of dark soliton trains: Without confinement

In this section we aim to validate the analytical results presented in Sec. III A (and more specifically to bear out the discrete eigenvalues identified there) by numerically solving the scalar GPE in the absence of a confining potential, i.e., $\Omega = 0$ [Eq. (2)]. For the dynamical evolution of the aforementioned scalar system, we employ a fourth-order Runge-Kutta integrator accompanied by a second-order finite-difference method that accounts for the spatial derivatives. The spatial and temporal discretizations introduced are $dx = 0.1$ and $dt = 0.001$, respectively, and the position of the boundaries used in the dynamics is at $|x| = 2500$ to avoid finite-size effects. In the following, we fix $L = 5$ and $q_o = 1$ and we consider as representative examples the values $h = \{0, 0.5\}$. Additionally, for this h selection, we further consider the cases of $\theta = \{0, \pi/2\}$ and $\alpha = \{0, \pi\}$.

Below we present our findings regarding the dynamical nucleation of dark solitons via the matter-wave interference of two colliding condensates [26–29] for various initial configurations. When comparing the analytical predictions to the numerical observations, it is important to keep in mind that the various solitons generated by the initial conditions (5) are in general interacting with each other. Therefore, one can expect to be able to visually identify individual solitons only in the asymptotic limit of $x \rightarrow \pm\infty$, after the solitons emerge from the creation process and can be considered to be

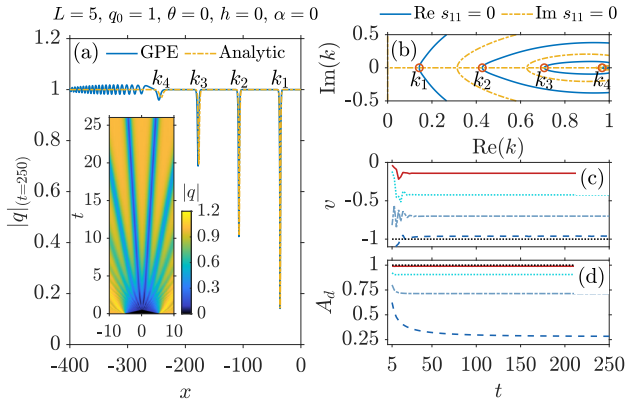


FIG. 5. Dark soliton solutions resulting from the box-type initial condition (5) with $L = 5$, $q_0 = 1$, $\theta = 0$, $h = 0$, and $\alpha = 0$, corresponding to a zero box and an in-phase background [cf. Fig. 2(e)]. (a) Snapshot of $|q|$ at $t = 250$ given by the GPE (solid blue line) and the analytical solutions with $\kappa_0(t = 0) = 0$ (dashed yellow line). The inset shows the spatiotemporal evolution of $|q|$ at initial times. (b) Contour plot of $\text{Re}s_{11} = 0$ (solid blue line) and $\text{Im}s_{11} = 0$ (dashed yellow line) on the complex k -plane for $\text{Re}k \geq 0$. The zeros, k_o , are depicted by red circles. Temporal evolution of the velocities (c) and the amplitudes (d) of the dark solitons. In both (c) and (d) the distinct lines (from bottom to top) correspond to the analytical predictions stemming from the zeros (from right to left) in (b). Dotted black line in (c) refers to the speed of sound and in (d) to the maximum amplitude. The zeros, k_o , follow the notation introduced in the legend of Fig. 2, with $k_1 = 0.1428$, $k_2 = 0.4271$, $k_3 = 0.7069$, and $k_4 = 0.9608$. Note that the quantities shown are measured in transverse oscillator units.

well separated and independent from one another. Conversely, during the initial stages of the dynamics one expects to see discrepancies between the analytically determined solitons and the numerically observed ones. One can also expect any such discrepancies to become smaller and gradually disappear as $t \rightarrow \pm\infty$. This expectation is indeed reflected by the results, as discussed below.

1. Zero box, in-phase background

We start presenting our findings in Fig. 5. According to our analytical estimates [see Fig. 2(e) and Eq. (27)] four pairs of dark solitons are expected and indeed form when a zero box ($h = 0$) IP ($\Delta\theta = 0$) configuration is utilized. Note that due to the symmetric nucleation of the matter waves only the solitons located at $x < 0$, having negative velocities, $v < 0$, and thus corresponding to the positive zeros, $k_o > 0$, occurring at $\text{Re}k \geq 0$ are shown in Figs. 5(a) and 5(b). Remarkable agreement between the analytical solutions and the dynamically nucleated matter waves is observed already at times $t = 250$ during evolution, as illustrated in this profile snapshot of the norm of the wave function $|q|_{t=250}$ [Fig. 5(a)]. Notice how the emergent dark solitons spread outwards at their initial stages of formation, i.e., right after the collision of the two sides of the initial box around $x = 0$. Such spreading at early times $t < 5$, as depicted in the spatiotemporal evolution of $|q|$ [inset of Fig. 5(a)], bends the trajectories of the solitons that are symmetrically emitted around the origin. However, already

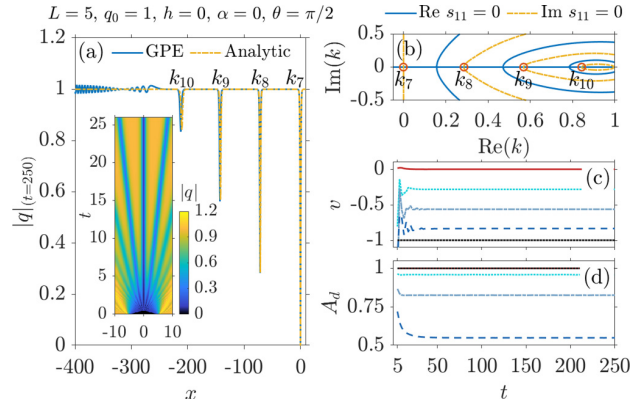


FIG. 6. Same as Fig. 5 but for $L = 5$, $q_0 = 1$, $\theta = \pi/2$, $h = 0$, and $\alpha = 0$, corresponding to a zero box and an out-of-phase background. From left to right the zeros, k_o , in (b) that lead to the solitons formed in (a) are located at $k_7 = 0.0$, $k_8 = 0.2852$, $k_9 = 0.5679$, $k_{10} = 0.8423$ (see the legends in Fig. 4). Note that the quantities shown are measured in transverse oscillator units.

at $t \approx 25$, where also the trajectories of the propagating solitons become linear, the instantaneous velocities, $v = dx_{CM}/dt$ (see below), of the individual coherent structures reach the asymptotic analytical predictions stemming from the zeros, k_o , identified in Fig. 5(b), remaining thereafter nearly constant for all times [Fig. 5(c)]. The same trend holds also for the amplitudes, A_d , of the emergent entities illustrated in Fig. 5(d). Note also that in both Figs. 5(c) and 5(d) the fastest dark wave denoted by k_4 has a velocity proximal to the speed of sound $c = q_0 = 1$ [dotted black line in Fig. 5(c)], while the slowest soliton denoted by k_1 has an amplitude close to the maximum one, i.e., $A_d^{\max} = q_0 = 1$ [dotted black line in Fig. 5(d)].

Finally, it is important to mention at this point that, in order to obtain the amplitude of each of the aforementioned solitons (and also for the cases to be presented below), we numerically followed the dark soliton minima during evolution. Then the amplitude corresponds to the value of $|q|$ at these minima. For measuring the instantaneous velocity, we used instead the position given by the center of mass, i.e., $x_{CM} = (\int_{x_l}^{x_r} x|q|^2 dx) / (\int_{x_l}^{x_r} |q|^2 dx)$, of each soliton with $x_{l,r}$ denoting the area of integration around each dark soliton's core. Therefore, at early times, the oscillations observed in the temporal evolution of v [Fig. 5(c)] stem from the discrepancies in the calculation of x_{CM} . Indeed, at the initial stages of the dynamics, the calculation of x_{CM} might present some irregular oscillations if a soliton is not well formed nor separated enough from its neighbors or the emitted radiation. The latter, seen for instance at $x < -275$ in Fig. 5, is a direct effect of the highly excited initial state introduced herein.

2. Zero box, out-of-phase background

Next we turn to the exploration of the dynamics upon considering a zero box but with OP ($\Delta\theta = \pi$) background. Here our analytical findings suggest the emergence of an odd number of solitons [see Fig. 4(e) at $h = 0$ and Eq. (27)]. This outcome is dynamically confirmed by Fig. 6, which shows three pairs of dark solitons being nucleated together with a central black soliton, adding up to the expected odd number

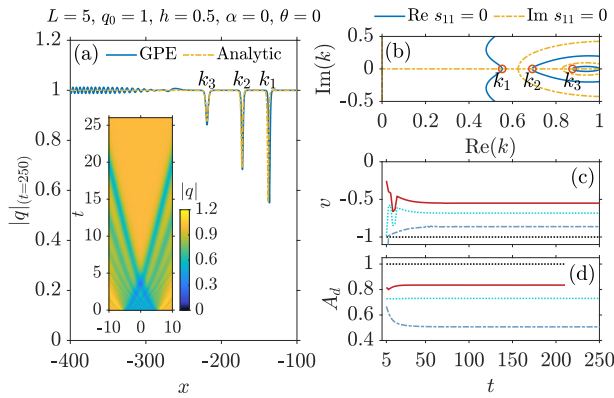


FIG. 7. Same as Fig. 5 but for $L = 5$, $q_0 = 1$, $h = 0.5$, and $\alpha = 0$, corresponding to a nonzero box in-phase with respect to its background. From left to right the zeros, k_n , in (b) that lead to the solitons formed in (a) are located at $k_1 = 0.5526$, $k_2 = 0.6914$, $k_3 = 0.8763$ (see the legends in Fig. 2). Note that the quantities shown are measured in transverse oscillator units.

[Fig. 6(a)]. Since once more the generation is symmetric with respect to the origin, only the left moving matter waves are shown in the snapshot of $|q|_{t=250}$ in Fig. 6(a) that correspond to the zeros $k_7 - k_{10}$ illustrated in Fig. 6(b). Notice the close similarities between this process and the previous one. Indeed, besides the number of nucleated waves, the only discernible difference at the early stages of soliton formation is the generation of the central black soliton [inset Fig. 6(a)]. The velocities and amplitudes of the evolved solitons also follow a trend analogous to the IP case with minor differences for the relevant magnitudes of v and A_d for each individual dark soliton [Figs. 6(c) and 6(d)]. The black soliton (k_7) has, as expected, $v = 0$ and the maximum amplitude $A_d^{\max} = q_0 = 1$.

3. Nonzero boxes, dispersive shock waves

We now discuss initial configurations whose shape resembles a density defect immersed in the BEC [23–25]. To achieve the latter we fix $h = 0.5$. Figure 7 and Fig. 8 illustrate representative examples of the dynamical evolution of the scalar system for IP initial configurations but with $\alpha = 0$ and $\alpha = \pi$, respectively [see also Fig. 2(e) and Fig. 3(e), respectively]. In both cases, at the initial stages of the dynamics, $t < 5$, multiple interference events significantly distort the homogeneous background and also disturb the nucleation process.

It should be noted how, in this case as well as the following two, the time evolution generates dispersive shock waves [54] as a result of the initial discontinuities. This is a well-known phenomenon, and in marked contrast to the case when the amplitude in the central box is zero, in which no such structures are generated [55]. The formation and initial dynamics of these dispersive shock waves can be effectively described using Whitham's modulation theory for the defocusing NLS equation [56–61]. In situations where more than one dispersive shock wave is generated, as in the present case (where each discontinuity generates a separate structure), their interactions can also be effectively studied, as in Refs. [62,63], using the Whitham modulation equations of higher genus

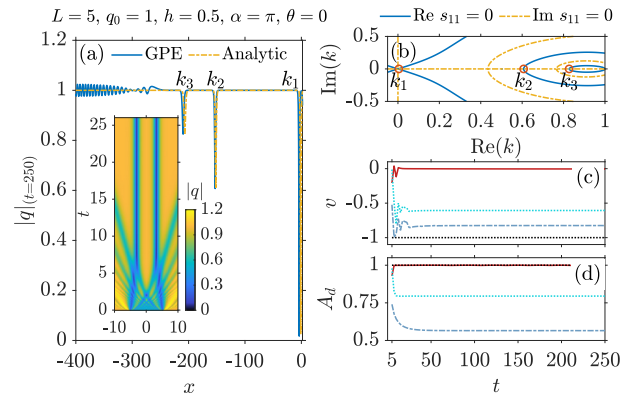


FIG. 8. Same as Fig. 5 but for $L = 5$, $q_0 = 1$, $h = 0.5$, and $\alpha = \pi$, corresponding to a nonzero box out-of-phase with respect to its background. From left to right the zeros, k_n , in (b) that lead to the solitons formed in (a) are located at $k_1 = 0.0045$, $k_2 = 0.06073$, $k_3 = 0.8269$ (see the legends in Fig. 3). Note that the quantities shown are measured in transverse oscillator units.

[64]. It is also interesting to note that one could still choose to look at the individual oscillations in these dispersive shocks as the initial manifestations of the dark solitons that are the main object of our study. Also note, however, that the initial speeds of propagation of these individual excitations are quite different from those predicted by the IST, and are instead very well in agreement with the predictions from Whitham modulation theory. Nonetheless, after these structures have interacted, the final state of the system does become a collection of solitons whose properties agree very well with the predictions of the IST, as per the calculations in Sec. II B.

An even more dramatic instance of the same phenomenon arises in the case of $\alpha = \pi$, as depicted in the inset of Fig. 8(a). Indeed, the spatiotemporal evolution of this configuration captures the formation of two counterpropagating dispersive shock waves whose downstream soliton emission [24,65] is illustrated in Fig. 8(a). As in the case shown in Fig. 7(a), these shock waves interact with the newly formed dark solitons, an interaction that is most pronounced for the two central nearly black solitons visible in the inset of Fig. 8(a). For both cases, close inspection of the relevant insets indeed reveals that solitons with positive velocities are initially formed at $x \approx -5$. On the other hand, the negative velocity ones arise symmetrically at $x \approx 5$. Despite the much more involved soliton generation, in both cases our simulations almost perfectly match the analytical predictions when we set the origin of the latter at $x = 0$ [see the identified zeros in Fig. 7(b) and Fig. 8(b), respectively]. Our results continue to hold even for significantly larger evolution times than those depicted herein. It is also at these later times, and in particular around $t \approx 1000$, that the two central dark solitons, whose zeros are identified at $k_1 = \pm 0.0045$ [see the $k_1 > 0$ in Fig. 8(b)], visibly repel [29] one another effectively, given their opposite but extremely small in magnitude velocities (results not shown here for brevity). Finally, due to the above-described dynamics, both the instantaneous velocities, v [Fig. 7(c), Fig. 8(c)], and the amplitudes, A_d [Fig. 7(d), Fig. 8(d)], of all three pairs

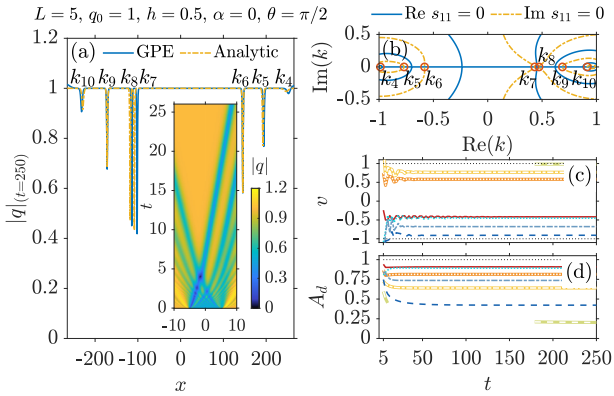


FIG. 9. Same as Fig. 5 but for $L = 5$, $q_0 = 1$, $\theta = \pi/2$, $h = 0.5$, and $\alpha = 0$ (see the legends in Fig. 4). In this case (b) depicts all the complex k -plane. From left to right the zeros, k_o , in (b) that lead to the solitons formed in (a) are located at: $k_4 = -0.9750$, $k_5 = -0.7700$, $k_6 = -0.5814$, $k_7 = 0.4329$, $k_8 = 0.4718$, $k_9 = 0.6869$, $k_{10} = 0.9155$. Note that the quantities shown are measured in transverse oscillator units.

of solitons formed in both scenarios acquire their expected nearly constant trend for $t \geq 25$.

4. Other configurations

In all cases discussed so far, the initial configuration gave rise to a symmetric distribution of solitons. We now explore a scenario corresponding to an OP initial configuration, the analytical predictions of which can be found in Fig. 4(e). The corresponding dynamical process is illustrated in Fig. 9. In contrast to the previously discussed IP box-type configurations, in the present case, since both $\Delta\theta = \pi$ and $\Delta\theta_{\pm} = \pi/2$, we do expect an asymmetric distribution of the zeros, k_o , and thus asymmetrically produced dark solitons. Both expectations are confirmed and shown in Figs. 9(a) and 9(b). In particular, seven distinct solitons are nucleated in Fig. 9(a), with each of them corresponding to each of the seven distinct solutions shown in Fig. 9(b). The spatiotemporal evolution of $|q|$ at early times [inset of Fig. 9(a)] shows that three of them have $v = -k_o > 0$ and four $v = -k_o < 0$. This asymmetric generation of matter waves entails also the largest deviations between our analytical findings and the numerically obtained ones. This can be easily inferred by inspecting either the profiles or even better the estimated velocities, v , and amplitudes, A_d , of the ensuing waves illustrated, respectively, in Figs. 9(c) and 9(d). For instance, the fastest soliton, $k_4 = -0.9750$, bears such a small amplitude that renders it indistinguishable from the background radiation for times up to $t \approx 180$. As such, the corresponding v and A_d are not depicted in Figs. 9(c) and 9(d), respectively, until $t > 180$. Yet, another example refers to the solitons labeled k_7 and k_8 . Namely, the two entities that are tightly close to one another [see here Eq. (30) and Eq. (32)] and thus interact continuously with each other. It is this continuous interaction that holds for $t \gtrsim 1000$, before the soliton repulsion sets in, to which the discrepancy in the amplitudes observed at $t = 250$ is attributed [Fig. 9(a)]. Even though the largest deviation between our analytical predictions, provided by the zeros of Eq. (20), and our numerical

findings, found for the aforementioned asymmetric initial configurations, still lies within our numerical precision, i.e., $\delta = \pm 0.01$.

We also explored cases for which h is close to q_0 but $h \geq q_0$. Here our results are found to be consistent with the limiting cases discussed in Sec. II C. In particular, $\theta = \alpha = 0$ leads to sound wave emission but no soliton production. For $\theta = 0$ and $\alpha = \pi$ the creation of two almost black solitons ($k_o \approx 0$) located at $x = \pm(L + \epsilon)$, where $\epsilon > 0$ is a small displacement caused by the emission of radiation, is seen. Last, $\theta = \pi/2$ and $\alpha = 0$ ($\theta = \pi/2$ and $\alpha = \pi$) results into two nearly equal zeros, with $\text{Re}k_o > 0$ ($\text{Re}k_o < 0$).

C. Nucleation of dark soliton trains: With confinement

We now aim to generalize our findings by taking into account the presence of a harmonic confinement that is naturally introduced in BEC experiments [8, 19, 66]. To this end, for the numerical considerations to be presented below we turn on the harmonic potential introduced in Eq. (2), and we further fix the trapping frequency to $\Omega = 0.01$ [66]. The latter choice, besides its experimental relevance, is also an optimal one since it allows for properly handling the sound wave emission that takes place at the initial stages of the interference process.

Indeed, for tighter trappings the radiation emitted remains also trapped and, as such, multiple collisions of the generated dark solitons with these sound waves would result in a much more involved dynamical evolution of the nucleated matter waves.

Yet another important point worth mentioning here refers to the analytical estimates regarding the soliton generation provided by solving the direct scattering problem (see Sec. II B). Specifically, in the trap setting under consideration these estimates can serve as approximate ones, since for instance the NZBC, which in turn define the asymptotic behavior of the solitons formed in terms of amplitude, velocity, and location, cannot be fulfilled. However, as we shall show later, the strength of the analytical predictions is not limited to the homogeneous setup but provides a particularly insightful tool for the confined case as well.

In the present setting, in order to induce the dynamics we initially find, by using imaginary time propagation, the ground state of the scalar system [Eq. (2)]. We then embed in it the wave function of Eq. (5). A schematic illustration of the aforementioned initial state is illustrated in Fig. 1(b). Moreover, in order to offer a direct comparison between the homogeneous and the confined cases, we consider as representative examples five distinct selections of the involved parameters. Namely, $L = 5$, $q_0 = 1$ while $h = \{0, 0.5\}$, $\alpha = \{0, \pi\}$ and $\theta = \{0, \pi/2\}$ (see also the relevant discussion around Figs. 5–9). Additionally, we design the analytical estimates for the trapped scenario by molding onto the ground state, q_{gs} , the analytical solutions of the corresponding homogeneous setting [see Eq. (21)] as follows:

$$|q(x, t)|^2 = q_0^2 \left| \prod_i \frac{q_d^{(i)}(x, t)}{q_0} \right|^2 - [q_0^2 - |q_{gs}(x)|^2]. \quad (35)$$

In Eq. (35) the product is performed over all the different solutions of a set of zeros k_o , while the first term on the right

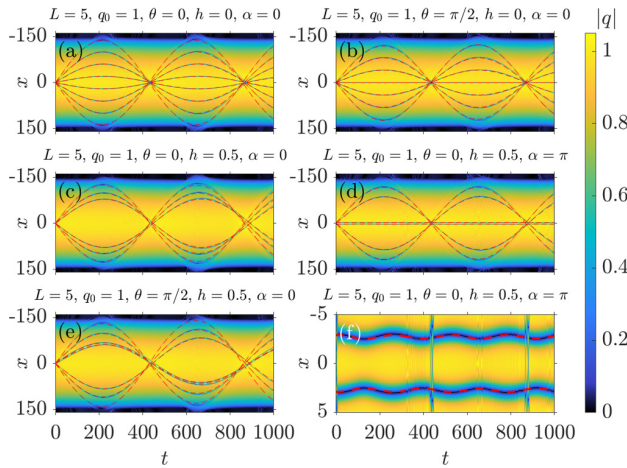


FIG. 10. Spatiotemporal evolution of $|q|$ for distinct choices of the involved parameters L , q_0 , h , α , and θ (see legends). Dashed red lines correspond to the analytical trajectories given by Eq. (36). Panel (f) is a magnified version of (d) which captures the two dark solitons that are symmetrically placed around the trap center ($x = 0$). The other four solitons that appear at the collision points are stretched due to the zoom. The trapping frequency is fixed to $\Omega = 0.01$. Note that the quantities shown are measured in transverse oscillator units.

side corresponds to a dark soliton train solution in the absence of a trapping potential having a background amplitude q_0 . The second term properly adjusts the former, by preserving the shape of each soliton, onto the in-trap ground state. It is important to remark that given our particular set of initial conditions and parameter selection, the right hand side of Eq. (35) is always positive. In particular, $\Omega = 0.01$ assures a trapping potential growth slow enough to satisfy the positivity of the right-hand side of Eq. (35). Additionally, the center of each dark soliton is now given by

$$\kappa_0(t) = -\frac{k_o}{\omega_o} \sin(\omega_o t + \phi_o) + x_0, \quad (36)$$

where the amplitude of the oscillation directly depends on k_o . Here ω_o is the characteristic in-trap oscillation frequency of a single dark soliton [29,67] (see our discussion below), x_0 is

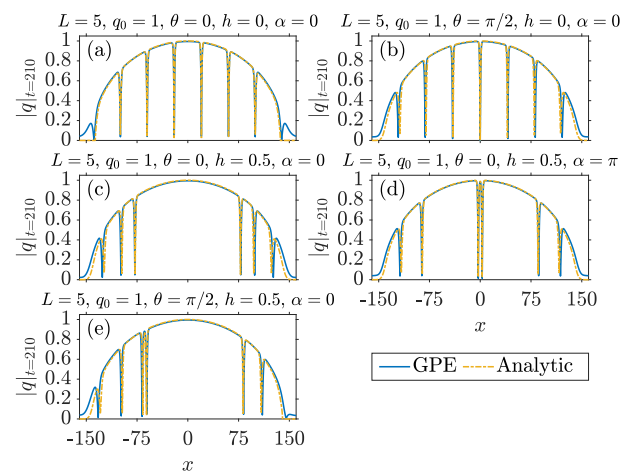


FIG. 11. Profile snapshots of $|q|$ at $t = 210$ for distinct choices of the involved parameters L , q_0 , h , α , and θ (see legends). The snapshots from (a) to (e) correspond to the relevant in each case dynamics presented in Figs. 10(a)–10(e), respectively. The analytical solutions are given by Eq. (35). The trapping frequency is fixed to $\Omega = 0.01$. Note that the quantities shown are measured in transverse oscillator units.

the equilibrium position, and ϕ_o is an additional phase factor. Both x_0 and ϕ_o are fixed to zero unless stated otherwise. Our results are summarized in Fig. 10 and Fig. 11, as well as in Table I.

In particular, Fig. 10 illustrates the spatiotemporal evolution of $|q|$, for different parametric variations, along with the trajectory of each soliton center obtained by using the analytical expression of Eq. (36) (see dashed red lines in Fig. 10). Additionally, Fig. 11 gives the corresponding profile snapshots of $|q|$ at $t = 210$ for each selection of parameters, together with the relevant analytical estimates stemming from Eq. (35). Notice here the very good agreement between the analytical predictions and the dynamically formed dark solitons. In general, it is found that the number of the dark solitons formed in each in-trap dynamical process is the same as in the homogeneous case, as dictated by Eq. (27). For

TABLE I. Numerically obtained oscillation frequencies ω_{num} . Each of the five groups of values contains the parameter characterizing each soliton (k_o) and the relative error (ε_o) with respect to the analytical prediction for the frequency of oscillation of a single dark soliton, i.e., $\omega_o = \Omega/\sqrt{2}$ [9], for different variations of the system's parameters. From left to right each group corresponds to Figs. 10(a) to Figs. 10(e), respectively. Other parameters used are $L = 5$, $q_0 = 1$, and $\Omega = 0.01$. Note that the quantities shown are measured in transverse oscillator units.

$h = 0, \alpha = 0, \theta = 0$			$h = 0, \alpha = 0, \theta = \pi/2$			$h = 0.5, \alpha = 0, \theta = 0$			$h = 0.5, \alpha = \pi, \theta = 0$			$h = 0.5, \alpha = 0, \theta = \pi/2$		
k_o	ω_{num}	ε_o	k_o	ω_{num}	ε_o	k_o	ω_{num}	ε_o	k_o	ω_{num}	ε_o	k_o	ω_{num}	ε_o
k_1	0.007184	0.016	k_7	0	–	k_1	0.007043	0.004	k_1^a	0.023905	0.023	k_4	0.007330	0.036
k_2	0.007229	0.022	k_8	0.007228	0.022	k_2	0.007169	0.014	k_2	0.007145	0.011	k_5	0.007226	0.022
k_3	0.007267	0.028	k_9	0.007233	0.023	k_3	0.007265	0.027	k_3	0.007253	0.026	k_6	0.007063	0.001
k_4	0.007330	0.036	k_{10}	0.007265	0.027							k_7	0.007077	0.0008
												k_8	0.007077	0.0008
												k_9	0.007246	0.025
												k_{10}	0.007297	0.032

^aSee Eq. (37) and the discussion around it.

instance, Figs. 10(a) and 11(a) show the generation of four pairs of dark solitons which is exactly the number of matter waves that are predicted and observed for the homogeneous counterpart of this parameter selection illustrated in Fig. 5. This outcome holds equally also for the dynamical processes shown in Figs. 10(b)–10(d) and Figs. 11(b)–11(d) (cf. Figs. 6–8, respectively). Here according to our homogeneous findings, three pairs of dark solitons are expected and indeed nucleate symmetrically around the trap center. Notice also the central black soliton in the former of these processes. Only one difference is worth commenting on, namely the last of the aforementioned cases [Fig. 10(d)]. By monitoring the dynamical evolution of the pair of dark solitons that are closer to the trap center, a magnified version of which is provided in Fig. 10(f), it is found that these two dark solitons instead of executing large amplitude oscillations as the remaining pairs do, they lock into an out-of-phase oscillation mode, similar to the ones explored previously (including experimentally) in the works of, e.g., Refs. [28,29]. In this case, their centers are provided by Eq. (36) but with $\phi_o = \pi/2$ since here, the oscillation of each solitary wave begins at maximum amplitude. Additionally, for this particular out-of-phase oscillation of this pair, the in-trap oscillation frequency, i.e., ω_{OP} , and equilibrium position, i.e., x_{\pm} , are given by Eq. (37) and Eq. (38), respectively (see our discussion below). As our last case example, in Fig. 10(e) we show the dynamical evolution of the system for parameters that lead to asymmetric soliton generation analogous to the one found in the homogeneous scenario (see Fig. 9). Also in this case the number of dark solitons coincides with the one found in the homogeneous setting, with seven such entities being generated. Even more importantly here, and also for all cases discussed above, it is not only the number of nucleated states that is in accordance with the analytical predictions discussed in the homogeneous case, but also the relative position and amplitude of the evolved states. The former is almost perfectly captured by Eq. (36), as depicted by the dashed red lines in Fig. 10 while the latter is also well captured by Eq. (35) as it is evident by inspecting Fig. 11. Note though that while the solitons corresponding to the solutions k_7 and k_8 shown in Fig. 9(a) propagate parallel to each other but eventually, due to repulsion, they will separate out, this is not the case for their trapped analogues shown in Fig. 10(e), which eventually feel the effect of the confining potential. Before proceeding, it is worth commenting at this point on why the solutions stemming from the homogeneous case so closely match those of the trapped one. This behavior can be attributed to the weak, yet experimentally relevant, confinement frequency introduced herein ($\Omega = 0.01$). Such a weak confinement leads to a condensate density around the trap center that is flat enough so that locally the initial conditions for both the homogeneous and trapped scenario are nearly equal, thus producing rather similar soliton trains.

In order to further shed light on the observed in-trap dynamics of the dark solitons generated in each case, we once more follow the center of mass, x_{CM} , of each entity for evolution times up to $t = 3000$. The numerically obtained oscillation frequencies, ω_{num} , are included in Table I. In particular, Table I contains ω_{num} for each soliton that can in turn be compared to the (asymptotic) analytical prediction $\omega_o \equiv \Omega/\sqrt{2} = 0.007071$ within the so-called Thomas-Fermi

regime where $q_o \gg \Omega$ [9,67]. From left to right, each of the five groups of values in Table I corresponds to Figs. 10(a)–10(e), respectively. Additionally, the different solutions are denoted by the different zeros, k_o , identified by the scattering problem (see the notation introduced in Figs. 5–9). Evidently, the faster moving solitons ($k_o \approx c$), such as the outermost illustrated in Fig. 10(a) corresponding to the solution labeled k_4 in the first group of Table I, have the largest ω_{num} and also the maximum deviation, $\varepsilon_o = |\omega_{num} - \omega_o|/\omega_o$, from the analytical prediction. In some cases, such waves are indistinguishable from the radiation itself. For these cases, we were not able to trace the center of mass of the ensuing soliton and thus obtain its oscillation frequency. One such example corresponds to the fastest soliton shown in Fig. 10(e), whose solution k_4 is depicted in the fifth group of Table I, for which we determined ω_{num} manually. It turns out that in all cases investigated herein, the maximum discrepancy between ω_{num} and ω_o is $\varepsilon_o = 3.6\%$ (see k_4 in the first and fifth groups), while the minimum is $\varepsilon_o = 0.08\%$ (see k_7 and k_8 in the fifth column). Recalling now that ω_o is the oscillation frequency of a single dark soliton within the parabolic trap when slightly displaced from its equilibrium position, the observed discrepancies can be attributed to (i) the existence of more than one dark solitons, (ii) the interaction of the dark solitons with the sound waves emitted during the dynamics, and (iii) the interactions among one another. These effects have been studied previously in some of the above cited works, such as Refs. [28,29], and hence are not examined further here. However, we can use these previous results to very accurately describe the out-of-phase oscillations from the soliton pair shown in Fig. 10(f), for which we numerically obtained an oscillation frequency $\omega_{num} = 0.023905$. From Ref. [29] the oscillation frequency of two solitons performing small out-of-phase oscillations around their equilibrium positions reads

$$\omega_{OP}^2 = \omega_o^2 + 32q_o^2 e^{-4q_o|x_{\pm}|}, \quad (37)$$

with the equilibrium positions, x_{\pm} , given by

$$x_{\pm} = \pm \frac{1}{4q_o} w \left[\frac{32q_o^4}{\omega_o^2} \right], \quad (38)$$

where $w(z)$ is the Lambert's w function defined as the inverse of $z(w) = we^w$. Then Eq. (37) yields $\omega_{OP} = 0.024487$. This result is in very good agreement with the numerically found frequency, which presents only a relative error $\varepsilon_{OP} = 0.023$.

IV. CONCLUSIONS AND PERSPECTIVES

In this work, we have investigated the on-demand nucleation of dark soliton trains arising in a 1D repulsively interacting scalar BEC system both in the absence and in the presence of a harmonic trap. In particular, by utilizing box-shaped initial configurations, we have shown that it is possible to *a priori* predict not only the number of nucleated dark matter waves, but also their amplitudes, velocities, and positions. We have done so by initially considering the integrable version of the problem, namely, the defocusing NLS equation. For this model and for the aforementioned flexible initial wave function the direct scattering problem has been solved analytically. The direct relation of the discrete eigenvalues of the latter with the velocities and amplitudes of the

emergent dark solitons has been showcased, while the exact soliton solutions are systematically extracted via IST.

By considering a wide range of parametric selections we have shown that the number and the symmetric or asymmetric distribution of the nucleated soliton trains can be tailored upon suitable adjustment of the initial configuration parameters. In general, and in line with earlier predictions based on interference processes [31], it is found that wider box-type configurations result in larger soliton trains. However, narrower box-type configurations, resembling, in turn, phase imprinting techniques that create defects within a BEC [24], lead to smaller soliton trains. We have explored different types of configurations involving shallow boxes, as well as two entirely separated condensates. Also, asymmetrically distributed dark trains can be dynamically realized when considering, e.g., shallow OP initial configurations. Here slowly interacting dark solitons coexisting with slow and extremely fast ones arise. In all the cases considered for the integrable defocusing NLS without a trap, our analytical findings are supported by the direct dynamical evolution of the scalar system. In particular, the velocities and amplitudes of the emergent soliton trains are traced during evolution and both approach the analytical predictions asymptotically, highlighting an excellent agreement between the two. Finally we also appreciated the strength of our analytical predictions even in the presence of a harmonic trap. Our findings for all cases investigated in the latter setting closely followed the ones identified in the homogeneous setup in terms of amplitudes and velocities of the emitted dark soliton trains but upon con-

sidering the modified, in each case scenario, in-trap analytical estimates. Remarkable agreement between the analytical estimates and our numerical findings is exposed, with deviations regarding, e.g., the estimated oscillation frequency of each nucleated matter wave being less than 4%.

An immediate extension of this work points towards a richer system, consisting of two-component [8,68] or even three-component BECs [19,31]. In this regard, while recent works already considered multi-component BEC setups with box-type initial configurations [31], revealing, among other things, the generation of dark-bright solitons trains, a systematic analytical treatment of the problem is still lacking. Yet another interesting perspective would be to generalize the diagnostics utilized herein in higher dimensions. There, naturally the toolbox of integrability is no longer available. Nevertheless, in this setting, topological excitations may be expected to emerge as a result of the interference process, in the presence of suitable phase structure, as has been shown, e.g., in the experiments of Ref. [69].

ACKNOWLEDGMENTS

P.G.K. is grateful to the Leverhulme Trust and to the Alexander von Humboldt Foundation for support and to the Mathematical Institute of the University of Oxford for its hospitality. This work was funded (P.S.) by the Deutsche Forschungsgemeinschaft (DFG, German Research Foundation) SFB-925 project 170620586 and (G.B.) by the National Science Foundation (grant DMS-2009487).

-
- [1] A. Chabchoub, O. Kimmoun, H. Branger, N. Hoffmann, D. Proment, M. Onorato, and N. Akhmediev, *Phys. Rev. Lett.* **110**, 124101 (2013).
- [2] W. Tong, M. Wu, L. D. Carr, and B. A. Kalinikos, *Phys. Rev. Lett.* **104**, 037207 (2010).
- [3] V. E. Zakharov and A. B. Shabat, *Sov. Phys. JETP* **37**, 823 (1973).
- [4] J. F. Corney, P. D. Drummond, and A. Liebman, *Opt. Commun.* **140**, 211 (1997).
- [5] Y. S. Kivshar and B. Luther-Davies, *Phys. Rep.* **298**, 81 (1998).
- [6] C. J. Pethick and H. Smith, *Bose-Einstein Condensation in Dilute Gases*, 2nd ed. (Cambridge University Press, Cambridge, 2008).
- [7] L. Pitaevskii and S. Stringari, *Bose-Einstein Condensation and Superfluidity*, International Series of Monographs on Physics, Vol. 164 (Oxford University Press, New York, 2016).
- [8] C. Becker, S. Stellmer, P. Soltan-Panahi, S. Dörscher, M. Baumert, E.-M. Richter, J. Kronjäger, K. Bongs, and K. Sengstock, *Nat. Phys.* **4**, 496 (2008).
- [9] D. J. Frantzeskakis, *J. Phys. A: Math. Theor.* **43**, 213001 (2010).
- [10] P. G. Kevrekidis, D. J. Frantzeskakis, and R. Carretero-González, *The Defocusing Nonlinear Schrödinger Equation: From Dark Soliton to Vortices and Vortex Rings*, Other Titles in Applied Mathematics (Society for Industrial and Applied Mathematics, Philadelphia, 2015).
- [11] P. G. Kevrekidis, D. J. Frantzeskakis, and R. Carretero-González, *Emergent Nonlinear Phenomena in Bose-Einstein Condensates: Theory and Experiment*, Springer Series on Atomic, Optical and Plasma Physics, Vol. 45 (Springer Science & Business Media, Berlin, 2007).
- [12] I. Bloch, J. Dalibard, and W. Zwerger, *Rev. Mod. Phys.* **80**, 885 (2008).
- [13] G. Huang, M. G. Velarde, and V. A. Makarov, *Phys. Rev. A* **64**, 013617 (2001).
- [14] S. Stellmer, C. Becker, P. Soltan-Panahi, E.-M. Richter, S. Dörscher, M. Baumert, J. Kronjäger, K. Bongs, and K. Sengstock, *Phys. Rev. Lett.* **101**, 120406 (2008).
- [15] A. M. Kamchatnov and M. Salerno, *J. Phys. B: At. Mol. Opt. Phys.* **42**, 185303 (2009).
- [16] D. M. Jezek, P. Capuzzi, and H. M. Cataldo, *Phys. Rev. A* **93**, 023601 (2016).
- [17] M. A. Hofer, J. J. Chang, C. Hamner, and P. Engels, *Phys. Rev. A* **84**, 041605(R) (2011).
- [18] D. Yan, J. J. Chang, C. Hamner, M. Hofer, P. G. Kevrekidis, P. Engels, V. Achilleos, D. J. Frantzeskakis, and J. Cuevas, *J. Phys. B: At. Mol. Opt. Phys.* **45**, 115301 (2012).
- [19] T. M. Bersano, V. Gokhroo, M. A. Khamehchi, J. D'Ambroise, D. J. Frantzeskakis, P. Engels, and P. G. Kevrekidis, *Phys. Rev. Lett.* **120**, 063202 (2018).
- [20] J. Denschlag, J. E. Simsarian, D. L. Feder, C. W. Clark, L. A. Collins, J. Cubizolles, L. Deng, E. W. Hagley, K. Helmerson, W. P. Reinhardt *et al.*, *Science* **287**, 97 (2000).

- [21] B. P. Anderson, P. C. Haljan, C. A. Regal, D. L. Feder, L. A. Collins, C. W. Clark, and E. A. Cornell, *Phys. Rev. Lett.* **86**, 2926 (2001).
- [22] I. Shomroni, E. Lahoud, S. Levy, and J. Steinhauer, *Nat. Phys.* **5**, 193 (2009).
- [23] S. Burger, K. Bongs, S. Dettmer, W. Ertmer, K. Sengstock, A. Sanpera, G. V. Shlyapnikov, and M. Lewenstein, *Phys. Rev. Lett.* **83**, 5198 (1999).
- [24] Z. Dutton, M. Budde, C. Slowe, and L. V. Hau, *Science* **293**, 663 (2001).
- [25] P. Engels and C. Atherton, *Phys. Rev. Lett.* **99**, 160405 (2007).
- [26] W. P. Reinhardt and C. W. Clark, *J. Phys. B: At. Mol. Opt. Phys.* **30**, 785 (1997).
- [27] T. F. Scott, R. J. Ballagh, and K. Burnett, *J. Phys. B: At. Mol. Opt. Phys.* **31**, 329 (1998).
- [28] A. Weller, J. P. Ronzheimer, C. Gross, J. Esteve, M. K. Oberthaler, D. J. Frantzeskakis, G. Theocharis, and P. G. Kevrekidis, *Phys. Rev. Lett.* **101**, 130401 (2008).
- [29] G. Theocharis, A. Weller, J. P. Ronzheimer, C. Gross, M. K. Oberthaler, P. G. Kevrekidis, and D. J. Frantzeskakis, *Phys. Rev. A* **81**, 063604 (2010).
- [30] V. A. Brazhnyi and A. M. Kamchatnov, *Phys. Rev. A* **68**, 043614 (2003).
- [31] A. Romero-Ros, G. C. Katsimiga, P. G. Kevrekidis, and P. Schmelcher, *Phys. Rev. A* **100**, 013626 (2019).
- [32] F. Demontis, B. Prinari, C. van der Mee, and F. Vitale, *Stud. Appl. Math.* **131**, 1 (2013).
- [33] G. Biondini and B. Prinari, *Stud. Appl. Math.* **132**, 138 (2014).
- [34] G. Biondini, E. Fagerstrom, and B. Prinari, *Physica D* **333**, 117 (2016).
- [35] J. A. Espínola-Rocha and P. Kevrekidis, *Math. Comput. Simul.* **80**, 693 (2009).
- [36] S. A. Gredeskul and Y. S. Kivshar, *Phys. Rev. Lett.* **62**, 977 (1989).
- [37] G. A. Swartzlander, D. R. Andersen, J. J. Regan, H. Yin, and A. E. Kaplan, *Phys. Rev. Lett.* **66**, 1583 (1991).
- [38] E. A. Ostrovskaya, Y. S. Kivshar, Z. Chen, and M. Segev, *Opt. Lett.* **24**, 327 (1999).
- [39] S. Inouye, M. R. Andrews, J. Stenger, H.-J. Miesner, D. M. Stamper-Kurn, and W. Ketterle, *Nature (London)* **392**, 151 (1998).
- [40] C. Chin, R. Grimm, P. Julienne, and E. Tiesinga, *Rev. Mod. Phys.* **82**, 1225 (2010).
- [41] D. Krökel, N. J. Halas, G. Giuliani, and D. Grischkowsky, *Phys. Rev. Lett.* **60**, 29 (1988).
- [42] A. M. Kamchatnov, R. A. Kraenkel, and B. A. Umarov, *Phys. Rev. E* **66**, 036609 (2002).
- [43] N. I. Nikolov, D. Neshev, W. Królikowski, O. Bang, J. J. Rasmussen, and P. L. Christiansen, *Opt. Lett.* **29**, 286 (2004).
- [44] B. J. Dabrowska-Wüster, S. Wüster, and M. J. Davis, *New J. Phys.* **11**, 053017 (2009).
- [45] B. Prinari, M. J. Ablowitz, and G. Biondini, *J. Math. Phys.* **47**, 063508 (2006).
- [46] G. Biondini and E. Fagerstrom, *SIAM J. Appl. Math.* **75**, 136 (2015).
- [47] G. Biondini and D. Kraus, *SIAM J. Math. Anal.* **47**, 706 (2015).
- [48] L. Faddeev and L. Takhtajan, *Hamiltonian Methods in the Theory of Solitons* (Springer Science & Business Media, 2007).
- [49] N. Bogoliubov, *J. Phys.* **11**, 23 (1947).
- [50] T. D. Lee, K. Huang, and C. N. Yang, *Phys. Rev.* **106**, 1135 (1957).
- [51] L. Dobrek, M. Gajda, M. Lewenstein, K. Sengstock, G. Birkel, and W. Ertmer, *Phys. Rev. A* **60**, R3381 (1999).
- [52] B. Wu, J. Liu, and Q. Niu, *Phys. Rev. Lett.* **88**, 034101 (2002).
- [53] A. R. Fritsch, M. Lu, G. H. Reid, A. M. Piñeiro, and I. B. Spielman, *Phys. Rev. A* **101**, 053629 (2020).
- [54] G. A. El and M. A. Hoefer, *Physica D* **333**, 11 (2016).
- [55] Y. Kodama and S. Wabnitz, *Opt. Lett.* **20**, 2291 (1995).
- [56] G. B. Whitham, *Linear and Nonlinear Waves* (John Wiley & Sons, 1974).
- [57] M. V. Pavlov, *Theor. Math. Phys.* **71**, 584 (1987).
- [58] V. Gurevich and A. L. Krylov, *Sov. Phys. JETP* **65**, 944 (1987).
- [59] G. A. El, V. V. Geogjaev, A. V. Gurevich, and A. L. Krylov, *Physica D* **87**, 186 (1995).
- [60] M. A. Hoefer, M. J. Ablowitz, I. Coddington, E. A. Cornell, P. Engels, and V. Schweikhard, *Phys. Rev. A* **74**, 023623 (2006).
- [61] M. A. Hoefer, M. J. Ablowitz, and P. Engels, *Phys. Rev. Lett.* **100**, 084504 (2008).
- [62] G. Biondini and Y. Kodama, *J. Nonlinear Sci.* **16**, 435 (2006).
- [63] M. A. Hoefer and M. J. Ablowitz, *Physica D* **236**, 44 (2007).
- [64] M. G. Forest and J.-E. Lee, in *Oscillation Theory, Computation, and Methods of Compensated Compactness*, IMA Volumes in Mathematics and Its Applications (IMA, Vol. 2), edited by C. Dafermos, J. L. Ericksen, D. Kinderlehrer, and M. Slemrod (Springer, New York, 1986), pp. 35–69.
- [65] G. C. Katsimiga, S. I. Mistakidis, G. M. Koutentakis, P. G. Kevrekidis, and P. Schmelcher, *Phys. Rev. A* **98**, 013632 (2018).
- [66] G. C. Katsimiga, S. I. Mistakidis, T. M. Bersano, M. K. H. Ome, S. M. Mossman, K. Mukherjee, P. Schmelcher, P. Engels, and P. G. Kevrekidis, *Phys. Rev. A* **102**, 023301 (2020).
- [67] T. Busch and J. R. Anglin, *Phys. Rev. Lett.* **84**, 2298 (2000).
- [68] G. C. Katsimiga, P. G. Kevrekidis, B. Prinari, G. Biondini, and P. Schmelcher, *Phys. Rev. A* **97**, 043623 (2018).
- [69] D. R. Scherer, C. N. Weiler, T. W. Neely, and B. P. Anderson, *Phys. Rev. Lett.* **98**, 110402 (2007).

On-demand generation of dark-bright soliton trains in Bose-Einstein condensates

A. Romero-Ros,¹ G. C. Katsimiga,^{1,2} P. G. Kevrekidis,³ B. Prinari,⁴ G. Biondini,^{4,5} and P. Schmelcher^{1,2}

¹Center for Optical Quantum Technologies, Department of Physics, University of Hamburg,
Luruper Chaussee 149, 22761 Hamburg, Germany

²The Hamburg Centre for Ultrafast Imaging, University of Hamburg, Luruper Chaussee 149, 22761 Hamburg, Germany

³Department of Mathematics and Statistics, University of Massachusetts Amherst, Amherst, Massachusetts 01003-4515, USA

⁴Department of Mathematics, State University of New York, Buffalo, New York 14260, USA

⁵Department of Physics, State University of New York, Buffalo, New York 14260, USA



(Received 23 September 2021; accepted 25 January 2022; published 24 February 2022)

The controlled creation of dark-bright (DB) soliton trains in multicomponent Bose-Einstein condensates (BECs) is a topic of ongoing interest. In this work we generalize earlier findings on the creation of dark soliton trains in single-component BECs [A. Romero-Ros *et al.*, *Phys. Rev. A* **103**, 023329 (2021)] to two-component BECs. By choosing suitable *filled* box-type initial configurations (FBTCs) and solving the direct scattering problem for the defocusing vector nonlinear Schrödinger equation with nonzero boundary conditions we obtain analytical expressions for the DB soliton solutions produced by a general FBTC. It is found that the size of the initial box and the amount of filling directly affect the number, size, and velocity of the solitons, while the initial phase determines the parity (even or odd) of the solutions. Our analytical results are compared to direct numerical integration of the coupled Gross-Pitaevskii equations, both in the absence and in the presence of a harmonic trap, and an excellent agreement between the two is demonstrated.

DOI: [10.1103/PhysRevA.105.023325](https://doi.org/10.1103/PhysRevA.105.023325)

I. INTRODUCTION

Nonlinear phenomena in Bose-Einstein condensates (BECs) have become a focus of attention during the last couple of decades [1,2], and solitary waves stemming from the balance between dispersion and the nonlinearities of the system have been a topic of intense investigation [3]. In single-component BECs, these macroscopic nonlinear excitations can have the form of local density suppressions (dark solitons [3,4]) or local density humps (bright solitons [5]) depending on whether the nonlinear interaction is repulsive or attractive, respectively.

The experimental realization of two-component BECs [6–8] has opened a window towards the study of more complex solitonic structures [9–18]. In repulsive two-component BECs, a fundamental excitation takes the form of a dark-bright (DB) soliton [9]. A single DB soliton consists of a dark soliton that acts as an effective potential in which the bright soliton is trapped and, consequently, waveguided. Importantly, bright solitons cannot be sustained (unless under such waveguiding) in self-repulsive BECs. The concept of waveguiding has its origin in nonlinear optics [19,20] (see also references therein), where DB solitons have been an active topic of theoretical and experimental research [21–23]. In this context, the DB soliton dynamics is described by the defocusing vector nonlinear Schrödinger (VNLS) equation [3], while in the context of BECs DB solitons similarly obey the so-called coupled Gross-Pitaevskii equation (CGPE) [1,24,25].

The first experimental realizations of DB solitons in BECs almost a decade ago [13,26–30], as well as subsequent experimental realizations of their variants and generalizations

[14,18,31–34], have motivated a significant amount of interest in studying their dynamics and interactions [17,35–47]. In particular, several methods have been proposed to create DB soliton structures. For instance, the combination of phase imprinting techniques [48,49], to create the dark soliton, and a local population transfer by means of a Raman process [50], to create the bright counterpart, allows the creation of individual DB solitons [26]. Other population transfer methods demonstrated how an alternating spatial distribution of the two components, via the creation of a winding pattern, can lead to the formation of DB soliton trains [30]. Additionally, counterflow techniques which involve a dynamical mixing of both components also give rise to DB soliton trains [13,29]. More recently, the controllable creation of DB pairs could generate the conditions for a systematic observation and measurement of their interactions, including in BECs with a higher (e.g., three) number of components [34].

Following the counterflow concept, matter-wave interference methods have been highly used in single-component BECs to generate dark soliton trains [51–55]. This method is based on the collision of two separated condensates, and allows for the systematic nucleation of a desired number of solitonic entities upon tailoring the initial separation of the colliding condensates and their relative phase. In this counterflow setting, exact results were originally derived for the defocusing NLS equation in the seminal work of Ref. [56] for a box-type pulse by means of the inverse scattering transform (IST) [57–61]. More recently, some theoretical works have exploited the integrable nature of the defocusing VNLS model and further developed an IST formalism with non-zero-boundary conditions (NZBC) [41,62,63].

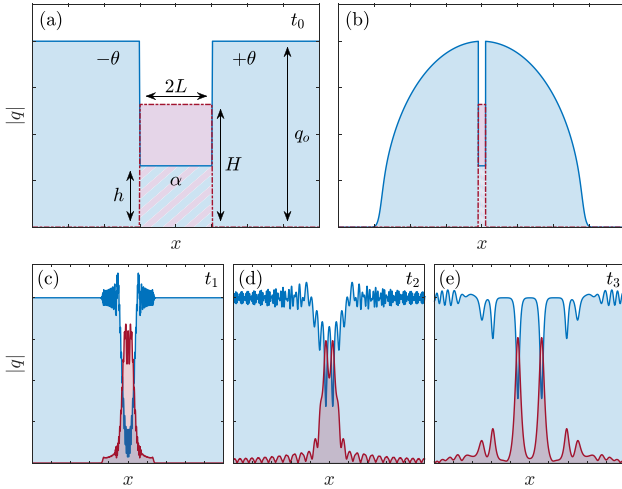


FIG. 1. Schematic illustration of the box-type configuration utilized herein, for arbitrary L , q_0 , θ , h , α , and H in the absence (a) and in (b) the presence of a harmonic trapping potential. Here, L is the parameter that controls the separation between the two sides of the box which play the role of the two colliding condensates in a matter-wave interference process. The matter-wave interference process is also schematically illustrated through snapshots in (c), (d), and (e) at times $t_1 < t_2 < t_3$, respectively. Note that the quantities shown are measured in transverse oscillator units.

In view of our previous work in single-component BECs [64] and the analytical tools provided by the direct scattering method and the IST with NZBC, in this work we exploit the unprecedented level of control that the ultracold environment offers [6–8,65,66] to study the response of a two-component, one-dimensional (1D), harmonically trapped BEC with repulsive intracomponent and intercomponent interactions, when a general *filled* box-type configuration (FBTC) is considered as an initial condition. In particular, in our setup the wave function of the first component is a box-type pulse whose sides play the role of the two colliding condensates in the matter-wave interference mechanism. On the other hand, the wave function of the second component is an inverted box that *fills* the space between the two sides of the box of the first component (see Fig. 1). A somewhat similar configuration (albeit with differences in the bright component) was considered in nonlinear optics to study vector soliton interaction dynamics [22]. First, we consider the integrable version of the problem, i.e., the defocusing VNLS equation with NZBC. Here, we solve analytically the direct scattering problem for the aforementioned box-type configuration and provide the discrete eigenvalues of the scattering problem for distinct parametric variations. The latter characterize the amplitudes and velocities of the ensuing DB solitons, whose exact waveform can be then extracted via the IST.

Having at hand the exact analytical expressions for the DB solitons, we then compare them with direct numerical simulations of the CGPE with a FBTC in the absence of confinement, finding remarkable agreement, as should be expected on the basis of the exact nature of the IST analysis. Moreover, to showcase the broader, as well as physical relevance of our results, we extend our analytical findings to the

case involving the presence of a harmonic confinement. Using the expressions for the eigenvalues from the direct scattering problem, we design analytical estimates to describe the in-trap oscillation dynamics of the generated DB solitons. Here, we provide explicit expressions accounting for the oscillating size of the dark and bright counterparts of a DB soliton in a trap. The latter is a feature that is absent in the single-component case, which we attribute to the intercomponent interaction. An excellent agreement between the analytical estimates and the numerical simulations confirms the extension of the predicted solutions of the direct scattering problem from the homogeneous setup to the harmonically trapped scenario. This also justifies the particular relevance and usefulness of the detailed IST analysis of the integrable case with a view towards the more physically relevant confined setting.

Our presentation is organized as follows. In Sec. II we introduce the model and solve the direct scattering problem for the defocusing VNLS equation with a general FBTC. Additionally, we discuss some analytical considerations regarding the eigenvalues of the scattering problem and the DB soliton solution. In Sec. III we present our findings. First, we extract the eigenvalues of the scattering problem for a wide range of different initial configurations. Then, we perform a direct comparison between our analytical findings and the numerical integration of the CGPE, both in the absence and in the presence of a harmonic trap. Finally, in Sec. IV we summarize our results and discuss possible directions for future study. In Appendix A we provide further details on the DB soliton solutions. In Appendix B we describe the change of amplitude of oscillating DB solitons in the presence of a trap.

II. NONLINEAR SCHRÖDINGER EQUATION AND DARK-BRIGHT SOLITON SOLUTION

We consider a one-dimensional (1D) pseudospinor BEC consisting of two different spin states, e.g., $|F, m\rangle = |1, -1\rangle$ and $|F, m\rangle = |2, 2\rangle$, of the same atomic species of ^{87}Rb [6], confined in a highly anisotropic trap with longitudinal and transverse trapping frequencies satisfying the relation $\omega_x \ll \omega_\perp$. In such a cigar-shaped geometry, the condensate wave function along the transverse direction, being the ground state of the respective harmonic oscillator, can be integrated out. This, in turn, leads to the following pair of coupled Gross-Pitaevskii equations (CGPEs) [3]:

$$i\hbar\partial_t\Psi_j = \mathcal{H}_0\Psi_j + \sum_{k=1}^2 g_{jk}^{(1D)}|\Psi_k|^2\Psi_j, \quad (1)$$

with $j = 1, 2$, which, in the mean-field framework, governs the BEC dynamics for the longitudinal part of the wave function. In the above expression, $\mathcal{H}_0 = -\frac{\hbar^2}{2m}\partial_x^2 + V(x)$ is the single-particle Hamiltonian, where m denotes the atomic mass and $V(x) = m\omega_x^2 x^2/2$ denotes the external harmonic potential. Also, $g_{jk}^{(1D)} = 2a_{jk}\hbar^2/ma_\perp^2$ accounts for the effective one-dimensional repulsive interaction strengths, with $a_{jk} > 0$ denoting the 1D scattering length and $a_\perp = \sqrt{\hbar/m\omega_\perp}$ being the transverse harmonic oscillator length. Under the following transformations, $\tilde{t} = t\omega_\perp$, $\tilde{x} = x a_\perp^{-1}$, and $\tilde{q}_j = \Psi_j \sqrt{2a_\perp}$,

Eq. (1) can be rewritten in the dimensionless form

$$i\partial_t q_j = \left[-\frac{1}{2}\partial_x^2 + \frac{1}{2}\Omega^2 x^2 \right] q_j + \sum_{k=1}^2 g_{jk}^{(1D)} |q_k|^2 q_j. \quad (2)$$

Here, $\Omega \equiv \omega_x/\omega_\perp$ and $g_{jk}^{(1D)} = a_{jk}/a_\perp$. Note that for convenience we dropped the tildes and that energy, time, and length are now measured in units of $\hbar\omega_\perp$, ω_\perp^{-1} , and $a_\perp = \sqrt{\hbar/m\omega_\perp}$, respectively.

In this work, we consider $g_{jk}^{(1D)} = 1$, i.e., we work with the classical Manakov model [67] in the case of the absence of confinement. Then, Eq. (2), with $\Omega = 0$, reduces to the vector nonlinear Schrödinger (VNLS) equation, namely,

$$i\mathbf{q}_t + \frac{1}{2}\mathbf{q}_{xx} - \|\mathbf{q}\|^2\mathbf{q} = 0, \quad (3)$$

to which we can further perform the rescaling $\tilde{\mathbf{q}}(x, t) = \mathbf{q}(\sqrt{2}x, t) \exp -2iq_o^2 t$ that leads, by dropping the tilde, to

$$i\mathbf{q}_t + \mathbf{q}_{xx} - 2(\|\mathbf{q}\|^2 - q_o^2)\mathbf{q} = 0, \quad (4)$$

which is subject to the following time-independent NZBC at infinity:

$$\lim_{x \rightarrow \pm\infty} \mathbf{q}(x, t) = \mathbf{q}_\pm = \mathbf{q}_o e^{i\theta_\pm}. \quad (5)$$

Hereafter, $\mathbf{q} \equiv \mathbf{q}(x, t)$ and \mathbf{q}_o are two-component vectors, $\|\cdot\|$ is the standard Euclidean norm, $q_o = \|\mathbf{q}_o\| > 0$, θ_\pm are real numbers, and subscripts x and t denote partial differentiation with respect to space and time hereafter.

Building on our recent investigation of scalar BECs [64], here we consider a box-type initial configuration in the first component whose *box* is being filled by the second component (so that the latter can induce the formation of bright solitons) in the following manner:

$$\mathbf{q}(x, 0) = \begin{cases} (q_o e^{-i\theta}, 0)^T, & x < -L \\ (h e^{i\alpha}, H)^T, & |x| < L \\ (q_o e^{i\theta}, 0)^T, & x > L. \end{cases} \quad (6)$$

A schematic illustration of Eq. (6) is given in Fig. 1(a). Here, $0 \leq h \leq q_o$ refers to the height of the box of the first component, and $0 \leq H \leq q_o$ refers to the height of the filling box of the second component. q_o is the amplitude of the box, θ_\pm are the phases on each side of the box, and α is the phase of the first component inside the box. The phase invariance of the VNLS equation allowed us to define $\theta_+ = -\theta_- = \theta$ without loss of generality in Eq. (6). For convenience, we further introduce the quantities

$$\Delta\theta = 2\theta, \quad \Delta\theta_- = \theta + \alpha, \quad \Delta\theta_+ = \theta - \alpha \quad (7)$$

to denote the distinct phase differences in each of the different regions of the box. We will refer to the cases $\Delta\theta = 0$ and $\Delta\theta = \pi$ as in-phase (IP) and out-of-phase (OP) configurations, respectively, and to the special case having $h = 0$ as the “zero-box” configuration, which describes the absence of atoms of the first component inside the box.

Additionally, L corresponds to the half-width of the box and it is the parameter that controls the distance between the two sides of the box playing the role of the two colliding condensates in the matter-wave interference mechanism. A schematic illustration of the latter is shown through snapshots in Figs. 1(c)–1(e) at $t_1 < t_2 < t_3$, respectively. At t_1 the two

sides of the box are spreading towards each other and form an interference pattern inside the box. Then, at t_2 , some of the fringes formed due to the interference process stabilize and start acting as effective potentials for the second component filling the box. Finally, at t_3 the stabilized fringes develop into dark solitons, while the second component trapped inside the latter becomes bright solitons, giving rise to a DB soliton train.

A. Direct scattering problem

The defocusing VNLS equation [see Eq. (4)] corresponds to a coupled system of integrable nonlinear partial differential equations that can be solved analytically by means of the IST in terms of a Lax pair. The 3×3 Lax pair associated with Eq. (4) is

$$\phi_x = \mathbf{X}\phi, \quad \phi_t = \mathbf{T}\phi, \quad (8)$$

where ϕ is a 3×3 matrix eigenvector,

$$\mathbf{X}(x, t, k) = ik\mathbf{J} + \mathbf{Q}, \quad (9)$$

$$\mathbf{T}(x, t, k) = 2ik^2\mathbf{J} - i\mathbf{J}(\mathbf{Q}_x - \mathbf{Q} + q_o^2) - 2k\mathbf{Q}, \quad (10)$$

with

$$\mathbf{J} = \begin{pmatrix} -1 & \mathbf{0}^T \\ \mathbf{0} & \mathbf{I} \end{pmatrix}, \quad \mathbf{Q}(x, t) = \begin{pmatrix} 0 & \mathbf{q}^T \\ \mathbf{q}^* & 0 \end{pmatrix}, \quad (11)$$

and \mathbf{I} and $\mathbf{0}$ are the appropriately sized identity and zero matrix, respectively. The first equation in Eq. (8) is referred to as the scattering problem and $k \in \mathbb{C}$ as the scattering parameter.

Under fairly general conditions on $\mathbf{q}(x, t)$, as $x \rightarrow \pm\infty$ the solutions of the direct scattering problem are approximated by those of the asymptotic scattering problems $\phi_x = \mathbf{X}_\pm\phi$, where $\mathbf{X}_\pm = ik\mathbf{J} + \mathbf{Q}_\pm$ and $\mathbf{Q}_\pm = \lim_{x \rightarrow \pm\infty} \mathbf{Q}(x, t)$. The eigenvalues of \mathbf{X}_\pm are ik and $\pm i\lambda$, where

$$\lambda(k) = \sqrt{k^2 - q_o^2}. \quad (12)$$

These eigenvalues have branch points, and therefore we introduce the two-sheeted Riemann surface defined by $\lambda(k)$. As in Refs. [60–62, 68], we take the branch cut along the semilines $(-\infty, -q_o)$ and (q_o, ∞) , and we label those sheets such that $\text{Im } \lambda(k) \geq 0$ on sheet I and $\text{Im } \lambda(k) \leq 0$ on sheet II.

We also define the Jost solutions $\phi_\pm(x, t, k)$ as the simultaneous solutions of both parts of the Lax pair satisfying the boundary conditions

$$\phi_\pm(x, t, k) \equiv \mathbf{Y}_\pm(k) e^{i\Theta(x, t, k)} + \mathcal{O}(1) \quad (13)$$

as $x \rightarrow \pm\infty$, where $\Theta(x, t, k) = \Lambda x - \Omega t$ with $\Lambda = \text{diag}(-\lambda, k, \lambda)$, $\Omega = \text{diag}(2k\lambda, -(k^2 + \lambda^2), -2k\lambda)$, and $\mathbf{Y}_\pm(k)$ are the simultaneous eigenvector matrices of \mathbf{X}_\pm and $\mathbf{T}_\pm = \lim_{x \rightarrow \pm\infty} \mathbf{T}(x, t, k)$. The two sets of Jost solutions are related to each other through the scattering relation

$$\phi_-(x, t, k) = \phi_+(x, t, k)\mathbf{S}(k), \quad (14)$$

valid for all $k \in (-\infty, -q_o) \cup (q_o, \infty)$. Moreover, the fact that ϕ_\pm are simultaneous solutions of both parts of the Lax pair implies that the scattering coefficients and the discrete eigenvalues of the scattering operator are time independent. Therefore, hereafter we will consider the scattering problem at $t = 0$ and we will omit the time dependence from the eigenfunctions.

At $t = 0$ the scattering problem in each of the three regions $x < -L$, $|x| < L$, and $x > L$ takes the form $\phi_x = (ik\mathbf{J} + \mathbf{Q}_j)\phi$ with the index $j = c, \pm$ and constant potentials \mathbf{Q}_\pm and \mathbf{Q}_c given by

$$\mathbf{Q}_\pm = \begin{pmatrix} 0 & q_0 e^{\pm i\theta} & 0 \\ q_0 e^{\mp i\theta} & 0 & 0 \\ 0 & 0 & 0 \end{pmatrix}, \quad (15a)$$

$$\mathbf{Q}_c = \begin{pmatrix} 0 & he^{i\alpha} & H \\ he^{-i\alpha} & 0 & 0 \\ H & 0 & 0 \end{pmatrix}. \quad (15b)$$

One can then easily find explicit solutions for the scattering problem in each of the aforementioned regions, namely,

$$\varphi_l(x, k) = \mathbf{Y}_-(k)e^{i\lambda x}, \quad x \leq -L \quad (16a)$$

$$\varphi_c(x, k) = \mathbf{Y}_c(k)e^{iMx}, \quad |x| \leq L \quad (16b)$$

$$\varphi_r(x, k) = \mathbf{Y}_+(k)e^{i\lambda x}, \quad x \geq L \quad (16c)$$

where $\mathbf{M} = \text{diag}(-\mu, k, \mu)$, $\mu = \sqrt{k^2 - (h^2 + H^2)}$, and

$$\mathbf{Y}_\pm(k) = \begin{pmatrix} \lambda + k & 0 & \lambda - k \\ iq_0 e^{\mp i\theta} & 0 & -iq_0 e^{\mp i\theta} \\ 0 & iq_0 e^{\pm i\theta} & 0 \end{pmatrix}, \quad (17a)$$

$$\mathbf{Y}_c(k) = \begin{pmatrix} \mu + k & 0 & \mu - k \\ ihe^{-i\alpha} & -iH & -ihe^{-i\alpha} \\ iH & ihe^{i\alpha} & -iH \end{pmatrix}. \quad (17b)$$

Equations (16) yield explicit representations for the Jost solutions $\phi_\pm(x, 0, k)$ in their respective regions, i.e., $\phi_-(x, 0, k) \equiv \varphi_l(x, k)$ for $x \leq -L$, and $\phi_+(x, 0, k) \equiv \varphi_r(x, k)$ for $x \geq L$. At the boundary of each region one can express the fundamental solution on the left as a linear combination of the fundamental solution on the right, and vice versa. In particular, we can introduce scattering matrices $\mathbf{S}_-(k)$ and $\mathbf{S}_+(k)$ such that

$$\varphi_-(-L, k) = \varphi_c(-L, k)\mathbf{S}_-(k), \quad (18a)$$

$$\varphi_c(L, k) = \varphi_+(L, k)\mathbf{S}_+(k). \quad (18b)$$

As a consequence, we can express the scattering matrix $\mathbf{S}(k)$ relating the Jost solutions $\phi_\pm(x, k)$ as

$$\begin{aligned} \mathbf{S}(k) &= \mathbf{S}_+(k)\mathbf{S}_-(k) \\ &= e^{-i\lambda L}\mathbf{Y}_+^{-1}\mathbf{Y}_c e^{2iML}\mathbf{Y}_c^{-1}\mathbf{Y}_- e^{-i\lambda L}. \end{aligned} \quad (19)$$

Computing the right-hand side of Eq. (19), we obtain the following expression for the first element, $s_{11}(k)$, of the scattering matrix $\mathbf{S}(k)$:

$$\begin{aligned} &4\lambda\mu q_0 (h^2 + H^2) e^{-2i\lambda L} s_{11}(k) \\ &= 4ih(h^2 + H^2) q_0^2 e^{i\theta} \cos \alpha \sin(2\mu L) \\ &\quad + 2q_0 h^2 e^{2i\theta} (\lambda - k) [\mu \cos(2\mu L) + ik \sin(2\mu L)] \\ &\quad + 2q_0 (h^2 + H^2) (\lambda + k) [\mu \cos(2\mu L) - ik \sin(2\mu L)] \\ &\quad + 2q_0 \mu H^2 (\lambda - k) e^{2i\theta} e^{2ikL}. \end{aligned} \quad (20)$$

The discrete eigenvalues of the scattering problem are the zeros of $s_{11}(k)$ for all $k \in \mathbb{C}$ with $\text{Im } \lambda(k) > 0$, where $s_{11}(k)$ is analytic [62]. It is important to remark that, in general, for the

defocusing VNLS equation the eigenvalues of the scattering problem are not only single zeros, but double zeros can also occur [61]. However, for the particular configuration used in this work [see Eq. (6)] all zeros will turn out to be simple.

B. Dark-bright soliton solution

In view of the inverse problem, it is convenient to introduce a uniformization variable z defined by

$$z = k + \lambda, \quad (21)$$

which is inverted by

$$k = \frac{1}{2} \left(z + \frac{q_0^2}{z} \right), \quad \lambda = \frac{1}{2} \left(z - \frac{q_0^2}{z} \right). \quad (22)$$

Thereby, sheets I and II of the Riemann surface are mapped onto the upper- and lower-half planes of the complex z plane, respectively; the continuous spectrum is [i.e., the semi-lines $(-\infty, -q_0) \cap (q_0, \infty)$ are] mapped onto the real z axis, while the spectral gaps $(-q_0, q_0)$ on both sheets are mapped onto the circle of radius q_0 (see Ref. [62] for further details). The discrete eigenvalues are found as zeros of $s_{11}(z) := s_{11}(k(z), \lambda(z))$, and in this case a zero of $s_{11}(z)$ on the upper semicircle of radius q_0 corresponds to a dark-dark soliton, i.e., a dark soliton in each component, while a zero inside the upper semicircle of radius q_0 corresponds to a DB soliton. In the presence of a single such zero, the inverse scattering problem yields the following DB soliton solution [62]:

$$\begin{aligned} q_d(x, t) &= \{q_0 \cos \beta_0 - iq_0 \sin \beta_0 \\ &\quad \times \tanh[v_0(x - x_0 + 2\xi_0 t)]\} e^{i(\beta_0 + \varphi_d + 2q_0^2 t)}, \end{aligned} \quad (23a)$$

$$\begin{aligned} q_b(x, t) &= -i \sin \beta_0 \sqrt{q_0^2 - |z_0|^2} \\ &\quad \times \text{sech}[v_0(x - x_0 + 2\xi_0 t)] e^{i(\xi_0 x - (\xi_0^2 - v_0^2)t + \varphi_b + 2q_0^2 t)}, \end{aligned} \quad (23b)$$

as a solution of Eq. (4). Here, q_d is the dark soliton component and q_b is the bright one. Also, x_0 is the center of the soliton and $\varphi_{d,b}$ are arbitrary constant phases. The DB solution of Eq. (23) is expressed in terms of the spectral parameter $z_0 = |z_0| e^{i\beta_0} \equiv \xi_0 + i v_0$, with

$$\xi_0 = |z_0| \cos \beta_0, \quad v_0 = |z_0| \sin \beta_0. \quad (24)$$

Therefore, the relevant soliton parameters can be uniquely specified in terms of z_0 , i.e.,

$$A_d = q_0 \sin \beta_0 \equiv \frac{q_0}{|z_0|} \text{Im } z_0, \quad (25a)$$

$$A_b = \sqrt{q_0^2 - |z_0|^2} \sin \beta_0 \equiv \text{Im } z_0 \sqrt{\frac{q_0^2}{|z_0|^2} - 1}, \quad (25b)$$

$$v = -2|z_0| \cos \beta_0 \equiv -2 \text{Re } z_0, \quad (25c)$$

where A_d and A_b are the dark and bright soliton amplitudes, respectively, and v denotes the DB soliton velocity.

Equivalently, the soliton parameters can be directly expressed in terms of k_0 (see Appendix A). Given a zero k_0 , one can substitute $z_0 = k_0 + \lambda_0$ into Eqs. (25) with the caveat that $\lambda_0 = \sqrt{k_0^2 - q_0^2}$ must be chosen with the appropriate branch

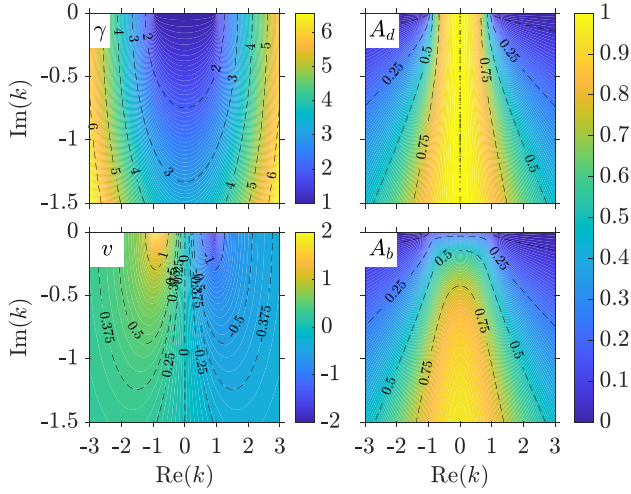


FIG. 2. γ and the soliton parameter amplitudes A_d , A_b , and velocity v as functions of the scattering parameter k for $q_o = 1$. Note that the quantities shown are measured in transverse oscillator units.

cut, and on the appropriate branch where $\text{Im } \lambda_o > 0$. Then, Eqs. (25) become

$$A_d = \frac{2\gamma \text{Im } \lambda_o}{\gamma^2 + 1}, \quad (26a)$$

$$A_b = -\frac{2 \text{Im } k_o}{\sqrt{\gamma^2 - 1}}, \quad (26b)$$

$$v = -\frac{4 \text{Re } k_o}{1 + \gamma^2}, \quad (26c)$$

where

$$\gamma = \frac{q_o}{|z_o|} > 1.$$

To get some physical insight on the DB solutions, we illustrate in Fig. 2 the dependence parameters γ , A_d , A_b , and v on the scattering parameter k , for the solutions provided by Eq. (A5b) and for $q_o = 1$. Here, one can see that indeed $\gamma > 1 \forall k$. Also, $A_d \leq q_o \forall k$, as expected, since dark solitons cannot have amplitudes greater than the background. Similarly, $A_b < A_d \forall k$. Obviously, larger (deeper) dark solitons can host larger bright solitons, but in turn the DB soliton itself becomes slower. In fact, v has a minimum ($v = 0$) at $\text{Re } k_o = 0$, where A_d has a maximum ($A_d = q_o$). The latter is known as a black soliton, and it can host a bright soliton of any smaller size, which explains why v and A_d are independent of $\text{Im } k$ at $\text{Re } k = 0$. On the other hand, v always has its maximum (absolute) value at $k = 2q_o$, coinciding with the speed of sound of the condensate $c = 2q_o$ [note that $c = \sqrt{gn}$ [69,70], where n is the peak density of the BEC, in the dimensionless units adopted herein for the CGPE (2)]. Yet, no soliton solution exists with $v = c$. Further details on the soliton parameters are discussed in Sec. III A.

III. DARK-BRIGHT SOLITON GENERATION AND DYNAMICS

A. Analytical results for the discrete spectrum

In this section, we aim at finding the zeros of $s_{11}(k)$ [see Eq. (20)] and analytically characterizing the DB solitons produced by the FBTC in Eq. (6), upon considering different variations of the system parameters. In particular, our initial FBTC is defined by six different parameters: the half-width L , the amplitude q_o , the side phases $\pm\theta$, the height h of the first component in the box, its phase α , and the filling of the second component in the box H . The corresponding values of our parameter exploration are the following:

$$L \in [1, 9], \quad \theta = \left\{ 0, \frac{\pi}{2} \right\},$$

$$h \in [0, q_o], \quad \alpha = \{0, \pi\}, \quad H \in [0, q_o],$$

together with $q_o = 1$. Furthermore, we introduce the filling angle $\sigma \in [0, \pi]$, which relates the heights h and H with the amplitude background q_o as follows:

$$h = q_o \cos \sigma, \quad (27a)$$

$$H = q_o \sin \sigma. \quad (27b)$$

Introducing σ allows us to explore different filling configurations using a single parameter. Notice that $h > 0$ in the regime $0 \leq \sigma < \pi/2$, while $h < 0$ in the regime $\pi/2 < \sigma \leq \pi$, which is equivalent to $h = |q_o \cos \sigma| > 0$ with $\alpha = \pi$ (see Fig. 1).

Since we are mostly interested in effects driven by the presence of the second component, we choose σ as our main parameter. We are also interested in considering the effect of distinct initial configurations, and we take L as our second representative parameter since it controls the separation between the colliding sides of the condensate. Thus, below we will vary σ for different values of L , denoting such variation as $L[\sigma]$.

To classify all spectra, we choose two different case scenarios. The first one consists of a zero-box configuration ($h = 0$), where the second component is the only component present inside the box. The second case is a full-box configuration, with the box being fully filled either by a single or by both components, i.e., $q_o^2 = h^2(\sigma) + H^2(\sigma)$ [see Eqs. (27)]. We start exploring IP-FBTCs ($\theta = 0$), followed by OP-FBTCs ($\theta = \pi/2$).

The corresponding spectra of zeros are presented in Figs. 3, 5, 6, and 8. All these figures share the same arrangement. In particular, each figure consists of 10 panels, (a)–(j), distributed along two rows and five columns. The latter correspond to five different values of L , ranging from $L = 1$ to 9. The top row shows the zeros of $s_{11}(k)$ in the $\text{Re } k$ - σ plane with $\text{Im } k$ depicted as a color gradient in a logarithmic scale. This representation provides a clearer disposition of the zeros. Additionally, zeros corresponding to $\alpha = 0$ ($\alpha = \pi$) are shown on a white (gray) background [see, e.g., Fig. 3 (Fig. 6)]. In contrast, bottom-row panels depict the zeros in the complex k plane, which can be directly mapped onto Fig. 2, containing the relevant physical information of the solitons, such as their amplitudes and velocities. In this case, σ is illustrated as a color gradient. Blue tones ($0 \leq \sigma \leq \pi/2$) correspond to

$\alpha = 0$, while red tones ($\pi/2 \leq \sigma \leq \pi$) correspond to $\alpha = \pi$. Recall that, in all cases, σ is the main varying parameter and both rows can be easily compared by following their common $\text{Re } k$ axis. Also, when looking at the zeros, e.g., in Fig. 3, one should keep in mind that in this system under consideration the zeros are single valued, i.e., $k_i \neq k_j$, where i, j denote different zeros, for any choice of parameters (see Sec. II A). This means that although some of the zeros appear to be on top of each other they never intersect, i.e., coincide, which is the case since our two-dimensional representation of the zeros, e.g., in Fig. 3, is a projection of a three-dimensional space ($\text{Re } k, \text{Im } k, \sigma$). Finally, if both spatial and phase symmetries of the FBTC are preserved, the zeros appear in pairs k_{\pm} , i.e., $\text{Re } k_+ = -\text{Re } k_-$ and $\text{Im } k_+ = \text{Im } k_-$. Note that the FBTC is always spatially symmetric [see Eq. (6)], and thus only FBTCs with $\theta \neq 0$ and $h \neq 0$ can present asymmetric solutions (Fig. 8). In those cases, we say that the phase symmetry of the system is broken.

Therefore, whenever $\theta = 0$ (Figs. 3 and 6) or both symmetries are preserved (Fig. 5), only k_o with $\text{Re } k_o \geq 0$ are shown.

1. Zero-box configuration

For the zero-box configuration we set $h = 0$, so that only the second component is present inside the box of the FBTC. At the same time, for our particular choice of parameters, the FBTC preserves both spatial and phase symmetries, independently of θ , and thus also do its solutions. In particular, IP-FBTCs ($\theta = 0$) always present an even number of paired zeros (k_{\pm}). On the other hand, for this zero-box configuration, OP-FBTCs ($\theta = \pi/2$) always possess a particular zero, $k_0 \in \mathbb{I}$, which is unpaired, resulting in an odd number of zeros. More specifically, as we later explain, k_0 corresponds to a

static DB soliton, with the dark counterpart being a so-called black soliton ($v = 0$ and $A_d = q_o$). Also note the distinct subscript 0 used when compared to o introduced for a general solution.

a. In-phase background. We begin by exploring the spectra of an IP zero-box configuration, for which $q_o = 1$, $\theta = 0$, and $h = 0$ ($\alpha = 0$) are held fixed. Additionally, $L \in [1, 9]$ and $\sigma \in [0, \pi/2]$, and thus $H(\sigma) \in [0, q_o]$. The corresponding spectra of zeros are presented in Fig. 3.

From Figs. 3(a)–3(e) (top row), it can be directly inferred that increasing L increases the number of zeros, and thus the number of solitons, an outcome analogous to the single-component case [64]. In particular, $L = 1$ has only one pair of zeros, k_1 , while $L = 5$ has up to four pairs, k_1, \dots, k_4 , and $L = 9$ has up to six pairs, k_1, \dots, k_6 . On the other hand, increasing σ (or equivalently increasing H) reduces the number of zeros. For example, in Fig. 3(c) the spectrum of solutions goes from four pairs of zeros at $\sigma = 0$ ($H = 0$) to two at $\sigma = \pi/2$ ($H = 1$). Here, k_4 ceases to exist right above $\sigma = \pi/8$, and k_3 is absent for $\sigma > 3\pi/8$. We attribute this effect to an increase of the second component in the box, hindering the emergence of solitonic structures due to the repulsive intercomponent interaction.

It is also important to understand how these parametric variations affect the characteristics of the solitonic entities, in particular their amplitudes and velocities [see Eq. (26)]. In this regard, Figs. 3(f)–3(j) (bottom row) are key towards easily mapping the zeros onto the relevant physical parameters of the solitons, shown in Fig. 2. Although in the complex k plane most of the zeros with a low imaginary contribution fall on top of each other (without intersecting), we can still use Figs. 3(a)–3(e) to follow, respectively, the zeros in Figs. 3(f)–3(j) by means of their common $\text{Re } k$ axis. It is clear that $\text{Re } k_o$

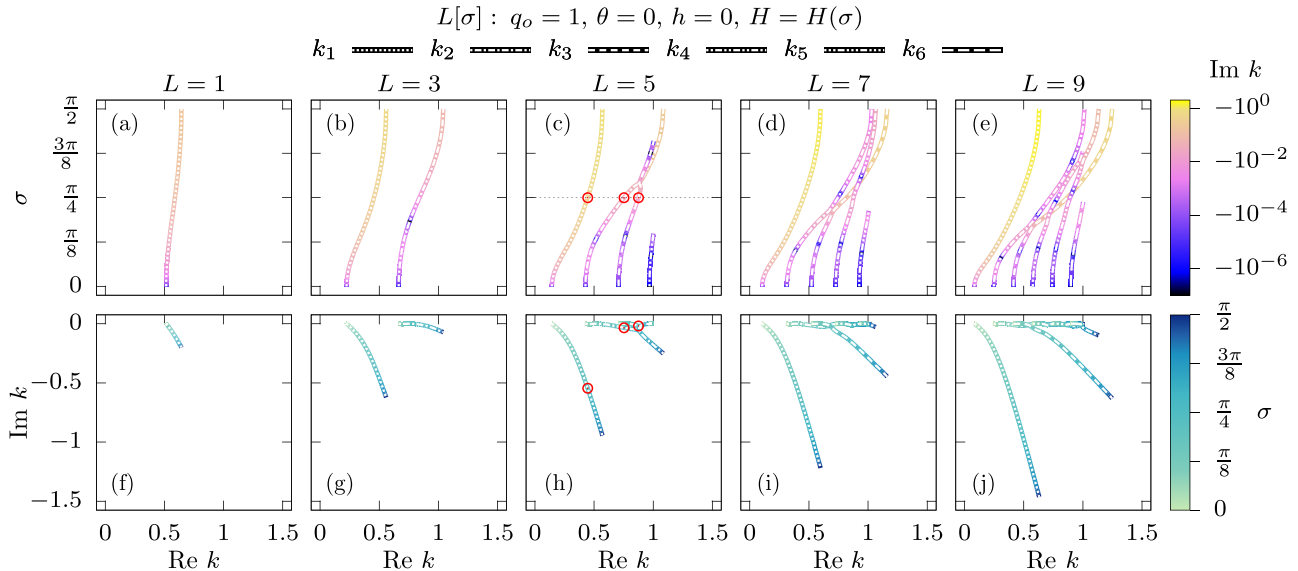


FIG. 3. Zeros of $s_{11}(k)$ as a function of σ for different values of L in the zero-box IP background configuration. The parameters $q_o = 1$, $\theta = 0$, $h = 0$ ($\alpha = 0$) remain fixed. The upper row shows the location of the zeros in the $\text{Re } k$ - σ plane whereas the bottom row shows the location of the zeros in the complex k plane. The complex k plane can be mapped onto Fig. 2 to retrieve the relevant physical information about the soliton solutions. The color coding shows the corresponding complementary quantity $\text{Im } k$ (upper row) and σ (bottom row). Only $\text{Re } k_o > 0$ are shown due to the symmetry of the zeros. Red circles in (c) and (h) correspond to the zeros shown in Fig. 9. Note that the quantities shown are measured in transverse oscillator units.

increases with σ . However, to infer about the behavior of $\text{Im } k_o$ it is convenient to distinguish between solutions with a high imaginary contribution (HIC) and those with a low imaginary contribution (LIC). We empirically define as HIC the solutions whose zeros have $|\text{Im } k_o| > 0.1$, and LIC the ones having $|\text{Im } k_o| < 0.01$.

First, let us focus on the LIC solutions. In Figs. 3(f)–3(j), LIC solutions lay on $\text{Im } k_o \approx 0$, indiscernible from one another. All solutions belong to this group when $\sigma \approx 0$ since $\text{Im } k_o$ is a quantity directly related to the presence of the second component. In particular, LIC solutions correspond to DB solitons with a negligible bright contribution (see Fig. 2), i.e., they are almost pure dark solitons (see also Fig. 10 below). However, as σ increases, v increases but A_d decreases. Similarly, $\text{Re } k_o$ also increases with σ and some LIC solutions cease to exist right before reaching $\text{Re } k_o = 1$ and $\text{Im } k_o = 0$ or, equivalently, before the solitons acquire the speed of sound. In order to avoid this point, a LIC solution must transition into a HIC one. In Fig. 3(c), the former zeros are k_3 and k_4 , and the latter are k_1 and k_2 . Additionally, in the zero-box configuration, LIC solutions present localized *drops* of the imaginary contribution as σ increases. At these drops, the imaginary contribution drastically decreases to $\text{Im } k_o \approx 0$ to rapidly increase again. The drops are depicted by the logarithmic color scale of $\text{Im } k_o$, where $\text{Im } k_o$ drops from $|\text{Im } k_o| \lesssim 10^{-3}$ (violet) to $|\text{Im } k_o| \lesssim 10^{-6}$ (blue), given our numerical precision [e.g., for $L = 3$, an increase in the numerical precision leads to $\text{Im } k_2(\sigma = 1.483\,998\,8) = 1.986\,48 \times 10^{-18}$]. For example, in Fig. 3(e), k_2 presents three drops (the region where the drops take place is blue). The first drop takes place at $\sigma \approx 0.17\frac{\pi}{2}$. Note that as σ increases, drops of k_3 , k_4 , and k_5 follow. The second drop of k_2 appears at $\sigma \approx 0.45\frac{\pi}{2}$. Again, drops of k_4 and k_5 follow. Notice that in this case, k_3 has already transitioned into a HIC solution (yellow tones). The last drop takes place at $\sigma \approx 0.72\frac{\pi}{2}$. In this case, neither k_4 nor k_5 present a drop since the former ceases to exist shortly after and the latter transitions into a HIC solution. Nevertheless, these drops do not represent any major additional change to the solitonic structures since A_d is almost independent of $\text{Im } k_o$ when $|\text{Re } k_o| < 1$ and $\text{Im } k_o \approx 0$ (see Fig. 2), and A_b is almost negligible. A visualization of the above discussion is presented in Fig. 4 for the LIC solution k_4 . Here, the effect of the drops is clearly visible on A_b , which decreases (almost) to zero at each drop. Additionally here, one can appreciate how k_4 becomes sonic, i.e., $v \approx c$, at $\sigma \approx 3\pi/8$ with a fast decrease of A_d towards $A_d = 0$, characteristic of the LIC solutions.

Next we focus on HIC solutions and take again as representative examples Figs. 3(e) and 3(j). Here, the HIC solutions are k_1 , k_3 , and k_5 , which become more evident after they transition from LIC to HIC solutions as σ increases. Mapping the zeros of Fig. 3(j) onto Fig. 2 reveals that HIC solutions are DB solitons with a higher bright contribution than LIC ones. Recall that the bright contribution increases with $\text{Im } k$. As stated before for LIC solutions, when σ increases, A_d decreases and v increases, while A_b increases or decreases depending on the increase or decrease of the imaginary contribution. However, the behavior of HIC solutions is different. Indeed, by following k_1 , which is a HIC solution already from low values of σ , it is obvious that this zero highly differs from the LIC solutions

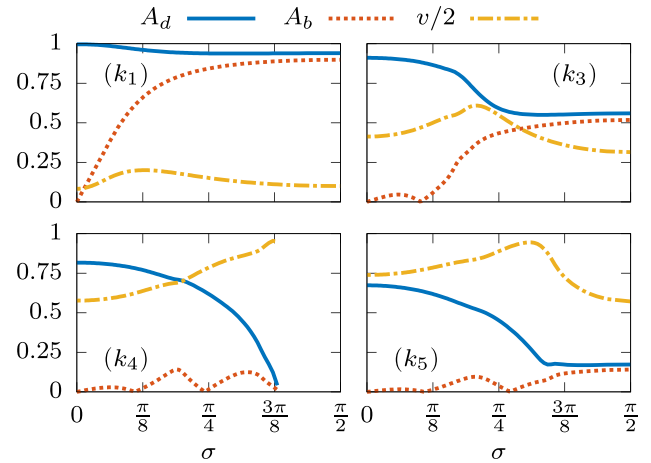


FIG. 4. Amplitudes A_d , A_b , and velocity v of k_1 , k_3 , k_4 , and k_5 shown in Figs. 3(e) and 3(j) (see legend) as a function of σ . The local maximum of v defines the transition point from LIC to HIC solutions for k_1 , k_3 , and k_5 . Note that v is halved to depict all parameters in the same scale. Note also that the quantities shown are measured in transverse oscillator units.

presented before. In particular, it quickly reaches a regime where the ratio $\text{Re } k_o / \text{Im } k_o$ is almost constant independently of σ . This regime is where we start to consider a zero as a HIC solution and, when mapped onto Fig. 2, we observe that k_1 has an almost constant A_d . On the other hand, in this regime A_b always increases while v always decreases. The latter directly shows that DB solitons with the same dark component but a bigger bright counterpart are slower than those with a smaller bright contribution. In the case of k_3 , it is found that this solution transitions from a LIC to a HIC one for $\sigma > \pi/8$. From this point onwards, the ratio $\text{Re } k_o / \text{Im } k_o$ also becomes almost constant, and so does again the A_d related to it. In this case, A_b increases and v decreases as well. The same holds true for k_5 , which transitions from a LIC to a HIC solution around $\sigma = 3\pi/8$.

Also in this case, Fig. 4 offers a visualization of the HIC solutions, i.e., k_1 , k_3 , and k_5 . Here, it can be seen that, once all LIC solutions have transitioned into HIC ones, they present an A_d plateau. On the other hand, it is also clear that the increase of A_b directly affects v , which starts decreasing right before A_d reaches its constant value. Therefore, it is possible to define the transition point from LIC to HIC solution not only by the saturation of A_d , but also from the local maximum of v .

b. Out-of-phase background. We next explore the OP zero-box configuration, again for $q_o = 1$, $L \in [1, 9]$, $h = 0$ ($\alpha = 0$), and $\sigma \in [0, \pi/2]$, corresponding to $H(\sigma) \in [0, q_o]$. However, we now fix $\theta = \pi/2$, namely, setting the sides of the box out of phase ($\Delta\theta = \pi$). The corresponding spectrum of zeros is illustrated in Fig. 5. Again, the choice of parameters presents a symmetric distribution of the zeros and thus only $\text{Re } k_o > 0$ are shown.

In the zero-box configuration, the peculiarity of an OP-FBTC with $\theta = \pi/2$ is that it gives rise to an odd number of solutions due to the presence of an unpaired static DB soliton, labeled k_0 . Note that k_0 is a HIC solution with $\text{Re } k_o = 0$. Therefore, it is straightforward to map its velocity and

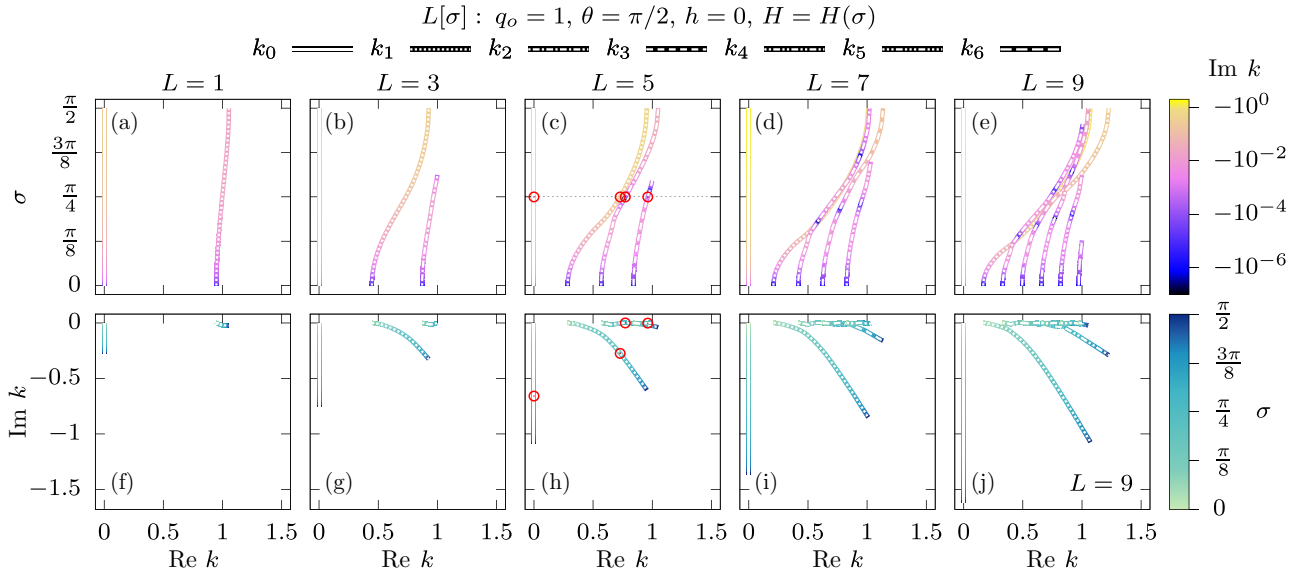


FIG. 5. Zeros of $s_{11}(k)$ as a function of σ for different values of L in the zero-box OP background configuration. The parameters $q_o = 1$, $\theta = \pi/2$, $h = 0$ ($\alpha = 0$) remain fixed. The upper row shows the location of the zeros in the $\text{Re } k$ - σ plane whereas the bottom row shows the location of the zeros in the complex k plane. The complex k plane can be mapped onto Fig. 2 to retrieve the relevant physical information about the soliton solutions. The color coding shows the corresponding complementary quantity $\text{Im } k$ (upper row) and σ (bottom row). Only $\text{Re } k_o > 0$ are shown due to the symmetry of the zeros. k_0 is an unpaired solution. Red circles in (c) and (h) correspond to the zeros shown in Fig. 10. Note that the quantities shown are measured in transverse oscillator units.

amplitudes. Indeed, from Fig. 2 one obtains that $v = 0$ and $A_d = 1$ independently of the value of σ . On the other hand, A_b increases with σ . Aside from this extra unpaired solution, OP-FBTCs have an additional difference when compared to the IP-FBTC case. With the OP-FBTC, as L increases, the emergence of the paired zeros, k_1, \dots, k_6 , is slightly delayed (parametrically) when compared to the IP case. This means that for some values of L , there are less paired zeros in the OP case than in the IP case. For example, for $L = 5$ [Fig. 5(c)] there exist three paired zeros, i.e., k_1, k_2 , and k_3 , contrary to the IP case [Fig. 3(c)] where also a fourth paired solution, i.e., k_4 , was identified.

Lastly, before proceeding to the full-box configuration, it is worth commenting on how the presence of a second component in the box affects the solutions when compared to the single-component case. As discussed before, when $\sigma = 0$ ($H = 0$) the single-component case is retrieved and the zeros identified herein coincide with the ones found in Ref. [64], for both the IP and the OP cases. However, as σ increases (H increases) and the box is filled with the second component, the interaction between the components prevents the emergence of all the single-component solutions, an effect which is more enhanced for overlapping components, as we will see in what follows.

2. Full-box configuration

For the full-box configuration we use Eq. (27). This implies that the box of the FBTC is always fully filled, either with one or both components, $q_o^2 = h^2(\sigma) + H^2(\sigma)$. By doing so, we are able to explore several configurations and elucidate the effect of the second component inside the box. In this regard, it

is important to distinguish the regimes where $H > |h|$ or $H < |h|$ and $h > 0$ or $h < 0$. Besides, for $\sigma = \pi/2$ ($H = q_o$ and $h = 0$) we recover the zeros from the zero-box configuration. As before, below we explore both IP-FBTC and OP-FBTC using the previously introduced notation and labeling. Recall that in the former case $\theta = 0$ and thus the symmetry of the system is preserved, leading to a symmetric set of solutions. On the other hand, $\theta = \pi/2$ breaks the phase symmetry of the system, leading in turn to asymmetric solutions.

a. In-phase background. We once more begin our investigation by exploring the spectra of an IP but full-box configuration. Also here, $q_o = 1$ and $\theta = 0$ are held fixed, while $\sigma \in [0, \pi]$ and $L \in [1, 9]$ are varied. Recall that now $H(\sigma) \in [0, q_o]$ and $h(\sigma) \in [-q_o, q_o]$. The corresponding spectrum of zeros is presented in Fig. 6. Since an IP configuration preserves symmetry, only the zeros of the pair with $\text{Re } k_o > 0$ are shown.

Let us first discuss the changes in the spectrum under an L variation. As in the zero-box configuration, increasing L increases the number of zeros, and thus the soliton solutions. This is readily seen in Figs. 6(a)–6(e) (top row). In Fig. 6(a), having $L = 1$, k_1 is the only pair of zeros, while for $L = 5$ [Fig. 6(c)] already three different pairs of zeros, k_1, k_2 , and k_3 , are potentially present. Finally, for $L = 9$ [Fig. 6(e)], up to six different pairs of zeros, k_1, \dots, k_6 , occur. Notice though that, in the latter panel, there is not a single value of σ where all six solutions coexist at the same time. Moreover, most of the zeros at large L values, i.e., $L = 7$ and 9 [see Figs. 6(d) and 6(e), respectively], remain around $\text{Re } k_o = 1$, some of which having $|\text{Im } k_o| < 0.01$. However, and in contrast to the zero-box configuration, the drops that characterized LIC solutions are absent in this setting.

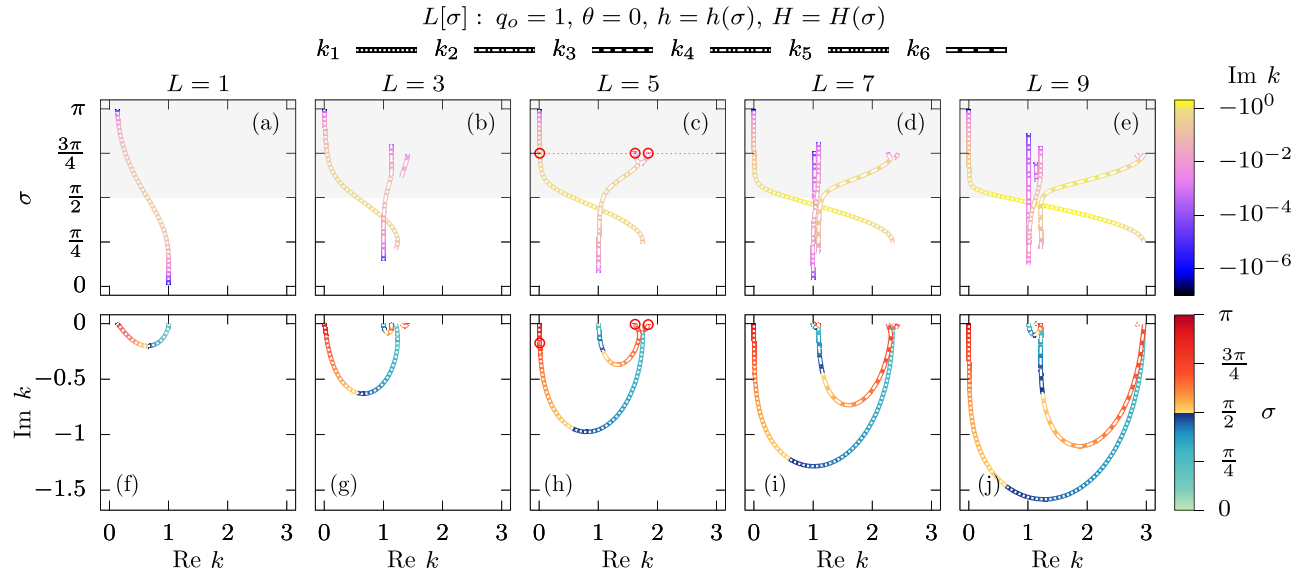


FIG. 6. Zeros of $s_{11}(k)$ as a function of σ for different values of L in the full-box IP background configuration, with $q_o^2 = h^2(\sigma) + H^2(\sigma)$ [see Eq. 27]. The parameters $q_o = 1$ and $\theta = 0$ remain fixed. The upper row shows the location of the zeros in the $\text{Re } k$ - σ plane whereas the bottom row shows the location of the zeros in the complex k plane. The complex k plane can be mapped onto Fig. 2 to retrieve the relevant physical information about the soliton solutions. The color coding shows the corresponding complementary quantity $\text{Im } k$ (upper row) and σ (bottom row). Only $\text{Re } k_o > 0$ are shown due to the symmetry of the zeros. The gray background in the top row panels corresponds to the equivalent case $h > 0$ and $\alpha = \pi$. Red circles in (c) and (h) correspond to the zeros shown in Fig. 11. Note that the quantities shown are measured in transverse oscillator units.

Now, let us monitor the changes in the spectra as σ increases. Focusing initially on Figs. 6(a)–6(e) (top row) it is observed that, in contrast to the zero-box configuration, $\text{Re } k_o$ does not always increase with σ . This becomes apparent upon inspecting k_1 , whose $\text{Re } k_1$ always decreases as σ increases. Other examples are k_2 in Fig. 6(d), or k_4 in Fig. 6(e), as well as the bifurcation close to $\sigma = 3\pi/4$, seen in Figs. 6(c)–6(e). We also need to distinguish between the regimes $\sigma \in [0, \pi/2)$ (white background) and $\sigma \in (\pi/2, \pi]$ (gray background). The former corresponds to $h > 0$ (and $\alpha = 0$), while the latter corresponds to $h < 0$ or, equivalently, $h > 0$ and $\alpha = \pi$ [see Eq. (6)].

In the first regime ($\sigma < \pi/2$) h decreases from q_o to 0, while H increases from 0 to q_o . This implies that the system starts as a homogeneous condensate ($\sigma = 0$) and, as σ increases, the presence of the first component in the box decreases while the presence of the second component increases (see Fig. 1). Therefore, it is expected that no soliton solution emerges until the FBTC reaches certain conditions. For example, in Fig. 6(a) ($L = 1$), k_1 is already present at very small values of σ . This means that a small box is already enough to produce a soliton solution. However, this soliton has a really low imaginary contribution, which means that the presence of the bright component is negligible. Moreover, it is created at $\text{Re } k_1 \approx 1$, which translates into a shallow ($A_d \approx 0$) fast moving ($v \approx c$) soliton (see Fig. 2). Then, as σ increases further, the box gets more and more filled by the second component, and thus the bright component of the ensuing DB soliton becomes dominant. Note also that as L increases k_1 emerges with larger $\text{Re } k_1$, reaching almost $\text{Re } k_1 = 3$ at $L = 9$ [see Fig. 6(e)]. It is also worth noticing

that most of the zeros emerge around $\sigma = \pi/4$. This is an important point since $h(\sigma = \pi/4) = H(\sigma = \pi/4) = 1/\sqrt{2}$. Basically, it shows that the presence of the second component inside the box hinders the formation of soliton structures. It is not until $h < H$ that the depth of the box is big enough to enhance the formation of DB solitons. Additionally, there exist also cases where zeros occur before $\sigma = \pi/4$. However, these zeros have a low imaginary contribution and appear around $\text{Re } k_o = 1$ which, as stated above, corresponds predominantly to small disturbances moving with velocities proximal to the speed of sound. Nevertheless, at $\sigma = \pi/2$ we recover the zeros from the zero-box configuration with $h = 0$ and $H = q_o$.

On the contrary, in the second regime ($\sigma > \pi/2$) $|h|$ increases from 0 to q_o and H decreases from q_o to 0. Importantly here, $\alpha = \pi$ represents a situation where the first component presents a phase difference between the walls and the inside of the box [see Eq. (6)]. Although this phase difference does not break the symmetry of the system, it introduces a constant perturbation in the system that needs to be taken into account, as we explain later on. Similarly to the first regime, most of the zeros are present also here while $|h| < H$ ($\sigma < 3\pi/4$). Interestingly enough, in this regime k_1 exists for all σ , having $\text{Re } k_1 \approx 0$ for a large range of σ , already from small L . This is a direct cause of the phase difference $\alpha = \pi$, which forces the existence of at least one pair of solutions (see Ref. [64] and references therein).

To better understand the existence of all aforementioned zeros, we inspect Figs. 6(f)–6(j) (bottom row), which can be directly connected to the soliton characteristics shown in Fig. 2. In the complex k plane, only the zeros with a high

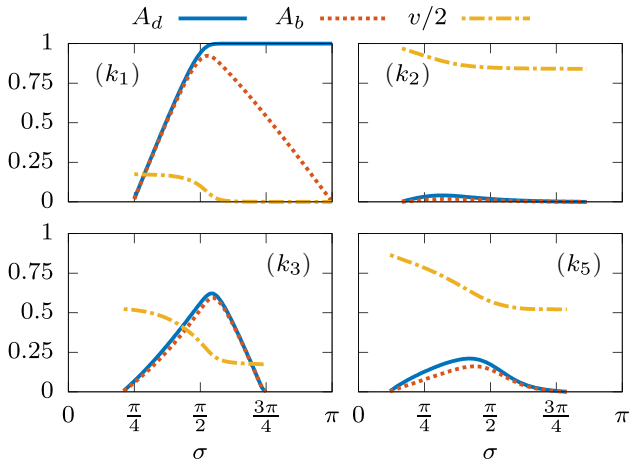


FIG. 7. Amplitudes A_d , A_b , and velocity v of k_1 , k_2 , k_3 , and k_5 shown in Figs. 6(e) and 6(j) (see legend) as a function of σ . Note that the quantities shown are measured in transverse oscillator units.

imaginary contribution are easily visible. In this case, the most important difference with respect to the zero-box configuration is the parabolically shaped trajectory of the zeros.

First, we focus on describing the zeros in Fig. 6(j) with the aid of Fig. 2. Most of the zeros with a low imaginary contribution are merely dots around $\text{Re } k_o = 1$ and $\text{Im } k_o = 0$, i.e., small-amplitude nearly sonic DB solitons with a negligible bright contribution. On the other hand, k_1 , k_3 , and k_5 possess a higher imaginary contribution. For instance, k_3 emerges at $\text{Re } k_3 = 1.2$ and $\text{Im } k_3 \approx 0$ already at $\sigma \approx \pi/4$. DB solitons with $\text{Re } k_o > 1$ and $\text{Im } k_o \approx 0$ are states that have extremely small amplitudes but large widths. As an example, here the DB soliton corresponding to k_3 has $A_d = 0.006$ and $A_b = 0.005$ at $\sigma = 0.21\pi$ (when k_3 initially emerges) and a full width at half-minimum for the dark (FWHM_d) and maximum for the bright component (FWHM_b) that read as $\text{FWHM}_d = 560$ and $\text{FWHM}_b = 837$ (in H.O. units presented in Sec. II). Of course, such structures are practically impossible to be seen. In addition, k_3 moves in this case with $v = c/2$. Then, as σ increases $|\text{Im } k_3|$ rapidly increases and so do A_d and A_b , which at the same time narrows the DB soliton. Of course, bigger solitons move slower and k_3 is no exception. Counterintuitively, the maximum bright contribution is found past $\sigma = \pi/2$, as indicated by the minimum of k_3 in Fig. 6(j) at $\sigma = 0.585\pi$. Past this point, $\text{Im } k_3$ starts to rapidly decrease, and so do A_d and A_b , reaching $\text{Re } k_3 = 3$ and $\text{Im } k_3 \approx 0$ before ceasing to exist at $\sigma = 3\pi/4$. Recall that before disappearing, k_3 ends up again being a small wide DB soliton. Also, note that $\text{Re } k_3$ is always an increasing function of σ . The trajectory of k_3 as σ is varied can be better appreciated by inspecting Fig. 7, where the mapping of k_3 onto Fig. 2 is shown along with further examples, i.e., k_1 , k_2 , and k_5 . Here, A_d , A_b , and v are plotted against σ . Interestingly, v remains almost constant for most of the values of σ in the second regime ($\sigma > \pi/2$), an outcome that is in turn related to the fact that $A_d \approx A_b$ in this regime.

A similar behavior to the k_3 one occurs also for k_1 within the first regime ($\sigma < \pi/2$). Obviously, since k_1 and k_3 are on top of each other around $\text{Re } k_o = 3$ [see Fig. 6(j)], when

k_1 emerges for the first time it does so as a small and wide DB soliton. Recall that different zeros never intersect, i.e., $k_i \neq k_j$. Also note that $\text{Re } k_1$ is a decreasing function with respect to a σ variation. Then, as σ increases, $\text{Re } k_1$ decreases and $|\text{Im } k_1|$ increases, which translates into larger A_d and A_b , with $A_d \approx A_b$, and v remaining almost constant. Interestingly here, slightly before $\sigma = \pi/2$, $|\text{Im } k_1|$ starts to decrease and both $\text{Re } k_1$ and $\text{Im } k_1$ rapidly approach 0. However, in this case only A_b decreases as σ keeps increasing. On the contrary, $A_d \approx q_o$ and $v \approx 0$ independently of σ . In Fig. 7 one can clearly discern the plateau of almost constant v within the first regime and the constant values of A_d and v within the second regime. The latter is a direct consequence of $\alpha = \pi$. As discussed for the OP zero-box configuration, a phase difference of $\Delta\theta = \pi$ between two regions of a condensate will always lead to the formation of a static soliton whose dark component is a black soliton with $A_d = q_o$ and $v = 0$ [64]. Hence, once $\sigma > \pi/2$, then $h > 0$ and $\alpha = \pi$ [see Eqs. (6) and (27)], which creates a phase jump at the edges that separate the inside of the box from its walls. What is seen in Fig. 7 for k_1 at large values of σ is a DB soliton formed by a black soliton and a bright counterpart that decreases as σ increases (H decreases). Remarkably, it seems that in this case, when compared to the single-component scenario [64], the presence of a second component does not affect the emergence of the black soliton but only that of the bright counterpart and the remaining soliton solutions.

b. Out-of-phase background. Our last exploration of the spectra of zeros of $s_{11}(k)$ is performed for an OP full-box configuration. Here, $q_o = 1$ and $\theta = \pi/2$ are held fixed, with the latter setting the two walls of the box out of phase. Additionally, $L \in [1, 9]$ and $\sigma \in [0, \pi]$ are varied. Recall that $H(\sigma) \in [0, q_o]$ and $h(\sigma) \in [-q_o, q_o]$. In this case the phase symmetry of the system is broken since $h \neq 0$ and $\theta \neq 0$, and the system yields asymmetric solutions, with none of the zeros being paired for any value of σ . The only exception here occurs for $\sigma = \pi/2$ (see below). Therefore, in Fig. 8 we show the entire spectrum of zeros, i.e., $\text{Re } k_o \in \mathbb{R}$.

It is worth noticing that given our particular choice of $\theta = \pi/2$ the zeros present an antisymmetry, evident in Figs. 8(a)–8(e), where the zeros are shown in the $\text{Re } k$ - σ plane. On the other hand, Figs. 8(f)–8(j) illustrate the zeros shown in the complex k plane. Here, the zeros are symmetric around $\text{Re } k = 0$ and the antisymmetry is encoded in the color code introduced for the σ variation. The symmetry in the complex k plane can be easily understood when looking back to Eq. (7). In the first regime $\sigma < \pi/2$, $\alpha = 0$ and $\Delta\theta_{\pm} = \pm\theta$, while in the second regime, $\sigma > \pi/2$, $\alpha = \pi$, and $\Delta\theta_{\pm} = \mp\theta$. This change of sign in $\Delta\theta$ implies a spatial reflection around $x = 0$ [see Fig. 1(a)] and gives rise to the (anti)symmetry of the spectra in a system with broken phase symmetry. Therefore, we use the same line style to identify antisymmetric zeros, i.e., $\text{Re } k_+ > 0$ and $\text{Re } k_- < 0$ (see legend in Fig. 8), and in what follows we will comment only the zeros with $\text{Re } k_o > 0$.

As in the previous cases, increasing L increases the number of zeros. In Figs. 8(a)–8(e) (top row) the number of zeros increases from two, in Fig. 8(a), to seven, in Fig. 8(e). Of course, in this case the number of zeros also depends on σ . In general, increasing σ while $\sigma < \pi/2$ (increasing H and decreasing h) also increases the number of zeros. On the other

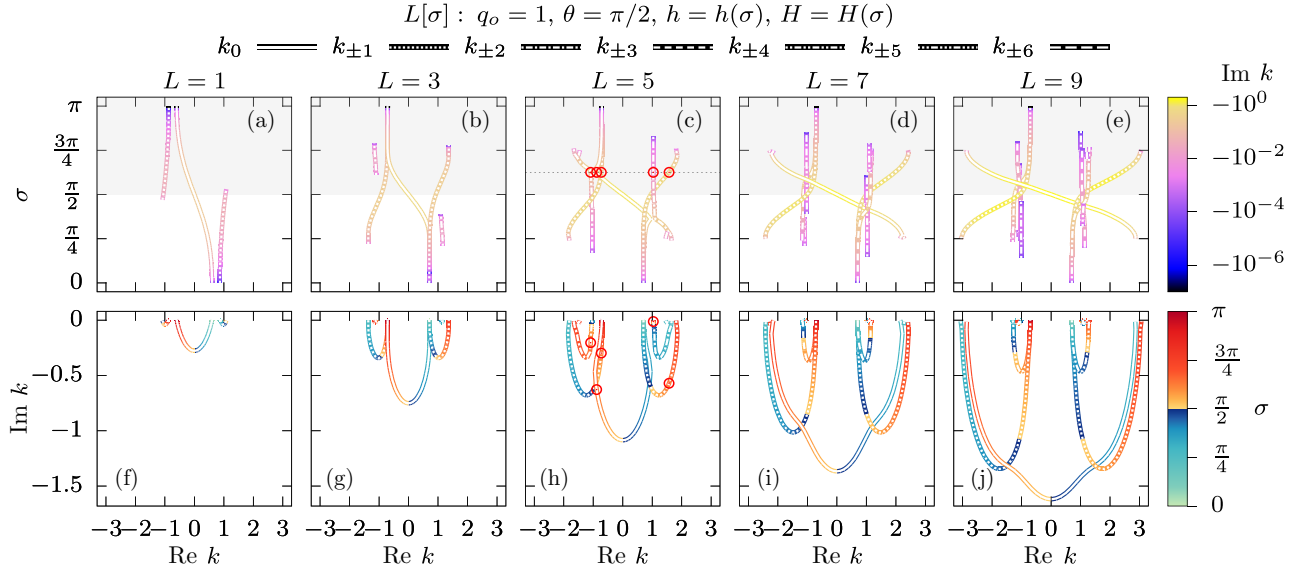


FIG. 8. Zeros of $s_{11}(k)$ as a function of σ for different values of L in the full-box OP background configuration, with $q_0^2 = h^2(\sigma) + H^2(\sigma)$ [see Eq. (27)]. The parameters $q_0 = 1$ and $\theta = \pi/2$ remain fixed. The upper row shows the location of the zeros in the $\text{Re } k$ - σ plane whereas the bottom row shows the location of the zeros in the complex k plane. The complex k plane can be mapped onto Fig. 2 to retrieve the relevant physical information about the soliton solutions. The color coding shows the corresponding complementary quantity $\text{Im } k$ (upper row) and σ (bottom row). k_+ (k_-) corresponds to zeros with $\text{Re } k_0 > 0$ ($\text{Re } k_0 < 0$). k_0 is an unpaired solution. The gray background in the top row panels corresponds to the equivalent case $h > 0$ and $\alpha = \pi$. Red circles in (c) and (h) correspond to the zeros shown in Fig. 12. Note that the quantities shown are measured in transverse oscillator units.

hand, increasing σ while $\sigma > \pi/2$ (decreasing H and increasing h) decreases the number of zeros. Additionally, one needs to keep in mind that $\sigma > \pi/2$ also implies that $\alpha = \pi$ (with $h > 0$). It is also worth noticing that in some cases some of the zeros are present only in the first ($\sigma < \pi/2$) or in the second ($\sigma > \pi/2$) regime. For instance, in Fig. 8(e) k_{+5} is found only for $\pi/4 < \sigma < \pi/2$ (first regime). Similarly, k_{+2} and k_{+6} are found only in the second regime. The former appears for $\pi/2 < \sigma < 7\pi/8$ and the latter right before $\sigma = 3\pi/4$. Recall that this feature, i.e., all zeros do not coexist at the same time, was also found in the full-box IP case. Yet another similarity with the IP case is that as L increases, most of the zeros appear only between $\pi/4 < \sigma < 3\pi/4$ and are found mostly around $\text{Re } k_0 \approx \pm 1$.

There are two peculiarities of the OP case also worth discussing. The first one is the emergence of a DB soliton with a black soliton contribution, corresponding to k_0 at $\sigma = \pi/2$. Notice that k_0 is the only unpaired zero and also the only zero bearing both positive and negative $\text{Re } k_0$ values. The change of sign, which is directly related to the velocity of the soliton [see Eq. (26)], happens at $\sigma = \pi/2$ ($H = q_0$ and $h = 0$), which coincides with the OP zero-box case discussed above (see Fig. 5). In particular, at $\sigma = \pi/2$ we recover the solutions of the zero-box OP configuration. The labeling of all k_0 is also kept accordingly. The other peculiarity is found by k_0 and k_{+1} in Figs. 8(b) and 8(c), k_{+1} and k_{+3} in Fig. 8(d), and k_{+1} and k_{+4} in Fig. 8(e). At low values of H , i.e., $\sigma \approx 0$ (or $\sigma \approx \pi$ for k_-), both zeros are almost on top of each other, implying that both solutions are almost identical, i.e., similar shape and velocity. Additionally, locally both edges of the box ($x = \pm L$) are equivalent, a situation more pronounced as

$H \rightarrow 0$ and $h \rightarrow \pm q_0$, which reduces to the single-component case. Basically, the formation of such similar solutions is a direct consequence of our choice of parameters which define an equivalent phase jump at both edges of the box, $\Delta\theta_- = \Delta\theta_+$ [see Eq. (7)].

Figures 8(f)–8(j) show the solutions in the complex k plane. Most of the properties for this representation are already mentioned in the IP case, whose zeros look alike. Yet, in this case, we were able to identify the only case where the maximum bright soliton contribution of a particular soliton solution coincides with the maximum presence of the second component in the box. Of course, this zero is k_0 and the maximum contribution of its bright component occurs at $\sigma = \pi/2$, precisely when the solution is the static DB soliton.

B. Nucleation of DB soliton trains: Without confinement

In this section we intend to verify the analytical results captured by the discrete eigenvalues identified in Sec. III A. Initially, we numerically solve the CGPE [Eq. (2)] in the absence of a trapping potential, i.e., $\Omega = 0$, by employing a fourth-order Runge-Kutta integrator accompanied by a second-order finite-differences method accounting for the spatial derivatives. The spatial and temporal discretizations are $dx = 0.1$ and $dt = 0.001$, respectively, while the domain of integration used is located at $|x| = 2500$ so as to avoid finite-size effects, for the times of interest herein. In the following, we fix $L = 5$ and $q_0 = 1$, while $\theta = \{0, \pi/2\}$ for both the zero- and the full-box configurations.

Below we present our findings regarding the dynamical nucleation of DB solitons via the matter-wave interference

method of two condensates in the presence of a second species in-between, also featuring the counterflow (see Fig. 1). It is important to note that the various DB solitons nucleated when utilizing the initial condition ansatz of Eq. (6) have finite velocities and, in general, interact with each other. Therefore, the analytical findings can be compared to the numerical ones only in the asymptotic limit $t \rightarrow \infty$. In this limit, each DB soliton can be considered well separated and independent from the rest of the solitary waves. In this sense, discrepancies between the analytical DB soliton solutions of Eq. (23) and the numerically formed ones are expected to decrease as $t \rightarrow \infty$, as it is found and discussed later on. Finally, in the results to be presented below, the analytical DB soliton solution is centered at $x_0 = 0$, unless stated otherwise.

1. Zero-box configuration

a. In-phase background. Our first result is presented in Fig. 9. It corresponds to the zero-box configuration ($h = 0$) with an IP background ($\theta = 0$). Here, we have chosen $\sigma = \pi/4$ as a representative example. The zeros of this particular initial configuration are shown in Figs. 3(c) and 3(h), pinpointed with red circles. In particular, three pairs of DB solitons are predicted by our analytical method and indeed found in the dynamical process. For instance, in Fig. 9(a) the norm of the wave function $|q|$ of each component at $t = 250$ is shown, and all three pairs of DB solitons are clearly formed. Note that due to the symmetry of the solutions, only the left-moving solitons $v < 0$ are illustrated. The same holds for their corresponding zeros shown in Fig. 9(b), where only the pair with $\text{Re } k_o > 0$ is depicted. In particular, Fig. 9(b) is equivalent to Fig. 3(h), as can be inferred from the location of the zeros in the complex k plane. Notice that for consistency the notation introduced here follows that of Fig. 3.

A remarkably good agreement between the analytical estimates and the numerically formed DB solitons occurs already at $t = 250$ (see Fig. 9). Particularly, both the numerically found solutions (solid lines) and the analytically obtained ones (dotted-dashed lines) fall almost perfectly on top of each other. This also confirms the validity of the numerical scheme, given the exact nature of the IST analysis at the level of the integrable Manakov model. The major discrepancy observed in this case corresponds to the shallower and faster DB soliton solution k_3 . There exist mainly three different sources that can give rise to such a discrepancy: (i) as previously discussed, one should only expect both solutions to exactly coincide at $t \rightarrow \infty$ or, equivalently, for such traveling solutions to $x \rightarrow \pm\infty$. Yet, the bright solitons of the k_2 and k_3 solutions still bear a finite background reminiscent of the filling of the box in the initial configuration. We attribute the presence of this background to the intercomponent interaction, an effect which is enhanced for initially overlapping components, as will be shown in the full-box configuration results; (ii) k_3 is the fastest DB soliton, which implies that k_3 is the wave that remains for longer times coupled to the emitted radiation, some of which is still visible around $x \approx 300$. This effect is enhanced the faster the soliton is; (iii) the interaction between the k_2 and k_3 DB solitons may play a role since both waves travel close to each other for a reasonable long amount of time. Indeed, Fig. 9(c) [9(d)] shows the spatiotemporal evolution of

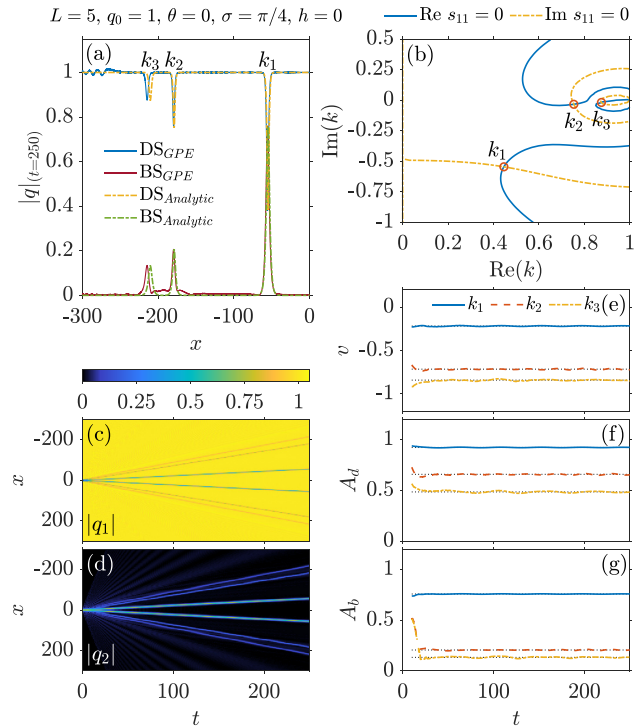


FIG. 9. Dark-bright soliton solutions stemming from a zero-box configuration with an in-phase background having $L = 5$, $q_o = 1$, $\theta = 0$, $\sigma = \pi/4$, and $h = 0$ [cf. Figs. 3(c) and 3(h)]. (a) Snapshot of $|q|$ at $t = 250$ given by the CGPE (2) (solid lines) and the analytical solutions (23) (dotted-dashed lines), for both dark (DS) and bright (BS) soliton counterparts. (b) Contour plot of $\text{Re } s_{11} = 0$ (solid blue line) and $\text{Im } s_{11} = 0$ (dashed yellow line) on the complex k plane. The zeros, k_o , are depicted with red circles and only the zeros of each pair with $\text{Re } k_o > 0$ are shown. The labeling of zeros is that of Fig. 3, with $k_1 = 0.4456 - i0.5455$, $k_2 = 0.7535 - i0.0339$, and $k_3 = 0.8751 - i0.0189$. (c), (d) Spatiotemporal evolution of the dark $|q_1|$ and bright $|q_2|$ soliton components. Temporal evolution of (e) the instantaneous velocity v , and (f) the dark A_d and (g) bright A_b soliton amplitudes. The corresponding asymptotic values are depicted with dotted black lines. Note that the quantities shown are measured in transverse oscillator units.

the wave function $|q_1|$ [$|q_2|$], which hosts the dark [bright] counterpart of the DB solitons in question. Here, it is clear that k_2 and k_3 , namely, the outermost traveling DB solitons, remain close to each other during evolution.

Next, in order to extract the DB soliton characteristics, we numerically follow the center of mass (c.m.) of each DB soliton, i.e., $x_{\text{c.m.}} = (\int_{x_l}^{x_r} x |q|^2 dx) / (\int_{x_l}^{x_r} |q|^2 dx)$ with $x_{l,r}$ defining the integration limits around each dark soliton core. This also provides access to their instantaneous velocity, $v = dx_{\text{c.m.}}/dt$. To obtain the c.m., we trace the dark soliton minima. From the position of the latter, we consecutively extract the dark A_d and bright A_b soliton amplitudes, and compare them with their corresponding asymptotic analytical values [Eq. (25)]. v , A_d , and A_b are depicted in Figs. 9(e)–9(g), respectively, for $t > 10$ since at the very beginning of the dynamics it is not possible to identify any individual solitonic structure. In all cases, it becomes apparent that the numerical predictions approach the

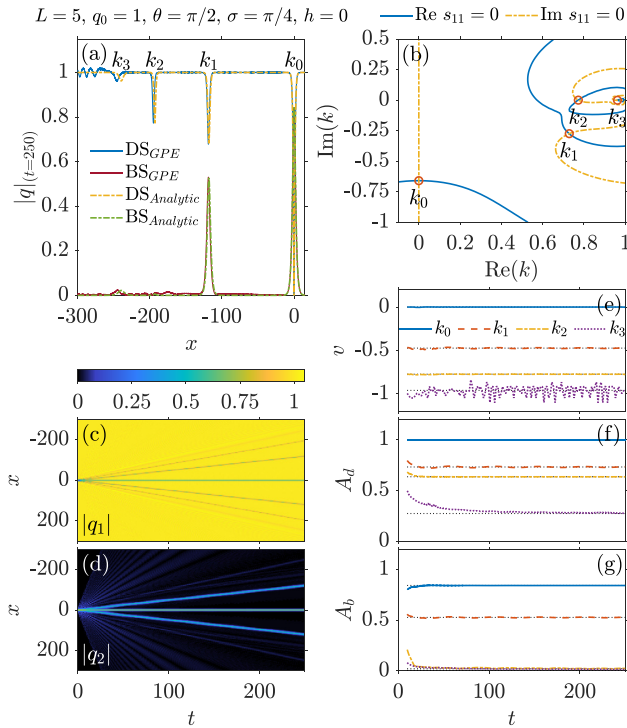


FIG. 10. Same as Fig. 9 but for $L = 5$, $q_0 = 1$, $\theta = \pi/2$, $\sigma = \pi/4$, and $h = 0$. This initial configuration corresponds to a zero-box configuration with an out-of-phase background [cf. Figs. 5(c) and 5(h)]. The labeling of zeros is that of Fig. 5 with $k_0 = -i0.6590$, $k_1 = 0.7287 - i0.2744$, $k_2 = 0.7726 - i2.5 \times 10^{-5}$, and $k_3 = 0.9622 - i8.8 \times 10^{-4}$. Note that the quantities shown are measured in transverse oscillator units.

analytical estimates (dotted black lines) as $t \rightarrow \infty$. Notice also the small-amplitude oscillations performed by v , A_d , and A_b around their asymptotic value, attributed to the counterflow process that leads to the soliton formation.

b. Out-of-phase background. Now, we present the results for a zero-box configuration ($h = 0$) but with an OP background ($\theta = \pi/2$). The zeros of this initial configuration were presented in Figs. 5(c) and 5(h), and we have chosen $\sigma = \pi/4$ as the most relevant case for this particular set of parameters. Our analytics predict, in this case, four zeros: a static unpaired DB soliton and three pairs of DB solitons. Such solutions are marked with red dots in Figs. 5(c) and 5(h), and are also shown in Fig. 10(b). Note that once more, the solutions are symmetric with respect to the origin ($x = 0$) and for clarity we only show those with $\text{Re } k_0 > 0$. Each of the zeros illustrated in Fig. 10(b) corresponds to a particular DB soliton solution, shown in Fig. 10(a). Again, the numerically observed waveforms (solid lines), obtained upon solving the CGPE with this particular OP zero-box configuration, fall on top of the analytical solutions (dotted-dashed lines) given by the zeros shown in Fig. 10(b). As in the IP zero-box configuration, we find also here that k_3 is again the DB soliton that presents the larger deviation from its analytical state. Nevertheless, this OP case features two interesting structures not seen in the IP case. The first one is the occurrence of a static DB soliton k_0 , located at $x = 0$. As we discussed in Sec. III A, an OP configuration

allows the formation of static DB solitons consisting of a black soliton ($v = 0$) and its symbiotic bright counterpart. The second one is related to the soliton $k_2 = 0.7726 - i2.5 \times 10^{-5}$, which possesses an almost negligible imaginary contribution. Recalling our discussion of Sec. III A, the bright counterpart of a DB soliton solution is mostly defined by the imaginary contribution of its corresponding zero. Therefore, since in this case $\text{Im } k_2 \sim 10^{-5}$ we expect and indeed confirm the formation solely of a dark soliton. Notice, however, the minuscule second component contribution that is in turn related, as in the IP case, to a small background reminiscent of the interaction between the two components during the dynamics. Similarly, k_3 with $\text{Im } k_3 \sim 10^{-4}$ can also be practically treated as a dark soliton.

In Figs. 10(c) and 10(d), the spatiotemporal evolution of $|q_1|$ and $|q_2|$, respectively, clearly shows a static DB soliton at $x = 0$ and the three pairs of DB solitons moving outwards. Note that, in Fig. 10(d), the bright component of k_2 is not seen and the bright component of k_3 is barely visible. Figures 10(e)–10(g) demonstrate the evolution of the numerically obtained v , A_d , and A_b , respectively, together with their asymptotic analytical values (dotted black lines). Yet, again, the numerical quantities asymptotically approach their corresponding analytical values. In this case, small-amplitude oscillations in v , A_d , and A_b , caused by the dynamical formation of the solitonic entities are also found [cf. k_1 in Figs. 10(e)–10(g)]. In contrast, the velocity of k_3 , the fastest DB soliton, features abrupt and irregular oscillations. This is due to the fact that we are computing the instantaneous velocity, $v = dx_{c.m.}/dt$, by integrating around each dark soliton core. A closer inspection of Fig. 10(a) reveals that some noise is still present around the DB structure at $t = 250$. Since this noise is not constant, when calculating $x_{c.m.}$ small irregular changes lead to the irregular oscillations observed in v .

2. Full-box configuration

a. In-phase background. In the full-box configuration, the center of the box is fully filled, i.e., $q_0^2 = h^2(\sigma) + H^2(\sigma)$ for all values of σ [see Eq. (27)]. Initially, we explore the IP background ($\theta = 0$) upon choosing $\sigma = 6\pi/8$. This in turn implies that the first component inside the box is OP with respect to the two sides of the box [see Eq. (7)]. The analytical solutions for this particular choice of parameters were presented in Figs. 6(c) and 6(h), with the relevant zeros being marked by red dots. In total, three pairs of DB soliton solutions are found. However, in what follows we only discuss the pair $k_{\pm 1}$. The other two pairs of solutions correspond to DB solitons with $\text{FWHM} \gtrsim 10^2$ and amplitudes $A_{d,b} \lesssim 10^{-3}$ (see also the discussion in Sec. III A), and thus we omit them.

Illustrated in Fig. 11(b) are the zeros $k_{\pm 1} = \pm 0.0098 - i0.1737$, which lie almost on top of each other since $\text{Re } k_{\pm 1} \approx 0$. In Fig. 11(a) we compare the numerically found DB solitons (solid lines), stemming from the CGPE, with the analytical ones (dotted-dashed lines), obtained using our analytical tools presented in Sec. II. Although, in this case, we show the DB soliton profiles at later evolution times ($t = 2000$), the numerical solutions do not completely coincide yet with the analytical ones. The reason why this happens is not only that our analytical method provides

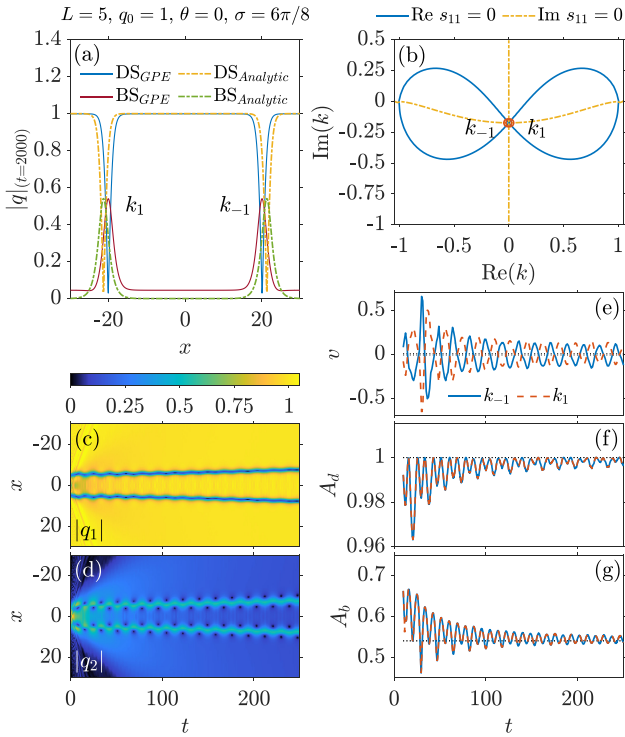


FIG. 11. Same as Fig. 9 but for $L = 5$, $q_0 = 1$, $\theta = 0$, $\sigma = 6\pi/8$. This initial configuration corresponds to a full-box configuration with an in-phase background [cf. Figs. 6(c) and 6(h)]. In this case the only relevant solutions are $k_{\pm 1} = \pm 0.0098 - i0.1737$. We omitted $k_{\pm 2} = \pm 1.6237 - i0.0060$ and $k_{\pm 3} = \pm 1.8440 - i0.0080$ (see text). Note the long-time dynamics in (a). Note also that the quantities shown are measured in transverse oscillator units.

solutions at $x \rightarrow \pm\infty$ or, equivalently, at $t \rightarrow \infty$, but also the interaction between the pair of DB solitons at early times. Additionally, note that at these earlier times, shown in Figs. 11(c) and 11(d), the pair of DB solitons does not emerge at $x_0 = 0$ but at $x_0 = \pm 5$ [see Eqs. (23)]. As discussed in Sec. III A 2, the phase jump $\Delta\theta_{\pm} = \pi$ in the first component between the inner and the outer sides of the box leads to the formation of a pair of (almost) black-bright solitons where the phase jump takes place. Moreover, the latter implies $v \sim 0$, which enhances the interaction between the pair of DB solitons for longer times than in the previously discussed cases, as mentioned before.

However, despite the fact that we cannot properly capture the early stages of the dynamics for these pairs of DB solitons, an interesting observation, absent in the previous explorations, can be made. For instance, during the early dynamics, the presence of a non-negligible background in the minority species radically changes the behavior of a typical DB soliton, and our numerically identified waveforms morph into beating DB solitons [13,71]. Indeed, the spatiotemporal evolution of both the dark and the bright soliton components [see Figs. 11(c) and 11(d), respectively] reveal the characteristic beating of such solitonic entities. Importantly, these beating solitons, however, are not “discernible” at the level of the eigenvalues of the IST analysis. Here, we want to point

out that the bright solitons of the DB entity $k_{\pm 1}$ are in phase and therefore the DB solitons interaction is repulsive [72], an effect that can be discerned by closely inspecting Figs. 11(c) and 11(d) at later times.

Now, let us discuss Fig. 11(e) showcasing v . Since $\Delta\theta_{\pm} = \pi$, and thus $\text{Re } k_{\pm 1} \approx 0$ (see Sec. III A 2), the analytic velocities of such solitons are close to zero. Also, since $k_{\pm 1}$ are a pair, their velocities have opposite signs. However, the interesting phenomenon found here is the beating performed by the DB soliton pair due to the presence of the finite background in the second component. Indeed, here we can clearly see how v oscillates while asymptotically approaching its analytical value, and that v undergoes damped oscillations while approaching its asymptotic value. The damping behavior is inherently related to a progressive decrease of the finite background over time. In order to reach their asymptotic velocities, one should wait for the finite background of the second component to vanish and for the solitons to be well separated from each other to avoid interacting. The same applies to the dark and bright amplitudes, shown in Figs. 11(f) and 11(g), respectively. Nonetheless, Figs. 11(f) and 11(g) provide a visual confirmation of the symmetry of the solutions, where solitons undergo the same amplitude oscillations, the latter being also a characteristic of beating DB solitons [71] [see the discussion around Eq. (33)].

b. Out-of-phase background. The last parametric selection consists on a full-box configuration, i.e., $q_0^2 = h^2(\sigma) + H^2(\sigma)$ [see Eq. (27)], with an OP background ($\theta = \pi/2$). The analytical solutions for such an initial configuration were shown in Figs. 8(c) and 8(h). Here, we choose as a case example $\sigma = 5\pi/8$, with the relevant zeros pinpointed with red dots.

In Fig. 12(b) the five zeros corresponding to this particular initial configuration are depicted with a red circle. In Fig. 12(a), the analytical solutions obtained using these zeros (dotted-dashed lines) are compared to the numerical solutions (solid lines), obtained by solving the CGPE. Both solutions almost fall on top of each other. Most of the discrepancies found here can be attributed as in the preceding sections to the presence of a finite background, as well as DB-DB soliton interactions. In Fig. 12(a), the most extreme case is that of $k_2 = 1.0381 - i0.0127$, where the dark component of the DB soliton cannot be identified. This is a direct consequence of the fact that $\text{Re } k_2 \approx 1$, as discussed in Sec. III A 2. Additionally, the corresponding bright part of k_2 is disturbed by the spreading of the finite background.

The spatiotemporal evolution of the dark and bright soliton components [see Figs. 12(c) and 12(d), respectively] demonstrates the asymmetric nature of the ensuing DB waves for this parametric selection. Of course, k_2 is not discernible in Fig. 12(c), while in Fig. 12(d) the finite background on top of which the bright solitons are formed is clearly visible. Among them, k_0 and k_{-1} are seen to undergo small-amplitude oscillations, resembling beating DB solitons. Unfortunately, the oscillations around their c.m. are not pronounced enough so as to be captured by the temporal evolution of the instantaneous velocity in Fig. 12(e). Nevertheless, we are still able to follow the c.m. of most of the evolved solitonic entities, showcasing this way that they approach their asymptotic analytical values (dotted black lines) as $t \rightarrow \infty$. The only exception here is the nearly sonic k_2 soliton, whose c.m. cannot be separated from

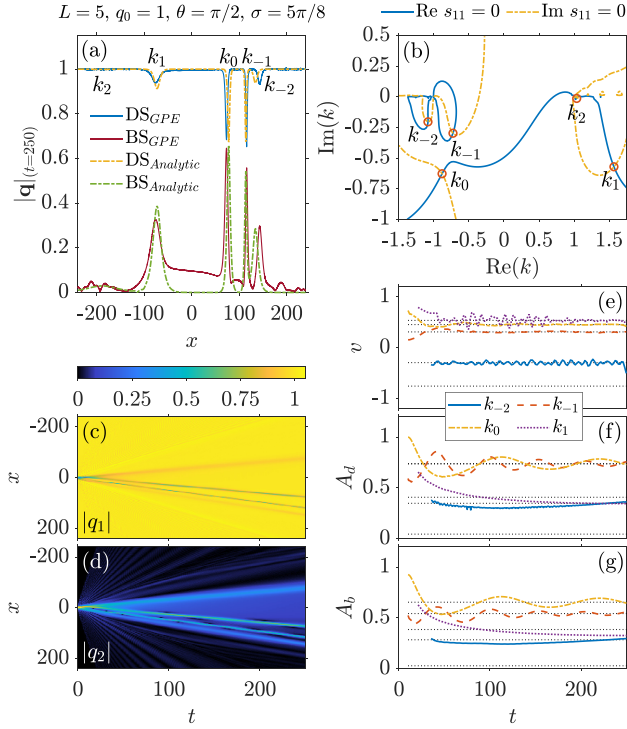


FIG. 12. Same as Fig. 9 but for $L = 5$, $q_0 = 1$, $\theta = \pi/2$, $\sigma = 5/\pi 8$. This initial configuration corresponds to a full-box configuration with an out-of-phase background [cf. Figs. 8(c) and 8(h)]. In this case the zeros are not symmetric. The labeling of zeros is that of Fig. 8 with $k_{-2} = -1.0858 - i0.2038$, $k_{-1} = -0.7285 - i0.29769$, $k_0 = -0.8843 - i0.6277$, $k_1 = 1.5701 - i0.5708$, and $k_2 = 1.0381 - i0.0127$. Note that the quantities shown are measured in transverse oscillator units.

the surrounding radiation. Yet, we left its analytical value as a reference. Figures 12(f) and 12(g) illustrate the evolution of A_d and A_b for each DB soliton formed. Noteworthy here is the damping behavior of A_d and A_b associated with the beating solitons k_0 and k_{-1} . Finally, it is worth commenting k_{-2} is still far below its asymptotic value, while k_1 closely approaches its asymptotic value from above around $t = 250$.

C. Nucleation of DB soliton trains: With confinement

In BEC experiments, harmonic confinement is naturally introduced. For this reason, in this section we aim to generalize our findings in the presence of a harmonic trapping potential and, for the numerical considerations to be presented below, we turn on the trapping potential in Eq. (2). Hereafter, we fix $\Omega = 0.011$. As in Sec. III B, we will first present the results for the zero-box configuration, and the results for the full-box configuration will follow.

Before proceeding to the results, first we want to remark that in the presence of a harmonic confinement our analytical estimates, obtained by solving the direct scattering problem (see Sec. II), are not expected to provide valid solutions. For example, we assumed NZBC which in turn define the asymptotic behavior of the solitons formed in terms of velocity and amplitude. It is clear that in the presence of the harmonic

potential such NZBC cannot be fulfilled. However, with an appropriate choice of parameters, the analytical solutions of the untrapped scenario (see Sec. III B) can be used as approximate solutions for the trapped scenario as we shall later show. For instance, our choice of a wide trapping potential ($\Omega = 0.011$) provides a ground state of the first component flatter around the center of the trap, which can at least locally resemble a constant background like that of the homogeneous case.

To induce the dynamics in our system, we first find the ground state of a single-component BEC by means of imaginary-time propagation. Then, we embed on top of the ground state our initial configuration [see Eq. (6)]. A schematic illustration of the aforementioned initial state is provided in Fig. 1(b). Moreover, to offer a direct comparison between the untrapped and the trapped scenarios, our choice of parameters is the same as in Sec. III B, i.e., $L = 5$, $q_0 = 1$, $\sigma = \pi/4$ with $\theta = \{0, \pi/2\}$, and $\sigma = \{6\pi/8, 5\pi/8\}$ with $\theta = \{0, \pi/2\}$, respectively (see also the relevant discussion around Figs. 9–12).

In order to characterize the solutions, we compute in each case the oscillation frequency of the DB solitons using the following, well-established expressions [9] (see also, e.g., [16]):

$$\omega_o^2 = \Omega^2 \left(\frac{1}{2} - \frac{\chi}{\chi_o} \right), \quad (28a)$$

$$\chi_o = 8 \sqrt{1 + \left(\frac{\chi}{4} \right)^2}, \quad \chi \equiv \frac{N_b}{q_o}, \quad (28b)$$

$$N_b \equiv \int_{-\infty}^{\infty} |q_b(x, t)|^2 dx = 2 \left(\frac{q_o^2}{|z_o|^2} - 1 \right) \text{Im } z_o, \quad (28c)$$

and describe the motion of the center of the DB solitons as

$$x_c(t) = \frac{v_o}{\omega_o} \sin(\omega_o t + \phi_o) + x_o. \quad (29)$$

Here, the amplitude of the oscillation is related to the velocity of the DB solitons [see Eq. (25c)] and the frequency of the trap [see Eq. (28a)]. Additionally, x_o is the equilibrium position, and ϕ_o is an additional phase factor. Both x_o and ϕ_o are fixed to zero unless stated otherwise.

It is important to remark here that, contrary to the single-component dynamics of dark and bright solitons in the presence of a harmonic potential, the amplitudes of each dark and bright counterpart of a DB soliton are not constant over time, but oscillate. Hence, we propose the following DB soliton estimate accounting for the amplitudes' dynamics (see Appendix B):

$$q_d^{(n)}(x, t) = q_o \cos \beta_n(t) - i q_o \sin \beta_n(t) \tanh \{v(t)[x - x_c(t)]\}, \quad (30a)$$

$$q_b^{(n)}(x, t) = -i \sin \beta_n(t) \sqrt{q_o^2 - |z_n|^2} \text{sech} \{v(t)[x - x_c(t)]\}, \quad (30b)$$

where we found that the angle parameter is now time dependent with the form

$$\cos^2 \beta_n(t) = \cos^2 \beta_n \cos^2(\omega_o t) + \frac{1}{2q_o^2} \Omega^2 \left(\frac{v_n}{\omega_o} \right)^2 \sin^2(\omega_o t). \quad (31)$$

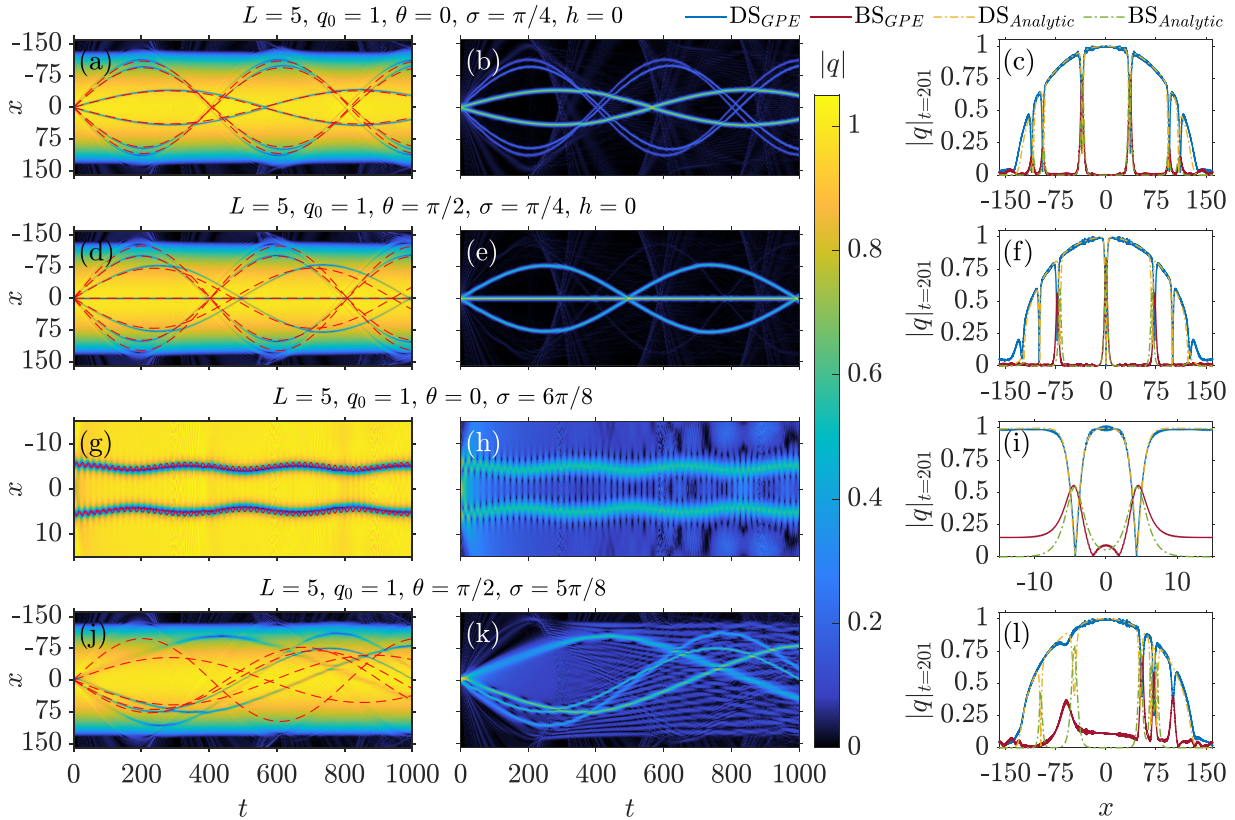


FIG. 13. Dark-bright solitons generated in the presence of a harmonic trap with a characteristic frequency $\Omega = 0.011$ for distinct choices of the involved parameters L, q_0, θ, σ (see legends). Each row, from top to bottom, has an initial configuration analogous to the FBTC from Figs. 9–12, respectively (see Sec. III B). Left (middle) column: Spatiotemporal evolution of $|q_1|$ ($|q_2|$) hosting the dark (bright) solitons. Red dashed lines correspond to the analytical trajectories [see Eq. (29)] using the eigenvalues from the untrapped scenario. Right column: Snapshots of $|q_1|$ and $|q_2|$ at $t = 201$ given by the CGPE (solid lines) and the analytic in-trap estimates of Eq. (32a) (dashed-dotted lines), for both dark (DS) and bright (BS) soliton counterparts. Note that the quantities shown are measured in transverse oscillator units.

From here, the uniformization variable can be expressed as $z(t) = |z_o|e^{i\beta(t)}$. The other time-dependent parameters can be obtained by substituting Eq. (31) in (24). Of course, if we turn off the trap ($\Omega = 0$ and $\omega_o = 0$) we recover $\beta(t) = \beta_o$.

Last, we design in-trap analytical estimates of the dark and bright soliton solutions as follows:

$$|q_1(x, t)|^2 = \left| q_o^2 \left| \prod_n \frac{q_d^{(n)}(x, t)}{q_o} \right|^2 - [q_o^2 - |q_{gs}(x)|^2] \right|, \quad (32a)$$

$$|q_2(x, t)|^2 = \left| \sum_n q_b^{(n)}(x, t) \right|^2. \quad (32b)$$

In Eq. (32a), the first term on the right-hand side corresponds to a dark soliton train solution in the absence of a trapping potential having a background amplitude q_o , where the product is performed over all the different solutions of a set of zeros $k_o = \{k_{-n}, \dots, k_n\}$. The second term properly shapes the former onto the trapped ground state $q_{gs}(x)$. Lastly, the absolute value on the right-hand side is introduced so as to ensure the positivity required by the left-hand side.

Our results are summarized in Fig. 13 and Table I. In Fig. 13 we show the spatiotemporal evolution of $|q_1|$ (left

column) and $|q_2|$ (middle column), each of which hosts, respectively, the dark and bright soliton counterparts of the dynamically generated DB solitons. Additionally, together with $|q_1|$ are depicted the DB soliton trajectories provided by Eq. (29) using the eigenvalues of the homogeneous solutions presented in Sec. III B (dashed red lines). Note here that each row corresponds to a different set of parameters, but with $L = 5$ and $q_o = 1$ fixed. For clarity, the dynamical evolution of the DB solitons formed is monitored up to times $t = 1000$ but the solitons remain intact while oscillating for times up to $t = 3000$. To offer a head-on comparison between the numerical results and the analytical in-trap estimates of Eq. (32) we also show a snapshot of $|q_1|$ and $|q_2|$ at $t = 201$ (right column) where both the numerical and the analytical results are placed on top of each other.

In Table I the analytically obtained oscillation frequency ω_o of each DB soliton illustrated in Fig. 13 is compared with the corresponding numerically identified frequency ω_{num} . The latter is measured by following the c.m. of each DB soliton and performing a fast Fourier transform on each obtained trajectory. In some cases, however, the presence of radiation hindered tracing the DB soliton c.m. and a manual fitting of ω_{num} was required. Since ω_o mostly depends on the number of particles hosted in the bright soliton N_b [see Eq. (28)],

TABLE I. Comparison between the analytically and numerically obtained oscillation frequencies ω_o and ω_{num} and the number of particles of a bright soliton N_b and N_b^{num} , respectively, for each identified DB soliton solution shown in Fig. 13. From left to right, each column set corresponds, from top to bottom, to each row in Fig. 13. Each soliton pair $k_{\pm i}$, with $i = 1, 2, \dots$, is identified using the notation introduced in Sec. III B. The relative error is defined as $\varepsilon_\omega = |\omega_o - \omega_{\text{num}}|/\omega_o$ (idem for ε_{N_b}). The frequencies ω_o and ω_{num} have an additional $\times 10^3$ factor. Other parameters used are $L = 5$, $q_o = 1$, and $\Omega = 0.011$. Note that the quantities shown are measured in transverse oscillator units (see text).

$h = 0, \sigma = \pi/4, \theta = 0$				$h = 0, \sigma = \pi/4, \theta = \pi/2$				$\sigma = 6\pi/8, \theta = 0^a$				$\sigma = 5\pi/8, \theta = \pi/2$			
k_o	ω_o	ω_{num}	ε_w	k_o	ω_o	ω_{num}	ε_w	$k_{\pm 1}$	ω_o	ω_{num}	ε_w	k_o	ω_o	ω_{num}	ε_w
				k_0	0	0	0	ω_β	0.3539	0.3537	0.0006	k_{-2}	6.958	6	0.14
$k_{\pm 1}$	5.615	5.548	0.025	$k_{\pm 1}$	6.670	6.35	0.048	ω_{OP}	0.0188	0.0195	0.032	k_{-1}	6.578	4.575	0.30
$k_{\pm 2}$	7.645	7.745	0.013	$k_{\pm 2}$	7.778	7.989	0.027					k_0	5.323	6.283	0.18
$k_{\pm 3}$	7.704	7.813	0.014	$k_{\pm 3}$	7.775	8.015	0.031					k_1	5.523	3.725	0.33
k_o	N_b	N_b^{num}	ε_{N_b}	k_o	N_b	N_b^{num}	ε_{N_b}	$k_{\pm 1}$	N_b	N_b^{num}	ε_{N_b}	k_o	N_b	N_b^{num}	ε_{N_b}
				k_0	2.636	2.648	0.005		0.695	0.790	0.14	k_{-2}	0.815	0.887	0.088
$k_{\pm 1}$	2.182	2.201	0.008	$k_{\pm 1}$	1.098	1.120	0.020					k_{-1}	1.188	1.277	0.075
$k_{\pm 2}$	0.135	0.137	0.009	$k_{\pm 2}$	0.0001	0.0003	2					k_0	2.511	2.524	0.005
$k_{\pm 3}$	0.0756	0.0831	0.099	$k_{\pm 3}$	0.0035	0.0034	0.034					k_1	2.283	2.601	0.13

^aSee the discussion around Eqs. (34).

we also compare N_b to N_b^{num} . In order to obtain the number of particles of each bright soliton N_b^{num} from the numerical solution, a numerical integration with the integration limits properly taken around the bright soliton maxima is carried out [see Eq. (28c)]. Yet, in the full-box case scenarios, the presence of a nonzero background makes the choice of the integration limits difficult, which adds a slight error to our calculation. Overall, in most of the cases the relative error $\varepsilon_\omega = |\omega_o - \omega_{\text{num}}|/\omega_o$ (idem for N_b) is pretty low, suggesting that our analytical solutions, obtained by solving the direct scattering problem in the homogeneous setting, are a good approximation to characterize the solutions in the trapped scenario. Some exceptions are also discussed below.

1. Zero-box configuration

The first case example, shown in Figs. 13(a)–13(c), corresponds to an initial IP ($\theta = 0$) zero-box configuration ($h = 0$) with $\sigma = \pi/4$, analogous to the homogeneous case shown in Fig. 9. Here, three pairs of DB solitons are generated, as expected. Moreover, the motion of each DB soliton is near perfectly captured by Eq. (29), as depicted by the dashed red lines in Fig. 13(a). Also, in Fig. 13(c) we find a very good match between the numeric and analytic DB solitons, bearing our in-trap estimate solution (30).

The second case corresponds to an initial OP ($\theta = \pi/2$) zero-box configuration ($h = 0$) with $\sigma = \pi/4$. The latter is almost analogous to the homogeneous case shown in Fig. 10, featuring a static DB soliton formed at the center of the trap, surrounded by a pair of DB solitons and two pairs of (almost) pure dark solitons. The resulting dynamics are shown in Figs. 13(d)–13(f). In Fig. 13(d), the analytic trajectories capture pretty well the dynamics of the two most external pairs of dark solitons. Recall that in the homogeneous scenario the fastest DB soliton pair (k_3) presented a nonzero bright counterpart, almost nonexistent in Fig. 13(e). Additionally, the in-trap estimates present a very good agreement with the numerical results. A noticeable discrepancy concerns the central pair of DB solitons. The comparison between ω_o and ω_o^{num} for this pair is shown in the second column set of Table I (see

$k_{\pm 1}$). Despite the relative error being not greater than 5%, the long-time dynamics clearly captures its effect.

Also, although we use analytical estimates to describe the in-trap dynamics, a possible source of error is N_b [see Eq. (28)]. However, for the same DB soliton solution ($k_{\pm 1}$), in Table I it is shown that the relative error between N_b and N_b^{num} is of about 2%. The latter suggests that additional sources of error might be present. For instance, the emitted radiation produced during the interference process might be taken into account. In this sense, some approximations to Eq. (6), e.g., the sigmoid function, have been used to smoothen the steplike shape of the box, decreasing the amount of emitted radiation and showing a small improvement towards the analytical solution (dynamics not shown for brevity).

2. Full-box configuration

In Sec. III B, we found how a homogeneous setup with an initial full-box configuration, where the two components overlap inside the box, leads to the presence of a nonzero background in the component hosting bright solitons (see Figs. 11 and 12).

In Figs. 13(g)–13(i) we present the dynamics resulting from an initial IP ($\theta = 0$) full-box configuration with $\sigma = 6\pi/8$, which is the in-trap analog of the homogeneous case example shown in Fig. 11. The homogeneous case resulted into a pair of almost static DB solitons ($v \sim 0$) traveling nearly parallel to each other and performing oscillations around their own c.m., i.e., beating. Here, we identified the same pair of beating DB solitons. Moreover, their beating behavior can be characterized by the following expression [71]:

$$\omega_\beta = \frac{1}{2}(\kappa^2 + D^2), \quad (33)$$

with $\kappa^2 = v^2$ and $D^2 = \mu \cos^2 \phi - \eta^2 = A_d^2 - A_b^2$. Using the expressions from Eq. (25) we can rewrite Eq. (33) in terms of z_o ,

$$\omega_\beta = 2(\text{Re } z_o)^2 + \frac{1}{2}(\text{Im } z_o)^2, \quad (34)$$

yielding $\omega_\beta = 0.3539$. On the other hand, we numerically followed the c.m. of our DB soliton pair during the dynamics using the previous procedure described and obtained $\omega_\beta^{\text{num}} = 0.3537$. Comparing ω_β with $\omega_\beta^{\text{num}}$, we find an extremely good agreement.

Furthermore, in the presence of a harmonic confinement an additional oscillation mode is present in the dynamics, driving both DB solitons to perform out-of-phase oscillations around the center of the trap. In particular, the out-of-phase mode of the oscillations stems from the presence of the trap and the DB-DB soliton repulsive interaction, characteristic of DB soliton pairs with in-phase bright counterparts [72]. Of course, Eq. (29) assumes an oscillation frequency for single DB solitons, and thus it cannot provide a valid description of the motion of this DB soliton pair because it is coupled.

Nonetheless, in Ref. [43] explicit expressions of the energy of the interactions of a pair of DB solitons are provided. This allows us to derive the expression of the forces involving the dark-dark, bright-bright, and dark-bright interactions $F_{jk}(x) = -\partial_x E_{jk}(x)$ where $j, k = \{D, B\}$ and numerically solve the equations of motion for our particular DB soliton pair, i.e., $\ddot{x} = -\omega_o^2 x - F_{DD}(x) - F_{BB}(x) - 2F_{DB}(x)$. By doing so, we obtain the trajectory of the DB soliton pair and find the out-of-phase oscillation frequency $\omega_{OP} = 0.0188$, which nicely captures the numerically identified one $\omega_{OP}^{\text{num}} = 0.0195$. The latter presents only a relative error $\varepsilon_{OP} = 3\%$. Therefore, we can fully characterize the trajectories of the beating pair of DB solitons by the following expression:

$$x_{\pm}(t) = \mp A_{\beta} \cos(\omega_{\beta} t + \varphi_{\beta}) \pm A_{OP} \cos(\omega_{OP} t + \varphi_{OP}) \pm x_o, \quad (35)$$

where $A_{\beta, OP}$ denote the amplitude of the beating and out-of-phase oscillations, respectively, and $\varphi_{\beta, OP}$ are additional phases. Although the expressions provided in Ref. [43] were derived by means of perturbation theory and predict the oscillation frequency and amplitude of small perturbations, they still provide a good approximation for ω_{OP} in this case. On the contrary, since perturbation theory cannot provide the amplitude of oscillation, we fitted $A_{\beta, OP}$ in Eq. (35) to obtain the trajectories in Fig. 13(g). We also set $\varphi_{\beta, OP} = 0$.

It is worth noticing in Fig. 13(i), also in this case, the good performance of our analytic in-trap estimates at capturing both the DB soliton profiles, regardless of the presence of the background.

Lastly, we comment on the dynamics of an initial OP ($\theta = \pi/2$) full-box configuration with $\sigma = 5\pi/8$. The resulting spatiotemporal evolutions of $|q_1|$ and $|q_2|$ are shown in Figs. 13(j) and 13(k), respectively, and snapshots of $|q_1|$ and $|q_2|$ at $t = 201$ are depicted in Fig. 13(l). First, one can notice that, in Fig. 13(j), the analytic solutions (red dashed lines) fail to appropriately capture the dynamics of the DB solitons. By inspecting once more the analogous homogeneous case shown in Fig. 12, it is observed that the main quantities, i.e., v , A_d , and A_b [see Figs. 12(e)–12(g), respectively], are still way off from their asymptotic values at $t = 250$. Consequently, the generated DB solitons monitored in the dynamics do not correspond to the analytically expected ones since the former started the in-trap oscillations at earlier times than $t = 250$, which interrupted their natural approach to the expected asymptotic solutions. For instance, from the expected five DB

soliton solutions only four are dynamically generated and, as mentioned above, ω_o and ω_{num} differ significantly, with errors well above 14%.

Nevertheless, with an appropriate fit of the parameters to Eq. (29), it can be shown that despite not having the predicted DB solitons, the dynamically formed structures perfectly follow the DB soliton trajectories (fitting not shown for brevity). Additionally, the fitted parameters applied to our analytical estimates provide a very accurate description of the DB soliton profiles. However, for consistency, in Figs. 13(j)–13(l) we compare the numerically obtained results with the analytical ones, rather than with the fitted estimates.

For completeness, we also considered in-trap dynamics beyond the Manakov limit, i.e., $g_{jk} \neq 1$ (results not shown here for brevity). In particular, and motivated by relevant studies such as those of Refs. [73,74], we first used for the intracomponent and intercomponent interaction strengths $g_{11} = 1.004$, $g_{22} = 0.95$, and $g_{12} = g_{21} = 0.98$, respectively, corresponding to a system of ^{87}Rb atoms in the $|1, -1\rangle$ and $|2, 1\rangle$ hyperfine states. This choice of parameters corresponds to a weakly immiscible mixture, i.e., $g_{11}g_{22} < g_{12}g_{21}$. Additionally, we also considered a weakly miscible regime $g_{11}g_{22} > g_{12}g_{21}$ by tuning $g_{12} = 0.95$. Experimentally, this could be achieved by means of a Feshbach resonance [66].

In both cases, the results are qualitatively similar to the ones presented in the Manakov limit (see Fig. 13), and the dark-bright soliton structures emerging in these more realistic setups survive even for long times. Not only that, but the overall picture is well preserved and the analytical estimates presented in the paper describe with great fidelity most of the cases, at least during the early-time dynamics. Some of the major differences when comparing these results with the dynamics in the Manakov limit are (i) the presence of a non-negligible amount of noise in the condensates, mostly caused by the overlap of the two components, and (ii) slightly faster dynamics than those in the Manakov limit.

IV. CONCLUSIONS AND FUTURE PERSPECTIVES

In this work, we have investigated the on-demand generation of DB soliton trains arising in a 1D two-component BEC both in the absence and in the presence of a harmonic trap. We have shown that it is possible to fully characterize a DB soliton array dynamically generated from a box-type initial configuration when a second component is present inside the box. In particular, we have analytically solved the direct scattering problem for the defocusing VNLS equation utilizing the aforementioned ansatz and obtained expressions for the discrete eigenvalues of the scattering problem. The latter are directly related to the amplitudes and velocities of the conforming DB solitons and allowed us to construct the exact DB soliton waveforms making use of the IST.

In order to better understand the role of the geometry of the initial box-type configuration in the generation of DB solitons, we explored a wide range of parametric selections. In general, a wider box generates a higher number of DB soliton structures. However, the presence of the second component inside the box hinders the appearance of such entities, compared to the single-component case. If instead both components are present inside the box, the intercomponent interactions

practically prevent the emergence of soliton structures unless the presence of the second component overcomes the presence of the first one. Moreover, we also investigated the effect of a possible phase difference between the distinct regions of the box. If all regions are in phase, the number of solitons formed is even, and all of them are paired. Specifically, each pair consists of DB solitons that share the same characteristics but travel with opposite velocities. On the contrary, when the sides of the box are out of phase, the number of DB solitons is odd and at least one DB soliton appears to be unpaired. In particular, if the second component is the only one present in the inner box region, the unpaired DB soliton is static. However, if the majority component is also inside the box, there exists an extra phase jump at the interphase separating the inner and the outer regions of the box, breaking the phase symmetry of the system and leading to the creation of asymmetric DB soliton arrays. In such a situation, all solutions are unpaired and the number of solitons formed depends on the presence of the components inside the box.

To test our analytical findings, we performed direct numerical integration of the multicomponent system at hand. In all the cases in the absence of confinement, we have found that the dynamically produced solitons approach asymptotically the analytically predicted DB amplitudes and velocities. In those cases where the initial configuration mixes both components inside the box, we found that the intercomponent interaction stimulates the presence of a finite background surrounding the bright solitons, which leads to the emergence of other exotic structures such as beating DB solitons. Moreover, we also designed approximate expressions using the analytical solutions of the homogeneous setup to describe the dynamics of DB solitons in the presence of a harmonic trap. Also, we provided expressions for the oscillations of the amplitudes of the dark and bright solitons. Our estimates showed in most cases a remarkably good agreement with the observed dynamics, with deviations not larger than 5%.

An immediate extension of this work points towards richer systems, e.g., spinor BECs [75–77]. These systems are already experimentally realizable [78–80], and several works have already exposed the existence of stable solitonic structures both experimentally [31] and theoretically [81–85]. Yet, another possibility for future study is the construction of more complex initial configurations, consisting, for example, of multiple boxes in order to mimic phase structures such as the dark-antidark solitons realized in the experiments of Refs. [18,30]. The latter case, however, requires the scenario of miscibility between the two components. Finally, the generalization of considerations to higher dimensions and, e.g., vortex-bright solitons therein [16], could be another fruitful direction for future exploration.

ACKNOWLEDGMENTS

This work was funded by the Deutsche Forschungsgemeinschaft (DFG, German Research Foundation)-SFB-925, Project No. 170620586. This work is supported (G.C.K. and P.S.) by the Cluster of Excellence “Advanced Imaging of Matter” of the Deutsche Forschungsgemeinschaft(DFG)-EXC 2056, Project No. 390715994. This material is based

upon work supported by the U.S. National Science Foundation under Grants No. PHY-2110030 and No. DMS-1809074 (P.G.K.), as well as No. DMS-2009487 (G.B.) and No. DMS-2106488 (B.P.).

APPENDIX A: FURTHER INSIGHTS OF THE DB SOLITON SOLUTIONS

Since we are finding the eigenvalues as zeros of $s_{11}(k)$, it is important to relate $\text{Re } k_o$ and $\text{Im } k_o$ to z_o . From the definition of the uniformization variable one has $z_o = k_o + \lambda(k_o)$, but this relationship requires dealing with the branches of $\lambda(k_o)$. However, this can be bypassed as follows. From Eqs. (22) we have

$$\text{Re } k = \frac{1}{2} \left(1 + \frac{q_o^2}{|z|^2} \right) \text{Re } z, \quad (\text{A1a})$$

$$\text{Im } k = \frac{1}{2} \left(1 - \frac{q_o^2}{|z|^2} \right) \text{Im } z, \quad (\text{A1b})$$

and

$$\text{Re } \lambda = \frac{1}{2} \left(1 - \frac{q_o^2}{|z|^2} \right) \text{Re } z, \quad (\text{A2a})$$

$$\text{Im } \lambda = \frac{1}{2} \left(1 + \frac{q_o^2}{|z|^2} \right) \text{Im } z. \quad (\text{A2b})$$

The second relation shows that $\text{Im } \lambda > 0 \iff \text{Im } z > 0$, which restricts the eigenvalues as zeros of $s_{11}(z)$ in the upper-half plane of z , and $\beta \in (0, \pi]$. Additionally, when $\text{Im } z > 0$, $|z| < q_o \iff \text{Im } k < 0$. Thus, given that the upper half of the circle of radius q_o in the z plane is in one-to-one correspondence with the lower-half plane of the upper sheet of the Riemann surface, k_o eigenvalues can have any $\text{Re } k$ and $\text{Im } k < 0$, provided that $\text{Im } \lambda(k) > 0$. Note that the latter differs from the scalar case of Ref. [64] where $-q_o < k < q_o$.

In Eq. (26) it remains to express γ in terms of k_o , which can be done as follows. Let us for brevity introduce $x = \text{Re } k_o$ and $y = \text{Im } k_o$. Then, from Eqs. (A1) one has $\text{Re } z_o = 2x/(1 + \gamma^2)$, $\text{Im } z_o = 2y/(1 - \gamma^2)$, and $|z_o|^2 = q_o^2/\gamma^2 = (\text{Re } z_o)^2 + (\text{Im } z_o)^2$ which upon substitution yields

$$4 \frac{x^2}{(1 + \gamma^2)^2} + 4 \frac{y^2}{(1 - \gamma^2)^2} = \frac{q_o^2}{\gamma^2}, \quad (\text{A3})$$

namely, a (simplified) quartic equation for $\Gamma \equiv \gamma^2$:

$$\begin{aligned} \Gamma^4 - \frac{4}{q_o^2} (x^2 + y^2) \Gamma^3 - 2 \left(1 - \frac{4}{q_o^2} x^2 + \frac{4}{q_o^2} y^2 \right) \Gamma^2 \\ - \frac{4}{q_o^2} (x^2 + y^2) \Gamma + 1 = 0. \end{aligned} \quad (\text{A4})$$

The solutions of Eq. (A4) are

$$\begin{aligned} q_o^2 \gamma_{\pm}^2 = |k_o|^2 - \beta \pm \sqrt{2} \\ \times \sqrt{|k_o|^4 - 2q_o^2 (\text{Re } k_o)^2 + |k_o|^2 (q_o^2 - \beta)}, \end{aligned} \quad (\text{A5a})$$

$$\begin{aligned} q_o^2 \gamma_{\pm}^2 = |k_o|^2 + \beta \pm \sqrt{2} \\ \times \sqrt{|k_o|^4 - 2q_o^2 (\text{Re } k_o)^2 + |k_o|^2 (q_o^2 + \beta)}, \end{aligned} \quad (\text{A5b})$$

with

$$\beta = \sqrt{(q_o^2 + |k_o|^2)^2 - 4q_o^2 \text{Re}^2 k_o}. \quad (\text{A6})$$

The pair of solutions in Eq. (A5a) are complex conjugate, while those in Eq. (A5b) are real. We are interested in real solutions with $\gamma > 1$, which are then given by γ_+ in Eq. (A5b). Notice that γ_+ involves only real square roots, thus avoiding complex branches. Hence, using γ_+ in Eq. (26) provides all the soliton parameters in terms of $k_o = \text{Re} k_o + i \text{Im} k_o$ for arbitrary $\text{Re} k_o \in \mathbb{R}$ and $\text{Im} k_o < 0$.

At this point, it is also possible to retrieve the soliton parameters for the single-component case. Recall that, for the scalar defocusing NLS equation, the zeros are real and simple, belonging to the spectral gap $k \in (-q_o, q_o)$ [57,64]. This directly implies that $|z_o| = q_o \forall k_o$. Therefore, Eqs. (25) read as

$$A_d = q_o \sin \beta_o \equiv \sqrt{q_o^2 - k_o^2}, \quad (\text{A7a})$$

$$A_b = 0, \quad (\text{A7b})$$

$$v = -2q_o \cos \beta_o \equiv -2k_o. \quad (\text{A7c})$$

For completeness, we note here that it is also possible to obtain the zeros k_o given the soliton parameters A_d , A_b , and v . In particular, using Eqs. (25) we obtain

$$A_b^2 = A_d^2 \left(1 - \frac{|z_o|^2}{q_o^2}\right), \quad (\text{A8a})$$

$$\cos \beta_o = \pm \sqrt{1 - \frac{A_d^2}{q_o^2}}, \quad (\text{A8b})$$

$$\sin \beta_o = \frac{A_d}{q_o}. \quad (\text{A8c})$$

Recalling now that

$$\begin{aligned} z_{o\pm} &\equiv |z_o|(\cos \beta_o + i \sin \beta_o) \\ &= q_o \sqrt{1 - \frac{A_b^2}{A_d^2}} \left(\pm \sqrt{1 - \frac{A_d^2}{q_o^2}} + i \frac{A_d}{q_o} \right), \end{aligned} \quad (\text{A9})$$

$|z_o| < q_o$ is automatically satisfied and the sign of $\cos \beta_o$ is determined by Eq. (25c). If $v > 0$, then $\cos \beta_o > 0$, while if $v < 0$, then $\cos \beta_o < 0$. Now, substituting Eq. (A9) into (A1) yields

$$\begin{aligned} \text{Re} k_o &= \text{sgn}(v) \frac{q_o}{2} \sqrt{1 - \frac{A_d^2}{q_o^2}} \\ &\quad \times \left[\left(1 - \frac{A_b^2}{A_d^2}\right)^{-\frac{1}{2}} + \left(1 - \frac{A_b^2}{A_d^2}\right)^{\frac{1}{2}} \right], \end{aligned} \quad (\text{A10a})$$

$$\text{Im} k_o = -\frac{A_d}{2} \left[\left(1 - \frac{A_b^2}{A_d^2}\right)^{-\frac{1}{2}} - \left(1 - \frac{A_b^2}{A_d^2}\right)^{\frac{1}{2}} \right]. \quad (\text{A10b})$$

It is clear from the above expression that $\text{Im} k_o < 0$, and since $\text{Im} z_o > 0$ it follows that $\text{Im} \lambda(k_o) > 0$.

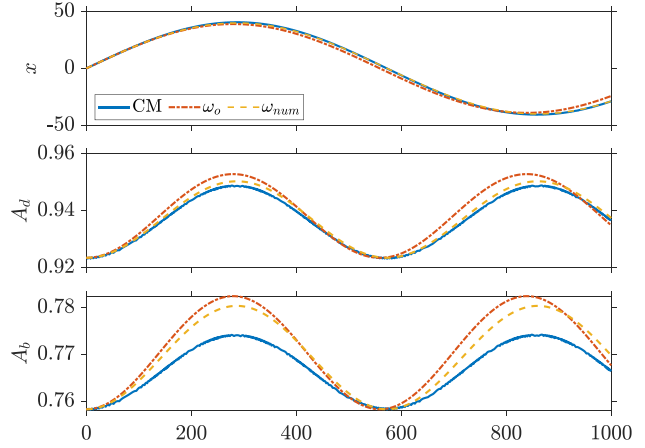


FIG. 14. Trajectory x and dark A_d and bright A_b amplitudes of the DB soliton solution k_1 shown in Fig. 9. The numerical magnitudes, obtained by following the c.m. (solid blue line), are compared to the analytical estimates in Eq. (29) and in Eqs. (25) [with $\beta_o \rightarrow \beta(t)$] given by the analytical in-trap oscillation frequency ω_o [see Eq. (28)] (dashed-dotted red lines), and the numerically obtained one ω_{num} (dashed yellow lines). Note that the quantities shown are measured in transverse oscillator units.

APPENDIX B: DARK-BRIGHT SOLITON AMPLITUDES IN THE PRESENCE OF A HARMONIC TRAPPING POTENTIAL

One important characteristic of solitons is that they preserve their shape. Also, it is well known that, in the presence of a harmonic trapping potential, DB solitons can undergo oscillations of frequency ω_o [see Eq. (28)]. However, here we found that DB solitons change size as they perform such oscillations in the trap. This particular feature is attributed to the intercomponent interaction g_{12} coupling the dark and bright counterparts, and to their constraints with the DB soliton velocity. Below we derive the expressions to describe such amplitude oscillations, but the role of $g_{12} = 1$ will be hidden in the equations.

At the turning points of their oscillatory trajectories ($x_t = \pm \text{Re} z_o / \omega_o$) the DB soliton velocity must be 0, which implies that its amplitudes are maximal [see Eqs. (25)]. In particular, for the dark counterpart that resides on top of the density background of the condensate $A_{d(\text{max})}^2 = |q_{gs}(x_t)|^2$. Following the same lines, at the center of the trap ($x = 0$) the velocity of the DB soliton is maximal, and thus its amplitudes are minimal and, more precisely, coincide with those of the homogeneous setup, i.e., $A_{d(\text{min})}^2 = q_o^2 \sin^2 \beta_o$.

Having now at hand the extremes of A_d , only the frequency of such oscillations is missing. In this case, it is enough to notice that in half of a trap oscillation period the dark amplitude would perform a full cycle. Therefore, it is straightforward to express the amplitude of the dark counterpart as

$$\begin{aligned} A_d^2(t) &= \frac{1}{2}(A_{d(\text{max})}^2 + A_{d(\text{min})}^2) \\ &\quad - \frac{1}{2}(A_{d(\text{max})}^2 - A_{d(\text{min})}^2) \cos(2\omega_o t), \end{aligned} \quad (\text{B1})$$

which after some algebra yields

$$A_d^2(t) = q_o^2 \sin^2 \beta_o \cos^2(\omega_o t) + |q_{gs}(x_t)|^2 \sin^2(\omega_o t). \quad (\text{B2})$$

Now, comparing Eq. (25a) to (B2), we obtain

$$\sin^2 \beta(t) = \sin^2 \beta_o \cos^2(\omega_o t) + \frac{|q_{gs}(x_t)|^2}{q_o^2} \sin^2(\omega_o t), \quad (\text{B3})$$

which is equivalent to Eq. (31), as shown below. From here, by replacing $\beta_o \rightarrow \beta(t)$ in Eqs. (23), (24), and (25), the DB soliton solution for in-trap oscillations follows [see Eq. (30)].

It is also important to notice that $|z(t)| = |z_o|$ does not change over time since the uniformization parameter z is unique to each DB soliton. Additionally, $\beta(t)$ satisfies the condition required by $0 < \beta_o \leq \pi$ which restricts the eigenvalues in the upper-half plane of z . For instance, $\beta(t) = \arcsin \frac{A_d(t)}{q_o}$ and, since $0 < A_d(t) \leq q_o \forall t$, then $0 < \beta(t) \leq \pi/2 \forall t$. Note that the values $\pi/2 < \beta(t) \leq \pi$, which are missing due to the $\arcsin(\dots)$, only affect the sign of the velocity of the soliton (25c). However, Eq. (25c) is not valid to define the DB soliton velocity in the presence of a trap, which instead is derived from Eq. (29).

One could also try to derive $A_d(t)$ from the velocity of the in-trap oscillations of the DB soliton provided by Eq. (29). It reads as

$$v(t) \equiv \frac{dx_c}{dt} = v_o \cos(\omega_o t). \quad (\text{B4})$$

Then, by comparing Eq. (B4) to (25c) we obtain

$$\cos \beta(t) = \cos \beta_o \cos(\omega_o t), \quad (\text{B5})$$

and, therefore,

$$A_d^2(t) = q_o^2 \sin^2 \beta(t) = q_o^2 - q_o^2 \cos^2 \beta_o \cos^2(\omega_o t). \quad (\text{B6})$$

In this case, we see that $A_d^2(\min) \leq A_d^2(t) \leq q_o^2$, with $A_d^2(\min) = q_o^2 \sin^2 \beta_o$. Obviously, $A_d^2(t)$ cannot be equal to q_o^2 since $|q_{gs}(x)|^2 \leq q_o^2$ and the only case with $A_d^2(t) = q_o^2$ corresponds to a static dark soliton centered at $x = 0$. Consequently, deriving $A_d(t)$ from Eq. (29) is clearly missing information about the trap geometry.

In particular, it would be enough to add the term $-V(x_t) \sin^2(\omega_o t)$ into Eq. (B6), where $x_t = \pm v_o/\omega_o$ is the turning point of the in-trap oscillations of the DB soliton. After some trivial calculations we recover

Eq. (B2):

$$A_d^2(t) = q_o^2 \sin^2 \beta_o \cos^2(\omega_o t) + [q_o^2 - V(x_t)] \sin^2(\omega_o t), \quad (\text{B7})$$

where $[q_o^2 - V(x_t)] = |q_{gs}(x_t)|^2$ is the well-known Thomas-Fermi approximation [86,87].

To adequately approach this problem, we can define a complex trajectory

$$\tilde{x}(t) = \frac{v_o}{\omega_o} \left(\sin(\omega_o t) + \frac{i}{\sqrt{2\gamma}} \frac{\Omega}{\omega_o} \cos(\omega_o t) \right), \quad (\text{B8})$$

where the soliton trajectory is $x_c(t) = \text{Re} \tilde{x}(t)$, and the trap geometry is taken into account by the imaginary term. From here, we derive $\tilde{x}(t)$ over time to obtain the (complex) velocity,

$$\tilde{v}(t) = v_o \left(\cos(\omega_o t) - \frac{i}{\sqrt{2\gamma}} \frac{\Omega}{\omega_o} \sin(\omega_o t) \right). \quad (\text{B9})$$

Then, comparing (B9) to Eq. (25c) we obtain our final expression (31),

$$\cos^2 \beta(t) = \cos^2 \beta_o \cos^2(\omega_o t) + \frac{1}{2q_o^2} \Omega^2 \left(\frac{v_o}{\omega_o} \right)^2 \sin^2(\omega_o t), \quad (\text{B10})$$

containing the information of the trap geometry. Again, Eq. (B3) can be retrieved by performing an appropriate manipulation of Eq. (B10).

In order to compare the analytical estimate of Eq. (B10) with numerical DB soliton dynamics, the DB soliton k_1 from Fig. 9 is placed alone at the center of a BEC trapped in the harmonic confinement used in this work (see Sec. III C). Since $v_{k_1}(t=0) \neq 0$ it undergoes oscillations. By following its c.m., we monitor its position x and its dark A_d and bright A_b amplitudes over time.

In Fig. 14, the trajectory and amplitudes of k_1 obtained from following its c.m. (solid blue lines) are compared to the analytical estimates in Eq. (29) and in Eq. (25) [with $\beta_o \rightarrow \beta(t)$] given by the analytical in-trap oscillation frequency ω_o [see Eq. (28)] (dashed-dotted red lines), and the numerically obtained one ω_{num} (dashed yellow lines). Here, the oscillations of A_d and A_b are clearly identified. Also, our analytical estimates are in good agreement with the numerical findings, with relative errors not larger than 1% at the instant of maximum discrepancy. In this case we define the relative error as $\varepsilon(A) = |A_{\text{c.m.}} - A_{\omega_{\text{num}}}|/A_{\text{c.m.}}$, which yields $\varepsilon(A_d) = 0.0015$ and $\varepsilon(A_b) = 0.0079$.

- [1] C. J. Pethick and H. Smith, *Bose-Einstein Condensation in Dilute Gases*, 2nd ed. (Cambridge University Press, Cambridge, 2008).
- [2] L. Pitaevskii and S. Stringari, *Bose-Einstein Condensation and Superfluidity*, International Series of Monographs on Physics, Vol. 164 (Oxford University Press, New York, 2016).
- [3] P. G. Kevrekidis, D. J. Frantzeskakis, and R. Carretero-González, *The Defocusing Nonlinear Schrödinger Equation: From Dark Soliton to Vortices and Vortex Rings*, Other Titles

in Applied Mathematics (Society for Industrial and Applied Mathematics, Philadelphia, 2015).

- [4] D. J. Frantzeskakis, *J. Phys. A: Math. Theor.* **43**, 213001 (2010).
- [5] F. K. Abdullaev, A. Gammal, A. M. Kamchatnov, and L. Tomio, *Int. J. Mod. Phys. B* **19**, 3415 (2005).
- [6] C. J. Myatt, E. A. Burt, R. W. Ghrist, E. A. Cornell, and C. E. Wieman, *Phys. Rev. Lett.* **78**, 586 (1997).
- [7] D. S. Hall, M. R. Matthews, J. R. Ensher, C. E. Wieman, and E. A. Cornell, *Phys. Rev. Lett.* **81**, 1539 (1998).

- [8] D. M. Stamper-Kurn, M. R. Andrews, A. P. Chikkatur, S. Inouye, H.-J. Miesner, J. Stenger, and W. Ketterle, *Phys. Rev. Lett.* **80**, 2027 (1998).
- [9] T. Busch and J. R. Anglin, *Phys. Rev. Lett.* **87**, 010401 (2001).
- [10] P. Öhberg and L. Santos, *Phys. Rev. Lett.* **86**, 2918 (2001).
- [11] P. G. Kevrekidis, H. E. Nistazakis, D. J. Frantzeskakis, B. A. Malomed, and R. Carretero-González, *Eur. Phys. J. D* **28**, 181 (2004).
- [12] B. J. Dabrowska-Wüster, E. A. Ostrovskaya, T. J. Alexander, and Y. S. Kivshar, *Phys. Rev. A* **75**, 023617 (2007).
- [13] M. A. Hofer, J. J. Chang, C. Hamner, and P. Engels, *Phys. Rev. A* **84**, 041605(R) (2011).
- [14] I. Danaïla, M. A. Khamehchi, V. Gokhroo, P. Engels, and P. G. Kevrekidis, *Phys. Rev. A* **94**, 053617 (2016).
- [15] C. Qu, L. P. Pitaevskii, and S. Stringari, *Phys. Rev. Lett.* **116**, 160402 (2016).
- [16] P. G. Kevrekidis and D. J. Frantzeskakis, *Rev. Phys.* **1**, 140 (2016).
- [17] I. Morera, A. Muñoz Mateo, A. Polls, and B. Juliá-Díaz, *Phys. Rev. A* **97**, 043621 (2018).
- [18] G. C. Katsimiga, S. I. Mistakidis, T. M. Bersano, M. K. H. Ome, S. M. Mossman, K. Mukherjee, P. Schmelcher, P. Engels, and P. G. Kevrekidis, *Phys. Rev. A* **102**, 023301 (2020).
- [19] A. P. Sheppard and Y. S. Kivshar, *Phys. Rev. E* **55**, 4773 (1997).
- [20] E. A. Ostrovskaya and Y. S. Kivshar, *Opt. Lett.* **23**, 1268 (1998).
- [21] Y. S. Kivshar and B. Luther-Davies, *Phys. Rep.* **298**, 81 (1998).
- [22] E. A. Ostrovskaya, Y. S. Kivshar, Z. Chen, and M. Segev, *Opt. Lett.* **24**, 327 (1999).
- [23] J. S. Kivshar and G. P. Agrawal, *Optical Solitons: From Fibers to Photonic Crystals* (Academic, San Diego, 2003).
- [24] E. P. Gross, *Nuovo Cimento* **20**, 454 (1961).
- [25] L. P. Pitaevskii, *Zh. Eksp. Teor. Fiz.* **40**, 646 (1961) [*Sov. Phys.–JETP* **13**, 451 (1961)].
- [26] C. Becker, S. Stellmer, P. Soltan-Panahi, S. Dörscher, M. Baumert, E.-M. Richter, J. Kronjäger, K. Bongs, and K. Sengstock, *Nat. Phys.* **4**, 496 (2008).
- [27] S. Middelkamp, J. Chang, C. Hamner, R. Carretero-González, P. Kevrekidis, V. Achilleos, D. Frantzeskakis, P. Schmelcher, and P. Engels, *Phys. Lett. A* **375**, 642 (2011).
- [28] D. Yan, J. J. Chang, C. Hamner, P. G. Kevrekidis, P. Engels, V. Achilleos, D. J. Frantzeskakis, R. Carretero-González, and P. Schmelcher, *Phys. Rev. A* **84**, 053630 (2011).
- [29] C. Hamner, J. J. Chang, P. Engels, and M. A. Hofer, *Phys. Rev. Lett.* **106**, 065302 (2011).
- [30] C. Hamner, Y. Zhang, J. J. Chang, C. Zhang, and P. Engels, *Phys. Rev. Lett.* **111**, 264101 (2013).
- [31] T. M. Bersano, V. Gokhroo, M. A. Khamehchi, J. D’Ambroise, D. J. Frantzeskakis, P. Engels, and P. G. Kevrekidis, *Phys. Rev. Lett.* **120**, 063202 (2018).
- [32] A. Farolfi, D. Trypogeorgos, C. Mordini, G. Lamporesi, and G. Ferrari, *Phys. Rev. Lett.* **125**, 030401 (2020).
- [33] X. Chai, D. Lao, K. Fujimoto, and C. Raman, *Phys. Rev. Research* **3**, L012003 (2021).
- [34] S. Lannig, C.-M. Schmied, M. Prüfer, P. Kunkel, R. Strohmaier, H. Strobel, T. Gasenzer, P. G. Kevrekidis, and M. K. Oberthaler, *Phys. Rev. Lett.* **125**, 170401 (2020).
- [35] S. Rajendran, P. Muruganandam, and M. Lakshmanan, *J. Phys. B: At., Mol. Opt. Phys.* **42**, 145307 (2009).
- [36] C. Yin, N. G. Berloff, V. M. Pérez-García, D. Novoa, A. V. Carpentier, and H. Michinel, *Phys. Rev. A* **83**, 051605(R) (2011).
- [37] V. Achilleos, P. G. Kevrekidis, V. M. Rothos, and D. J. Frantzeskakis, *Phys. Rev. A* **84**, 053626 (2011).
- [38] A. Álvarez, J. Cuevas, F. R. Romero, and P. G. Kevrekidis, *Phys. D (Amsterdam)* **240**, 767 (2011).
- [39] A. Álvarez, J. Cuevas, F. R. Romero, C. Hamner, J. J. Chang, P. Engels, P. G. Kevrekidis, and D. J. Frantzeskakis, *J. Phys. B: At., Mol. Opt. Phys.* **46**, 065302 (2013).
- [40] W. Wang and P. G. Kevrekidis, *Phys. Rev. E* **91**, 032905 (2015).
- [41] G. Biondini, D. K. Kraus, B. Prinari, and F. Vitale, *J. Phys. A: Math. Theor.* **48**, 395202 (2015).
- [42] G. C. Katsimiga, G. M. Koutentakis, S. I. Mistakidis, P. G. Kevrekidis, and P. Schmelcher, *New J. Phys.* **19**, 073004 (2017).
- [43] G. C. Katsimiga, J. Stockhofe, P. G. Kevrekidis, and P. Schmelcher, *Phys. Rev. A* **95**, 013621 (2017).
- [44] G. C. Katsimiga, S. I. Mistakidis, G. M. Koutentakis, P. G. Kevrekidis, and P. Schmelcher, *Phys. Rev. A* **98**, 013632 (2018).
- [45] M. O. D. Alotaibi and L. D. Carr, *J. Phys. B: At., Mol. Opt. Phys.* **51**, 205004 (2018).
- [46] M. O. D. Alotaibi and L. D. Carr, *J. Phys. B: At., Mol. Opt. Phys.* **52**, 165301 (2019).
- [47] M. Arazo, M. Guilleumas, R. Mayol, and M. Modugno, *Phys. Rev. A* **104**, 043312 (2021).
- [48] S. Burger, K. Bongs, S. Dettmer, W. Ertmer, K. Sengstock, A. Sanpera, G. V. Shlyapnikov, and M. Lewenstein, *Phys. Rev. Lett.* **83**, 5198 (1999).
- [49] J. Denschlag, J. E. Simsarian, D. L. Feder, C. W. Clark, L. A. Collins, J. Cubizolles, L. Deng, E. W. Hagley, K. Helmerson, W. P. Reinhardt, S. L. Rolston, B. I. Schneider, and W. D. Phillips, *Science* **287**, 97 (2000).
- [50] R. Dum, J. I. Cirac, M. Lewenstein, and P. Zoller, *Phys. Rev. Lett.* **80**, 2972 (1998).
- [51] A. Weller, J. P. Ronzheimer, C. Gross, J. Esteve, M. K. Oberthaler, D. J. Frantzeskakis, G. Theocharis, and P. G. Kevrekidis, *Phys. Rev. Lett.* **101**, 130401 (2008).
- [52] M. Hofer, P. Engels, and J. Chang, *Phys. D (Amsterdam)* **238**, 1311 (2009).
- [53] W. P. Reinhardt and C. W. Clark, *J. Phys. B: At., Mol. Opt. Phys.* **30**, 785 (1997).
- [54] T. F. Scott, R. J. Ballagh, and K. Burnett, *J. Phys. B: At., Mol. Opt. Phys.* **31**, 329 (1998).
- [55] G. Theocharis, A. Weller, J. P. Ronzheimer, C. Gross, M. K. Oberthaler, P. G. Kevrekidis, and D. J. Frantzeskakis, *Phys. Rev. A* **81**, 063604 (2010).
- [56] V. E. Zakharov and A. B. Shabat, *Zh. Eksp. Teor. Fiz.* **64**, 1627 (1973) [*Sov. Phys.–JETP* **37**, 823 (1973)].
- [57] L. Faddeev and L. Takhtajan, *Hamiltonian Methods in the Theory of Solitons* (Springer, New York, 2007).
- [58] J. A. Espínola-Rocha and P. Kevrekidis, *Math. Comput. Simul.* **80**, 693 (2009).
- [59] F. Demontis, B. Prinari, C. van der Mee, and F. Vitale, *Stud. Appl. Math.* **131**, 1 (2013).
- [60] G. Biondini and B. Prinari, *Stud. Appl. Math.* **132**, 138 (2014).
- [61] G. Biondini and D. Kraus, *SIAM J. Math. Anal.* **47**, 706 (2015).
- [62] B. Prinari, M. J. Ablowitz, and G. Biondini, *J. Math. Phys.* **47**, 063508 (2006).

- [63] B. Prinari, G. Biondini, and A. D. Trubatch, *Stud. Appl. Math.* **126**, 245 (2011).
- [64] A. Romero-Ros, G. C. Katsimiga, P. G. Kevrekidis, B. Prinari, G. Biondini, and P. Schmelcher, *Phys. Rev. A* **103**, 023329 (2021).
- [65] S. Inouye, M. R. Andrews, J. Stenger, H.-J. Miesner, D. M. Stamper-Kurn, and W. Ketterle, *Nature (London)* **392**, 151 (1998).
- [66] C. Chin, R. Grimm, P. Julienne, and E. Tiesinga, *Rev. Mod. Phys.* **82**, 1225 (2010).
- [67] S. V. Manakov, *Zh. Eksp. Teor. Fiz.* **65**, 505 (1973) [*Sov. Phys.–JETP* **38**, 693 (1974)].
- [68] G. Biondini and E. Fagerstrom, *SIAM J. Appl. Math.* **75**, 136 (2015).
- [69] N. Bogoliubov, *J. Phys.* **11**, 23 (1947).
- [70] T. D. Lee, K. Huang, and C. N. Yang, *Phys. Rev.* **106**, 1135 (1957).
- [71] D. Yan, J. J. Chang, C. Hamner, M. Hofer, P. G. Kevrekidis, P. Engels, V. Achilleos, D. J. Frantzeskakis, and J. Cuevas, *J. Phys. B: At., Mol. Opt. Phys.* **45**, 115301 (2012).
- [72] M. Segev and G. Stegeman, *Phys. Today* **51**(8), 42 (1998).
- [73] K. M. Mertes, J. W. Merrill, R. Carretero-González, D. J. Frantzeskakis, P. G. Kevrekidis, and D. S. Hall, *Phys. Rev. Lett.* **99**, 190402 (2007).
- [74] M. Egorov, B. Opanchuk, P. Drummond, B. V. Hall, P. Hannaford, and A. I. Sidorov, *Phys. Rev. A* **87**, 053614 (2013).
- [75] Y. Kawaguchi and M. Ueda, *Phys. Rep.* **520**, 253 (2012).
- [76] D. M. Stamper-Kurn and M. Ueda, *Rev. Mod. Phys.* **85**, 1191 (2013).
- [77] G. C. Katsimiga, S. I. Mistakidis, P. Schmelcher, and P. G. Kevrekidis, *New J. Phys.* **23**, 013015 (2021).
- [78] D. M. Stamper-Kurn and W. Ketterle, in *Coherent Atomic Matter Waves*, Les Houches–Ecole d’Ete de Physique Theorique, edited by R. Kaiser, C. Westbrook, and F. David (Springer, Berlin, 2001), pp. 139–217.
- [79] M.-S. Chang, C. D. Hamley, M. D. Barrett, J. A. Sauer, K. M. Fortier, W. Zhang, L. You, and M. S. Chapman, *Phys. Rev. Lett.* **92**, 140403 (2004).
- [80] M.-S. Chang, Q. Qin, W. Zhang, L. You, and M. S. Chapman, *Nat. Phys.* **1**, 111 (2005).
- [81] H. E. Nistazakis, D. J. Frantzeskakis, P. G. Kevrekidis, B. A. Malomed, and R. Carretero-González, *Phys. Rev. A* **77**, 033612 (2008).
- [82] B. Xiong and J. Gong, *Phys. Rev. A* **81**, 033618 (2010).
- [83] A. Romero-Ros, G. C. Katsimiga, P. G. Kevrekidis, and P. Schmelcher, *Phys. Rev. A* **100**, 013626 (2019).
- [84] C.-M. Schmied and P. G. Kevrekidis, *Phys. Rev. A* **102**, 053323 (2020).
- [85] A. Abeya, B. Prinari, G. Biondini, and P. G. Kevrekidis, *Eur. Phys. J. Plus* **136**, 1126 (2021).
- [86] L. H. Thomas, *Math. Proc. Cambridge Philos. Soc.* **23**, 542 (1927).
- [87] E. Fermi, *Rend. Accad. Naz. Lincei* **6**, 602 (1927).

Observation of dense collisional soliton complexes in a two-component Bose-Einstein condensate

S. Mossman,^{1,2} G. C. Katsimiga,^{3,4} S. I. Mistakidis,^{5,6} A. Romero-Ros,⁴
T. M. Bersano,² P. Schmelcher,^{4,7} P. G. Kevrekidis,³ and P. Engels^{2,*}

¹Department of Physics and Biophysics, University of San Diego, San Diego, CA 92110

²Department of Physics and Astronomy, Washington State University, Pullman, Washington 99164-2814

³Department of Mathematics and Statistics, University of Massachusetts, Amherst MA 01003-4515

⁴Center for Optical Quantum Technologies, Department of Physics,

University of Hamburg, Luruper Chaussee 149, 22761 Hamburg, Germany

⁵ITAMP, Center for Astrophysics | Harvard & Smithsonian, Cambridge, MA 02138 USA

⁶Department of Physics, Harvard University, Cambridge, Massachusetts 02138, USA

⁷The Hamburg Centre for Ultrafast Imaging, University of Hamburg,
Luruper Chaussee 149, 22761 Hamburg, Germany

We present an experimental and theoretical study of hydrodynamic phenomena in a two-component atomic Bose-Einstein condensate emerging from the imprinting of a periodic spin pattern. By employing a microwave pulse-based winding technique, we prepare a tunable initial state which evolves into an array of solitary waves. We observe the ensuing dynamics, including shape deformations, the emergence of dark-antidark solitons, apparent spatial frequency tripling, and decay and revival of contrast related to soliton collisions. For the densest arrays, we obtain soliton complexes where solitons undergo continued collisions for long evolution times providing an avenue towards the investigation of soliton gases in atomic condensates.

Introduction. Since their first observation in water waves [1, 2], the dynamics of solitary wave structures has evolved into a major thrust within nonlinear science. These dispersionless, localized, coherent structures, which can undergo collisions without changing shape, are found in a wide range of integrable and near-integrable systems with broad applicability in optics [3], atomic physics [4], plasmas [5], fluids [6] and other fields [6, 7].

Dilute gas Bose-Einstein condensates (BECs) [8, 9] offer a highly flexible and controllable platform towards investigating the nonlinear dynamics and interactions of such solitary wave structures [4]. The experimental realization of multi-component BECs, discussed in Refs. [10, 11], has led to an additional wealth of nonlinear states including dark-bright (DB), dark-dark, and dark-antidark vector solitons, among many others summarized, e.g., in Ref. [12], as well as three-component [13, 14] and magnetic solitons [15]. While these works merely represent a small fraction of recent experimental and theoretical developments, they exemplify the remarkable flexibility offered by ultracold atomic systems for engineering and interrogating superfluid hydrodynamics.

Despite the intense research efforts directed towards solitons and their dynamics, most of the associated experimental BEC studies have concentrated on individual solitons or very small clusters (or molecules) thereof [16] and their interactions [14]. However, over the past few years there has been a substantial interest devoted to the realization and exploration of soliton gases, given their intriguing generalized hydrodynamic properties [17]. First theoretically introduced in 1971 as a dilute soliton gas [18], the concept was later extended to the dense soliton gas in the theory works of Refs. [19–

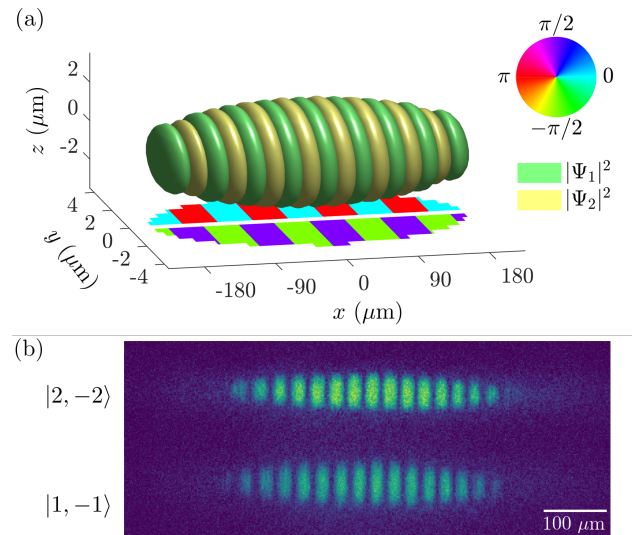


FIG. 1. (a) Example of a numerical initial configuration of the two-component elongated BEC. On the $x - y$ plane the condensate phase pattern corresponding to the $|2, -2\rangle$ ($|1, -1\rangle$) state is projected along the negative (positive) y -axis. (b) Example absorption image of the wound configuration after a winding time of $\tau = 40$ ms with the $|2, -2\rangle$ (top) imaged after 6 ms time-of-flight and $|1, -1\rangle$ (bottom) states imaged after 7.5 ms time-of-flight.

21]. However, experimental evidence for the realization of a soliton gas has been obtained only recently in the setting of shallow water waves [22, 23]. The relevant theory for integrable systems has been summarized in Ref. [24]. These investigations, along with earlier efforts, namely on light pulses in optical fiber ring resonators [25] and also

ones in soliton turbulence in shallow water waves [26], usher us into a new era of soliton lattices, soliton fluids, and soliton gases, as well as transitions between them [27]. Each of these experimental platforms provides a different framework for probing the physics underlying nonlinear hydrodynamics, each with their own advantages and limitations. In this work we will make use of the unique tunability, reproducibility, and mature numerical modeling methods of ultracold atomic gases to provide a new perspective on these topics.

In this Letter, we present a combined experimental and numerical study of hydrodynamic excitations arising from a periodic phase winding in a two-component BEC. This phase winding manifests as a sinusoidal magnetization pattern, alternating between spin-up and spin-down components of the condensate, which then evolves under nonlinear interactions into different hydrodynamic phenomena depending on the initial magnetization pattern. Previously, experimental efforts along these lines have led to different examples of pattern formation in atomic BECs including Faraday waves [28–31], space-time crystals [32], and bright soliton trains produced from a dynamical (modulational) instability [33–35]. In contrast to these earlier works, our method provides an initial condition from which exceptionally regular, highly tunable solitonic arrays will develop. In a first example, we demonstrate how a magnetic gradient applied to a broad magnetization pattern leads to the emergence of solitons from an array of hydrodynamic shock fronts. We then demonstrate the formation of an array of dark-antidark solitons which subsequently interact and evolve. For our tightest arrays, we obtain dense, long-lived collisional soliton complexes spanning essentially the full extent of the BEC.

Experimental Methods. Our experimental technique for the generation of dense nonlinear excitations is based on a two-pulse Ramsey sequence in the presence of a small magnetic gradient. We begin with elongated BECs of approximately 9×10^5 ^{87}Rb atoms in the $|F, m_F\rangle = |1, -1\rangle$ hyperfine state held in an optical trap with harmonic trap frequencies of $\omega/2\pi = \{2.5, 245, 258\}$ Hz. In the presence of a 10 G magnetic bias field oriented in the vertical direction, a fast microwave $\pi/2$ pulse is applied which coherently creates an equal superposition of atoms in the $|1, -1\rangle$ and the $|2, -2\rangle$ states. The intra- and intercomponent scattering lengths in the system are all very similar, but not exactly equal, which (see [36]) contributes to weakly miscible longtime dynamics.

During a subsequent wait time, referred to as the winding time τ , the 10 G bias field is supplemented by a slight gradient of 5.12(1) mG/cm along the long axis of the BEC. This leads to an accumulation of phase difference between the spin components which varies linearly across the length of the cloud. Then a second $\pi/2$ pulse is applied which, depending on the phase between the precessing spins and the microwave pulse, transfers

atoms into the $|2, -2\rangle$ state or back into the $|1, -1\rangle$ state. This process produces a sinusoidal magnetization pattern which, crucially for the subsequent dynamics, contains domains with π phase differences as shown in Fig. S1(a). Notice that contrary to earlier works, e.g. Ref. [37], there is no continuous application of the Rabi drive as we are interested in the undriven dynamics of the system after an original pattern has been established. Subsequent mean-field dynamics allow the sinusoidal phase pattern to relax into an array of alternating nonlinear waves as described below. The spatial periodicity of the produced pattern can be experimentally adjusted over a wide range by varying the winding time between the two microwave pulses.

Finally, we directly image the atomic density profile through absorption imaging of the $|2, -2\rangle$ spin state. The two spin components add together to form a uniform Thomas-Fermi distribution because the energy associated with deforming the overall density of the cloud far exceeds the energy scale for spin-mixing in this system. More precisely, the second spin state forms a complementary pattern to the observed state (see Fig. S1(b)) and will therefore be omitted in the forthcoming figures.

Numerical Method. To simulate the dynamics of the nonlinear phenomena of interest, we utilize the following system of coupled 3D Gross-Pitaevskii equations [8, 38]:

$$i\hbar\partial_t\Psi_j = \left(-\frac{\hbar^2}{2m}\nabla^2 + V(\mathbf{r}) + \sum_{k=1}^2 g_{jk}|\Psi_k|^2 \right) \Psi_j. \quad (1)$$

Here, $g_{jk} = 4\pi\hbar^2 a_{jk} N_j/m$ with $j = 1, 2$ indexing the relevant spin states, $N_j = 4.5 \times 10^5$ is the particle number per component, a_{jk} are the 3D intra- ($j = k$) and inter-component ($j \neq k$) scattering lengths, and m is the mass of a ^{87}Rb atom [36]. Additionally, the trapping potential $V(\mathbf{r}) = \sum_{\xi=x,y,z} m\omega_\xi^2 \xi^2/2$ is characterized by the aforementioned experimental trapping frequencies whose aspect ratio leads to a cigar-shaped geometry and hence precludes transverse instabilities [4, 9].

To initialize the dynamics, we first obtain the ground state of the self-interacting, yet intercomponent-decoupled, time-independent system of Eqs. (1). Then, we imprint the desired complementary configuration between the two components with wave number k_0 and a phase jump of π between adjacent domains [36] as shown in Fig. S1(a), while switching on the intercomponent coupling. Subsequently, the resulting waveform is evolved in time.

Dynamics. We begin discussing the dynamics in mixtures with the case of a 10 ms winding time, which generates the pattern of very wide windings shown in Fig. 2(a). While later in this work we remove the axial gradient after the winding process to observe the unbiased evolution, in this experiment we apply a magnetic gradient of 5 mG/cm along the long axis of the BEC to induce a small amount of counterflow between the two compo-

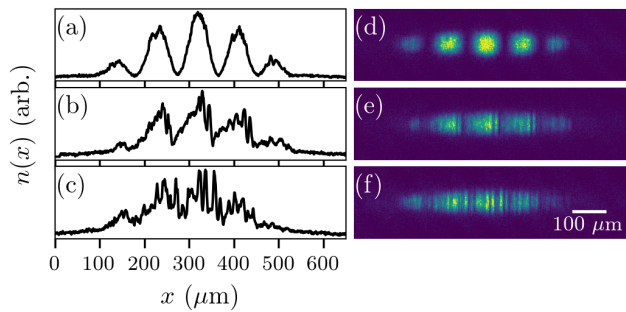


FIG. 2. Shock-wave formation and gradient catastrophe. Dynamics after a winding time of 10 ms in the presence of slight counterflow. Evolution times after end of winding are (a) 10 ms, (b) 110 ms, and (c) (130 ms). Panels (a-c) show integrated cross sections of panels (d-f).

nents. During the in-trap evolution, the initial sinusoidal shapes of the windings, seen in Fig. 2(a), steepen on their right side, approaching a gradient catastrophe [39]. The steepening is arrested by the formation of dark notches which first emerge at the steep edges [Fig. 2(b)] and then spread throughout the cloud [Fig. 2(c)], similarly to previous work in superfluid counterflow [40]. Such dynamics are a hallmark phenomenon of dispersive hydrodynamics where, in the absence of viscosity, a gradient catastrophe is regularized by the formation of dispersive shock waves [39]. These shock structures involve the formation of solitons, which persist for long times. These observations lay the foundation for the following dynamics in tighter wound clouds, where the size of each wound domain is reduced, offering less space for the shock-like dynamics to unfold.

Next, we consider a case where the initial pattern size is too small for a full dispersive shock wave train to evolve, but wide enough for the initial stages of such dynamics to still emerge. This case is reached after 20 ms winding, showcased in Fig. 3. Here, no magnetic gradient is applied during the evolution following the initial winding, and the dynamics sets in symmetrically on either side of each winding. In an initial stage, the sinusoidal shape of the initial windings [Fig. 3(c)] deforms and becomes triangular. This evolution transitions to the formation of plateaus with a bright peak in the center of each plateau as depicted in Fig. 3 (d), taken after an evolution time of 50 ms. The corresponding density profile is shown in Fig. 3(a) and is compared against the prediction of the 3D Gross-Pitaevskii equation for this winding configuration, shown in Fig. 3(b). These peaks, corroborated through our simulations, have the character of antidark solitons: bright solitonic peaks sitting on a finite background with a corresponding dark soliton in the other spin component [16, 41]. On both sides of each antidark peak, the steep edges of the plateaus lead to further evolution, as intuitively expected from

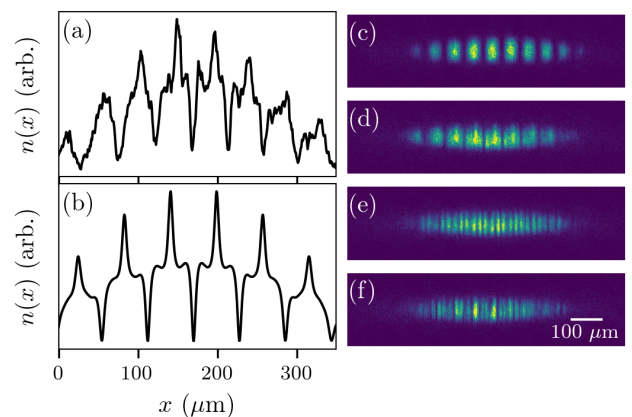


FIG. 3. Emergence of antidark solitons after a winding time of 20 ms. Evolution times after the winding process are (c) 0 ms, (d) 50 ms, (e) 80 ms and (f) 135 ms. Panel (a) is an integrated cross section of (d), revealing the formation of plateaus with antidark solitons and (b) is the corresponding cross section of the 3D simulations showing similar emergence of antidark solitons.

the edge dynamics seen in Fig. 2 (or, mathematically, from the well-known Riemann problem of nonlinear differential equations [39]). Notches appear and deepen, leading in this case to a tripling of the initial spatial period [Fig. 3(e) after 80 ms]. The width of these features is approximately on the length scale that we experimentally observe for DB solitons in our system, as demonstrated in Fig. 2, restricting the space against further soliton formation. Instead, the pattern becomes more irregular in amplitude at longer evolution times [Fig. 3(f) at 135 ms]. A noticeable observation is the occasional occurrence of peaks that are higher than the typical height of modulations in the cloud. We interpret these peaks as structures where adjacent solitons have constructively interfered – an effect that is familiar from the collision of bright solitons [35], in which the apparent number and height of peaks can vary through interactions.

For a winding time of 60 ms, a pattern periodicity of $16 \mu\text{m}$ is achieved. This pattern periodicity is too fine to allow for the formation of pronounced plateaus as was observed in the previous case. Here, the pattern remains virtually unchanged for the first 70 ms, as dynamics gradually set in, shown in Figs. 4(a) and 4(d). A prominent and reproducible new feature of the evolution is the emergence of a “fuzzy” stage in which the contrast of the peak structure is strongly diminished in large areas of the BEC, nearly disappearing into a uniform Thomas-Fermi profile [Figs. 4(b) and 4(e)], followed by a revival of the peaks [Figs. 4(c) and 4(f)]. This peculiar stage is also reproduced qualitatively in our full 3D simulations when slight residual counterflow induces currents in the two components [36]. We interpret this stage as a nearly simultaneous collision among the nonlinear waves

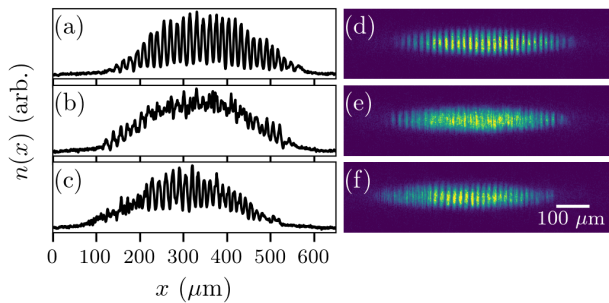


FIG. 4. Nucleation of a regular dense soliton train featuring a transient fuzzy phase. Stage of reduced contrast and revival after 60 ms of winding. Evolution times after end of winding are (a) 70 ms, (b) 80 ms, (c) 90 ms. Panels (a)–(c) depict integrated cross sections of (d)–(f), respectively.

throughout the array, enabled by the highly ordered initial conditions of the system and the good matching between the array periodicity and the natural length scale of the solitonic features.

Finally, as the culmination of the progression described above, we arrive at the case of a dense pattern obtained after a winding time of 100 ms (with a pattern spacing of about $9 \mu\text{m}$) presented in Fig 5. Here we observe dense collisional soliton complexes that maintain their qualitative character for long times. Figs. 5(a) and 5(d) show the initial magnetization pattern. The pattern contrast appears reduced due to imaging effects including imaging resolution, expansion of the atomic cloud during time of flight, and residual thermal fraction. After approximately 25 ms of evolution, the pattern becomes irregular. However, comparing the density profile after an evolution of 45 ms [Figs. 5(b) and 5(e)] with that after 400 ms [Figs. 5(c) and 5(f)] reveals that the pattern remains qualitatively unchanged in its overall characteristics (i.e., features widths, peak heights, cloud size etc.) for surprisingly long times.

A close inspection reveals that the disordered pattern maintains some structure: overlaying integrated cross sections with different evolution times (such as the particularly clear example in Fig. 6 with a cross section obtained after 150 ms) with the original pattern demonstrates that in many instances the original pattern periodicity is still maintained [Fig. 6(a-I)] but the amplitude of the peaks has changed. A frequent observation is also that individual original peaks seem to be missing or strongly reduced and their neighboring peaks have grown in amplitude [Fig. 6(a-II)]. Further corroborating evidence of this view is provided through one-dimensional simulations of the system provided in Fig. 6(b), where the time evolution of the location and phase of individual solitons can be traced through time.

Such dynamics are familiar from colliding bright solitons – we note in passing that it is interesting to com-

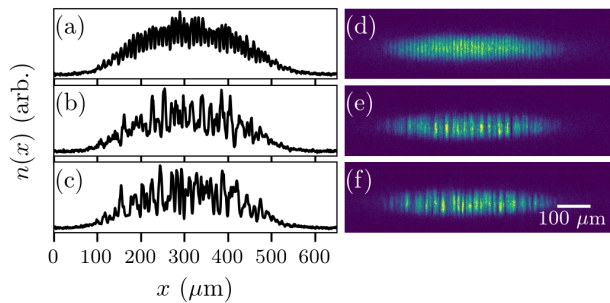


FIG. 5. Experimental observations of dense collisional soliton complex emerging after 100 ms of winding. Evolution times after end of winding are (a) 0 ms, (b) 45 ms, and (c) 400 ms. Panels (a-c) show integrated cross sections of (d-f), respectively.

pare, on a qualitative level, the cross sections in Figs. 5(e) and 5(f) to those published in Ref. [42]. There, a 128-soliton solution was numerically calculated for the focusing, one-dimensional, nonlinear Schrödinger equation – a challenging task involving arbitrary-precision techniques to achieve reliable accuracy. What sets our observations apart is that the experimentally observed collisional complexes are maintained for long periods of time as the solitons are held together by the harmonic trap confining the BEC. This provides a new experimental platform for the

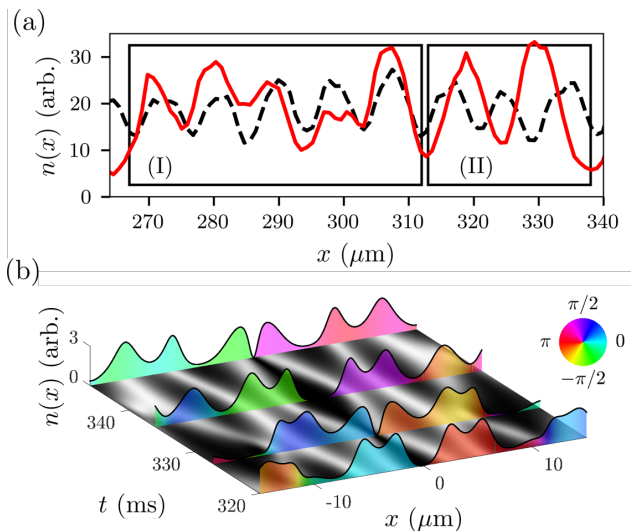


FIG. 6. Detailed observation of soliton crossings in dense collisional complexes emerging after 100 ms of winding. (a) Experimental cross sections after an evolution time of 150 ms (red, solid line) overlaid with initial cross section at 0 ms evolution (black, dashed) featuring regular soliton periodicity followed by tell-tale signatures of soliton collisions. (b) One-dimensional simulations show similar features in the time evolution of the wound system with the relative phase indicated by the color under the cross sections.

future experiments focusing on the intricate dynamics of interacting soliton complexes, including aspects of “thermalization” of the initial regular pattern.

Conclusions. Having reached the regime of dense collisional soliton complexes, our experiments open up a path to the study of dense soliton gases and soliton condensates as a new chapter for hydrodynamics in ultracold quantum gases. Recently, two pioneering experiments have reported the formation of a soliton gas in a long water tank [22, 23]. In the future, a comparison of soliton gases in different systems including water waves, nonlinear optics, and BECs will be highly insightful for developments in theoretical physics, applied mathematics and nonlinear optics. With BECs, a novel aspect is the possibility to dynamically change an axial harmonic confinement of the gas to modify the relevant “stress”. An analysis which will involve the development of the inverse scattering transform for the two-component nonlinear Schrödinger type problem [21], while out of the scope of the present manuscript, appears to us to be fully within reach. Excitations evolving on top of a regular soliton background, in terms of hypersolitons [43] or topological breathers [44, 45], are another exciting research directions that will provide new connections to condensed-matter systems.

Acknowledgements. We acknowledge Maren Mossman for early contributions to the experimental investigation as well as Gino Biondini and Barbara Prinari for helpful theory discussions. We acknowledge fruitful discussions lending context to this work at the Dispersive Hydrodynamics Program (2022) hosted by the Issac Newton Institute for Mathematical Sciences. S.M, T.B, and P.E. acknowledge funding from NSF through Grant No. PHY-1912540. P.E. acknowledges support from the Ralph G. Yount Distinguished Professorship at WSU. S.I.M. acknowledges support from the NSF through a grant for ITAMP at Harvard University. This research was also supported in part by the National Science Foundation under Grant No. NSF PHY-1748958 (S.I.M and P.S.). This work (P.S.) has been funded by the Deutsche Forschungsgemeinschaft (DFG, German Research Foundation) – SFB-925 – project 170620586. This material is also based upon work supported by the US National Science Foundation under Grant No. PHY-2110030 (P.G.K.).

* Email address: engels@wsu.edu

- [1] J. S. Russell, *The wave of translation in the oceans of water, air, and ether* (Trübner & Company, 1885).
- [2] D. J. Korteweg and G. De Vries, *The London, Edinburgh, and Dublin Philosophical Magazine and Journal of Science* **39**, 422 (1895).
- [3] Y. S. Kivshar and G. P. Agrawal, *Optical Solitons: From Fibers to Photonic Crystals* (Academic Press, 2003) pp. 1–540.
- [4] P. G. Kevrekidis, D. J. Frantzeskakis, and R. Carretero-González, *The Defocusing Nonlinear Schrödinger Equation* (SIAM, Philadelphia, 2015).
- [5] M. Kono and M. Skorić, *Nonlinear Physics of Plasmas* (Springer-Verlag, Heidelberg, 2010).
- [6] M. Ablowitz, *Nonlinear Dispersive Waves, Asymptotic Analysis and Solitons* (Cambridge University Press, Cambridge, 2011).
- [7] E. Infeld and G. Rowlands, *Nonlinear waves, solitons and chaos* (Cambridge University Press, Cambridge, 2000).
- [8] C. J. Pethick and H. Smith, *Bose-Einstein Condensation in Dilute Gases* (Cambridge University Press, Cambridge, United Kingdom, 2002).
- [9] L. Pitaevskii and S. Stringari, *Bose-Einstein condensation* (Oxford University Press, Oxford, 2003).
- [10] Y. Kawaguchi and M. Ueda, *Phys. Rep.* **520**, 253 (2012).
- [11] D. M. Stamper-Kurn and M. Ueda, *Rev. Mod. Phys.* **85**, 1191 (2013).
- [12] P. Kevrekidis and D. Frantzeskakis, *Rev. Phys.* **1**, 140 (2016).
- [13] T. Bersano, V. Gokhroo, M. Khamehchi, J. D’Ambroise, D. Frantzeskakis, P. Engels, and P. Kevrekidis, *Phys. Rev. Lett.* **120**, 063202 (2018).
- [14] S. Lannig, C.-M. Schmied, M. Prüfer, P. Kunkel, R. Strohmaier, H. Strobel, T. Gasenzer, P. G. Kevrekidis, and M. K. Oberthaler, *Phys. Rev. Lett.* **125**, 170401 (2020).
- [15] C. Qu, L. P. Pitaevskii, and S. Stringari, *Phys. Rev. Lett.* **116**, 160402 (2016).
- [16] G. C. Katsimiga, S. I. Mistakidis, T. M. Bersano, M. K. H. Ome, S. M. Mossman, K. Mukherjee, P. Schmelcher, P. Engels, and P. G. Kevrekidis, *Phys. Rev. A* **102**, 023301 (2020).
- [17] B. Doyon, T. Yoshimura, and J.-S. Caux, *Phys. Rev. Lett.* **120**, 045301 (2018).
- [18] V. Zakharov, *Sov. Phys. JETP* **33**, 538 (1971).
- [19] G. El, *Physics Letters A* **311**, 374 (2003).
- [20] G. A. El and A. M. Kamchatnov, *Physical Review Letters* **95**, 204101 (2005).
- [21] G. El and A. Tovbis, *Physical Review E* **101**, 052207 (2020).
- [22] I. Redor, E. Barthélemy, H. Michallet, M. Onorato, and N. Mordant, *Phys. Rev. Lett.* **122**, 214502 (2019).
- [23] P. Suret, A. Tikan, F. Bonnefoy, F. Copie, G. Ducrozet, A. Gelash, G. Prabhudesai, G. Michel, A. Cazaubiel, E. Falcon, G. El, and S. Randoux, *Physical Review Letters* **125**, 264101 (2020).
- [24] G. A. El, *Journal of Statistical Mechanics: Theory and Experiment* **2021**, 114001 (2021).
- [25] A. Schwache and F. Mitschke, *Phys. Rev. E* **55**, 7720 (1997).
- [26] A. Costa, A. R. Osborne, D. T. Resio, S. Alessio, E. Chrivi, E. Saggese, K. Bellomo, and C. E. Long, *Phys. Rev. Lett.* **113**, 108501 (2014).
- [27] W. Wang and P. G. Kevrekidis, *Phys. Rev. E* **91**, 032905 (2015).
- [28] P. Engels, C. Atherton, and M. A. Hoefer, *Phys. Rev. Lett.* **98**, 095301 (2007).
- [29] K. Kwon, K. Mukherjee, S. J. Huh, K. Kim, S. I. Mistakidis, D. K. Maity, P. G. Kevrekidis, S. Majumder, P. Schmelcher, and J.-y. Choi, *Phys. Rev. Lett.* **127**, 113001 (2021).
- [30] D. Hernández-Rajkov, J. E. Padilla-Castillo, A. del Río-Lima, A. Gutiérrez-Valdés, F. J. Poveda-Cuevas, and

- J. A. Seman, *New Journal of Physics* **23**, 103038 (2021).
- [31] R. Cominotti, A. Berti, A. Farolfi, A. Zenesini, G. Lamporesi, I. Carusotto, A. Recati, and G. Ferrari, *Phys. Rev. Lett.* **128**, 210401 (2022).
- [32] J. Smits, L. Liao, H. T. C. Stoof, and P. van der Straten, *Phys. Rev. Lett.* **121**, 185301 (2018).
- [33] K. Strecker, G. Partridge, A. Truscott, and R. Hulet, *Nature* **417**, 150 (2002).
- [34] P. J. Everitt, M. A. Sooriyabandara, M. Guasoni, P. B. Wigley, C. H. Wei, G. D. McDonald, K. S. Hardman, P. Manju, J. D. Close, C. C. N. Kuhn, S. S. Szigeti, Y. S. Kivshar, and N. P. Robins, *Phys. Rev. A* **96**, 041601 (2017).
- [35] J. H. V. Nguyen, D. Luo, and R. G. Hulet, *Science* **356**, 422 (2017).
- [36] See Supplemental Materials for additional details.
- [37] M. R. Matthews, B. P. Anderson, P. C. Haljan, D. S. Hall, M. J. Holland, J. E. Williams, C. E. Wieman, and E. A. Cornell, *Phys. Rev. Lett.* **83**, 3358 (1999).
- [38] S. Stringari and L. Pitaevskii, *Bose–Einstein Condensation* (Oxford University Press, Oxford, United Kingdom, 2003).
- [39] G. El and M. Hoefer, *Physica D: Nonlinear Phenomena* **333**, 11 (2016).
- [40] C. Hamner, J. J. Chang, P. Engels, and M. A. Hoefer, *Phys. Rev. Lett.* **106** (2011), 10.1103/physrevlett.106.065302.
- [41] I. Danaila, M. Khamehchi, V. Gokhroo, P. Engels, and P. Kevrekidis, *Phys. Rev. A* **94**, 053617 (2016).
- [42] A. A. Gelash and D. S. Agafontsev, *Phys. Rev. E* **98**, 042210 (2018).
- [43] M. Ma, R. Navarro, and R. Carretero-González, *Physical Review E* **93**, 022202 (2016).
- [44] Y. Mao, S. Chandramouli, and M. Hoefer, in *APS Division of Fluid Dynamics (Fall) 2021*, abstract id.E27.007 (APS, 2021).
- [45] M. Bertola, R. Jenkins, and A. Tovbis, *arXiv preprint arXiv:2210.01350* (2022), 10.48550/ARXIV.2210.01350.
- [46] D. A. Steck, “Rubidium 87 d line data,” .
- [47] Personal correspondence with Servaas Kokkelmans (2017).
- [48] C. T. Kelley, *Solving nonlinear equations with Newton’s method* (SIAM, 2003).
- [49] P. Ao and S. T. Chui, *Phys. Rev. A* **58**, 4836 (1998).
- [50] S. I. Mistakidis, A. G. Volosniev, R. E. Barfknecht, T. Fogarty, T. Busch, A. Foerster, P. Schmelcher, and N. T. Zinner, *arXiv preprint arXiv:2202.11071* (2022), <https://doi.org/10.48550/arXiv.2202.11071>.

Supplemental Material: “Observation of dense collisional soliton complexes in a two-component Bose-Einstein condensate”

EXPERIMENT CHARACTERIZATION

In this section, we provide a more complete description of the winding process described in the main text. We begin with an elongated BEC entirely in the $|1, -1\rangle$ state, which we will refer to as spin up, with a magnetic bias field of 10 G in the vertical direction perpendicular to the long axis of the condensate. Here, it is helpful to consider a collection of Bloch spheres, one for each point along the long axis, as schematically illustrated in Fig. S1, with all Bloch vectors pointing up and in phase.

A near-resonant microwave pulse is tuned to coherently transfer half of the atomic population to the $|2, -2\rangle$ state, which we will refer to as spin down, with a pulse time of approximately 0.1 ms. The pulse produces a uniform spin mixture across the condensate. Equivalently, this corresponds to a $\pi/2$ rotation of the Bloch vectors, leaving them in phase along the equator of the Bloch sphere. Hence, we refer to this pulse protocol as a $\pi/2$ pulse. The superposition state, shown in Fig. S1 on the second row, is then allowed to evolve in the optical trap during a variable amount of time, referred to as the winding time τ .

During the winding time, each Bloch vector precesses at a different rate and adjacent Bloch vectors will acquire a phase difference proportional to their energy difference as $\delta\phi = (\delta U/\hbar)t$. In the single particle limit, this energy difference is given by the differential Zeeman splitting induced by a small gradient of the magnetic field strength along the long axis of the BEC. We take the energy to be locally linear in the magnetic field for small changes giving $\delta\phi = \left(\frac{1}{\hbar} \frac{\partial U}{\partial B}\right)_{B=B_0} \Delta B t$, where the variation in

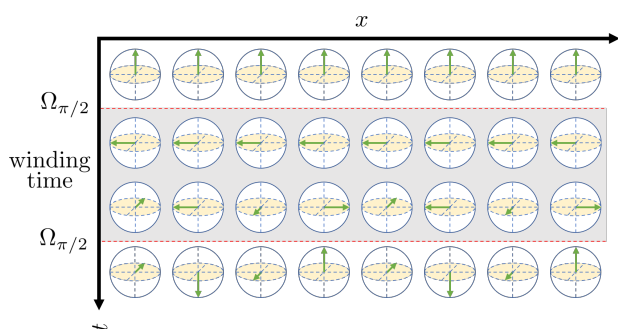


FIG. S1. Schematic of the winding process where position in the BEC is represented on the horizontal axis and time progresses downwards. A microwave pulse rotates the Bloch vector into the equatorial plane which then precesses at an increasing rate from left to right due to a magnetic field gradient during the winding time, shown in grey. A second microwave pulse then rotates the Bloch vectors again depending on their orientation at the end of the winding time.

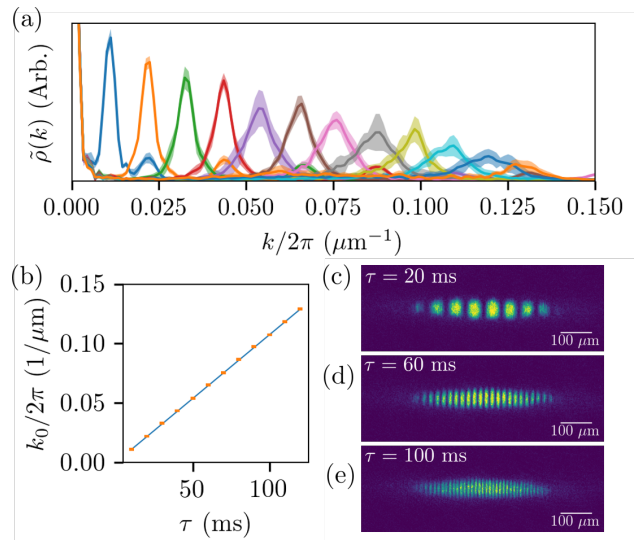


FIG. S2. (a) Experimental Fourier spectra for a range of winding times from $\tau = 10$ ms to $\tau = 120$ ms in steps of 10 ms. The k -vector of the corresponding fundamental peak k_0 increases monotonically with τ . Each spectrum is averaged over ten experimental realizations for a given winding time. The standard deviation in the averaged spectra is shown as a shaded region around each curve. (b) The center value wavenumber from fits to the peaks in panel (a). The standard error in each fit is smaller than the size of the markers. A linear fit indicates a winding rate of $1.074(2) (\mu\text{m s})^{-1}$. (c)–(e) Absorption images of the wound configuration after $\tau = 20, 60$ and 100 ms of winding, respectively.

the energy between the $|1, -1\rangle$ and $|2, -2\rangle$ states of ^{87}Rb at $B_0 = 10$ G is $2.0972h$ MHz/G using the Breit-Rabi formalism [46]. The change in magnetic field between two points in the condensate can then be approximated by assuming that the gradient is linear along the long axis of the condensate, leading to

$$\delta\phi = \left(\frac{1}{\hbar} \frac{\partial U}{\partial B}\right)_{B=B_0} \left(\frac{\partial B}{\partial x}\right) \Delta x t. \quad (\text{S1})$$

Finally, a second $\pi/2$ pulse is applied which continues to rotate the Bloch vector about the same axis as the initial pulse. The last row of Fig. S1 shows how, depending on the acquired phase, the Bloch vectors will be unaffected, rotated back to the up state, rotated to the down state, or someplace in between along a sinusoidal pattern. When the phase difference between two points in the condensate is 2π , both of those regions will be rotated in the same way by the final $\pi/2$ pulse and thus represent a full wavelength of the final magnetization pattern. Fig. S2(a) presents the progression of the winding density as the winding time is increased obtained through a

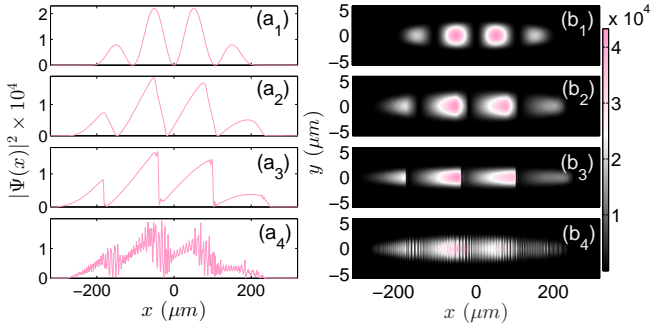


FIG. S3. Density snapshots for $\tau = 10\text{ms}$ windings depicting the integrated profiles along (a1)–(a4) y - z plane and (b1)–(b4) z direction. The time-instants illustrated from top (a_1), (b_1) to bottom (a_4), (b_4) correspond to $t = 0, 80, 125$, and 190 ms. In all cases, only the second component is visualized since the first is complementary to it. A counterdirectional displacement of the component's harmonic trap enforces inter-component counterflow with dark solitons initially emerging at the right shifted steep edges of the cloud.

Fourier transform of the density. Choosing $\Delta x = \lambda$, we identify the winding wavenumber

$$k_0(t) = \frac{2\pi}{\lambda} = \left(\frac{1}{\hbar} \frac{\partial U}{\partial B} \right)_{B=B_0} \left(\frac{\partial B}{\partial x} \right) t. \quad (\text{S2})$$

The slope extracted from Fig. S2(b) is the winding rate in Eq. (S2) from which we determine the magnetic field gradient in our experiment to be $5.12(1)$ mG/cm. Examples of the wound configuration are shown for winding time $\tau = 20, 60$, and 100 ms in Fig. S2(c)–(e), respectively.

As each spin domain of the prepared magnetization pattern has undergone an additional phase rotation on the Bloch sphere relative to the adjacent domains, we would expect the condensate wave function to also acquire phase gradients of π across each winding. In the condensate picture, the effect of the small magnetic gradient during the winding time can be understood as a force which accelerates the spin-up and spin-down components in opposite directions. This acceleration results in a relative velocity corresponding to the phase difference in the condensate wave function between the two spin components. This phase difference then emerges as phase windings after the final $\pi/2$ pulse remixes the two spin components, which then localize as phase jumps under mean field interactions to produce nearly stationary dark-bright solitons.

MEAN-FIELD IMPLEMENTATION OF THE SOLITON ARRAYS

To numerically study the nonequilibrium dynamics of the distinct arrays of nonlinear excitations we employ the dimensionless version of the 3D coupled Gross-Pitaevskii

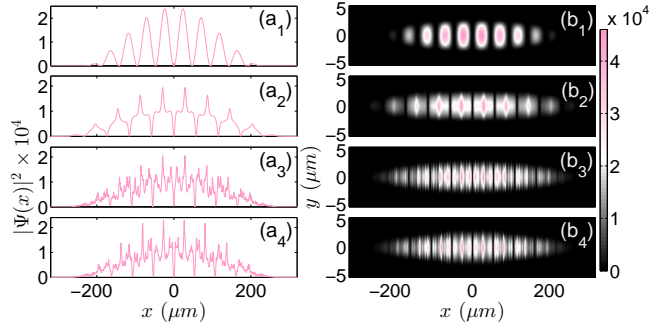


FIG. S4. Density profiles for $\tau = 20\text{ms}$ windings integrated along (a1)–(a4) y - z plane and (b1)–(b4) z direction. The evolution times shown from top (a_1), (b_1) to bottom (a_4), (b_4) are $t = 0, 80, 140$, and 190 ms. Solely the second component is illustrated since the first is complementary to it. Progressively antidark structures develop throughout the cloud.

equations [13, 16] provided in the main text, see also Eq. (1). As such, the underlying particle ($N_1 = N_2 = N/2 = 4.5 \times 10^5$) and mass ($m_1 = m_2 = m$) balanced ^{87}Rb mixture is described by

$$\begin{aligned} i\partial_t \Phi_1(\mathbf{r}, t) &= -\frac{1}{2} \nabla^2 \Phi_1(\mathbf{r}, t) + V(\mathbf{r}) \Phi_1(\mathbf{r}, t) \\ &\quad + (4\pi a_{1,1} N_1 |\Phi_1(\mathbf{r}, t)|^2 + 4\pi a_{1,2} N_2 |\Phi_2(\mathbf{r}, t)|^2) \Phi_1(\mathbf{r}, t), \\ i\partial_t \Phi_2(\mathbf{r}, t) &= -\frac{1}{2} \nabla^2 \Phi_2(\mathbf{r}, t) + V(\mathbf{r}) \Phi_2(\mathbf{r}, t) \\ &\quad + (4\pi a_{2,1} N_1 |\Phi_1(\mathbf{r}, t)|^2 + 4\pi a_{2,2} N_2 |\Phi_2(\mathbf{r}, t)|^2) \Phi_2(\mathbf{r}, t), \end{aligned} \quad (\text{S3})$$

Here, the Laplacian operator is $\nabla^2 \equiv \partial_x^2 + \partial_y^2 + \partial_z^2$, whilst the employed 3D scattering lengths for ^{87}Rb are $a_{1,1} = 100.40(10)$, $a_{2,2} = 98.98(4)$, and $a_{1,2} = 98.98(4)$ in units of the Bohr radius a_0 [47]. State 1 is $|F, m_F\rangle = |1, -1\rangle$, state 2 is $|2, -2\rangle$, and m is the mass of ^{87}Rb . The dimensionless 3D parabolic external potential reads $V(\mathbf{r}) = \frac{1}{2} \omega_x^2 (x^2 + (\omega_y/\omega_x)^2 y^2 + (\omega_z/\omega_x)^2 z^2)$ with $\mathbf{r} = (x, y, z)$. Following the experimental implementation the axial and transverse trapping frequencies are $(\omega_x, \omega_y, \omega_z) = 2\pi \times (2.5, 245, 258)$ Hz justifying a highly-elongated (cigar-shaped) geometry possessing an aspect ratio $\omega_x/\omega_y \approx \omega_x/\omega_z \approx 0.01$.

Moreover, the rescaling used for the spatial and temporal coordinates is $x' = a_{\text{ho}}^{-1} x$, $y' = a_{\text{ho}}^{-1} y$, $z' = a_{\text{ho}}^{-1} z$, with $a_{\text{ho}} = \sqrt{\hbar/m\omega_x}$ denoting the harmonic oscillator length along the longitudinal x -direction, and $t' = \omega_x t$, respectively. Accordingly, the wave function of each hyperfine state ($j = 1, 2$) is rescaled as $\Phi_j(x', y', z') = \sqrt{N_j/a_{\text{ho}}^3} \Psi_j(x, y, z)$ and the Laplacian is rescaled as $\nabla_{r'}^2 = a_{\text{ho}}^2 \nabla^2$.

To emulate the experimental preparation we first obtain the ground state of the intracomponent interacting 3D binary setting with suppressed intercomponent couplings utilizing a fixed point iterative scheme of the New-

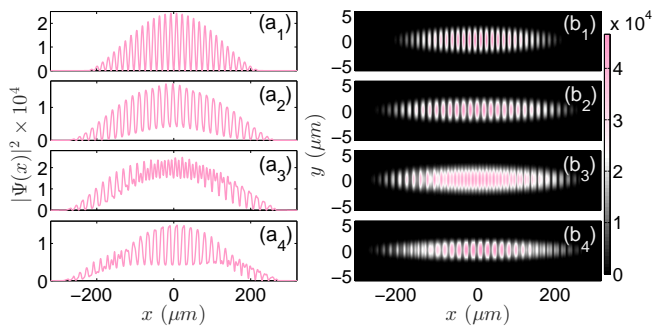


FIG. S5. Density profiles for $\tau = 60\text{ms}$ windings integrated along (a1)–(a4) y - z plane and (b1)–(b4) z direction. The times depicted from top (a₁), (b₁) to bottom (a₄), (b₄) are $t = 0, 70, 80,$ and 90 ms. Only the second component is depicted because the first complements it. The initial soliton array loses its contrast around $t = 80\text{ms}$ and a recurrence of the pattern takes place at later times ($t \sim 90\text{ms}$). A counterflow is induced by a counterdirectional displacement of each component's external trap.

ton type [48]. As such, the ground state wave functions of the individual components are spatially miscible (since $a_{1,2}^2 \ll a_{1,1}a_{2,2}$) [49, 50], while the total density has a Thomas-Fermi profile. As a subsequent step, we craft on top of the aforementioned ground states the following sinusoidal ansatz [see Fig. 1(a) in the main text]

$$\tilde{\Phi}_1(\mathbf{r}) = \sqrt{\cos^2(kx)}\Phi_1(\mathbf{r};0)e^{i\pi\cos(kx/2)}, \quad (\text{S4})$$

$$\tilde{\Phi}_2(\mathbf{r}) = \sqrt{\sin^2(kx)}\Phi_2(\mathbf{r};0)e^{i\pi\cos(\pi/4+kx/2)}, \quad (\text{S5})$$

where $\Phi_j(\mathbf{r};0)$ is the ground state of each component at $t = 0$. Notice that these crafted wave functions of the two components along the longitudinal x -direction are complementary with respect to one another. An almost perfect total Thomas-Fermi density profile occurs in the decoupled case with weak spatial undulations appearing for increasing (principal) wavenumbers $k = k_0/(2\pi)$. Finite intercomponent interactions for a fixed k_0 lead to more pronounced spatial undulations. To trigger the dynamics we switch on the intercomponent interactions and let the above system evolve for times up to $t = 200\text{ms}$. The spatiotemporal evolution of the two-component bosonic system is captured using a fourth-order (in time) Runge-Kutta method characterized by temporal and spatial discretization $dt = 10^{-4}$ and $dx = 0.03, dy = dz = 0.05$ respectively. Also, a second order finite difference scheme is employed to resolve the spatial derivatives.

DYNAMICAL FEATURES OF THE DISTINCT SOLITON ARRAYS

Characteristic density profiles during the nonequilibrium dynamics of the 3D system of coupled GPEs

[Eq. (S3)] are presented in Figs. S3, S4 and S5 for three winding protocols discussed in the main text, namely for $\tau = 10$ ms, 20 ms, and 60 ms, allowing us to dynamically generate a plethora of nonlinear excitations.

We start with the dilute winding pattern of $\tau = 10$ ms while also considering a counterflow between the two components. Counterflow is triggered via a counterdirectional displacement of the individual component's harmonic trap with strength $3\mu\text{m}$ and $6.5\mu\text{m}$ following the experimental procedure. The initial regular pattern consisting of four (five) density peaks in the second (first) component [Figs. S3(a1) and S3(b1)] gradually develops a triangular sharp edged configuration [Figs. S3(a2) and S3(b2)]. This is attributed to the counterflow featured by the participating hyperfine states. We remark that in the absence of counterflow, dark-antidark solitons build upon the components in a complementary fashion. These persistent waveforms also emerge for larger winding protocols, see our discussion below and the main text. Consecutively, these sharp density fronts develop at their edges dark solitons [Figs. S3(a3) and S3(b3)] stemming from the interference among the components. These solitary waves are progressively spread throughout the bosonic cloud [see in particular Figs. S3(a4) and S3(b4)]. Notice that all the above-described qualitative features are in line with the experimental observations [see Fig. 2 in the main text].

To investigate the dynamics of denser soliton trains we employ a $\tau = 20$ ms winding pattern in the absence of counterflow. At initial times a periodic pattern illustrated in Figs. S4(a1) and S4(b1) occurs, acquiring a triangular shape around $t = 35$ ms. The latter subsequently deforms into an antidark configuration [Figs. S4(a2)–(a4) and S4(b2)–(b4)] as it is also demonstrated in the experimental cross section, e.g., of Fig. 3(a) and 3(d) of the main text. These antidark structures persist in the course of the evolution even when drastic dynamics sets in with the antidarks becoming more irregular in amplitude [Figs. S4(a3) and S4(b3)]. Additionally, at later times ($t > 100\text{ms}$) due to adjacent soliton interactions high density peaks appear in both components having a complementary nature [Figs. S4(a4) and S4(b4)]. Notice that the amplitude of these density humps is significantly larger when compared to the overall background one. This observation is also captured by the actual experiment shown in Fig. 3(f) of the main text.

Turning to the $\tau = 60$ ms wound scenario, we again consider a residual counterflow as for the case of $\tau = 10$ ms in order to dynamically drive soliton interactions. It is found that the regularity of the initial pattern is sustained for evolution times up to 20 ms [Figs. S5(a1) and S5(b1)] as per the pertinent experimental process described in the main text and depicted in Fig. 4. Modifications in the depth of the ensuing waveforms take place e.g. around 70 ms, an outcome that can be traced back to the presence of currents induced by the aforementioned

counterflow [Figs. S5(a2) and S5(b2)]. A lower contrast region occurs at later evolution times [Fig. S5(a3) and S5(b3)] followed by a recurrence tendency towards the original array where solitons at the trap center are almost equally spaced and regularly ordered [Figs. S5(a4) and S5(b4)] in accordance with the experimental observations.

Additionally, a video depicting the real-time evolution

after $\tau = 100$ ms winding in a one-dimension simulation is provided in <https://wolke.physnet.uni-hamburg.de/index.php/s/cK5sCaSS9ZgtHRA>. These simulations are in qualitative agreement with the experimental observations made in Fig. 5 of the main text. Namely, the emergent highly dense soliton arrays feature collisions leading to spatial irregularities, while maintaining their overall characteristics for large evolution times.

Theoretical and numerical evidence for the potential realization of the Peregrine soliton in repulsive two-component Bose-Einstein condensates

A. Romero-Ros,¹ G. C. Katsimiga,^{1,2} S. I. Mistakidis^{3,4}, B. Prinari,⁵ G. Biondini^{5,6},
P. Schmelcher,^{1,2} and P. G. Kevrekidis⁷

¹Center for Optical Quantum Technologies, Department of Physics, University of Hamburg,
Luruper Chaussee 149, 22761 Hamburg, Germany

²The Hamburg Center for Ultrafast Imaging, University of Hamburg, Luruper Chaussee 149, 22761 Hamburg, Germany

³ITAMP, Center for Astrophysics | Harvard & Smithsonian, Cambridge, Massachusetts 02138, USA

⁴Department of Physics, Harvard University, Cambridge, Massachusetts 02138, USA

⁵Department of Mathematics, State University of New York, Buffalo, New York 14260, USA

⁶Department of Physics, State University of New York, Buffalo, New York 14260, USA

⁷Department of Mathematics and Statistics, University of Massachusetts Amherst, Amherst, Massachusetts 01003-4515, USA



(Received 12 December 2021; revised 30 March 2022; accepted 25 April 2022; published 17 May 2022)

The present work is motivated by the recent experimental realization of the Townes soliton in an effective two-component Bose-Einstein condensate by B. Bakkali-Hassan *et al.* [*Phys. Rev. Lett.* **127**, 023603 (2021)]. Here, we use a similar multicomponent platform to exemplify theoretically and numerically, within the mean-field Gross-Pitaevskii framework, the potential toward the experimental realization of a different fundamental wave structure, namely the Peregrine soliton. Leveraging the effective attractive interaction produced within the mixture's minority species in the immiscible regime, we illustrate how initialization of the condensate with a suitable power-law decaying spatial density pattern yields the robust emergence of the Peregrine wave in the absence and in the presence of a parabolic trap. We then showcase the spontaneous emergence of the Peregrine soliton via a suitably crafted wide Gaussian initialization, again both in the homogeneous case and in the trap scenario. It is also found that narrower wave packets may result in periodic revivals of the Peregrine soliton, while broader ones give rise to a cascade of Peregrine solitons arranged in a so-called Christmas-tree structure. Strikingly, the persistence of these rogue-wave structures is demonstrated in certain temperature regimes as well as in the presence of transversal excitations through three-dimensional computations in a quasi-one-dimensional regime. This proof-of-principle illustration is expected to represent a practically feasible way to generate and observe this rogue wave in realistic current ultracold atom experimental settings.

DOI: [10.1103/PhysRevA.105.053306](https://doi.org/10.1103/PhysRevA.105.053306)

I. INTRODUCTION

In 1966, Draper *et al.* [1] reported the detection of an oceanic wave event featuring a *freak* wave, namely a wave several times bigger than the average sea state. Nowadays these freak waves are referred to as rogue waves [2]. Rogue waves are extreme wave events that emerge out of nowhere and disappear without a trace [3,4]. Under appropriate approximations, they can be mathematically described by solutions of the nonlinear Schrödinger equation (NLS) [5–9]. This mathematical description of rogue waves allowed extrapolation of these phenomena to a large variety of nonlinear physical systems other than oceanic waves, ranging from nonlinear optics [10–14] to plasmas [15–17] and from liquid helium [18] to Bose-Einstein condensates (BECs) [19,20] (see also the reviews of Refs. [21–23]).

Among the different members of the rogue-wave family, arguably, the most celebrated one is the rational solution known as the Peregrine soliton [24]. Contrary to the Kuznetsov-Ma soliton [5,6], which is periodic in time, or the Akhmediev breather [8], which is periodic in space, the Peregrine soliton is a wave localized both in time and in space. In recent years, Peregrine solitons have been successfully real-

ized in water tank experiments [25–28], plasmas [29], and optical fibers [10,11,30,31], demonstrating the active interest of distinct communities in these, as well as similar wave events of higher order [32]. All of the above-mentioned physical settings, however, involve self-focusing media. Here, we report on the theoretical formulation and numerical implementation of the spontaneous nucleation of the Peregrine soliton in self-defocusing media within the mean-field framework.

Within the ultracold superfluid realm, scalar and multi-component BECs in the mean-field framework are accurately described by a variant of the NLS equation, the well-known Gross-Pitaevskii equation (GPE) [33]. In that light, it is natural to expect that rogue waves can exist in BEC systems [19,20,34–36]. Importantly, the high degree of controllability of such settings, e.g., in terms of tunable interatomic interactions through the aid of Feshbach [37,38] or confinement-induced [39,40] resonances, as well as the flexibility to realize almost arbitrary potential landscapes [41,42], renders these platforms ideal test beds for the study of rogue-wave formation.

It is also in this BEC context that the recent experimental realization of the so-called Townes soliton [43] came to fruition [20]. The Townes soliton is a planar,

real, nodeless, and radially symmetric stationary solution of the two-dimensional one-component *focusing* (i.e., attractive interaction) GPE. Interestingly, the Townes soliton was conceived theoretically [43] and realized experimentally [20] by reducing a two-component *defocusing* (i.e., repulsive interaction) setting to an effective *focusing* single-component one for a minority component [44] (in the presence of a dominant majority component [45]). Motivated by this recent realization of an effectively attractive dynamics, manifested in the broadly experimentally accessible two-component repulsive BEC setting [33,46], and the earlier work of Ref. [44], here we utilize this multicomponent platform to study the formation of the Peregrine soliton by solving the underlying GPEs. Recall that the realization of this rogue wave, which is an exact solution of the focusing NLS equation [24], in the BEC context, remains until now an experimental challenge, at least in part due to the modulational instability which the background of this wave suffers [4]. Here, we propose an alternative route for achieving the nucleation of this rational solution, paving the way for its controllable experimental observation in a repulsive BEC environment which can be routinely and stably produced in the laboratory.

More concretely, we initially exemplify how, under the appropriate choice of the inter- and intracomponent interactions, a two-component repulsive BEC can be effectively reduced to an attractive single-component one [20,44], thus allowing for the spontaneous emergence of the Peregrine soliton. We investigate such a rogue-wave generation both in the absence and in the presence of an external harmonic trapping potential but also within the two- and the effective single-component model. Here, very good agreement between the two models is demonstrated, verifying the existence of the Peregrine wave for the homogeneous setting while unveiling its recurrence in the confined setup.

We then study the nucleation of the rogue-wave pattern in the so-called semiclassical limit. The latter is addressed by initializing an experimentally accessible sufficiently wide Gaussian wave packet. It is found that the width of the Gaussian directly impacts the resulting dynamics, from the periodic revival of the Peregrine soliton toward the so-called umbilical gradient catastrophe [47]. The latter leads, in turn, to the formation of a cascade of Peregrine waves, also referred to as a Christmas-tree pattern. In our numerical computations, a Christmas-tree configuration is found to decay in the confined geometry, emitting dark-bright soliton-type structures which oscillate inside the parabolic trap featuring unexpected trajectories. For a recent experiment on the controllable generation and current state-of-the-art on multicomponent dark-bright solitons, see, e.g., Ref. [48]. Furthermore, in order to expose the robust features of the Peregrine wave, we also explore a number of variations of the two-component setup. Namely, by considering mass-imbalanced mixtures, we unveil that Peregrine formation, in general, can take place only in mixtures where the minority component is the heaviest one. Specifically, in this mass-imbalanced situation, the dark-bright patterns experience a breathing motion, on top of their in-trap oscillation, whose frequency depends on the size of the solitons formed.

Additionally, the robustness of the Peregrine in certain temperature regimes is unveiled through the dissipative Gross-

Pitaevskii framework [49,50]. Last, but definitely not least, the spontaneous nucleation of the Peregrine and Christmas-tree configurations is showcased in genuinely three-dimensional (3D) computations featuring a quasi-one-dimensional (1D) geometry. We believe that the numerical persistence of the configuration in this setting is strongly suggestive of the feasibility of our proposed experimental realization.

The flow of our presentation is as follows. In Sec. II, we provide a description of the repulsive two-component setup along with its reduction to an effective single-component attractive model. In Sec. III, we elaborate on the dynamical generation and features of the Peregrine soliton. First, we show the emergence of the Peregrine soliton in the absence and in the presence of an external trapping potential. Then, we extend our considerations to the semiclassical setting by using as an initial condition a broad Gaussian wave packet, again without and with a trap. In this latter scenario, we also consider the impact of mass imbalance. The effect of temperature on the nucleation of the Peregrine soliton is subsequently discussed in Sec. IV. Importantly, Sec. V elaborates on the generation of the Peregrine in 3D geometries yet in the realm of the quasi-1D regime. Finally, Sec. VI provides our conclusions and future perspectives. The Appendix presents a modulational instability structure that arises at long time dynamics, recently described and found in Refs. [51,52] but, contrary to our setup, for focusing media.

II. THE PEREGRINE WAVE IN A TWO-COMPONENT SETTING

A. Mean-field description

To emulate spontaneous Peregrine soliton generation, our starting point and the primary focus of our considerations will be the zero-temperature limit. The impact of dissipation is appreciated later on in Sec. IV. In the aforementioned limit, and also in 1D, the wave functions obey the following dimensionless system of coupled GPEs [33,46,53]:

$$i u_t = -\frac{1}{2\tilde{m}_u} u_{xx} + V_u(x)u + (g_{11}|u|^2 + g_{12}|v|^2)u, \quad (1a)$$

$$i v_t = -\frac{1}{2\tilde{m}_v} v_{xx} + V_v(x)v + (g_{21}|u|^2 + g_{22}|v|^2)v, \quad (1b)$$

The subscripts t and x indicate the time and spatial derivatives, respectively. The field u (v) describes the wave function of the majority (minority) component. Additionally, $\tilde{m}_u = m_u/M$, $\tilde{m}_v = m_v/M$, where m_u , m_v denote the mass of the corresponding components and $M = m_u m_v / (m_u + m_v)$ is the reduced mass. For our demonstration, we will assume the scenario $m_u = m_v \equiv m = 1$, unless stated otherwise. Such a mass-balanced mixture could be realized, for example, by the two different hyperfine states of ^{87}Rb [54] (see also the discussion below). The external potential of the system is given in the familiar parabolic form $V_j(x) = \frac{1}{2}\tilde{m}_j\Omega^2 x^2$. Here $\Omega = \omega_x/\omega_\perp$, where ω_x and ω_\perp denote the longitudinal and transverse trapping frequencies of the system, respectively. For a 1D cigar-shaped trap, they should obey $\omega_x \ll \omega_\perp$. Also, $g_{jj} = \frac{1}{\tilde{m}_j} \frac{a_{jj}}{a_\perp}$ and $g_{jk} = \frac{1}{2} \frac{a_{jk}}{a_\perp}$ are the effective intra- and intercomponent 1D interaction strengths, respectively, with a_{jk} denoting the s -wave scattering lengths accounting for

collisions between atoms of the same ($j = k$) or different ($j \neq k$) species.

In the dimensionless units used here, the densities $|u|^2$ and $|v|^2$, length, energy, and time are measured in units of $(2a_\perp)^{-1}$, $a_\perp = \sqrt{\hbar/(M\omega_\perp)}$, $\hbar\omega_\perp$, and ω_\perp^{-1} , respectively. In this sense, typical evolution times of the order of 10^3 when considering, for instance, a trap with $\omega_x \approx 2\pi \times 1$ Hz and $\omega_\perp = 2\pi \times 400$ Hz correspond to ~ 400 ms; see also Sec. V.

B. Reduction to a single-component model

The key feature of our analysis lies in considering the limit where $|g_{12} - g_{11}| \ll g_{11}$, as well as $|g_{22} - g_{11}| \ll g_{11}$. In this setup, an effective single-component description of the two-component system can be achieved assuming that one component is effectively immersed in a bath of atoms of the second one [20,44]. Notice that similar considerations [55–57] are also utilized in rather distinct contexts such as the dressing of impurities by the excitations of a many-body medium, leading to the concept of polarons [58]. This scheme can be implemented experimentally via a two-photon Raman transition, where a transfer of a fraction of atoms (in wave functions of different types—for details, see below) from the majority component will be made to the minority species. Importantly, this allows us to keep the total density constant. In line with the recent experimental description of Ref. [20], our assumption will be that the two species add up to a Thomas-Fermi profile (since the chemical potential $\mu_u \gg \Omega$ will be used in the majority species) when $\Omega \neq 0$. In the case of $\Omega = 0$ (which will be employed first in order to showcase the ideas in a uniform setup), the total density of the two species is a constant background.

Then, following the above considerations, the dynamics of the minority species in the two-component system can be described by an effective single-component GPE given by [44]

$$i\partial_t v_{\text{eff}} = -\frac{1}{2}\partial_x^2 v_{\text{eff}} + V(x)v_{\text{eff}} + g|v_{\text{eff}}|^2 v_{\text{eff}}. \quad (2)$$

The key feature of this description is that the effective nonlinearity parameter g here reads

$$g = g_{22} - \frac{g_{12}^2}{g_{11}}. \quad (3)$$

As a result, if the condensates are on the (weakly) immiscible side, as is the case for ^{87}Rb hyperfine states, we expect the effective nonlinearity to be attractive for our effective single-component species v_{eff} that is approximately equal to v . Here, motivated by relevant studies, such as those of Ref. [59] and, more recently, Ref. [54], we will consider $g_{11} = 1.004$ and $g_{22} = 0.95$. The value of g_{12} is considered to be close to 0.98; however, in order to enable the relevant (weak) immiscibility effect to be amplified and be visible at shorter timescales, here we will assume that $g_{12} = 1.1$. Effectively, it is well known that one of the scattering lengths can be tuned via techniques such as Feshbach resonance over wide parametric windows [60]. In that light, the relevant phenomenology should be observable, for example, in the hyperfine states $|1, -1\rangle$ and $|2, 1\rangle$ of ^{87}Rb for which the above parameters are given. Besides, the tunability to different g_{12} as used here is, in principle, accessible. It is relevant to note also that it is not central to

our considerations that g_{12} is tuned. Indeed, the results presented herein will be valid for the minority component more generally within the immiscible regime, as the latter leads to the negativity of the expression of Eq. (3) for g and, hence, the attractive nature of the effective one-component description considered.

C. Peregrine ansatz and computational setup

Having set up this effectively attractive interaction, it is then relevant to discuss the coherent structure of interest, namely the Peregrine soliton, as a prototypical member of the family of rogue waves. The relevant solution of Eq. (2) with $V(x) = 0$ reads [24]

$$v_{\text{eff}}(x, t) = \sqrt{P_o} \left[1 - \frac{4(1 + 2i\frac{t-t_o}{T_p})}{1 + 4(\frac{x-x_o}{L_p})^2 + 4(\frac{t-t_o}{T_p})^2} \right] e^{i\frac{t-t_o}{T_p}}. \quad (4)$$

Here, $T_p = L_p^2 = 1/(gP_o)$ represents the characteristic scales of time and space of the density variation of the solution, respectively, while P_o represents the background density of the minority component. This implies that this is a monoparametric family of solutions, i.e., once P_o is set, so are T_p and L_p . Moreover, t_o and x_o denote, respectively, the time instant and location at which the Peregrine soliton emerges. In what follows, we set $x_o = 0$, unless stated otherwise.

Equation (4) is the solution that we will seek to effectively realize in our investigation in two distinct ways. The first one, which involves the proof of principle, will consist of the initialization of the Peregrine waveform and the monitoring of its time evolution. It is assumed, therefore, that such a profile is transferred to the minority component at a substantially lower density P_o than that of the $\mathcal{O}(1)$ majority component (i.e., $P_o \ll \mu_u$), while the majority component represents the remainder of the background toward a cumulative density of either constant value when $V(x) = 0$, or a Thomas-Fermi cloud when $V(x) \neq 0$. By Thomas-Fermi cloud, here, we mean the ground-state profile in our setting of large chemical potential μ_u . As mentioned above, we perform two types of investigations, one without an external trapping potential and one in the presence of the parabolic trap. Furthermore, in each of the examples, we perform two complementary explorations. In the first one, we simulate the full two-component system of Eqs. (1a) and (1b), while in the second one we restrict our considerations to the one-component effective system of Eq. (2). Our scope is to illustrate the relevance of the reduction of the former to the latter and to identify the case examples where this reduction may fail.

In addition to the proof-of-principle demonstration that an initialization of the Peregrine initial condition (well before its formation) will indeed lead to its emergence, we also want to address a more practical question. In particular, it is straightforward to appreciate that the slowly decaying spatial wave form of Eq. (4) (to a constant intensity background P_o , no less) may be more difficult to achieve in practice. Hence, it is natural to seek a “generic” wave form that may lead to such an emergence, upon a straightforward initialization, e.g., with a Gaussian profile. Here, we leverage the earlier findings of the rigorous work of Ref. [47] in the integrable NLS setting, within the so-called semiclassical regime. For

our purposes, practically, this concerns wave functions with sufficiently large spatial width. In this context, the authors of Ref. [47] have identified a generic so-called umbilical gradient catastrophe which leads to the formation of a cascade of Peregrine waves, a structure that has been referred to as Christmas tree in Ref. [19] and has recently been identified also in single and coupled phononic crystals [61,62]. The relevant wave structures emerge at the poles of the so-called tritronquée solution of the Painlevé I equation. The principal result for our purposes is that the Peregrine and the Christmas-tree structures should emerge *spontaneously* from quite generic (wide, and thus effectively semiclassical) wave forms, such as a Gaussian, but also sech-shaped ones and others [63]; indeed, the key feature is the width of the localized wave form, rather than its concrete functional form. Specifically, it has been demonstrated that the occurrence of the Christmas-tree structure is rather universal, in the sense that it appears as a result of strong modulational instability from different initial configurations [63]. This motivates the second set of our numerical experiments where, instead of initializing a precise Peregrine, we exploit a broad Gaussian of the form $v = A \exp(-x^2/w^2)$ and observe the resulting evolution. Typical values of the Gaussian amplitude $A = 0.2$ and width $w = 50, 150$ are used in the results below [64]. For the numerical investigations that follow, we use a fourth-order Runge-Kutta integrator with spatial and temporal discretization steps $dx = 0.1$ and $dt = 0.001$, respectively. Additionally, the system size for the homogeneous settings is $[-3000, 3000]$, in the dimensionless units adopted herein, while for the trapped studies it is $[-\frac{3}{2}r_{\text{TF}}, \frac{3}{2}r_{\text{TF}}]$. Here, $r_{\text{TF}} = \sqrt{2\mu_u}/\Omega$ denotes the Thomas-Fermi radius of the majority u component.

III. DYNAMICS OF THE PEREGRINE SOLITON

A. Proof of principle

First, we consider the scenario of a Peregrine initial condition in the absence of a trap in both the two-component setup, described by Eqs. (1a) and (1b), and within the effective single-component framework of Eq. (2). Here, we initialize the minority v component and effective single-component one with Eq. (4), with $P_0 = 0.01$ and $t_0 = 1000$. In the two-component setup, the majority u -component wave function has the form $u(x) = \sqrt{\mu_u - |v(x)|^2}$, while the chemical potential $\mu_u = 1$ is held fixed. The relevant dynamics is shown in Fig. 1. In terms of the minority v component, the evolution of the two-component setup clearly follows that of the effective single-component one [cf. Figs. 1(a) and 1(c), respectively]. Note also how the majority u component in Fig. 1(b) naturally accompanies the density bump of the Peregrine formation with a corresponding (complementary) density dip. The latter is reminiscent of dark-bright (DB) solitonic entities [65] and naturally stems from the repulsive interaction between the components.

For a more accurate comparison of the two models, the density difference of the v components is shown in Fig. 1(d). Here, one can observe that around the Peregrine formation the two- and the single-component setups differ at most by $|v|^2 - |v_{\text{eff}}|^2 \approx 10^{-3}$ (recall that the color bar is rescaled by a factor of 10^3). In particular, their difference may grow, but

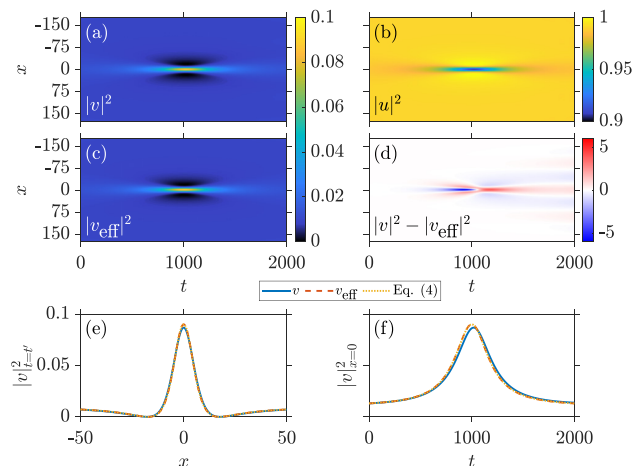


FIG. 1. Density evolution of the Peregrine initial condition [Eq. (4)] in the absence of a trap for (a) the minority and (b) the majority species of the two-component setting with $\mu_u = 1$. Equation (4) is initialized with $P_0 = 0.01$ and $t_0 = 1000$. (c) Dynamics of the density within the effective single-component model. (d) Density difference between the (a) two- and the (c) single-component dynamics (the color bar is rescaled by a factor of 10^3). (e) Density profile of the v component for the two- and single-component setups at the time instant of Peregrine formation, namely $t'_{\text{two}} = 1019$ and $t'_{\text{single}} = 1000$. (f) Temporal evolution of the Peregrine wave emerging in the v component of both the two- and single-component setups at $x = 0$ (see legend). In both panels (e) and (f), the corresponding analytical Peregrine solution of Eq. (4) is provided. Note that length and time are measured in units of a_{\perp} and ω_{\perp}^{-1} , respectively.

this only happens past the initial formation of the Peregrine soliton. This is rather natural to expect, given that for large densities the correction to the single-component approximation of v becomes substantial. As discussed in Ref. [20], such a correction is proportional to $(\sqrt{\mu_u - |v|^2})_{xx} / (2\sqrt{\mu_u - |v|^2})$ and can thus become relevant when the spatially varying wave form of $|v|^2$ grows substantially, upon the emergence of the Peregrine.

Indeed, by inspecting in Fig. 1(e) each Peregrine soliton at the instant of its formation, t' , it is observed that the Peregrine of the two-component system is slightly smaller in amplitude and slightly wider when compared to the one formed in the single-component setting. Also, as shown in Fig. 1(f), we find that the Peregrine formation in the two-component setup takes place later than in the single-component one. In particular, the former occurs at $t'_{\text{two}} = 1019$, while the latter occurs at $t'_{\text{single}} = 1000$. In Figs. 1(e) and 1(f), we also provide the analytical solution of Eq. (4), which, as expected, falls on top of the wave form stemming from the single-component setup. Hence, we can conclude that in the two-component scenario the presence of the majority component slightly hinders and/or delays the Peregrine formation. Additionally, a closer inspection of Fig. 1(d) reveals progressively stronger deviations between the single- and two-component description past the Peregrine formation time. This stems from the differences in the manifestation of the modulational instability of the background for large and positive times (see, for example, Ref. [61] for a discussion of the relevant instability in the presence of

the Peregrine wave). Moreover, we also found that at those large positive times a wedge-like structure emerges, similar to that described in Ref. [51] and, more recently, experimentally found in Ref. [52] (see also the Appendix).

In the presence of a parabolic trapping potential ($\Omega = 0.002$), we prepare our initial state as follows. On the one hand, we obtain the single-component ground state, u_{GS} , of the majority u component for $\mu_u = 1$. On the other hand, we find the ground state, v_{GS} , of the minority v component in a super-Gaussian trapping potential of the form

$$V_{\text{SG}}(x) = 1 - \exp\left[-\left(\frac{x}{r_{\text{TF}}}\right)^{100}\right], \quad (5)$$

but for $\mu_v = P_o = 0.01$, which throughout the text refers to the chemical potential of the minority v component. For this initially decoupled two-component system, $r_{\text{TF}} = \sqrt{2\mu_u}/\Omega$ in Eq. (5) denotes the Thomas-Fermi radius of the majority u component. From here, we imprint Eq. (4) with $t_o = 1000$ onto the minority ground state as $v(x) = v_{\text{GS}}(x)v_{\text{eff}}(x, 0)/\sqrt{P_o}$. The reason for using a super-Gaussian is to obtain an initial state with an almost constant (flat) background achieving also a smoother decay of the tails of the Peregrine, as described by Eq. (4). Lastly, we construct the majority u -component wave function by subtracting the minority v component from the majority single-component ground state, i.e., $u(x) = \sqrt{|u_{\text{GS}}(x)|^2 - |v(x)|^2}$. Note that the latter operation emulates a particle transfer from the majority component to the minority one, while keeping the total density constant, which experimentally can be implemented by means of a two-photon Raman transition, as in the recent Townes soliton realization [20]. Having carried out these three steps (ground state under super-Gaussian, Peregrine imprinting, and formation of the complementary majority component), we are ready to perform our direct numerical simulations in the presence of a parabolic trap. During the dynamics, the super-Gaussian is turned off, interspecies interactions are switched on, and both components evolve under the influence of the same harmonic trapping potential.

The in-trap dynamical evolution of the two-component system is presented in Fig. 2. Specifically, Figs. 2(a) and 2(b) illustrate the spatiotemporal evolution of the density of the v and u components, respectively, showcasing the complementary nature of the latter. The spontaneous emergence of a Peregrine soliton, and of the corresponding density-dip appearing in the majority u component, takes place at $t' = 1053$. This precise time instant is captured in Fig. 2(c), where we further compare the emergent wave against the analytical solution of Eq. (4). The latter is fitted so as to match the maximum amplitude of the nucleated Peregrine, i.e., $P_o = |v_{\text{max}}|^2/9 = 0.0093$. Notice that this value is rather proximal to the initial amplitude of the Peregrine wave form, namely $P_o = 0.01$. A nearly excellent agreement is observed between our numerical observation and the analytical estimate, an outcome that can also be inferred by inspecting Fig. 2(d). In the latter, the evolution of the density of the v component at $x = 0$ is also depicted along with the theoretical prediction. Indeed, the observed structure almost coincides around its core with the theoretically predicted one, but the numerically obtained one is found to be (very) slightly wider. Similarly, small devi-

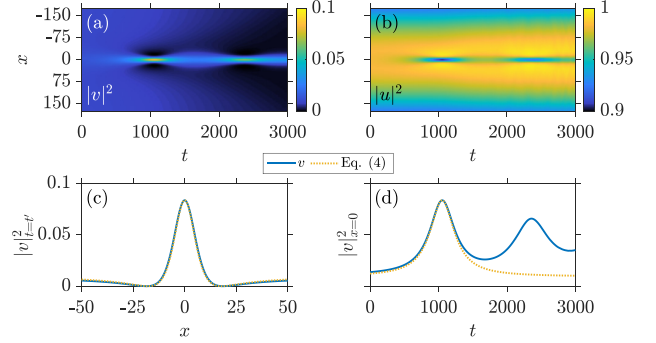


FIG. 2. Spatiotemporal density evolution of a Peregrine initial condition in the presence of a trap with $\Omega = 0.002$ for (a) the minority and (b) the majority species of the two-component case with $\mu_u = 1$. Equation (4) is initialized with $P_o = 0.01$ and $t_o = 1000$ on top of the ground state obtained for the super-Gaussian potential of Eq. (5) using $\mu_v = P_o$ (see text). (c) Density snapshot of the v component capturing the instantaneous formation, $t'_{\text{two}} = 1053$, of the Peregrine soliton. (d) The temporal density profile of the v component at the fixed spatial location of $x = 0$. In both panels (c) and (d), the relevant theoretical prediction of Eq. (4) is provided for a direct comparison (see legend). Length (time) is given in terms of $a_{\perp} (\omega_{\perp}^{-1})$.

ations between the two occur also in the far field (at the tails of the wave) but with their density difference never being greater than $\sim 10^{-3}$. Even more importantly, at later evolution times the numerical solution recurs as a rogue pattern reminiscent of the Kuznetsov-Ma soliton [5,6,11]. Recall that the latter is a time-periodic family of solutions, of which the Peregrine is the asymptotic limit when the temporal periodicity tends to ∞ . A clear example of such a revival, that is related to the trapped setting at hand, can be seen in Fig. 2(a), but also in Fig. 2(d) around $t = 2358$.

B. Semiclassical regime: Gaussian profile

We now turn to the example of a Gaussian initial condition in order to cement the generic nature of the Peregrine soliton formation, as well as to showcase an example of an initial condition that could be (far more) straightforwardly accessible in BEC experiments. The Gaussian profile here is representative of a wide initial condition in the minority v component, so as to capture the semiclassical limit of the work of Ref. [47]. As in the preceding section, we initialize the dynamics of the two- and effective single-component system under consideration first in the absence and subsequently in the presence of a harmonic confinement. Additionally, two different representative case examples corresponding to two distinct widths, namely $w = 50$ and $w = 150$, of the initial Gaussian wave packet are considered, while in both cases the amplitude, $A = 0.2$, of this Gaussian initial condition is held fixed.

The first case example, i.e., that of a narrower Gaussian initial condition ($w = 50$), is shown in Fig. 3. Here, the spatiotemporal evolution of the v component of both the two- and the single-component setups [see Figs. 3(a) and 3(c), respectively] present the same *chain*-like temporal pattern within which periodic recurrences of a localized pattern reminiscent

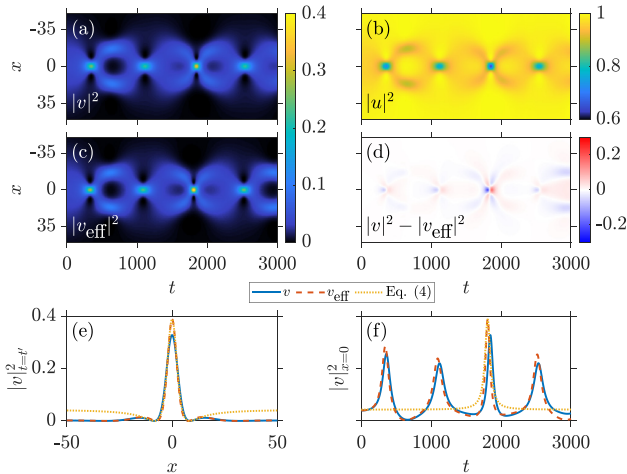


FIG. 3. Time evolution of the density of a Gaussian wave packet with $A = 0.2$ and $w = 50$ depicting the dynamics of the (a) minority and (b) majority species of the two-component system with $\mu_u = 1$. (c) Evolution of the minority v component within the effective single-component description. (d) Density difference between the (a) two- and the (c) single-component dynamics. (e) Density profile of the v component for the two- and single-component setups at the times of their largest amplitudes, namely at $t'_{\text{two}} = 1846$ and $t'_{\text{single}} = 1808$, respectively. (f) Evolution of the center position $x = 0$ of the density of the v component for the two- and the single-component setups. In both panels (e) and (f), the corresponding analytical solution of Eq. (4) is given, with its peak fitted to the single-component case (see text). Length and time are expressed in units of a_{\perp} and ω_{\perp}^{-1} , respectively.

of the Peregrine wave take place. Also, the majority u component of the two-component model, illustrated in Fig. 3(b), showcases the complementary *dark chain* temporal pattern. The array of individual rogue wave patterns can be clearly discerned and once again there is a close correspondence between the single- and two-component dynamics. To demonstrate this correspondence, the density difference of the v components is provided in Fig. 3(d). Clearly, the larger deviation between the two systems occurs around the location of the formation of the localized peaks ($x = 0$). To further expand on the comparison of the observed structures, in Fig. 3(e) we illustrate their density profiles at the formation of their maximum, namely at $t'_{\text{two}} = 1846$ and $t'_{\text{single}} = 1808$, respectively, as compared with an exact Peregrine solution. In particular, the largest among the localized patterns that emerged during the evolution is considered here. Notice that an adequate agreement is observed in the vicinity of the core, with the two-component pattern being slightly wider but also having a smaller amplitude when compared to the single-component Peregrine wave that follows the theoretical prediction [see Eq. (4)]. The latter is fitted to the Peregrine of the single-component setup, having $P_o = |v_{\text{eff}}^{\text{max}}|^2/9 = 0.043 \approx A^2$ and selecting $t_o = t'_{\text{single}}$. Naturally, the Gaussian evolution, given its decaying tail, cannot lead to the constant background of the Peregrine wave form, hence the observed deviations in the far field. Additionally, monitoring in Fig. 3(f) the density at $x = 0$ in the course of the evolution shown in Figs. 3(a) and 3(c) reveals that the emergent recurring structures in the

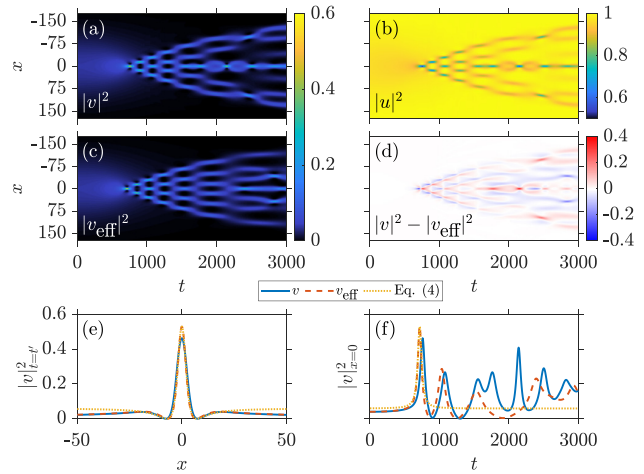


FIG. 4. Same as Fig. 3 but considering a significantly broader Gaussian initial condition with $w = 150$. In this case, the Peregrine soliton formation within the two models occurs at $t'_{\text{two}} = 758$ and $t'_{\text{single}} = 716$, respectively. Notice also the subsequent emergence of the Christmas-tree structure. Recall that length and time are given in units of a_{\perp} and ω_{\perp}^{-1} , respectively.

chain slightly differ in their time of formation. Namely, within the effective model, each member of the chain (i.e., each recurrence event) appears earlier in time, presenting also a larger amplitude spike when compared to the two-component setting. The aforementioned results are in line with the trends of the ones found in the homogeneous case [see Figs. 1(e) and 1(f)].

As a second representative example, a significantly wider, with $w = 150$, Gaussian initial condition is considered again both in the two- and in the effective single-component setups (see Fig. 4). It turns out that increasing the width of the Gaussian leads to the dynamical formation of the Christmas-tree structure (see Sec. II C). Indeed, as also explained previously, the mechanism underlying the fragmentation of the solution is the existence of strong modulational instability of the (in our case, effectively) focusing NLS equation [47]. The various asymptotic regions (smooth versus highly oscillatory) are separated by “breaking curves”, and the solution of the focusing NLS inside the oscillation region is approximately given by modulated genus-2 waves. More specifically, as shown in Ref. [47], near each oscillation peak the solution takes on (locally) the universal shape of the Peregrine soliton. In our computations, a Christmas-tree pattern is clearly seen in Figs. 4(a) and 4(c), corresponding to the two- and single-component setups, respectively, while the complementary *dark* Christmas-tree structure appearing in the majority u component of the two-component system is presented in Fig. 4(b). Notice here the ramifications of the emerging Christmas-tree structure right after the formation of the Peregrine soliton at $t'_{\text{two}} = 758$ ($t'_{\text{single}} = 716$) within the two-component (single-component) model.

The relevant Peregrine profiles are depicted in Fig. 4(e) at the time instant of their formation together with the analytical Peregrine solution of Eq. (4). Recall that the latter is fitted so as to match the amplitude of the single-component Peregrine

wave. Also in this case an excellent agreement is observed around the waves' core when comparing the exact solution to the single- and the two-component outcome. Thus, increasing the width of the initial Gaussian profile leads to an overall increase in size of the emerging Peregrine soliton and to the formation of the Christmas-tree structure. However, so as to stretch the comparison of the patterns appearing in the distinct settings, in Fig. 4(f) we illustrate the temporal evolution of the central density of both v components. Evidently, this quantity perfectly captures the instant where the dynamics begins to differ, i.e., $t \approx 1500$ [cf. Figs. 4(a) and 4(c)]. The observed discrepancy between the two models is a direct consequence of the presence of the majority u component in the two-component setup. This is an effect which will be even more pronounced in the case of the presence of harmonic confinement that follows.

Next, we extend the above Gaussian state considerations to the case where a parabolic trap, with trapping frequency $\Omega = 0.002$, is also present. Also in this case, the initial state preparation consists of obtaining the decoupled, single-component ground state of the majority u component for a fixed chemical potential ($\mu_u = 1$), and then approximating the particle transfer to the minority v component by subtracting the latter from the former. It turns out that the dynamical evolution of narrower Gaussian wave packets leads to qualitatively identical results to those found in the relevant homogeneous investigations discussed above, and thus these findings are not included herein for brevity.

On the contrary, a more complex evolution takes place when a wider ($w = 150$) Gaussian initial condition is considered. Here, we observe a particularly interesting phenomenon that we did not encounter in the previous settings, so it is convenient for our purposes to monitor the dynamics both at long [Fig. 5(a)] and short timescales [Fig. 5(b)]. At initial times, and in particular around $t'_{\text{two}} = 800$, the Peregrine soliton forms, being subsequently followed by the emergence of the Christmas-tree structure. Note that the Peregrine formation takes place at later times as compared to the relevant untrapped scenario. Also, in this case the presence of a modulated density profile does not appear to sustain this Christmas-tree structure, which is seen to break into several DB soliton-like entities after $t = 2000$. Following these soliton-like structures for longer evolution times [Fig. 5(a)] reveals that these patterns oscillate inside the parabolic trap over a *very* large period. In particular, their oscillation frequency is substantially smaller than that of the trap. Also, their corresponding period is much longer than that expected for regular DB solitary waves under the same confinement conditions [46,66], which would typically be of the order of a few hundred time units. By comparing the trajectories of these peculiar DB entities to regular ones, we observe a distinct concavity between the two. Namely, the present patterns feature (unprecedented, to our knowledge) convex trajectories until very close to the turning point, contrary to the usual (nearly) harmonic oscillations experienced by standard DB solitons. Nevertheless, after an extremely long period of time and around $t = 11394$ the two outermost individual patterns interfere to produce a revival of a Peregrine wave form. While the latter is not identical to the early one formed at $t'_{\text{two}} = 800$, it is very proximal to a Peregrine pattern having a distinct

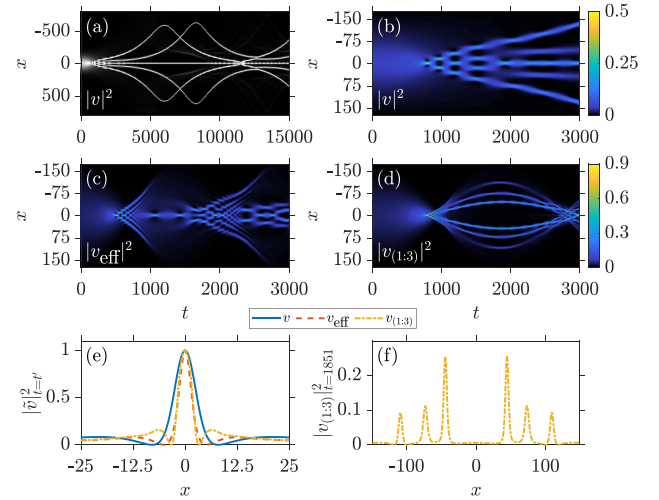


FIG. 5. Evolution of the density of a Gaussian wave packet with $A = 0.2$ and $w = 150$ in the presence of a harmonic trap with $\Omega = 0.002$. (a) Temporal evolution of the minority v component. (b) A magnification of (a) is provided. (c) Effective single-component case. (d) Same as (b) but upon considering a mass-imbalanced BEC mixture (see text). (e) Density profiles of the v component for the single-component and mass-balanced and mass-imbalanced two-component setups at the instant of formation of the Peregrine soliton $t'_{\text{single}} = 516$, $t'_{\text{two}} = 800$, and $t'_{\text{two}}^{(1:3)} = 795$, respectively. All Peregrine amplitudes are normalized to unity for direct comparison. (f) Density profile at $t'_{\text{two}}^{(1:3)} = 1851$, depicting the pairwise DB soliton nucleation that follows the decay of the Christmas-tree pattern, for the mass-imbalanced mixture. In all cases, the majority u component complements its relevant minority one, and thus it is omitted. The length and time units shown are in terms of a_{\perp} and ω_{\perp}^{-1} , respectively.

amplitude. Hence, the system can access a very long timescale revival of the relevant pattern in this parabolically trapped setting that is interesting in its own right. Recall also that in all of the above cases the majority u -component evolution complements the minority v component shown in Figs. 5(a) and 5(b). Hence, it is not included here.

For completeness, the effective single-component evolution is illustrated in Fig. 5(c). Here, the dynamics appears to be dramatically faster when compared to the aforementioned two-component scenario, with the Peregrine soliton appearing at $t'_{\text{single}} = 516$ and being of higher amplitude [cf. Figs. 5(b) and 5(c) color bars on the right side]. Also, faster is the formation of the corresponding Christmas-tree structure which once more, due to the presence of the trap, cannot be sustained and around $t \approx 1000$ it blurs out into a smooth background within which the recurrence of two Peregrine solitons, one at $t = 1068$ and one at $t = 1425$, is evident. Note that the smoothing of the Christmas-tree pattern is a unique feature of this effective single-component setup. Strikingly enough, also a recurrence of a second larger Christmas-tree structure is observed in this single-component setting, around $t \approx 2500$, after an interval where interference processes take place. This, in turn, confirms the fact that in the two-component setting, the majority u component plays a major role, not only on the speed of the events, but also in the formation of more complex

and robust structures, such as the numerically observed DB soliton-like waves found in this work.

C. Impact of the mass imbalance

As a next step, our aim is to generalize our findings by considering mixtures in which the two species bear different masses. In particular, in the way of a concrete example, here we focus our investigations on mass-imbalanced mixtures having a mass ratio of (1:3) to gain a qualitative overview of the main phenomenology, while mimicking the potentially experimentally relevant situation of heteronuclear BEC mixtures of, e.g., ^{87}Rb - ^{174}Yb , ^{23}Na - ^7Li , or ^{87}Rb - ^{23}Na atoms. Although the initial state preparation considered in this case is the same as before, it is important to note that the trapping potential will now affect each component differently [see Eq. (1)]. In general, it is found that if the majority component is the heaviest one, Peregrine wave generation, similar to that shown in Fig. 2, occurs only for narrow initial Gaussian wave functions ($w \lesssim 60$). Therefore, the Christmas-tree structure is absent and in particular for $w > 60$ a delocalization of the Gaussian takes place. On the other hand, if the minority component is the heaviest one we retrieve the overall phenomenology, namely that of the Peregrine soliton formation being followed by the nucleation of a Christmas-tree pattern. Interestingly, the value of the Gaussian width above which the Christmas-tree pattern appears is affected by the intercomponent mass ratio. For instance, for $m_u/m_v = 1/3$ it occurs for $w > 30$, while in the mass-balanced case it occurs for $w > 52$.

A case example is shown in Fig. 5(d) for an initial Gaussian profile with $A = 0.2$ and $w = 150$. For mass-imbalanced mixtures, the dynamical rogue-wave pattern formation ($t' = 795$) is slightly accelerated when compared to the equal mass scenario discussed above [cf. Fig. 5(a)]. Moreover, as mentioned earlier, the heaviest minority component experiences now a tighter trapping potential. This has as a result the emergence of a Peregrine wave that has its side humps higher in amplitude and closer to the core of the structure. A direct comparison of the Peregrine soliton formed in this setting with the relevant waves generated within the mass-balanced and the effective single-component models is provided in Fig. 5(e). Furthermore, after the decay of the Christmas-tree structure, we again observe DB soliton-like structures being emitted around $t \approx 1000$. The first half oscillation period of these configurations can be seen in Fig. 5(d), and the corresponding bright solitary-wave density profile is depicted in Fig. 5(f) at $t = 1851$, i.e., at the maximum amplitude of its oscillation. Besides their oscillation inside the parabolic trap, these structures further undergo a periodic amplitude breathing. The frequency of this breathing is found to increase with the size of the soliton; i.e., it appears to be larger for the solitary-waves that are closer to the trap center. Additionally, it is also found that these structures emerge always in counterpropagating pairs, the number of which is directly proportional to the width of the initial Gaussian profile. For instance, for $w = 50$ ($w = 150$) the number of counterpropagating pairs is one (three).

IV. THERMAL EFFECTS ON PEREGRINE GENERATION

Having established Peregrine soliton generation stemming from generic initial conditions, below, we shall exemplify the validity of our findings in the presence of dissipation.

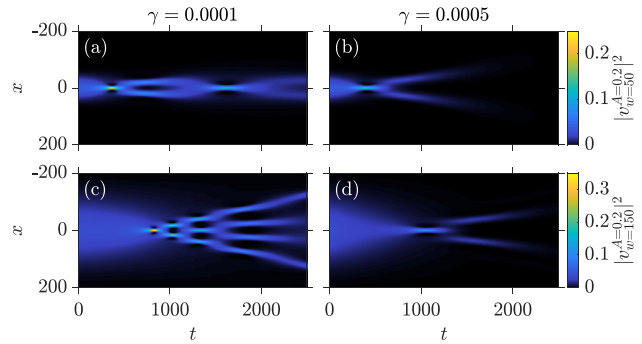


FIG. 6. Dynamical evolution of the density of the minority v component for $A = 0.2$ and [(a), (b)] $w = 50$ and [(c), (d)] $w = 150$. The dissipation strength is [(a), (c)] $\gamma = 10^{-4}$ and [(b), (d)] $\gamma = 5 \times 10^{-4}$. Other parameters used are $\mu_u = 1$, $\mu_v = 0.01$, $m_u = m_v$, and $\Omega = 0.002$. Note that length (time) is in units of a_{\perp} (ω_{\perp}^{-1}).

To this end, we consider the general system of two coupled dissipative GPEs [49,67,68] for the mass-balanced mixture

$$(i - \gamma)u_t = -\frac{1}{2}u_{xx} + V_u(x)u + (g_{11}|u|^2 + g_{12}|v|^2)u, \quad (6a)$$

$$(i - \gamma)v_t = -\frac{1}{2}v_{xx} + V_v(x)v + (g_{21}|u|^2 + g_{22}|v|^2)v. \quad (6b)$$

In these equations, γ represents the dimensionless dissipation strength which is in turn related to the system's temperature. For instance, when $\gamma \ll 1$ lies in the interval $[2 \times 10^{-4}, 2 \times 10^{-3}]$, it corresponds in dimensional units to temperatures [10, 100] nK [67–69]. The reduction of the above-mentioned system of dissipative GPEs follows the assumption that only the thermal modes along the longitudinal direction are populated. The relevant dynamics of a trapped ($\Omega = 0.002$) narrow Gaussian wave packet having $A = 0.2$, $w = 50$ in the case of $\gamma = 10^{-4}$ and $\gamma = 5 \times 10^{-4}$ is presented in Figs. 6(a) and 6(b), respectively. As previously, we only show the time evolution of the minority v -component density. The majority u component is complementary to it while being significantly less affected by the presence of dissipation, at least within the considered timescales. Notice that even though the Peregrine soliton emerges around $t = 400$ in both scenarios it is of smaller amplitude as γ increases. Moreover, due to faster particle loss for larger γ 's, the pattern observed for smaller γ is lost [see Fig. 6(b)]. Dissipation affects in a similar manner also the nucleation of the Christmas-tree configuration. The latter is generated only for $\gamma < 5 \times 10^{-4}$ when broader ($w = 150$) Gaussian wave packets are used [Fig. 6(c)], while its signature is lost for larger values of the dissipative parameter [Fig. 6(d)]. In this latter situation, only a single Peregrine occurs around $t \approx 1100$, i.e., at later times when compared to its faster (around $t \approx 750$) nucleation for $\gamma = 10^{-4}$. In conclusion, nucleation of Peregrine solitons in repulsive media takes place for $\gamma < 10^{-3}$ corresponding to temperatures smaller than 100 nK. However, more composite structures such as the above-discussed Christmas-tree and other observed (e.g., breathing) patterns are less robust,

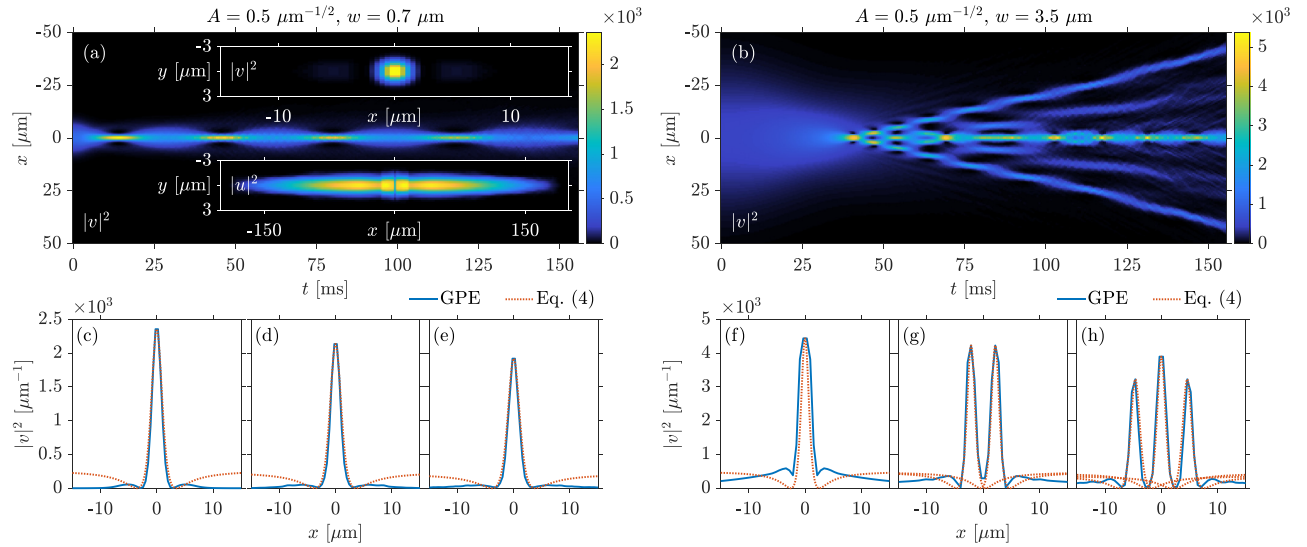


FIG. 7. (a) [(b)] Spatiotemporal evolution of the integrated along the yz direction density, of the minority v component for $A = 0.5 \mu\text{m}^{-1/2}$ and $w = 0.7 \mu\text{m}$ [$w = 3.5 \mu\text{m}$]. Insets in panel (a) depict density snapshots of the (top) v and (bottom) u components, rescaled by a factor of $1/3$ and $1/7$, respectively, in the x - y plane at $t_0 \approx 13.5$ ms when the Peregrine initially forms. Panels (c)–(e) [(f)–(h)]: Integrated density profiles at selective time instants during evolution of the Peregrine and its revivals [of the Christmas tree]. A comparison with the relevant analytical prediction of Eq. (4) is also provided (see legends). For this quasi-1D evolution, the corresponding trapping frequencies are $(\omega_x, \omega_y, \omega_z) = 2\pi \times (3.06, 400, 400)$ Hz and $N = 7 \times 10^5$.

surviving only if $\gamma < 5 \times 10^{-4}$, namely for temperatures roughly above 10 nK.

V. QUASI-1D PEREGRINE AND CHRISTMAS-TREE FORMATION

Next, we aim to also testify Peregrine soliton nucleation in a 3D (yet quasi-1D) environment that can be readily implemented in recent experimental setups [48,70,71]. In this case, the dissipative effect stemming from the transverse directions on this intrinsically 1D wave will be appreciated. Specifically, we consider a system of 3D coupled GPEs:

$$iu_t = -\frac{1}{2}\nabla^2 u + V(\mathbf{r})u + (4\pi a_{11}N_1|u|^2 + 4\pi a_{12}N_2|v|^2)u, \quad (7a)$$

$$iv_t = -\frac{1}{2}\nabla^2 v + V(\mathbf{r})v + (4\pi a_{21}N_1|u|^2 + 4\pi a_{22}N_2|v|^2)v, \quad (7b)$$

that describes a mass-balanced binary mixture. The above set of equations is cast in this dimensionless form by rescaling space and time coordinates as $x' = a_{\text{ho}}^{-1}x$, $y' = a_{\text{ho}}^{-1}y$, $z' = a_{\text{ho}}^{-1}z$, with $a_{\text{ho}} = \sqrt{\hbar/m\omega_x}$ being the harmonic oscillator length along the longitudinal x direction, and $t' = \omega_x t$. The corresponding wave functions are also rescaled as $u(x', y', z') = \sqrt{N_i/a_{\text{ho}}^3}u(x, y, z)$ and $v(x', y', z') = \sqrt{N_i/a_{\text{ho}}^3}v(x, y, z)$ where N_i is the particle number per component. $\nabla^2 \equiv (\partial_x^2 + \partial_y^2 + \partial_z^2)$ is the Laplacian operator and a_{jk} is the 3D scattering length accounting for the intra- ($j = k$) and intercomponent ($j \neq k$) interactions. In particular, the experimentally relevant $a_{11} = 100.04a_0$, $a_{22} = 95.44a_0$, and $a_{12} = a_{21} = 110.0a_0$ are utilized with a_0 denoting the Bohr radius. Additionally, $V(\mathbf{r}) = \frac{1}{2}[x^2 + (\omega_y/\omega_x)^2 y^2 + (\omega_z/\omega_x)^2 z^2]$

is the 3D parabolic potential, where $\mathbf{r} = (x, y, z)$, with axial and transverse trapping frequencies assumed here to be $(\omega_x, \omega_y, \omega_z) = 2\pi \times (3.06, 400, 400)$ Hz. Notice that the above choice provides an aspect ratio $\omega_x/\omega_{\perp} \approx 0.008$ leading to a highly elongated (cigar-shaped) trapping geometry.

To initiate the dynamics in this 3D yet quasi-1D setting, we assume that the system contains $N = 7 \times 10^5$ particles and that it remains in the ground state along the transverse yz directions. Accordingly, each component's wave function at $t = 0$ is expressed as $u(x, y, z) = u(x)u_0(y)u_0(z)$ and $v(x, y, z) = v(x)v_0(y)v_0(z)$, with $u_0(y) = v_0(y)$, $u_0(z) = v_0(z)$ denoting the normalized Gaussian wave functions along the transverse directions. Similarly to the 1D initial conditions of the preceding section, the wave functions of the two components along the x direction are given by a Thomas-Fermi approximation in the u component, complementary to the v component for which we assume a Gaussian initial condition $v(x) = A \exp(-x^2/2w^2)$. The dynamical evolution of the density of the v component when considering two distinct initializations corresponding to a narrow ($w = 0.7 \mu\text{m}$) and a broad ($w = 3.5 \mu\text{m}$) Gaussian initial profile with amplitude $A = 0.5 \mu\text{m}^{-1/2}$ is demonstrated in Figs. 7(a)–7(h). Note that since the spatiotemporal evolution of the u component is complementary to the one shown, it is not illustrated here but it can be inferred, for instance, by inspecting the insets in Fig. 7(a) where the instantaneous density profiles of both components in the x - y plane are shown. Remarkably, the spontaneous nucleation of a Peregrine structure along with its revivals takes place in this 3D, quasi-1D setting [Fig. 7(a)] with its integrated, along the transverse yz directions, density profiles presented in Figs. 7(c)–7(e). Additionally, and as suggested by the relevant 1D situation, for wider initial wave packets a configuration reminiscent of the Christmas

tree is generated [Fig. 7(b)]. In both cases, very good agreement is found when fitting the analytical 1D solution to the numerically obtained rogue wave pattern appearing initially at $t_0 \approx 13.5$ ms, but recurring at $t_1 \approx 46$ ms and $t_2 \approx 81$ ms for narrow pulses [Figs. 7(c)–7(e)] and around $t_3 = 41$ ms, $t_4 \approx 47$ ms, and $t_5 \approx 53.6$ ms for wider ones [Figs. 7(f)–7(h)]. The observation and persistence of the Peregrine structure in such a 3D setting with a quasi-1D geometry constitutes, to the best of our knowledge, an unprecedented result that sets the stage for an experimental realization of this rogue wave.

VI. CONCLUSIONS AND FUTURE PERSPECTIVES

In this work, we have presented an experimentally realizable setup to explore the formation of Peregrine solitons in repulsive two-component BECs. First, as a proof of principle, we showed the formation of the Peregrine soliton by direct initialization on the wave function of the minority component and demonstrated how an effective single-component picture accurately captures the dynamics. Additionally, we argued that in the presence of a wide external harmonic trapping potential Peregrine solitons can also be realized in a two-component setup, with periodic revivals stemming as a result of the presence of the trap.

We then extended our work to a more experimentally relevant situation by utilizing wide and thus effectively semiclassical Gaussian wave packets as initial conditions, both in the absence and in the presence of a parabolic trap. In particular, by employing differently sized Gaussian profiles we were able to showcase that narrower wave packets lead to periodic revivals of a localized Peregrine-like structure resulting in a *chainlike* pattern. Contrary to this dynamical evolution, broader Gaussian profiles entail the formation of a cascade of Peregrine waves, also known as a Christmas-tree structure. Moreover, we demonstrated that in the presence of the trap the dynamics of a narrower Gaussian initial condition remains qualitatively identical to that observed in the homogeneous cases under consideration. On the other hand, for wider Gaussian profiles, we encountered a particularly interesting phenomenon that was absent in the aforementioned settings. While at short timescales the dynamical evolution of both the two-component and the effective single-component models is similar to their corresponding untrapped settings, this is not the case for longer evolution times. At these longer times, dark-bright soliton-type structures are formed in the two-component setup and, contrary to the standard dark-bright solitary waves, feature unexpected *very* long-time convex (up to the vicinity of the turning point) trajectories within the parabolic trap. Strikingly, these unprecedented—to our knowledge—patterns are seen to interfere anew, suggesting that the system can access very long timescale recurrences of the Peregrine-like structures.

Furthermore, we attempted yet another generalization of our findings by considering also the case of mass-imbalanced mixtures. Here, we were able to exemplify that the overall dynamical response persists for mixtures in which the minority component is the heaviest one, with the rogue and Christmas-tree pattern formation being accelerated when compared to the mass-balanced model. Moreover, in such mass-imbalanced mixtures we observed the emergence of dark-bright soliton-

like entities that, besides oscillating within the parabolic trap, were also seen to exhibit a characteristic breathing.

Additionally, we examined the robustness of Peregrine soliton nucleation in the presence of dissipation. Specifically, it is demonstrated that the overall phenomenology persists for values of the dissipative parameter γ of the order of $\sim 10^{-3}$ (i.e., temperatures of about ~ 100 nK) before any signature of the Peregrine wave is lost. A key finding toward the realizability of our proposal in experimental settings consists of the successful numerical realization of both the Peregrine soliton with its revivals and the Christmas-tree pattern in a 3D geometry involving a quasi-1D cigar-shaped harmonic trap.

Until now, the realization of a Peregrine soliton has been a challenge in the field of ultracold atoms. This mainly stems from difficulties to highly control experiments with attractive BECs, even more so in the presence of the modulationally unstable background that supports the Peregrine soliton. Yet, in this work we have argued that the presence of a majority component contributes to the formation of more robust structures, rendering two-component *repulsive* BECs an appealing and potentially more suitable platform for the realization and further study of Peregrine waves in the effective form proposed herein. At the same time, we observed the peculiar formation of dark-bright soliton-like structures bearing unusual oscillatory trajectories. The latter, along with the quantification of the oscillation period of such entities, constitute fruitful directions of study worthwhile to pursue in the future. Another interesting pathway is the inclusion of three-body loss rates in order to inspect the robustness of the Peregrine wave in the long time evolution where their effect might become appreciable. Finally, unraveling the correlation properties of these structures when embedded in a many-body environment, e.g., as has been demonstrated for dark-bright solitons [72–74], is an intriguing topic especially so when beyond mean-field effects may come into play, potentially affecting the validity of the single-component effective description.

ACKNOWLEDGMENTS

A.R.-R. and P.S. acknowledge financial support by the Deutsche Forschungsgemeinschaft (DFG, German Research Foundation)—SFB-925—Project No. 170620586. G.C.K. gratefully acknowledges financial support by the Cluster of Excellence “Advanced Imaging of Matter” of the Deutsche Forschungsgemeinschaft (DFG)—EXC 2056—Project ID No. 390715994. S.I.M. acknowledges support from the NSF through a grant for ITAMP at Harvard University. This material is based upon work supported by the U.S. National Science Foundation under Grants No. PHY-2110030 and No. DMS-1809074 (P.G.K.), as well as Grants No. DMS-2009487 (G.B.) and No. DMS-2106488 (B.P.). P.G.K. is grateful to Markus Oberthaler and the Synthetic Quantum Systems group for numerous useful discussions and insights.

APPENDIX: MODULATIONAL INSTABILITY AND STRUCTURE FORMATION IN THE LONG-TIME DYNAMICS

In nonlinear focusing media, a small localized perturbation on a constant background can lead to a modulationally unstable region. The latter acquires a wedge-like shape

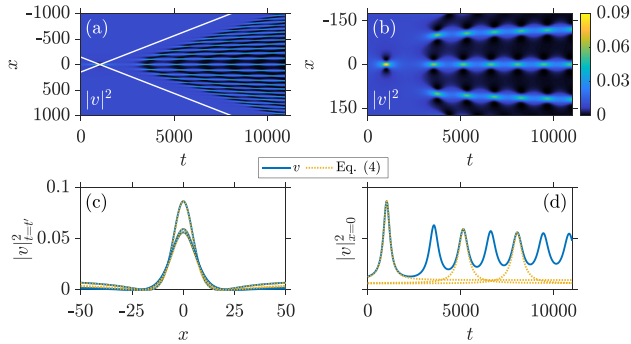


FIG. 8. (a) Density evolution of the Peregrine initial condition of Eq. (4), for $P_o = 0.01$ and $t_o = 1000$, in the homogeneous two-component setup. The majority u component is complementary to the minority v component and thus omitted. White lines, corresponding to Eq. (A1), designate the borders of the wedge-like pattern formed. (b) Enlargement of panel (a). (c) Density profile of the minority v component at the time instant of Peregrine soliton formation, namely at $t'_0 = 1023$, $t'_2 = 5148$, and $t'_4 = 8052$. (d) Temporal evolution of the modulation wave at $x = 0$. In both panels (c) and (d), the corresponding analytical solutions of Eq. (4) are provided for the chosen Peregrine solitons. Length and time units are expressed in terms of a_{\perp} and ω_{\perp}^{-1} , respectively.

characterized by a universal envelope, known as the nonlinear stage of the modulational instability (see Refs. [51,75] and references therein). For the integrable case of the NLS equation, such a region is defined by the boundaries $x_{\pm} = \pm 4\sqrt{2P_o}t$, with P_o denoting the background density. On the other hand, beyond the integrable limit, the boundaries depend also on the nonlinearity as follows [52,76,77]:

$$x_{\pm} = \pm 2\sqrt{-2gP_o}t. \quad (\text{A1})$$

This expression refers to a focusing system, and thus $g < 0$. In our case, g is given by Eq. (3). In Fig. 8, we show the long time dynamics of a system initialized with Eq. (4),

with $P_o = 0.01$ and $t_o = 1000$, in a repulsive two-component system (see Sec. II for details). The short time dynamics of this initial state is presented in Fig. 1. Here, we find that the long time dynamics of such an initialization develops into a wedge-like structure similar to the one described in Ref. [51] and recently found experimentally in Ref. [52]. The analytical estimate of Eq. (A1) characterizing the boundaries of the wedge structure is illustrated in Fig. 8(a) with white solid lines. Evidently, a good agreement with the numerical prediction is found.

However, in this case we observe a particularly interesting behavior not reported in the previous works. There, the wedge structure consisted of homogeneous fringes. In our case, the fringes composing this entity are revivals of the Peregrine soliton, both in time and space. As such, they are reminiscent of the Kuznetsov-Ma soliton [5,6] and the Akhmediev breather [8] and more generally of the doubly periodic solutions in space and time [78].

To better showcase this behavior, in Fig. 8(b) we present the inner region of the wedge structure. Clearly, each of the fringes constituting the wedge structure possesses revivals of the Peregrine soliton. However, every revival has a smaller amplitude than the previous one. In Fig. 8(c), we depict several Peregrine solitons emerging at $x = 0$. In decreasing amplitude, they correspond to the initial Peregrine solitons ($t'_0 = 1023$), the second revival ($t'_2 = 5148$), and the fourth revival ($t'_4 = 8052$). Additionally, we fitted Eq. (4) to each of the aforementioned wave forms to verify that indeed they are Peregrine solitons. Lastly, the temporal evolution of the density of the central fringe of the wedge structure is shown in Fig. 8(d). Here, each revival of the original Peregrine soliton is clearly discernible, as well as the corresponding decrease in amplitude. Again, a fitting to the wave form of Eq. (4) exhibits an adequate agreement with the selected revivals of the density, exposing their Peregrine character. It is important to remind the reader here that this wedge structure was predicted and found in focusing media. In contrast, our setup corresponds to a manifestation thereof in a repulsive (defocusing) two-component BEC.

- [1] L. Draper, *Weather* **21**, 2 (1966).
 [2] C. Kharif, E. Pelinovsky, and A. Slunyaev, *Rogue Waves in the Ocean*, Advances in Geophysical and Environmental Mechanics and Mathematics (Springer-Verlag, Berlin, 2009).
 [3] N. Akhmediev, J. M. Soto-Crespo, and A. Ankiewicz, *Phys. Lett. A* **373**, 2137 (2009).
 [4] M. J. Ablowitz and J. T. Cole, *Phys. Rev. Lett.* **127**, 104101 (2021).
 [5] E. A. Kuznetsov, *Dokl. Akad. Nauk SSSR* **236**, 575 (1977) [*Sov. Phys. Dokl.* **22**, 507 (1977)].
 [6] Y.-C. Ma, *Stud. Appl. Math.* **60**, 43 (1979).
 [7] K. B. Dysthe and K. Trulsen, *Phys. Scr.* **1999**, 48 (1999).
 [8] N. N. Akhmediev and V. I. Korneev, *Theor. Math. Phys.* **69**, 1089 (1986).
 [9] N. Karjanto, *Front. Phys.* **9**, 599767 (2021).
 [10] B. Kibler, J. Fatome, C. Finot, G. Millot, F. Dias, G. Genty, N. Akhmediev, and J. M. Dudley, *Nat. Phys.* **6**, 790 (2010).
 [11] B. Kibler, J. Fatome, C. Finot, G. Millot, G. Genty, B. Wetzell, N. Akhmediev, F. Dias, and J. M. Dudley, *Sci. Rep.* **2**, 463 (2012).
 [12] P. T. S. DeVore, D. R. Solli, D. Borlaug, C. Ropers, and B. Jalali, *J. Opt.* **15**, 064001 (2013).
 [13] J. M. Dudley, F. Dias, M. Erkintalo, and G. Genty, *Nat. Photon.* **8**, 755 (2014).
 [14] B. Frisquet, B. Kibler, P. Morin, F. Baronio, M. Conforti, G. Millot, and S. Wabnitz, *Sci. Rep.* **6**, 20785 (2016).
 [15] R. Sabry, W. M. Moslem, and P. K. Shukla, *Phys. Plasmas* **19**, 122903 (2012).
 [16] A. S. Bains, B. Li, and L.-D. Xia, *Phys. Plasmas* **21**, 032123 (2014).
 [17] R. E. Tolba, W. M. Moslem, N. A. El-Bedwehy, and S. K. El-Labany, *Phys. Plasmas* **22**, 043707 (2015).
 [18] A. N. Ganshin, V. B. Efimov, G. V. Kolmakov, L. P. Mezhev-Deglin, and P. V. E. McClintock, *Phys. Rev. Lett.* **101**, 065303 (2008).

- [19] E. G. Charalampidis, J. Cuevas-Maraver, D. J. Frantzeskakis, and P. G. Kevrekidis, *Rom. Rep. Phys.* **70**, 504 (2018).
- [20] B. Bakkali-Hassani, C. Maury, Y.-Q. Zou, É. Le Cerf, R. Saint-Jalm, P. C. M. Castilho, S. Nascimbene, J. Dalibard, and J. Beugnon, *Phys. Rev. Lett.* **127**, 023603 (2021).
- [21] Z. Yan, *J. Phys.: Conf. Ser.* **400**, 012084 (2012).
- [22] M. Onorato, S. Residori, U. Bortolozzo, A. Montina, and F. T. Arecchi, *Phys. Rep.* **528**, 47 (2013).
- [23] D. Mihalache, *Rom. Rep. Phys.* **69**, 403 (2017).
- [24] D. H. Peregrine, *J. Aust. Math. Soc. Series B, Appl. Math.* **25**, 16 (1983).
- [25] A. Chabchoub, N. P. Hoffmann, and N. Akhmediev, *Phys. Rev. Lett.* **106**, 204502 (2011).
- [26] A. Chabchoub, N. Hoffmann, M. Onorato, and N. Akhmediev, *Phys. Rev. X* **2**, 011015 (2012).
- [27] A. Chabchoub and M. Fink, *Phys. Rev. Lett.* **112**, 124101 (2014).
- [28] A. Tikan, F. Bonnefoy, G. Roberti, G. El, A. Tovbis, G. Ducrozet, A. Cazaubiel, G. Prabhudesai, G. Michel, F. Copie, E. Falcon, S. Randoux, and P. Suret, [arXiv:2108.02698](https://arxiv.org/abs/2108.02698) [nlin, physics:physics].
- [29] H. Bailung, S. K. Sharma, and Y. Nakamura, *Phys. Rev. Lett.* **107**, 255005 (2011).
- [30] A. Tikan, C. Billet, G. El, A. Tovbis, M. Bertola, T. Sylvestre, F. Gustave, S. Randoux, G. Genty, P. Suret, and J. M. Dudley, *Phys. Rev. Lett.* **119**, 033901 (2017).
- [31] G. Marcucci, D. Pierangeli, A. J. Agranat, R.-K. Lee, E. DelRe, and C. Conti, *Nat. Commun.* **10**, 5090 (2019).
- [32] A. Chowdury and W. Chang, *Phys. Rev. Res.* **3**, L032060 (2021).
- [33] L. P. Pitaevskii and S. Stringari, *Bose-Einstein Condensation*, Oxford Science Publications No. 116 (Clarendon Press, Oxford, UK, 2003).
- [34] L.-C. Zhao, *Ann. Phys.* **329**, 73 (2013).
- [35] Z.-D. Li, C.-Z. Huo, Q.-Y. Li, P.-B. He, and T.-F. Xu, *Chin. Phys. B* **27**, 040505 (2018).
- [36] H. Chaachoua Sameut, S. Pattu, U. Al Khawaja, M. Benarous, and H. Belkroukra, *Phys. Wave Phen.* **28**, 305 (2020).
- [37] T. Köhler, K. Góral, and P. S. Julienne, *Rev. Mod. Phys.* **78**, 1311 (2006).
- [38] C. Chin, R. Grimm, P. Julienne, and E. Tiesinga, *Rev. Mod. Phys.* **82**, 1225 (2010).
- [39] M. Olshanii, *Phys. Rev. Lett.* **81**, 938 (1998).
- [40] J. I. Kim, V. S. Melezhik, and P. Schmelcher, *Phys. Rev. Lett.* **97**, 193203 (2006).
- [41] K. Henderson, C. Ryu, C. MacCormick, and M. G. Boshier, *New J. Phys.* **11**, 043030 (2009).
- [42] R. Grimm, M. Weidemüller, and Y. B. Ovchinnikov, *Adv. At. Mol. Opt. Phys.* **42**, 95 (2000).
- [43] R. Y. Chiao, E. Garmire, and C. H. Townes, *Phys. Rev. Lett.* **13**, 479 (1964).
- [44] Z. Dutton and C. W. Clark, *Phys. Rev. A* **71**, 063618 (2005).
- [45] It is relevant to note as an aside here that the Townes soliton has also been created via a different method very recently in Ref. [79]; the latter method involved the modulational instability of a bright solitonic stripe in two-dimensional space.
- [46] P. G. Kevrekidis, D. J. Frantzeskakis, and R. Carretero-González, *The Defocusing Nonlinear Schrödinger Equation: From Dark Soliton to Vortices and Vortex Rings*, Other Titles in Applied Mathematics (Society for Industrial and Applied Mathematics, Philadelphia, 2015).
- [47] M. Bertola and A. Tovbis, *Commun. Pure Appl. Math.* **66**, 678 (2013).
- [48] S. Lannig, C.-M. Schmied, M. Prüfer, P. Kunkel, R. Strohmaier, H. Strobel, T. Gasenzer, P. G. Kevrekidis, and M. K. Oberthaler, *Phys. Rev. Lett.* **125**, 170401 (2020).
- [49] N. P. Proukakis and B. Jackson, *J. Phys. B: At. Mol. Opt. Phys.* **41**, 203002 (2008).
- [50] G. C. Katsimiga, S. I. Mistakidis, P. Schmelcher, and P. G. Kevrekidis, *New J. Phys.* **23**, 013015 (2021).
- [51] G. Biondini and D. Mantzavinos, *Phys. Rev. Lett.* **116**, 043902 (2016).
- [52] A. E. Kraych, P. Suret, G. El, and S. Randoux, *Phys. Rev. Lett.* **122**, 054101 (2019).
- [53] C. J. Pethick and H. Smith, *Bose-Einstein Condensation in Dilute Gases*, 2nd ed. (Cambridge University Press, Cambridge, UK, 2008).
- [54] M. Egorov, B. Opanchuk, P. Drummond, B. V. Hall, P. Hannaford, and A. I. Sidorov, *Phys. Rev. A* **87**, 053614 (2013).
- [55] T. H. Johnson, M. Bruderer, Y. Cai, S. R. Clark, W. Bao, and D. Jaksch, *EPL* **98**, 26001 (2012).
- [56] S. I. Mistakidis, G. C. Katsimiga, G. M. Koutentakis, T. Busch, and P. Schmelcher, *Phys. Rev. Lett.* **122**, 183001 (2019).
- [57] S. I. Mistakidis, G. M. Koutentakis, F. Grusdt, H. R. Sadeghpour, and P. Schmelcher, *New J. Phys.* **23**, 043051 (2021).
- [58] P. Massignan, M. Zaccanti, and G. M. Bruun, *Rep. Prog. Phys.* **77**, 034401 (2014).
- [59] K. M. Mertes, J. W. Merrill, R. Carretero-González, D. J. Frantzeskakis, P. G. Kevrekidis, and D. S. Hall, *Phys. Rev. Lett.* **99**, 190402 (2007).
- [60] S. E. Pollack, D. Dries, M. Junker, Y. P. Chen, T. A. Corcovilos, and R. G. Hulet, *Phys. Rev. Lett.* **102**, 090402 (2009).
- [61] E. G. Charalampidis, J. Lee, P. G. Kevrekidis, and C. Chong, *Phys. Rev. E* **98**, 032903 (2018).
- [62] Y. Miyazawa, C. Chong, P. G. Kevrekidis, and J. Yang, *Phys. Rev. E* **105**, 034202 (2022).
- [63] G. Biondini and J. Oregero, *Stud. Appl. Math.* **145**, 325 (2020).
- [64] For a transverse confinement with $\omega_{\perp} = 2\pi \times 150$ Hz these widths refer to a range from 45 to 135 μm .
- [65] P. G. Kevrekidis and D. J. Frantzeskakis, *Rev. Phys.* **1**, 140 (2016).
- [66] T. Busch and J. R. Anglin, *Phys. Rev. Lett.* **87**, 010401 (2001).
- [67] D. Yan, R. Carretero-González, D. J. Frantzeskakis, P. G. Kevrekidis, N. P. Proukakis, and D. Spirm, *Phys. Rev. A* **89**, 043613 (2014).
- [68] S. P. Cockburn, H. E. Nistazakis, T. P. Horikis, P. G. Kevrekidis, N. P. Proukakis, and D. J. Frantzeskakis, *Phys. Rev. Lett.* **104**, 174101 (2010).
- [69] S. P. Cockburn and N. P. Proukakis, *Laser Phys.* **19**, 558 (2009).
- [70] T. M. Bersano, V. Gokhroo, M. A. Khamehchi, J. D'Ambroise, D. J. Frantzeskakis, P. Engels, and P. G. Kevrekidis, *Phys. Rev. Lett.* **120**, 063202 (2018).
- [71] G. C. Katsimiga, S. I. Mistakidis, T. M. Bersano, M. K. H. Ome, S. M. Mossman, K. Mukherjee, P. Schmelcher, P. Engels, and P. G. Kevrekidis, *Phys. Rev. A* **102**, 023301 (2020).
- [72] G. C. Katsimiga, G. M. Koutentakis, S. I. Mistakidis, P. G. Kevrekidis, and P. Schmelcher, *New J. Phys.* **19**, 073004 (2017).

- [73] G. C. Katsimiga, S. I. Mistakidis, G. M. Koutentakis, P. G. Kevrekidis, and P. Schmelcher, *Phys. Rev. A* **98**, 013632 (2018).
- [74] S. I. Mistakidis, G. C. Katsimiga, P. G. Kevrekidis, and P. Schmelcher, *New J. Phys.* **20**, 043052 (2018).
- [75] G. A. El', A. V. Gurevich, V. V. Khodorovskiĭ, and A. L. Krylov, *Phys. Lett. A* **177**, 357 (1993).
- [76] V. E. Zakharov and A. A. Gelash, *Phys. Rev. Lett.* **111**, 054101 (2013).
- [77] G. Biondini, *Phys. Rev. E* **98**, 052220 (2018).
- [78] N. N. Akhmediev, V. M. Eleonskii, and N. E. Kulagin, *Theor. Math. Phys.* **72**, 809 (1987).
- [79] C.-A. Chen and C.-L. Hung, *Phys. Rev. Lett.* **127**, 023604 (2021).

Experimental Realization of the Peregrine Soliton in Repulsive Two-Component Bose-Einstein Condensates

A. Romero-Ros,¹ G. C. Katsimiga,² S. I. Mistakidis^{3,4}, S. Mossman,^{5,6} G. Biondini^{7,8},
P. Schmelcher,^{1,9} P. Engels⁶, and P. G. Kevrekidis²

¹Center for Optical Quantum Technologies, Department of Physics, University of Hamburg,
Luruper Chaussee 149, 22761 Hamburg, Germany

²Department of Mathematics and Statistics, University of Massachusetts Amherst, Amherst, Massachusetts 01003-4515, USA

³ITAMP, Center for Astrophysics | Harvard & Smithsonian, Cambridge, Massachusetts 02138, USA

⁴Department of Physics, Harvard University, Cambridge, Massachusetts 02138, USA

⁵Department of Physics and Biophysics, University of San Diego, San Diego, California 92110, USA

⁶Department of Physics and Astronomy, Washington State University, Pullman, Washington 99164-2814, USA

⁷Department of Mathematics, State University of New York, Buffalo, New York 14260, USA

⁸Department of Physics, State University of New York, Buffalo, New York 14260, USA

⁹The Hamburg Centre for Ultrafast Imaging, University of Hamburg, Luruper Chaussee 149, 22761 Hamburg, Germany



(Received 27 April 2023; revised 20 November 2023; accepted 12 December 2023; published 19 January 2024)

We experimentally realize the Peregrine soliton in a highly particle-imbalanced two-component repulsive Bose-Einstein condensate in the immiscible regime. The effective focusing dynamics and resulting modulational instability of the minority component provide the opportunity to dynamically create a Peregrine soliton with the aid of an attractive potential well that seeds the initial dynamics. The Peregrine soliton formation is highly reproducible, and our experiments allow us to separately monitor the minority and majority components, and to compare with the single component dynamics in the absence or presence of the well with varying depths. We showcase the centrality of each of the ingredients leveraged herein. Numerical corroborations and a theoretical basis for our findings are provided through three-dimensional simulations emulating the experimental setting and via a one-dimensional analysis further exploring its evolution dynamics.

DOI: [10.1103/PhysRevLett.132.033402](https://doi.org/10.1103/PhysRevLett.132.033402)

Introduction.—The fascination with rogue or freak waves has a time-honored history that can be argued to artistically go all the way back to Hokusai’s famous drawing of “The Great Wave off Kanagawa.” In a more quantitative form, for over half a century and since the early observations [1], the term “rogue wave” has been used for waves of elevation several times bigger than the average sea state. Further, and more well-documented occurrences of rogue waves have arisen in recent years and, in particular, since the notable observation of the so-called Draupner wave [2].

Recent progress has been catalyzed by a sequence of remarkable experiments in nonlinear optics, enabling the observation of rogue waves via novel detection techniques [3] and their practical use, e.g., for supercontinuum generation [4], and continued through a sequence of detailed analyses of related waveforms [5–9]. One candidate solution for rogue waves appearing in nature is the Peregrine soliton (PS) [10]. Subsequently, both fundamental, but also more complex (higher-order) rogue-wave patterns were observed in highly controlled fluid experiments [11–13], including the very recreation of the Draupner wave [14]. In turn, this progress prompted related

investigations in other fields, including plasmas [15–17], and the associated activity has more recently been summarized in a number of related reviews [18–23].

Bose-Einstein condensates (BECs) [24,25] have constituted a fertile playground where various types of nonlinear waves, including bright and dark solitons, vortices, vortex lines, and rings, among others [26], have been realized experimentally at a mean-field level. Importantly, the above list also extends to numerous salient features of attractive condensates, including the formation of bright solitons [27], the modulational instability that may produce trains thereof [28–30], or the nature of their interactions and collisions [31]. Yet, to the best of our knowledge, the creation of one of the most quintessential nonlinear waveforms, i.e., the PS [10], a structure localized in time and space that emerges from a modulationally unstable background and decays back to it, has remained elusive. This situation may be attributed to numerous key factors associated with the fairly precise control needed to produce such an entity. Such factors include the structure’s modulationally unstable background, the temporally localized nature of its existence (together with the typically destructive imaging), and the “dimensionality reduction” from

three-dimensions (3D) to quasi-one-dimension (1D) and its impact on the resulting dynamics.

The aim of the present work is to overcome these major obstacles and report the first experimental observation of the PS in BECs. To do so, we leverage a number of crucial ingredients. Adapting the earlier idea of a two-component *self-defocusing* but immiscible setting consisting of a majority and a minority component creates an *effectively self-focusing medium* for the minority component [32,33]. This approach was utilized in two spatial dimensions to produce the well-known Townes soliton [34] that prompted the theoretical proposal of the PS realization [35].

We experimentally deploy a highly elongated trap geometry with an initial (weak) potential well at the condensate center. This well seeds the modulational instability of the minority component, providing a reproducible focal point for the spontaneous reshaping of the associated wave function into a PS, before eventually the modulationally unstable dynamics takes over and leads to the emergence of multiple peaks. Our numerical 3D and 1D analysis of the setting corroborates the nature of our experimental observations, while providing information about the phase structure. Moreover, we provide experimental evidence for the centrality of each of our above-mentioned experimental ingredients, since the absence of any one of them is detrimental to the PS formation.

Experimental results.—We experimentally demonstrate the formation of the PS in a ^{87}Rb BEC of $N \approx 9 \times 10^5$ atoms where all interatomic interactions are repulsive. Initially, the atoms occupy the single hyperfine state $|F, m_F\rangle = |1, -1\rangle$. The BEC is confined in a highly elongated harmonic trap with frequencies $(\omega_x, \omega_y, \omega_z) = 2\pi \times (2.5, 245, 258)$ Hz. The 100:1 aspect ratio of the optical trap ensures effectively 1D dynamics, leaving at most collective excitations (i.e., absence of any nonlinear

structure) along the transverse direction observed in experiment and confirmed numerically. An additional attractive optical potential is present in the central part of the BEC producing a small density hump in the center of the cloud; see Supplemental Material (SM) [36] for further details. This optical potential, characterized by waists $s_x \approx 13 \mu\text{m}$ and $s_y \approx 25 \mu\text{m}$ and approximate depth of 97 nK, is radially uniform but has a Gaussian shape along the long axis of the BEC. From this static initial condition with chemical potential $\mu \approx 97$ nK [36], the dynamics is initiated by rapidly transferring a small fraction ($\sim 15\%$) of the atoms to the $|2, 0\rangle$ state with a $55 \mu\text{s}$ microwave pulse, and transferring the remaining atoms to the $|1, 0\rangle$ state in a $102 \mu\text{s}$ rf pulse. Both pulses are applied uniformly across the whole BEC.

In the following, we focus on the dynamics of the $|2, 0\rangle$ hyperfine state (minority component) for which an effective self-focusing description applies. Snapshots of the corresponding density distributions are presented both in experiment and theory in Fig. 1. The experimental images [Figs. 1(a)–1(h)] include an additional 9 ms of time of flight to avoid image saturation of the high density peak. The initially prepared Gaussian hump in the center of the BEC is seen to evolve into a narrow, high peak flanked by two clear dips on either side, after approximately 65 ms [Figs. 1(c) and 1(g)]. These dips are a characteristic feature of a PS and are related to the formation of a π phase jump of the wave function in the peak region relative to the surrounding BEC, leading to destructive interference at the position of the dips (see also Fig. 3). Subsequently, the peak height decreases, leading to the emergence of side peaks and excitations on either side around 85 ms [Figs. 1(d) and 1(h)]. We note that the observed timescales are highly reproducible, indicating that the dynamics is a well-defined consequence of the initial conditions prepared

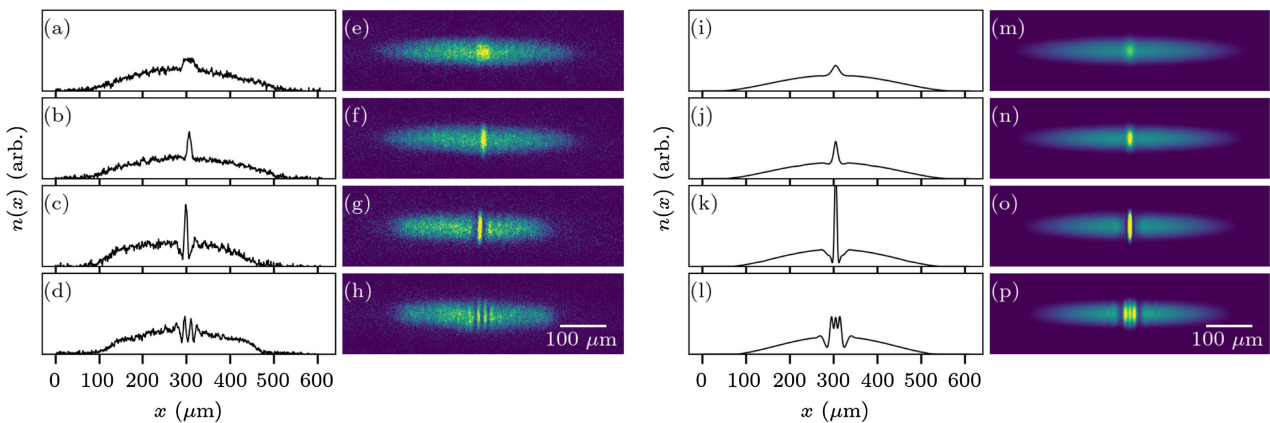


FIG. 1. Comparison between (a)–(h) experimental and (i)–(p) numerical observations for the emergence of the PS. (a)–(d) Cross sections of (e)–(h) showing single-shot absorption images after 10, 30, 65, and 85 ms of evolution, respectively, with an additional 9 ms of free expansion for imaging. (i)–(l) Cross sections of (m)–(p) represent the density profiles obtained from the 3D mean-field simulations under the experimental conditions. The vertical axis in the numerical images has been stretched for comparison with the experiment.

in the experiment. This is also confirmed by our 3D simulations [Figs. 1(i) to 1(p)], further discussed below.

Mean-field dynamics.—Following the experimental conditions, we consider a ^{87}Rb BEC in the aforementioned hyperfine states with a spin population imbalance of 85%–15%. To model the dynamical generation of the PS, we employ two coupled 3D Gross-Pitaevskii equations [24–26],

$$i\hbar\partial_t\Psi_F(\mathbf{r},t) = \left[-\frac{\hbar^2}{2m}\nabla_{\mathbf{r}}^2 + V(\mathbf{r}) + V_G(\mathbf{r}) + \sum_{F'=1}^2 g_{FF'}|\Psi_{F'}(\mathbf{r},t)|^2 \right] \Psi_F(\mathbf{r},t). \quad (1)$$

Here, $\Psi_F(\mathbf{r},t)$ is the 3D mean-field wave function with $F = 1, 2$ denoting each hyperfine state, $\mathbf{r} = (x, y, z)$, and m is the atomic mass. The external trap is given by $V(\mathbf{r}) = \sum_{\alpha=x,y,z} m\omega_{\alpha}^2\alpha^2/2$, and the coupling constants $g_{FF'} = 4\pi N_{F'}\hbar^2 a_{FF'}/m$ refer to the intra- ($F = F'$) and interspecies ($F \neq F'$) interaction strengths, with $a_{FF'}$ being the 3D s -wave scattering lengths, and N_F is the atom number in the F spin channel. Specifically, the scattering lengths corresponding to the experimental setup are $a_{11} = 100.86a_0$, $a_{22} = 94.57a_0$, and $a_{12} = a_{21} = 98.9a_0$, where a_0 designates the Bohr radius. These coefficients give rise to an *effective* attractive nonlinear coefficient $a_{\text{eff}} = a_{22} - a_{12}^2/a_{11} < 0$, allowing for a reduced single-component description of the minority component [32,33].

Consequently, our system now supports the emergence of focusing nonlinear phenomena such as the PS. Neglecting the transverse coordinate dependence, the form of the PS is given by [10]

$$\Psi_P(x,t) = \sqrt{P_0} \left[1 - \frac{4\left(1 + 2i\frac{t-t_0}{T_P}\right)}{1 + 4\left(\frac{x-x_0}{L_P}\right)^2 + 4\left(\frac{t-t_0}{T_P}\right)^2} \right] e^{i\frac{x-x_0}{L_P}}, \quad (2)$$

where $T_P/\hbar = L_P^2 m/\hbar^2 = 1/(|g_{\text{eff}}|P_0)$. Here, T_P and L_P are the characteristic scales of time and space of the PS solution, respectively. P_0 represents the background density of the minority component in a homogeneous system, and $g_{\text{eff}} = g_{22}^{(\text{1D})} - (g_{12}^{(\text{1D})})^2/g_{11}^{(\text{1D})}$ denotes the effective 1D interaction in the single-component description; see also SM [36].

To dynamically seed the PS nucleation, we employ the optically induced Gaussian well $V_G(\mathbf{r}) = -V_0 \exp\{-2[(x/s_x)^2 + (y/s_y)^2]\}$. The widths and the potential depth V_0 are fixed in accordance with the experimental setup. Note that the transverse spatial profile of the Gaussian potential does not significantly affect the PS generation, in line with the experimental observations,

as long as its width is larger than the transverse spatial extent of the BEC.

We initially place all N atoms in the $|1, -1\rangle$ state and identify the ground state of this system in the presence of the optical well utilizing the time-independent version of Eq. (1). We then instantaneously transfer a fraction of typically 15% (85%) of the atoms to the $|2, 0\rangle$ ($|1, 0\rangle$) state, thus emulating the rf experimental process. Additionally, we approximately account for the experimental thermal fraction ($< 10\%$) and for the observed atom-loss rate in $|2, 0\rangle$ of around 0.23% per ms (see SM [36]). The two-component system is then allowed to evolve according to Eq. (1). Initially, the dynamical evolution of the stationary states described above entails the counterpropagating emission of sound waves with the subsequent PS generation reaching maximal amplitude around $t \approx 70$ ms [see the slightly earlier snapshots in Figs. 1(k) and 1(o)], before its structural deformation toward three equidistant peaks [Figs. 1(l) and 1(p)]. A clear agreement with the experimental PS realization and the overall dynamics [Figs. 1(a) to 1(h)] is observed. Any residual deviations in the intensity of the PS are principally traced back to the time of flight performed in the experiment but not taken into account in the simulations.

Controllability of Peregrine generation.—To unveil the necessary conditions for the formation of a PS, Fig. 2 presents a collection of various alterations of the experimental procedure discussed above. As a baseline for comparison, Figs. 2(a) and 2(g) show a PS beginning to form under the conditions described in Fig. 1 after 50 ms of evolution. If an identical experiment is performed but with a single-component cloud, no PS is observed [Figs. 2(b) and 2(h)], demonstrating the key role of interspecies interactions for the emergent dynamics. The deformation of the initially Gaussian bulge is due to expansion during time of flight. Specifically, the initial Gaussian shaped density hump spreads out, leading to sound wave pulses propagating away from each other. Also, when conducting experiments with the two-component mixture in the absence of the well, instability takes longer to set in and no PS forms within accessible timescales [Figs. 2(c) and 2(i)].

Having identified the presence of the optical well and the genuine two-component mixture as key ingredients, we can further elucidate their roles. Figures 2(d) and 2(j) show a mixture of 15% of atoms in the $|2, 0\rangle$ state embedded in a 85% background of atoms in the $|1, -1\rangle$ state [as opposed to $|2, 0\rangle$ and $|1, 0\rangle$ atoms used for Figs. 2(a) and 2(g)]. The dynamical generation of the PS is again clearly observed, although this mixture is characterized by a less attractive effective scattering length of $a_{\text{eff}} = -1.34a_0$ for the $|2, 0\rangle$ atoms, as compared to $-2.41a_0$ for the $|2, 0\rangle$ atoms embedded in a $|1, 0\rangle$ background. The formation of a PS, as discussed above, is not highly specific to some of the exact parameters of the Gaussian well, e.g., if the well

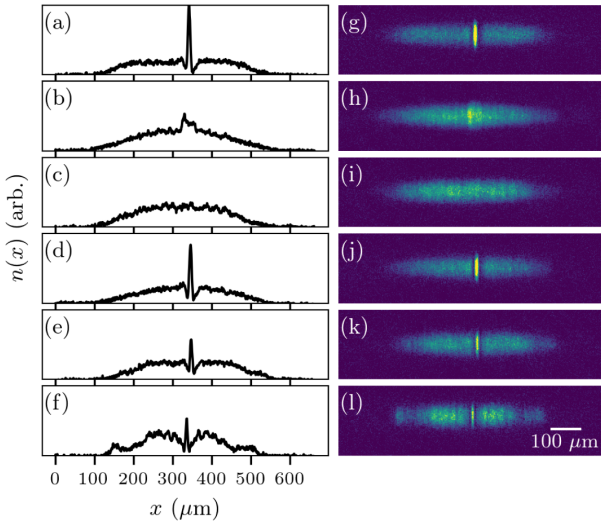


FIG. 2. Impact of the optical trap features on PS nucleation. (a), (g) Standard PS sequence after 50 ms of evolution. (b), (h) All atoms in a single component ($|1, 0\rangle$) showing no PS formation. (c), (i) Minority component prepared without the potential well leading to the absence of PS. (d), (j) A PS forming in the $|1, -1\rangle$ & $|2, 0\rangle$ mixture after 50 ms of evolution (instead of the $|1, 0\rangle$ & $|2, 0\rangle$ mixture). (e), (k) Well depth cut by half compared to panel (a), then 80 ms evolution. (f), (l) Well [with the same depth as in panel (a)] switched off at 20 ms, with the image taken after 110 ms (i.e., 90 ms after the well was switched off). For further details on the interplay of PS generation and the well characteristics see SM [36].

depth is reduced by a factor of two, the PS still emerges, but at later evolution times. In particular, in Figs. 2(e) and 2(k) the PS starts to manifest after 80 ms of evolution time, compared to the approximately 50 ms needed in the case depicted in Figs. 2(a) and 2(g).

Importantly, the PS can emerge even if the well is only present for a short time after the initial preparation of the mixture, and it is then switched off. Figures 2(f) and 2(l) showcase a pertinent example, where the well was switched off abruptly at 20 ms after the preparation of the atomic mixture, and the image was taken after an additional evolution time of 90 ms after the switch-off (see also the discussion in SM [36]). This comparison demonstrates that the continued presence of the potential well is not required: the well only serves to “seed” the relevant dynamics leading to the PS generation. The possibility to trigger the dynamics in a controlled way is a powerful feature of our experimental setting, which enables us to produce the PS in a highly repeatable way, making it possible to study its time evolution. The instrumental role played by the well is further elucidated through more elaborated numerical investigations of the impact of its characteristics provided in Fig. 3.

Further characterization of the Peregrine.—Leveraging the 1D nature of the PS, we additionally employ a 1D reduction of Eq. (1) to further numerically characterize the

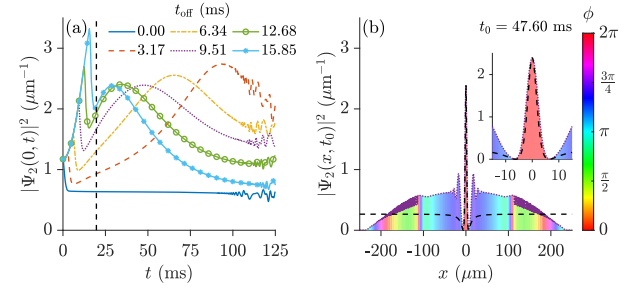


FIG. 3. 1D simulations of the minority component switching off the Gaussian well at indicated times before the expected nucleation of the PS (vertical black dashed line). (a) Time evolution of the central density, $|\Psi_2|^2$, of $|2, 0\rangle$. (b) Snapshot of $|\Psi_2|^2$ at the time instant of the PS formation after the well switch-off at $t = 9.51$ ms. The color gradient denotes the phase of Ψ_2 . A magnification of the central region in the inset showcases the good agreement between $|\Psi_2|^2$ and the analytical PS solution (2) (black dashed line) and the characteristic π phase jump between the core and the wings of the PS. The Gaussian well parameters used here are $V_0 = 60$ nK and $s_x = 4.8$ μm .

features of the PS in the context of these experiments. Here, we follow the experimental procedure described above while averaging over the transverse coordinates (see SM for details [36]).

Figure 3 demonstrates how the presence of the well assists in controllably seeding the emergence of the PS. In this particular case, we employ a well with $V_0 = 60$ nK and $s_x = 4.8$ μm . In Fig. 3(a) we present the time evolution of the central density of the minority component, $|\Psi_2(0, t)|^2$, when switching off the well at various time instants, t_{off} (see legend), before the PS nucleation would occur if the well was always present (vertical dashed line at $t = 19.68$ ms). In all cases, the PS emerges at some time, t_0 , after switching off the well. The exception is $t_{\text{off}} = 0$ ms (blue solid line), for which no PS forms. This supports the fact that, without the well, the above initial condition is not sufficient to form the PS. The earlier the switch-off, the later the PS emerges. Note that the process of switching off the well generates shock waves and their effect is visible after $t > 100$ ms.

To better understand the structure and properties of the PS, in Fig. 3(b), we provide an instantaneous density profile of $|2, 0\rangle$ and its corresponding phase (depicted by a color gradient) at t_0 when switching off the well at $t_{\text{off}} = 9.51$ ms. Additionally, we provide the profile of Eq. (2) with $P_0 = \max(|\Psi_2(x, t_0)|^2)/9$ (black dashed lines) to compare the emerging structure with the analytical PS solution. A close inspection of the central region of the condensate [inset of Fig. 3(b)] evinces the excellent agreement of the PS core among the two and the telltale π phase jump between the core and the wings of the waveform.

Conclusions.—We have experimentally demonstrated the dynamical formation of a PS in a two-component

BEC featuring a suitable mixture of repulsive interactions that emulate an effective attractive environment. This work shows how self-focusing interactions together with an attractive well as an effective catalyst cause a time-dependent localization to emerge from a modulationally unstable background resulting in the realization of a PS. Utilizing the attractive potential well it was possible to reproducibly and rapidly, i.e., comfortably within the condensate lifetimes, produce such wave structures in a highly controlled manner. A single repulsive component, not being modulationally unstable, is unable to produce such a phenomenon. Importantly, our experimental observations are in good quantitative agreement with 3D mean-field simulations. Simultaneously, a systematic 1D analysis revealed additional features of the phenomenology, such as the telltale phase gradient across the PS, and a detailed examination of the effect of switching off the well at different times.

Our platform paves the way for a closer inspection of rogue waves and higher-order rogue structures [12], or rogue waves in other ultracold atomic gas implementations such as intrinsically attractive BECs [27,29–31]. A natural question is the persistence of the PS generation in the dimensional crossover to 3D and how (parametrically) the 2D or 3D character comes into play. Another direction would be to extend these considerations to a larger number of components (e.g., spinor condensates [48,49]), to reveal the interplay of magnetic excitations and possibly emergent spin domains on the PS formation. Yet another possibility may be to study the formation of the mixed-bubble phase [50–52] that is inherently related to the presence of quantum fluctuations and occurs at the immiscibility threshold.

We acknowledge fruitful discussions lending context to this work at the Dispersive Hydrodynamics Program (2022) hosted by the Isaac Newton Institute for Mathematical Sciences. This material is based upon work supported by the U.S. National Science Foundation (NSF) under the Grants No. PHY-2110030 and No. DMS-2204702 (P. G. K.). S. I. M. acknowledges support from the NSF through a grant for ITAMP at Harvard University. P. E. acknowledges support from the NSF through Grant No. PHY-1912540 and from the Ralph G. Yount Distinguished Professorship at WSU. G. B. acknowledges support from the NSF through Grant No. DMS-2004987. The work of P. S. was funded by the Deutsche Forschungsgemeinschaft (German Research Foundation) under Grant No. SFB-925—Project No. 170620586.

[1] L. Draper, *Weather* **21**, 2 (1966).

[2] C. Kharif, E. Pelinovsky, and A. Slunyaev, *Rogue Waves in the Ocean*, Advances in Geophysical and Environmental Mechanics and Mathematics (Springer-Verlag, Berlin Heidelberg, 2009), 10.1007/978-3-540-88419-4.

- [3] D. R. Solli, C. Ropers, P. Koonath, and B. Jalali, *Nature (London)* **450**, 1054 (2007).
- [4] D. R. Solli, C. Ropers, and B. Jalali, *Phys. Rev. Lett.* **101**, 233902 (2008).
- [5] B. Kibler, J. Fatome, C. Finot, G. Millot, F. Dias, G. Genty, N. Akhmediev, and J. M. Dudley, *Nat. Phys.* **6**, 790 (2010).
- [6] B. Kibler, J. Fatome, C. Finot, G. Millot, G. Genty, B. Wetzel, N. Akhmediev, F. Dias, and J. M. Dudley, *Sci. Rep.* **2**, 463 (2012).
- [7] P. T. S. DeVore, D. R. Solli, D. Borlaug, C. Ropers, and B. Jalali, *J. Opt.* **15**, 064001 (2013).
- [8] B. Frisquet, B. Kibler, P. Morin, F. Baronio, M. Conforti, G. Millot, and S. Wabnitz, *Sci. Rep.* **6**, 20785 (2016).
- [9] A. Tikan, C. Billet, G. El, A. Tovbis, M. Bertola, T. Sylvestre, F. Gustave, S. Randoux, G. Genty, P. Suret, and J. M. Dudley, *Phys. Rev. Lett.* **119**, 033901 (2017).
- [10] D. H. Peregrine, *J. Aust. Math. Soc. Series B, Appl. Math.* **25**, 16 (1983).
- [11] A. Chabchoub, N. P. Hoffmann, and N. Akhmediev, *Phys. Rev. Lett.* **106**, 204502 (2011).
- [12] A. Chabchoub, N. Hoffmann, M. Onorato, and N. Akhmediev, *Phys. Rev. X* **2**, 011015 (2012).
- [13] A. Chabchoub and M. Fink, *Phys. Rev. Lett.* **112**, 124101 (2014).
- [14] M. L. McAllister, S. Draycott, T. A. A. Adcock, P. H. Taylor, and T. S. van den Bremer, *J. Fluid Mech.* **860**, 767 (2019).
- [15] H. Bailung, S. K. Sharma, and Y. Nakamura, *Phys. Rev. Lett.* **107**, 255005 (2011).
- [16] R. Sabry, W. M. Moslem, and P. K. Shukla, *Phys. Plasmas* **19**, 122903 (2012).
- [17] R. E. Tolba, W. M. Moslem, N. A. El-Bedwehy, and S. K. El-Labany, *Phys. Plasmas* **22**, 043707 (2015).
- [18] Z. Yan, *J. Phys. Conf. Ser.* **400**, 012084 (2012).
- [19] M. Onorato, S. Residori, U. Bortolozzo, A. Montina, and F. T. Arecchi, *Phys. Rep.* **528**, 47 (2013).
- [20] J. M. Dudley, F. Dias, M. Erkintalo, and G. Genty, *Nat. Photonics* **8**, 755 (2014).
- [21] D. Mihalache, *Rom. Rep. Phys.* **69**, 403 (2017), <https://rrp.nipne.ro/2017/AN403.pdf>.
- [22] J. M. Dudley, G. Genty, A. Mussot, A. Chabchoub, and F. Dias, *Nat. Rev. Phys.* **1**, 675 (2019).
- [23] A. Tikan, S. Randoux, G. El, A. Tovbis, F. Copie, and P. Suret, *Front. Phys.* **8** (2021).
- [24] C. J. Pethick and H. Smith, *Bose–Einstein Condensation in Dilute Gases*, 2nd ed. (Cambridge University Press, Cambridge, England, 2008), 10.1017/CBO9780511802850.
- [25] L. P. Pitaevskii and S. Stringari, *Bose-Einstein Condensation*, Oxford Science Publications No. 116 (Clarendon Press, Oxford; New York, 2003).
- [26] P. G. Kevrekidis, D. J. Frantzeskakis, and R. Carretero-González, *The Defocusing Nonlinear Schrödinger Equation: From Dark Soliton to Vortices and Vortex Rings*, Other Titles in Applied Mathematics (Society for Industrial and Applied Mathematics, Philadelphia, 2015), 10.1137/1.9781611973945.
- [27] L. Khaykovich, F. Schreck, G. Ferrari, T. Bourdel, J. Cubizolles, L. D. Carr, Y. Castin, and C. Salomon, *Science* **296**, 1290 (2002).

- [28] K. E. Strecker, G. B. Partridge, A. G. Truscott, and R. G. Hulet, *Nature (London)* **417**, 150 (2002).
- [29] K. E. Strecker, G. B. Partridge, A. G. Truscott, and R. G. Hulet, *New J. Phys.* **5**, 73 (2003).
- [30] P. J. Everitt, M. A. Sooriyabandara, M. Guasoni, P. B. Wigley, C. H. Wei, G. D. McDonald, K. S. Hardman, P. Manju, J. D. Close, C. C. N. Kuhn, S. S. Szigeti, Y. S. Kivshar, and N. P. Robins, *Phys. Rev. A* **96**, 041601(R) (2017).
- [31] J. H. V. Nguyen, P. Dyke, D. Luo, B. A. Malomed, and R. G. Hulet, *Nat. Phys.* **10**, 918 (2014).
- [32] Z. Dutton and C. W. Clark, *Phys. Rev. A* **71**, 063618 (2005).
- [33] B. Bakali-Hassani, C. Maury, Y.-Q. Zou, É. Le Cerf, R. Saint-Jalm, P. C. M. Castilho, S. Nascimbene, J. Dalibard, and J. Beugnon, *Phys. Rev. Lett.* **127**, 023603 (2021).
- [34] R. Y. Chiao, E. Garmire, and C. H. Townes, *Phys. Rev. Lett.* **13**, 479 (1964).
- [35] A. Romero-Ros, G. C. Katsimiga, S. I. Mistakidis, B. Prinari, G. Biondini, P. Schmelcher, and P. G. Kevrekidis, *Phys. Rev. A* **105**, 053306 (2022).
- [36] See Supplemental Material at <http://link.aps.org/supplemental/10.1103/PhysRevLett.132.033402> for additional details on the experimental methods and complementary results, further comparisons between 3D mean-field simulations and experiment, and the parametric dependence of the PS generation, which includes Refs. [37–47].
- [37] M. Bertola and A. Tovbis, *Commun. Pure Appl. Math.* **66**, 678 (2013).
- [38] R. H. J. Grimshaw and A. Tovbis, *Proc. R. Soc. Math. Phys. Eng. Sci.* **469**, 20130094 (2013).
- [39] G. Biondini and D. Mantzavinos, *Phys. Rev. Lett.* **116**, 043902 (2016).
- [40] N. P. Proukakis and B. Jackson, *J. Phys. B* **41**, 203002 (2008).
- [41] P. Jain and M. Boninsegni, *Phys. Rev. A* **83**, 023602 (2011).
- [42] S. I. Mistakidis, G. C. Katsimiga, P. G. Kevrekidis, and P. Schmelcher, *New J. Phys.* **20**, 043052 (2018).
- [43] G. A. El', A. V. Gurevich, V. V. Khodorovskii, and A. L. Krylov, *Phys. Lett. A* **177**, 357 (1993).
- [44] L.-C. Zhao and L. Ling, *J. Opt. Soc. Am. B* **33**, 850 (2016).
- [45] V. E. Zakharov and A. A. Gelash, *Phys. Rev. Lett.* **111**, 054101 (2013).
- [46] G. Biondini, *Phys. Rev. E* **98**, 052220 (2018).
- [47] A. E. Kraych, P. Suret, G. El, and S. Randoux, *Phys. Rev. Lett.* **122**, 054101 (2019).
- [48] Y. Kawaguchi and M. Ueda, *Phys. Rep.* **520**, 253 (2012).
- [49] D. M. Stamper-Kurn and M. Ueda, *Rev. Mod. Phys.* **85**, 1191 (2013).
- [50] P. Naidon and D. S. Petrov, *Phys. Rev. Lett.* **126**, 115301 (2021).
- [51] S. I. Mistakidis, A. G. Volosniev, R. E. Barfknecht, T. Fogarty, T. Busch, A. Foerster, P. Schmelcher, and N. T. Zinner, *Phys. Rep.* **1042**, 1 (2023).
- [52] P. Stürmer, M. N. Tengstrand, and S. M. Reimann, *Phys. Rev. Res.* **4**, 043182 (2022).

Supplement: Experimental realization of the Peregrine soliton in repulsive two-component Bose-Einstein condensates

A. Romero-Ros,¹ G. C. Katsimiga,² S. I. Mistakidis,^{3,4} S. Mossman,^{5,6}
G. Biondini,^{7,8} P. Schmelcher,^{1,9} P. Engels,⁶ and P. G. Kevrekidis²

¹Center for Optical Quantum Technologies, Department of Physics,
University of Hamburg, Luruper Chaussee 149, 22761 Hamburg, Germany

²Department of Mathematics and Statistics, University of Massachusetts Amherst, Amherst, MA 01003-4515, USA

³ITAMP, Center for Astrophysics | Harvard & Smithsonian, Cambridge, MA 02138 USA

⁴Department of Physics, Harvard University, Cambridge, Massachusetts 02138, USA

⁵Department of Physics and Biophysics, University of San Diego, San Diego, CA 92110

⁶Department of Physics and Astronomy, Washington State University, Pullman, Washington 99164-2814

⁷Department of Mathematics, State University of New York, Buffalo, New York 14260, USA

⁸Department of Physics, State University of New York, Buffalo, New York 14260, USA

⁹The Hamburg Centre for Ultrafast Imaging, University of Hamburg, Luruper Chaussee 149, 22761 Hamburg, Germany

(Dated: November 20, 2023)

I. EXPERIMENTAL METHODS AND SUPPLEMENTARY RESULTS

Our experiments are conducted with ^{87}Rb atoms in the $F = 1$ and $F = 2$ spin states. Initially, BECs containing approximately $N = 9 \times 10^5$ atoms in the $|F, m_F\rangle = |1, -1\rangle$ hyperfine state are confined in a highly elongated optical dipole trap with harmonic trap frequencies of $(\omega_x, \omega_y, \omega_z) = 2\pi \times (2.5, 245, 258)$ Hz. A magnetic bias field of 10 G is applied in the vertical direction. During the evaporative cooling that leads to the formation of the BEC, an attractive Gaussian potential is continuously superimposed on the optical dipole trap. This potential is generated by an elliptical dipole beam with a wavelength of 850 nm and is characterized by a Gaussian width of $s_x = 13 \mu\text{m}$ along the long axis of the BEC and $s_y = 25 \mu\text{m}$ along the tightly confined horizontal direction. The beam propagates in the vertical direction, in both tightly confined directions the beam is significantly larger than the diameter of the BEC (approximately $3 \mu\text{m}$), and its profile is relevant only along the weakly confined, long axis of the BEC. The potential depth produced by this dipole beam is $V_0 = 40$ nK (for Fig. 1 and 2 in the main text with the exception of Fig. 2(e,k) where the potential depth was reduced by a factor of two), and $V_0 = 30$ nK for the case of the wide well in Fig. S4. This potential produces a density hump in the center of the BEC. This leads to a static initial condition with no detectable dynamics, see in particular the inset of Fig. S1. Notice that larger widths lead to less deformed yet broader initial state configurations. The values of the respective chemical potential, μ , of this initial state are provided in Fig. S1 for different widths, s_x , of the attractive Gaussian potential. All other parameters are kept fixed. As it can be seen, μ is reduced for increasing s_x since the latter enforces a wider Thomas-Fermi profile. On the other hand, μ is shifted to larger values for smaller V_0 and fixed s_x .

A rapid microwave and RF pulse sequence then generates

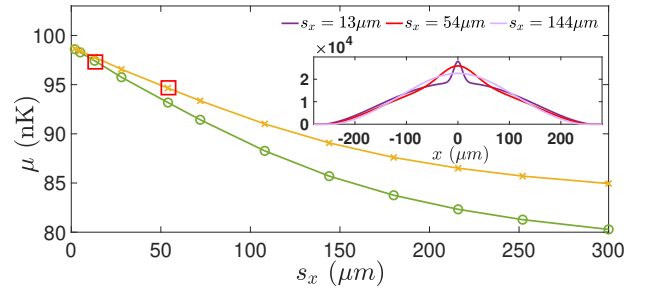


Figure S1. Chemical potential variation of the initial state as a function of the width, s_x , of the attractive Gaussian potential along the long axis of the BEC. Distinct solid lines correspond to the specific choices of V_0 (see legend) employed in the main text. Red rectangles mark the values used in Figs. 1 and 4 of the main text. Notice that $s_x = 300 \mu\text{m} \approx R_{TF}$ representing the Thomas-Fermi radius in the absence of the Gaussian well. The inset depicts characteristic integrated density profiles of the initial state for different s_x (see legend). Other parameters used are the same as in Fig.1 of the main text.

a two-component mixture comprised of 85% of all atoms in the $|F, m_F\rangle = |1, 0\rangle$ state and 15% of all atoms in the $|F, m_F\rangle = |2, 0\rangle$. We remark that the mean-field interaction coefficients, $g_{ij} = 4\pi\hbar^2 a_{ij} / m(^{87}\text{Rb})$, correspond to $g_{11} = 5.16 \times 10^{-51}$ ($\text{kg m}^5/\text{s}^2$), $g_{22} = 4.84 \times 10^{-51}$ ($\text{kg m}^5/\text{s}^2$) and $g_{12} = g_{21} = 5.06 \times 10^{-51}$ ($\text{kg m}^5/\text{s}^2$). State purity has been confirmed using Stern Gerlach imaging. This initiates the dynamics leading to the formation of a Peregrine soliton. As described in the main text, the attractive Gaussian potential in the center of the BEC only serves to induce the initial dynamics. It can either be left on, or it can be switched off after a brief initial period, even before a clear Peregrine peak has formed (see the example shown in Fig. S2). In both cases the formation of a Peregrine soliton can be observed, though after different evolution times.

In the example of Fig. S2, which will be described in greater

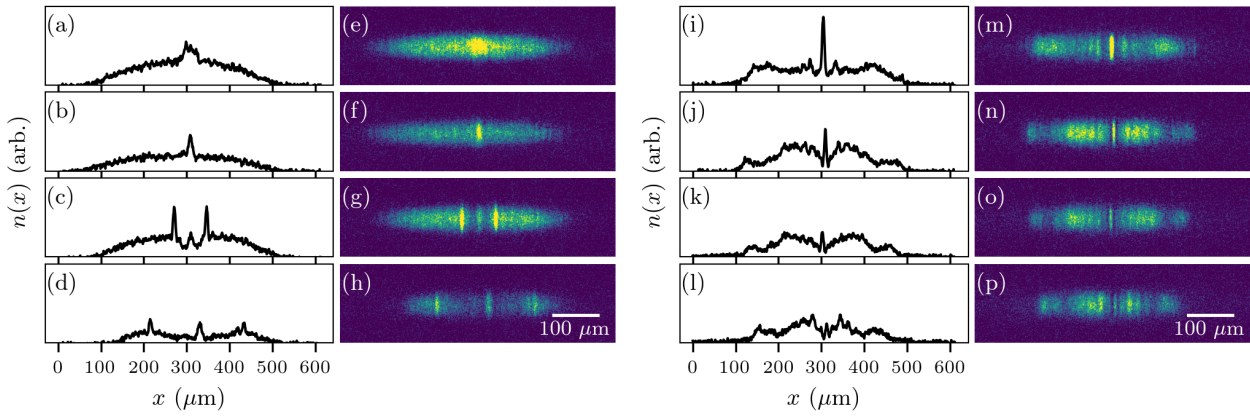


Figure S2. Time evolution for the case of an early switch-off of the well. The BEC is prepared with the same parameters as in Fig. 1 of the main text. The different panels show images taken after (a, e) 10 ms, (b, f) 20 ms, (c, g) 30 ms, (d, h) 60 ms, (i, m) 100 ms, (j, n) 110 ms, (k, o) 130 ms, and (l, p) 150 ms. The well is switched off after 20 ms, corresponding to panels (b, f). The images depict the atoms in the $|F, m_F\rangle = |2, 0\rangle$ state and are taken with 9 ms time-of-flight.

detail later in this Supplement, the well was switched off 20 ms after the formation of the mixture, which is clearly before a Peregrine soliton would reach its peak height in the continued presence of the well. As a consequence of the switch-off, sound excitations are seen to propagate outwards to the edge of the BEC. Their propagation speed provides a sense for mean-field time scales of the system. The central peak still continues to grow after the switch-off, reaching a peak height approximately 80 ms after the switch-off in this example. Also, the observation of the Peregrine soliton is not specific to the chosen hyperfine mixture [a mixture of atoms in the $|F, m_F\rangle = |1, -1\rangle$ and $|2, 0\rangle$ has also been used successfully, see Fig. 2(d,j) of the main text] and also does not critically depend on the specific component ratios. The slight asymmetry observed in the wings of the Peregrine solitons, as seen e.g. in Fig. 1(c,g) of the main text, can possibly be attributed to a minute and otherwise undetectable amount of counterflow between the two components of the mixture.

The fractional atom number for both the majority and minority components is shown in Fig. S3 in the case where the attractive barrier is left on throughout the experiment. The majority component atom number shows minor changes, comparable to a single component BEC held in a similar trap. The minority component experiences an atom number decay rate of approximately 0.23% per ms, resulting in roughly half of the minority population remaining in the system after 200 ms. To shed light on the impact of these loss rates, we take them into account in the corresponding 3D mean-field simulations through the appropriate renormalization of the corresponding component wave function every millisecond such that they follow the fractional atom loss rates provided in Fig. S3. It turns out that there is only a minor effect on the timescale of Peregrine formation (delayed by ~ 2 ms compared to the zero loss case), but it drastically affects the

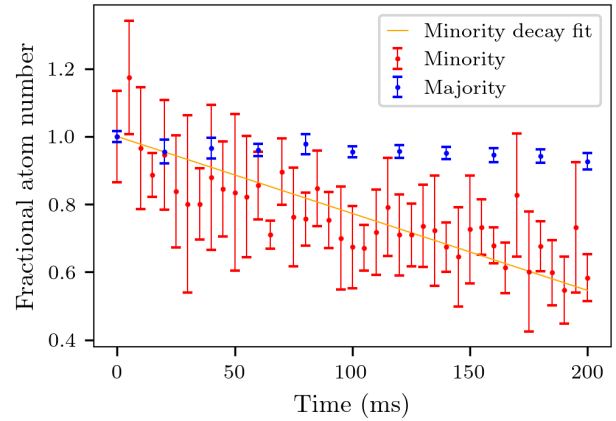


Figure S3. Fractional atom number in the majority and minority components (see legend) in the case where the attractive well is left on throughout the dynamics. The majority component shows negligible atom loss over this time scale, while the minority component features nearly linear decrease at a rate of 0.23% per ms. Error bars are given by one standard deviation over five independent realizations.

amplitude of the ensuing wave which is found, as expected, to be significantly reduced.

Lastly, our experiments with a “too wide” attractive well show modulationally unstable dynamics which, including thermal effects, do not appear to manifest a clearly distinguishable isolated Peregrine solitary wave within the time scales of experimental observation. The Gaussian widths resulting in the corresponding experimental observations shown in Figs. S4 are $s_x \approx 54 \mu\text{m}$ and $s_y \approx 25 \mu\text{m}$. The initial wide pattern [Figs. S4 (a,e)] having $\mu \approx 94$ nK features in the course of the evolution a decrease in its intensity with

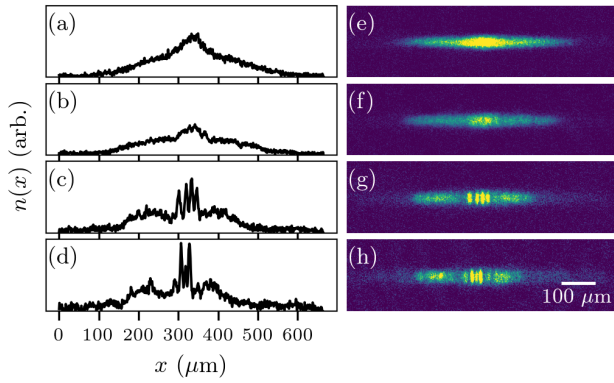


Figure S4. Experimental observation of nucleation of solitonic features under a wider attractive well. (a)–(d) Cross sections of (e)–(h) showing single-shot absorption images after 0, 90, 158, and 230ms of evolution, respectively.

the central peak becoming more transparent around 90 ms [Figs. S4(b,f)]. Subsequently, this central peak structure becomes gradually more prominent but instead of focusing towards a Peregrine wave signature starts to break into multiple peaks [Figs. S4(c,g)] which later on interfere [Figs. S4(d,h)]. As was shown in [1, 2], the significance of the Peregrine soliton is that it quantitatively captures the generic mechanism of spontaneous self-focusing and gradient catastrophe formation in attractive nonlinear media. The dynamics described above is also a precursor of a nonlinear modulational instability behavior similarly to Ref. [3], whose early signature is also visible in the later stages of the time evolution, as seen in Figs. 1(d,h) and 1(l,p).

II. DELINEATING THE IMPACT OF DIFFERENT PROTOCOLS

To explore the origin of deviations observed between the 3D mean-field simulations and the experiment we further checked possible experimental imperfections and mechanisms that are not emulated by the theory. As such, we identified three main sources that may lead to discrepancies among theory and experiment, see also Table I. These refer to a residual thermal fraction (less than 10%) detected in the experiment, the associated fitting procedure to infer the Peregrine formation time extracted from the experimental images and the time-of-flight imaging technique that is not modeled in the simulations. Below, we explain the impact of these distinct processes on the Peregrine nucleation, while following in all cases the dynamical protocol outlined in the main text. Peregrine manifestation is estimated by identifying the maximum peak density of the minority component during evolution.

To mimic the experimentally observed deformations of the

Switch-off time	Experiment	Simulations
∞	65 ± 14 ms	70 ms
30 ms	107 ± 29 ms	114 ms
20 ms	155 ± 47 ms	178 ms
10 ms	> 200 ms	240 ms

Table I. Time-instant of the Peregrine soliton’s maximum amplitude upon switching-off at different times (first column) the Gaussian potential. The time at which the Peregrine amplitude maximizes in the experiment (second column) and within the 3D mean-field simulations (third column) emulating the presence of a finite thermal fraction and atom loss of the minority component ~ 0.23 per ms. The experimental uncertainties are given by the width of a Gaussian fit to the Peregrine’s amplitude as it emerges and recedes.

condensate configuration due to thermal effects we exploit a weak perturbation modeled by a random noise term. The latter is added to the mean-field zero temperature ground state of the F-component, $\Psi_F^G(x, y, z)$, according to the following ansatz $\Psi_F(x, y, z, t) = \Psi_F^G(x, y, z) + \epsilon \delta(x, y, z)$. Here, $\delta(x, y, z)$ refers to a Gaussian random distribution with zero mean and unit variance, while $\epsilon \sim 0.1$ accounts for a 10% thermal fraction. To adequately estimate the effect of the random distribution on the dynamics we consider a sample of at least twenty different realizations ensuring that the results do not alter upon further sampling. It is found that the presence of the above thermal fraction accelerates the Peregrine formation which in the case depicted in Fig. 1 of the main text occurs at 70 ms, while the experiment identifies the maximum Peregrine amplitude at 65 ms, see Table I. However, the intensity of the Peregrine appears to be enhanced in the 3D simulations as compared to the experimental observations. Note in passing that an interesting possibility for future endeavors would be to rely on the stochastic Gross-Pitaevskii model describing the thermal component and its interplay with the condensed fraction [4].

Turning to the discrepancy in terms of the Peregrine intensity we additionally explored the effect of quenching the trap frequency to lower values studying this way the consequences stemming from the time-of-flight imaging. The aforementioned ansatz of the perturbed wave function is maintained. Interestingly, the major outcomes of this process are i) to lower the intensity of the Peregrine, ii) slightly shift its occurrence to earlier times and iii) sharpening of the observed features such as the counterpropagating sound-wave emission. Specifically, we establish that a trap quench to half of the initial frequency is able to quantitatively match the intensity of the Peregrine as captured by the experiment. Concluding, very good agreement in terms of both occurrence times and intensity of the Peregrine requires both the presence of thermal fraction and the mimicking of the time-of-flight process. Despite the fact that the trap quench can be used to infer a semi-quantitative understanding of the effect of the expansion it is not equivalent to the free expansion process in the experiment. For this reason, the times of Peregrine formation pre-

sented in Table I stem solely from the inclusion of the random noise term.

Having the above-described knowledge, we subsequently simulated the Peregrine realization utilizing different switch-off times of the external Gaussian well. Once more, good quantitative agreement for the time where the Peregrine maximizes its amplitude is identified in Table I. It should be noted that the observed finite background in all experimental cross sections, see e.g. Fig. S2, of the minority component renders the measurement of the peak intensity and the time of the Peregrine formation unclear. The times of peak Peregrine formation for the experiment shown in Table I are extracted by analyzing the time sequence of Peregrine formation for each initial condition. The Peregrine amplitude is approximated by considering the central region of the condensate's integrated cross section, around the forming Peregrine, then using the difference between the maximum and minimum densities as a proxy for the Peregrine amplitude. This approach captures both the extent of the soliton peak and the depth of the adjacent density depressions. The time of maximum amplitude was extracted by fitting a Gaussian to the Peregrine amplitude as the soliton emerges and recedes. The time of maximum Peregrine amplitude then corresponds to the central point of the amplitude fits and the uncertainties given in Table I correspond to the Gaussian width of the Peregrine formation curve in time.

III. CHARACTERISTICS OF THE PEREGRINE WITHIN A 1D MEAN-FIELD DESCRIPTION

A. Setup and transfer protocol

The quasi-one-dimensional (1D) geometry of the experimental setup, and its corresponding dynamics reported by both the experiments and the three-dimensional (3D) simulations (see main text) allow for a 1D description of the system under consideration. This can be traced back to the fact that in the transverse directions the cloud exhibits a collective motion and any kind of nonlinear excitations is suppressed. As such, a pure 1D treatment is adequate to capture the Peregrine nucleation but not its quantitative features. For instance, it predicts earlier times of formation and a reduced Peregrine intensity due to the absence of the transverse directions. Nevertheless, it is able to capture the main properties of the Peregrine. By integrating out the transverse degrees of freedom, the 3D Gross-Pitaevskii Eqs. (1) reduce [5–7] to

$$i\hbar\partial_t\Psi_F(x,t) = \left[-\frac{\hbar^2}{2m}\partial_x^2 + V(x) + V_G(x) + \sum_{F'=1}^2 g_{FF'}^{(1D)} |\Psi_{F'}(x,t)|^2 \right] \Psi_F(x,t). \quad (\text{S1})$$

Here, $\Psi_F(x,t)$ denote the longitudinal wave functions normalized to the number of particles $N_F = \int |\Psi_F|^2 dx$, with $F = 1, 2$ signifying the appropriate hyperfine level. The 1D coupling strength $g_{FF'}^{(1D)} = 2\hbar\omega_\perp a_{FF'}$ refers to the intra- ($F = F'$) and inter-species ($F \neq F'$) interaction, while $a_{FF'}$ is the 3D s-wave scattering length among the corresponding hyperfine states, F and F' . Motivated by the experimental setup we use herein the transverse trapping frequency $\omega_\perp = 2\pi \times 251$ Hz (see also Sec. I). Moreover, the external trapping potential is $V(x) = m(\omega/\omega_\perp)^2 x^2/2$, with ω representing the trap frequency in the x -direction, and the optically induced Gaussian well in 1D reads $V_G(x) = -V_0 \exp(-2x^2/s_x^2)$, where V_0 (s_x) refers to its amplitude (width).

Following the experimental procedure to initialize the dynamics, we first obtain the ground state of the Ψ_1 hyperfine state, by means of imaginary time propagation. Simultaneously, we ensure that the Thomas-Fermi radius of the condensate is in agreement with that of the experiment, fixing this way the total number of particles in this 1D setup. Next, the following unitary transformation

$$\begin{pmatrix} \Psi_1 \\ \Psi_2 \end{pmatrix} = \exp\left[-i\frac{\pi}{p_0} \begin{pmatrix} 0 & 1 \\ 1 & 0 \end{pmatrix}\right] \begin{pmatrix} \Psi_1 \\ \Psi_2 \end{pmatrix}, \quad (\text{S2})$$

is applied on the two-component wave function to mimic the instantaneous transfer atoms from Ψ_1 to Ψ_2 , according to the experimental protocol (see Sec. II). In the above expression the parameter p_0 allows to adjust the percentage of transferred atoms. For instance, $p_0 = 4, 8, 16$ corresponds to 50%, $\sim 15\%$, $\sim 4\%$ population transfer, respectively.

B. Seeding the Peregrine soliton through a Gaussian-well

While the methodology proposed in Ref. [8] is, in principle, suitable for producing a Peregrine soliton, the long appearance times of the latter and the limited controllability of the scheme prompted us to devise *key* structural modifications in the experiment herein including, notably, the inclusion of the Gaussian potential well.

Relying on the 1D mean-field description [Eq. (S1)] we unravel the emergence of the Peregrine wave as a function of the characteristics of the Gaussian well within the range $V_0 \in [6, 120]$ nK and $s_x \in [2.4, 96.3]$ μm . Specifically, the system is allowed to evolve up to ~ 320 ms and the time-instant of peak formation, t_0 , as well as the spatial overlap, Λ , between the numerically obtained structure and the analytic Peregrine solution (2) are estimated [see Fig. S5]. The underlying spatial overlap [9, 10] is defined as,

$$\Lambda(t) = \frac{[\int dx |\Psi_2|^2 |\Psi_P|^2]^2}{\int dx |\Psi_2|^4 \int dx |\Psi_P|^4}, \quad (\text{S3})$$

where $\Psi_2(x, t_0)$ corresponds to the emergent structure at t_0

- ematics, Philadelphia, 2015).
- [8] A. Romero-Ros, G. C. Katsimiga, S. I. Mistakidis, B. Prinari, G. Biondini, P. Schmelcher, and P. G. Kevrekidis, *Phys. Rev. A* **105**, 053306 (2022).
- [9] P. Jain and M. Boninsegni, *Phys. Rev. A* **83**, 023602 (2011).
- [10] S. I. Mistakidis, G. C. Katsimiga, P. G. Kevrekidis, and P. Schmelcher, *New J. Phys.* **20**, 043052 (2018).
- [11] G. A. El', A. V. Gurevich, V. V. Khodorovskii, and A. L. Krylov, *Physics Letters A* **177**, 357 (1993).
- [12] L.-C. Zhao and L. Ling, *J. Opt. Soc. Am. B, JOSAB* **33**, 850 (2016).
- [13] V. E. Zakharov and A. A. Gelash, *Phys. Rev. Lett.* **111**, 054101 (2013).
- [14] G. Biondini, *Phys. Rev. E* **98**, 052220 (2018).
- [15] A. E. Kraych, P. Suret, G. El, and S. Randoux, *Phys. Rev. Lett.* **122**, 054101 (2019).
- [16] Z. Dutton and C. W. Clark, *Phys. Rev. A* **71**, 063618 (2005).
- [17] B. Bakkali-Hassani, C. Maury, Y.-Q. Zou, É. Le Cerf, R. Saint-Jalm, P. C. M. Castilho, S. Nascimbene, J. Dalibard, and J. Beugnon, *Phys. Rev. Lett.* **127**, 023603 (2021).

Chapter 8

Conclusions

In this cumulative thesis, we presented our research on the generation of nonlinear structures in BECs. First, we provided some historical background and the basic general concepts to familiarize the reader with the nonlinear phenomena and techniques appearing and employed in our investigations. This includes BECs and the equations that govern them; the NLS and its soliton solutions provided by the IST; as well as rogue waves and the proposed soliton breathers and MI to explain their formation. Subsequently, we discussed the motivation of our investigations and outlined the main contributions of our works. The objective of this thesis was to provide the nonlinear community with robust methods to study solitons in multi-component BECs. Our first works focused on the controlled formation of soliton trains, ranging from single-component to two-component, three-component and spinor BECs. Then, in an experimental work, we developed a protocol to generate dense soliton ensembles, in the spirit of soliton gases. Last, we wrote a theoretical proposal to generate the Peregrine soliton in a two-component BEC, and put it successfully in practice in a following experimental work. Below, we conclude this thesis summarizing the most relevant contributions and discussing some future perspectives.

Soliton trains

In the first three works presented in this thesis [A1–A3], we investigated the generation of soliton trains in a controllable manner in multi-component BECs. The main mechanism behind our investigations has been the matter-wave interference or counterflow process that dynamically occurs during the collision of two BECs. Given the wave nature of a condensate, interference patterns emerge during collision, some of which develop into solitons. In order to initialize such dynamical processes, we employed a versatile BTC. The choice of a BTC has been proven convenient, as it can capture most of the techniques and mechanism employed in the generation of solitons and soliton trains in single-component BECs, and can be easily extended to multi-component systems. Moreover, its simple mathematical description allowed us to solve analytically the direct scattering problem of the IST formalism for the NLS and the VNLS, and thus completely characterize the formation of dark and DB soliton trains.

With the tools developed in these works, we are now able to determine beforehand the expected number of solitons, as well as their velocities and amplitudes, given an initial BTC, for both single- and two-component BECs. At the same time, we unraveled the symmetries of the system, which depend only on the phase difference between the different regions of

the BTC because it is spatially symmetric. For instance, if the central region of the BTC is in-phase with the outer ones, the solitons are generated in pairs, with each soliton of a pair being equal in amplitude but moving with opposite velocities. However, the aforementioned symmetry can be broken when the relative phase between the central and outer regions is non-zero and all the emerging solitons in the train are different. Moreover, in the two-component case, if in the central region of the component hosting the dark solitons surpasses the component hosting bright solitons, then no solitons form at all.

The generation of soliton trains in three-component and spinor BECs has been numerically investigated, as currently the IST formalism for these particular setups is still under development [47]. Interestingly, we found that the analytical results of two-component BECs can be qualitatively extrapolated to the three-component case, either for DDB or DBB soliton trains. When it comes to spinor BECs, the former results only apply in the absence of spin-mixing dynamics. Otherwise, the number of atoms in each hyperfine state oscillates over time. This generates a finite background in the component hosting bright solitons, which leads to the generation of beating DB solitons in all three components.

Notwithstanding, in all cases we also investigated the generation of solitons trains employing the BTC in the presence of an experimentally relevant harmonic potential. We found out that, as long as the BTC is way smaller than the condensate, the results of the homogeneous cases can be extrapolated to the trapped one. Moreover, the generated solitons undergo oscillations which are captured by the analytic solutions known in the literature [317, 318] upon fitting on the soliton parameters. Yet, in the single- and two-component scenarios, these were completely determined by the analytical solutions obtained from the IST and no fitting was required.

From here, future direct investigations suggest solving the three-component and the spinor cases employing the IST. Also, in view of the successful results under a harmonic confinement, it would be interesting to attest the BTC in experiments with multi-component BECs. Another research direction is the natural emergence of beating DB solitons in spinor systems undergoing spin-mixing dynamics. To the best of our knowledge, this type of solitons were not yet reported in spinor BECs. Hence, a more exhaustive study of this objects is a path to consider.

Soliton gas

While in our first works we addressed the question of *how* to generate soliton trains, in [A4] we experimentally addressed the question of *how many* solitons can we generate in a two-component BEC. In this case, we employed a sequence of two $\pi/2$ -pulses in the presence of a magnetic gradient to produce a winding pattern. The wavelength of the pattern can be controlled by the winding time between pulses, i.e., long wavelengths correspond to short times, and vice versa. The result is a sinusoidal pattern complementary between the components. In addition, the windings in the same component are out-of-phase between each other.

Our results showed that depending on the winding time, the dynamics in the system differ. For short winding times, we found that the dynamics lead to dark-soliton like notches that

spread over the condensate as a renormalization of the gradient catastrophe. In order to form stable solitons, the wavelength of the winding pattern needs to be close to the order of magnitude of a typical DB soliton. In this regard, winding patterns with wavelengths slightly larger than the threshold drive the system into the formation of dark-antidark soliton structures during the early times of the dynamics. Afterwards, they decay into DB solitons as the wavelength of the pattern naturally adapts to the solitonic length scale. If the achieved wavelengths are close to the DB-soliton length scale, the pattern remains stable up to 70 ms. However, at later times, we found that the system enters a *fuzzy* stage in which the whole pattern smooths out, followed by a revival of the initial pattern.

The interesting dynamics took place preparing a pattern with shorter wavelengths than the characteristic DB soliton length scale. In this case, we obtained a dense soliton system. During dynamics, we observed a highly interacting system, with the different structures undergoing collisions continuously. Yet, the qualitative traits of the initial pattern, namely the number of entities and amplitudes thereof, remained unchanged. This behavior is characteristic from soliton gases, in which the collective motion of the solitons needs to be treated statistically [427].

Withal, the $\pi/2$ -pulse protocol employed in this experimental study opens a new door, not only to study large arrays of DB solitons, but more importantly, to access the dynamics of soliton gases. This is an emerging field due to its unique hydrodynamic properties [334, 428–430, 437, 439], which to this day has not been realized in BECs. Other directions to be explored aim at the possible realization of hypersolitons [416], i.e., solitons traveling on top of a soliton lattice.

Peregrine soliton

The last contribution to this thesis is focused on the realization of the PS in BECs [A5, A6]. The PS is a solution of the focusing NLS. One of the major obstacles to circumvent in focusing nonlinear-media experiments is the modulational instability. In addition, attractive BECs have a limiting threshold to the number of particles above which it collapses. Also, the PS is a purely 1D object. Yet, we overcame these difficulties by employing a highly imbalanced weakly immiscible mixture of a repulsive two-component BEC.

In [A5], we showed that the minority component of this mixture could effectively be described as an attractive single-component BEC. This solved the problem of using genuine attractive BECs. This was verified by computing direct simulations of the PS wave function in the mixture and employing the effective single-component description. Moreover, in order to approach an experimentally relevant setup, we further investigated the formation of the Peregrine soliton employing a wide Gaussian pulse. The latter choice allowed us to work in the semi-classical regime, where it was proven that the PS can emerge from any generic pulse as long as it is wide enough [448]. Depending on the width of the Gaussian pulse, we not only encountered the PS, but also a cascade of PSs as a consequence of the gradient catastrophe, referred to as the Christmas-tree pattern.

In view of possible experimental realizations, we extended our calculations to the presence of a harmonic potential and included thermal dissipative effects. In both cases, we confirmed

the formation of a PS employing the method exposed above. Regarding the Christmas-tree pattern, we observed that in the presence of the trap the pattern emitted DB soliton-like structures undergoing unprecedented convex trajectories, opposite to the expected classic concave ones. However, the Christmas tree was not found in the presence of dissipative effects due to particle loss mechanisms. We also performed simulations with a mass-imbalanced mixture, and found that in the case of a heavier minority, the dynamics resemble those in the mass-balanced case. However, if the minority component is lighter, the Christmas-tree pattern emerges only above a particular width of the Gaussian pulse. Last, we verified the emergence of the PS in a quasi-1D BEC employing 3D simulations of the GPE.

In [A6] we employed the aforementioned setup and realized experimentally, for the first time, the PS in a BEC. In this case, we additionally employed a tight Gaussian well at the center of the harmonic trapping potential. The latter was proven to act as a catalyst for the formation of the PS, shortening the emerging time, and providing a consistent location of emergence in the condensate. We also found that the PS can emerge from a wide range of Gaussian wells. Yet, independently of its amplitude, the optimal width of the Gaussian well was found to be given by the natural length scale of the PS. Moreover, we were able to realize the PS employing two different hyperfine-state mixtures of the same atomic species, both of which provided the effective attractiveness required in the system.

This experiment is of important relevance for the nonlinear community, as it opens the window to BECs as platforms to investigate rogue waves [107, 348] and higher-dimensional variants thereof [376, 450–452]. In addition to the PS, in our works we came across the nonlinear stage of MI, which occurs only in purely nonlinear focusing media. The latter has been studied in several mathematical works [390, 392, 396, 397, 448, 453] and our platform could be ideal to study this phenomenon experimentally avoiding the need of attractive BECs [106, 108, 246, 362] or other focusing media [359–361, 379]. Other interesting features unveiled in this setup were the unusual concave trajectories described by the soliton-like structures emitted from the Christmas-tree pattern in the trap. Similar trajectories have only been reported in the generation of solitons through Floquet engineering [454] as a consequence of an effective negative mass. Hence, it would be interesting to understand the mechanisms leading to the formation of such structures.

Bibliography

- [1] J. S. Russell, *Report on Waves*, Report of the 14th Meeting of the British Association for the Advancement of Science, York, September 1844 (London, 1845).
- [2] H. C. Yuen and B. M. Lake, “Nonlinear deep water waves: Theory and experiment”, *Phys. Fluids* **18**, 956 (1975).
- [3] R. M. Miura, “The Korteweg–deVries Equation: A Survey of Results”, *SIAM Rev.* **18**, 412 (1976).
- [4] A. Chabchoub, O. Kimmoun, H. Branger, N. Hoffmann, D. Proment, M. Onorato, and N. Akhmediev, “Experimental Observation of Dark Solitons on the Surface of Water”, *Phys. Rev. Lett.* **110**, 124101 (2013).
- [5] Y. Kodama and S. Wabnitz, “Analytical theory of guiding-center nonreturn-to-zero and return-to-zero signal transmission in normally dispersive nonlinear optical fibers”, *Opt. Lett.* **20**, 2291 (1995).
- [6] Y. S. Kivshar and B. Luther-Davies, “Dark optical solitons: physics and applications”, *Phys. Rep.* **298**, 81 (1998).
- [7] J. S. Kivshar and G. P. Agrawal, *Optical Solitons: From Fibers to Photonic Crystals* (Academic Press, San Diego, California, 2003).
- [8] Z. Chen, M. Segev, and D. N. Christodoulides, “Optical spatial solitons: historical overview and recent advances”, *Rep. Prog. Phys.* **75**, 086401 (2012).
- [9] P. G. Kevrekidis, D. J. Frantzeskakis, and R. Carretero-González, *Emergent Nonlinear Phenomena in Bose-Einstein Condensates: Theory and Experiment*, Vol. 45, Springer Series on Atomic, Optical and Plasma Physics (Springer Science & Business Media, Berlin, 2008).
- [10] R. Carretero-González, D. J. Frantzeskakis, and P. G. Kevrekidis, “Nonlinear waves in Bose–Einstein condensates: physical relevance and mathematical techniques”, *Nonlinearity* **21**, 139 (2008).
- [11] D. J. Frantzeskakis, “Dark solitons in atomic Bose–Einstein condensates: from theory to experiments”, *J. Phys. A: Math. Theor.* **43**, 213001 (2010).
- [12] P. G. Kevrekidis, D. J. Frantzeskakis, and R. Carretero-González, *The Defocusing Nonlinear Schrödinger Equation: from dark soliton to vortices and vortex rings*, Other Titles in Applied Mathematics (Society for Industrial and Applied Mathematics, Philadelphia, Mar. 2015).
- [13] M. Kono and M. Skoric, *Nonlinear Physics of Plasmas*, Vol. 62 (Jan. 2010).

- [14] V. M. Lashkin and O. K. Cheremnykh, *Nonlinear internal gravity waves in the atmosphere: Rogue waves, breathers and dark solitons*, July 2023, [arXiv:2307.01116](https://arxiv.org/abs/2307.01116) [[nlin](#)].
- [15] L. Brizhik, “Soliton generation in molecular chains”, *Phys. Rev. B* **48**, 3142 (1993).
- [16] A. C. Scott, “Soliton oscillations in DNA”, *Phys. Rev. A* **31**, 3518 (1985).
- [17] A. Hasegawa, “Optical soliton: Review of its discovery and applications in ultra-high-speed communications”, *Front. Phys.* **10**, 1044845 (2022).
- [18] A. Hasegawa and F. Tappert, “Transmission of stationary nonlinear optical pulses in dispersive dielectric fibers. I. Anomalous dispersion”, *Appl. Phys. Lett.* **23**, 142 (1973).
- [19] A. Hasegawa and F. Tappert, “Transmission of stationary nonlinear optical pulses in dispersive dielectric fibers. II. Normal dispersion”, *Appl. Phys. Lett.* **23**, 171 (1973).
- [20] M. I. Shaukat, E. V. Castro, and H. Terças, “Quantum dark solitons as qubits in Bose-Einstein condensates”, *Phys. Rev. A* **95**, 053618 (2017).
- [21] T. V. Ngo, D. V. Tsarev, R.-K. Lee, and A. P. Alodjants, “Bose–Einstein condensate soliton qubit states for metrological applications”, *Sci Rep* **11**, 19363 (2021).
- [22] C. Hang, G. Gabadadze, and G. Huang, “Soliton diffusion in a Bose-Einstein condensate: A signature of the analogue Hawking radiation”, *Phys. Lett. B* **793**, 390 (2019).
- [23] R. Balbinot, A. Fabbri, S. Fagnocchi, A. Recati, and I. Carusotto, “Nonlocal density correlations as a signature of Hawking radiation from acoustic black holes”, *Phys. Rev. A* **78**, 021603 (2008).
- [24] I. Carusotto, S. Fagnocchi, A. Recati, R. Balbinot, and A. Fabbri, “Numerical observation of Hawking radiation from acoustic black holes in atomic Bose–Einstein condensates”, *New J. Phys.* **10**, 103001 (2008).
- [25] O. Lahav, A. Itah, A. Blumkin, C. Gordon, S. Rinott, A. Zayats, and J. Steinhauer, “Realization of a Sonic Black Hole Analog in a Bose-Einstein Condensate”, *Phys. Rev. Lett.* **105**, 240401 (2010).
- [26] P.-É. Larré, A. Recati, I. Carusotto, and N. Pavloff, “Quantum fluctuations around black hole horizons in Bose-Einstein condensates”, *Phys. Rev. A* **85**, 013621 (2012).
- [27] J. Steinhauer, “Observation of self-amplifying Hawking radiation in an analogue black-hole laser”, *Nat. Phys.* **10**, 864 (2014).
- [28] J. Steinhauer, “Observation of quantum Hawking radiation and its entanglement in an analogue black hole”, *Nat. Phys.* **12**, 959 (2016).
- [29] E. W. Lentz, *Breaking the Warp Barrier: Hyper-Fast Solitons in Einstein-Maxwell-Plasma Theory*, Aug. 2020, [arXiv:2006.07125](https://arxiv.org/abs/2006.07125) [[astro-ph](#), [physics:gr-qc](#), [physics:hep-ph](#)].

- [30] M. Alcubierre, “The warp drive: hyper-fast travel within general relativity”, *Class. Quantum Grav.* **11**, L73 (1994).
- [31] C. S. Gardner, J. M. Greene, M. D. Kruskal, and R. M. Miura, “Method for Solving the Korteweg-deVries Equation”, *Phys. Rev. Lett.* **19**, 1095 (1967).
- [32] P. D. Lax, “Integrals of nonlinear equations of evolution and solitary waves”, *Commun. Pure Appl. Math.* **21**, 467 (1968).
- [33] M. J. Ablowitz, D. J. Kaup, A. C. Newell, and H. Segur, “The Inverse Scattering Transform-Fourier Analysis for Nonlinear Problems”, *Stud. Appl. Math.* **53**, 249 (1974).
- [34] M. J. Ablowitz and H. Segur, *Solitons and the Inverse Scattering Transform* (SIAM, Philadelphia, 1981).
- [35] M. A. Ablowitz and P. A. Clarkson, *Solitons, Nonlinear Evolution Equations and Inverse Scattering*, London Mathematical Society Lecture Note Series (Cambridge University Press, Cambridge, 1991).
- [36] T. Aktosun, in *Encyclopedia of Complexity and Systems Science*, edited by R. A. Meyers (Springer, New York, NY, 2009), pp. 4960–4971.
- [37] G. Biondini and G. Kovačič, “Inverse scattering transform for the focusing nonlinear Schrödinger equation with nonzero boundary conditions”, *J. Math. Phys.* **55**, 031506 (2014).
- [38] G. Biondini and D. Kraus, “Inverse Scattering Transform for the Defocusing Manakov System with Nonzero Boundary Conditions”, *SIAM J. Math. Anal.* **47**, 706 (2015).
- [39] G. Biondini, E. Fagerstrom, and B. Prinari, “Inverse scattering transform for the defocusing nonlinear Schrödinger equation with fully asymmetric non-zero boundary conditions”, *Physica D* **333**, 117 (2016).
- [40] G. Biondini, I. Gabitov, G. Kovačič, and S. Li, “Inverse scattering transform for two-level systems with nonzero background”, *J. Math. Phys.* **60**, 073510 (2019).
- [41] M. J. Ablowitz, B. Prinari, and A. D. Trubatch, *Discrete and continuous nonlinear Schrödinger systems*, London Mathematical Society Lecture Note Series 302 (Cambridge University Press, Cambridge, UK ; New York, 2004).
- [42] B. Prinari, M. J. Ablowitz, and G. Biondini, “Inverse scattering transform for the vector nonlinear Schrödinger equation with nonvanishing boundary conditions”, *J. Math. Phys.* **47**, 063508 (2006).
- [43] J. Ieda, M. Uchiyama, and M. Wadati, “Inverse scattering method for square matrix nonlinear Schrödinger equation under nonvanishing boundary conditions”, *J. Math. Phys.* **48**, 013507 (2007).
- [44] B. Prinari, G. Biondini, and A. D. Trubatch, “Inverse Scattering Transform for the Multi-Component Nonlinear Schrödinger Equation with Nonzero Boundary Conditions”, *Stud. Appl. Math.* **126**, 245 (2011).

- [45] J. Garnier and K. Kalimeris, “Inverse scattering perturbation theory for the nonlinear Schrödinger equation with non-vanishing background”, *J. Phys. A: Math. Theor.* **45**, 035202 (2011).
- [46] A. Abeya, B. Prinari, G. Biondini, and P. G. Kevrekidis, “Solitons and soliton interactions in repulsive spinor Bose–Einstein condensates with nonzero background”, *Eur. Phys. J. Plus* **136**, 1126 (2021).
- [47] B. Prinari, “Inverse Scattering Transform for Nonlinear Schrödinger Systems on a Nontrivial Background: A Survey of Classical Results, New Developments and Future Directions”, *J. Nonlinear Math. Phys.* **30**, 317 (2023).
- [48] V. E. Zakharov and A. B. Shabat, “Exact Theory of Two-dimensional Self-focusing and One-dimensional Self-modulation of Waves in Nonlinear Media”, *Sov. Phys. JETP* **34**, 62 (1972).
- [49] V. E. Zakharov and A. B. Shabat, “Interaction between solitons in a stable medium”, *Sov. Phys. JETP* **37**, 823 (1973).
- [50] E. P. Gross, “Structure of a quantized vortex in boson systems”, *Nuovo Cim* **20**, 454 (1961).
- [51] L. P. Pitaevskii, “Vortex Lines in an Imperfect Bose Gas”, *Sov. Phys. JETP* **13**, 451 (1961).
- [52] L. P. Pitaevskii and S. Stringari, *Bose-Einstein condensation*, Oxford Science Publications 116 (Clarendon Press, Oxford; New York, 2003).
- [53] C. J. Pethick and H. Smith, *Bose–Einstein Condensation in Dilute Gases*, 2nd ed. (Cambridge University Press, Cambridge, 2008).
- [54] M. Ueda, *Fundamentals and New Frontiers of Bose-Einstein Condensation* (WORLD SCIENTIFIC, July 2010).
- [55] T. Tsuzuki, “Nonlinear waves in the Pitaevskii-Gross equation”, *J. Low Temp. Phys.* **4**, 441 (1971).
- [56] M. H. Anderson, J. R. Ensher, M. R. Matthews, C. E. Wieman, and E. A. Cornell, “Observation of Bose-Einstein Condensation in a Dilute Atomic Vapor”, *Science* **269**, 198 (1995).
- [57] C. C. Bradley, C. A. Sackett, J. J. Tollett, and R. G. Hulet, “Evidence of Bose-Einstein Condensation in an Atomic Gas with Attractive Interactions”, *Phys. Rev. Lett.* **75**, 1687 (1995).
- [58] K. B. Davis, M. O. Mewes, M. R. Andrews, N. J. van Druten, D. S. Durfee, D. M. Kurn, and W. Ketterle, “Bose-Einstein Condensation in a Gas of Sodium Atoms”, *Phys. Rev. Lett.* **75**, 3969 (1995).
- [59] U. Fano, “Effects of Configuration Interaction on Intensities and Phase Shifts”, *Phys. Rev.* **124**, 1866 (1961).
- [60] H. Feshbach, “Unified theory of nuclear reactions”, *Ann. Phys. (N. Y.)* **5**, 357 (1958).

- [61] A. J. Moerdijk, B. J. Verhaar, and A. Axelsson, “Resonances in ultracold collisions of ${}^6\text{Li}$, ${}^7\text{Li}$, and ${}^{23}\text{Na}$ ”, *Phys. Rev. A* **51**, 4852 (1995).
- [62] S. Inouye, M. R. Andrews, J. Stenger, H.-J. Miesner, D. M. Stamper-Kurn, and W. Ketterle, “Observation of Feshbach resonances in a Bose–Einstein condensate”, *Nature* **392**, 151 (1998).
- [63] Ph. Courteille, R. S. Freeland, D. J. Heinzen, F. A. van Abeelen, and B. J. Verhaar, “Observation of a Feshbach Resonance in Cold Atom Scattering”, *Phys. Rev. Lett.* **81**, 69 (1998).
- [64] S. L. Cornish, N. R. Claussen, J. L. Roberts, E. A. Cornell, and C. E. Wieman, “Stable ${}^{85}\text{Rb}$ Bose-Einstein Condensates with Widely Tunable Interactions”, *Phys. Rev. Lett.* **85**, 1795 (2000).
- [65] J. L. Roberts, N. R. Claussen, S. L. Cornish, and C. E. Wieman, “Magnetic Field Dependence of Ultracold Inelastic Collisions near a Feshbach Resonance”, *Phys. Rev. Lett.* **85**, 728 (2000).
- [66] C. Chin, R. Grimm, P. Julienne, and E. Tiesinga, “Feshbach resonances in ultracold gases”, *Rev. Mod. Phys.* **82**, 1225 (2010).
- [67] L. Khaykovich, F. Schreck, G. Ferrari, T. Bourdel, J. Cubizolles, L. D. Carr, Y. Castin, and C. Salomon, “Formation of a Matter-Wave Bright Soliton”, *Science* **296**, 1290 (2002).
- [68] K. E. Strecker, G. B. Partridge, A. G. Truscott, and R. G. Hulet, “Formation and propagation of matter-wave soliton trains”, *Nature* **417**, 150 (2002).
- [69] S. Burger, K. Bongs, S. Dettmer, W. Ertmer, K. Sengstock, A. Sanpera, G. V. Shlyapnikov, and M. Lewenstein, “Dark Solitons in Bose-Einstein Condensates”, *Phys. Rev. Lett.* **83**, 5198 (1999).
- [70] J. Denschlag, J. E. Simsarian, D. L. Feder, C. W. Clark, L. A. Collins, J. Cubizolles, L. Deng, E. W. Hagley, K. Helmerson, W. P. Reinhardt, S. L. Rolston, B. I. Schneider, and W. D. Phillips, “Generating Solitons by Phase Engineering of a Bose-Einstein Condensate”, *Science* **287**, 97 (2000).
- [71] B. P. Anderson, P. C. Haljan, C. A. Regal, D. L. Feder, L. A. Collins, C. W. Clark, and E. A. Cornell, “Watching Dark Solitons Decay into Vortex Rings in a Bose-Einstein Condensate”, *Phys. Rev. Lett.* **86**, 2926 (2001).
- [72] Z. Dutton, M. Budde, C. Slowe, and L. V. Hau, “Observation of Quantum Shock Waves Created with Ultra- Compressed Slow Light Pulses in a Bose-Einstein Condensate”, *Science* **293**, 663 (2001).
- [73] C. J. Myatt, E. A. Burt, R. W. Ghrist, E. A. Cornell, and C. E. Wieman, “Production of Two Overlapping Bose-Einstein Condensates by Sympathetic Cooling”, *Phys. Rev. Lett.* **78**, 586 (1997).

- [74] J. Stenger, S. Inouye, D. M. Stamper-Kurn, H.-J. Miesner, A. P. Chikkatur, and W. Ketterle, “Spin domains in ground-state Bose–Einstein condensates”, *Nature* **396**, 345 (1998).
- [75] D. M. Stamper-Kurn, M. R. Andrews, A. P. Chikkatur, S. Inouye, H.-J. Miesner, J. Stenger, and W. Ketterle, “Optical Confinement of a Bose-Einstein Condensate”, *Phys. Rev. Lett.* **80**, 2027 (1998).
- [76] M.-S. Chang, C. D. Hamley, M. D. Barrett, J. A. Sauer, K. M. Fortier, W. Zhang, L. You, and M. S. Chapman, “Observation of Spinor Dynamics in Optically Trapped ^{87}Rb Bose-Einstein Condensates”, *Phys. Rev. Lett.* **92**, 140403 (2004).
- [77] G. Modugno, G. Ferrari, G. Roati, R. J. Brecha, A. Simoni, and M. Inguscio, “Bose-Einstein Condensation of Potassium Atoms by Sympathetic Cooling”, *Science* **294**, 1320 (2001).
- [78] G. Roati, M. Zaccanti, C. D’Errico, J. Catani, M. Modugno, A. Simoni, M. Inguscio, and G. Modugno, “ ^{39}K Bose-Einstein Condensate with Tunable Interactions”, *Phys. Rev. Lett.* **99**, 010403 (2007).
- [79] F. Schäfer, N. Mizukami, P. Yu, S. Koibuchi, A. Bouscal, and Y. Takahashi, “Experimental realization of ultracold $\text{Yb-}^7\text{Li}$ mixtures in mixed dimensions”, *Phys. Rev. A* **98**, 051602 (2018).
- [80] A. Burchianti, C. D’Errico, M. Prevedelli, L. Salasnich, F. Ancilotto, M. Modugno, F. Minardi, and C. Fort, “A Dual-Species Bose-Einstein Condensate with Attractive Interspecies Interactions”, *Condens. Matter* **5**, 21 (2020).
- [81] C. Warner, A. Z. Lam, N. Bigagli, H. C. Liu, I. Stevenson, and S. Will, “Overlapping Bose-Einstein condensates of ^{23}Na and ^{133}Cs ”, *Phys. Rev. A* **104**, 033302 (2021).
- [82] P. G. Kevrekidis, H. E. Nistazakis, D. J. Frantzeskakis, B. A. Malomed, and R. Carretero-González, “Families of matter-waves in two-component Bose-Einstein condensates”, *Eur. Phys. J. D* **28**, 181 (2004).
- [83] D. Frantzeskakis, “Vector solitons supported by the third-order dispersion”, *Phys. Rev. A* **285**, 363 (2001).
- [84] P. G. Kevrekidis and D. J. Frantzeskakis, “Solitons in coupled nonlinear Schrödinger models: A survey of recent developments”, *Rev. Phys.* **1**, 140 (2016).
- [85] M. Olagnon and G. A. Athanassoulis, *Rogue waves 2000.- Brest, 29-30 november 2000* (Jan. 2001).
- [86] G. F. Clauss, “Dramas of the sea: episodic waves and their impact on offshore structures”, *Appl. Ocean Res.* **24**, 147 (2002).
- [87] G. B. Whitham, *Linear and Nonlinear Waves* (John Wiley & Sons, 1974).
- [88] A. R. Osborne, M. Onorato, and M. Serio, “The nonlinear dynamics of rogue waves and holes in deep-water gravity wave trains”, *Phys. Lett. A* **275**, 386 (2000).
- [89] P. Müller, C. Garrett, and A. Osborne, “Rogue waves”, *Oceanography* **18**, 66 (2005).

- [90] K. Dysthe, H. E. Krogstad, and P. Müller, “Oceanic Rogue Waves”, *Annu. Rev. Fluid Mech.* **40**, 287 (2008).
- [91] V. P. Ruban, “Two different kinds of rogue waves in weakly crossing sea states”, *Phys. Rev. E* **79**, 065304 (2009).
- [92] M. Onorato, D. Proment, G. Clauss, and M. Klein, “Rogue Waves: From Nonlinear Schrödinger Breather Solutions to Sea-Keeping Test”, *PLOS ONE* **8**, e54629 (2013).
- [93] M. L. McAllister, S. Draycott, T. a. A. Adcock, P. H. Taylor, and T. S. van den Bremer, “Laboratory recreation of the Draupner wave and the role of breaking in crossing seas”, *J. Fluid Mech.* **860**, 767 (2019).
- [94] D. R. Solli, C. Ropers, P. Koonath, and B. Jalali, “Optical rogue waves”, *Nature* **450**, 1054 (2007).
- [95] D. R. Solli, C. Ropers, and B. Jalali, “Active Control of Rogue Waves for Stimulated Supercontinuum Generation”, *Phys. Rev. Lett.* **101**, 233902 (2008).
- [96] B. Kibler, J. Fatome, C. Finot, G. Millot, F. Dias, G. Genty, N. Akhmediev, and J. M. Dudley, “The Peregrine soliton in nonlinear fibre optics”, *Nat. Phys.* **6**, 790 (2010).
- [97] B. Kibler, J. Fatome, C. Finot, G. Millot, G. Genty, B. Wetzl, N. Akhmediev, F. Dias, and J. M. Dudley, “Observation of Kuznetsov-Ma soliton dynamics in optical fibre”, *Sci. Rep.* **2**, 463 (2012).
- [98] C. Lecaplain, Ph. Grelu, J. M. Soto-Crespo, and N. Akhmediev, “Dissipative Rogue Waves Generated by Chaotic Pulse Bunching in a Mode-Locked Laser”, *Phys. Rev. Lett.* **108**, 233901 (2012).
- [99] P. T. S. DeVore, D. R. Solli, D. Borlaug, C. Ropers, and B. Jalali, “Rogue events and noise shaping in nonlinear silicon photonics”, *J. Opt.* **15**, 064001 (2013).
- [100] J. M. Dudley, F. Dias, M. Erkintalo, and G. Genty, “Instabilities, breathers and rogue waves in optics”, *Nat. Photon* **8**, 755 (2014).
- [101] B. Frisquet, B. Kibler, P. Morin, F. Baronio, M. Conforti, G. Millot, and S. Wabnitz, “Optical Dark Rogue Wave”, *Sci. Rep.* **6**, 20785 (2016).
- [102] A. Tikan, C. Billet, G. El, A. Tovbis, M. Bertola, T. Sylvestre, F. Gustave, S. Randoux, G. Genty, P. Suret, and J. M. Dudley, “Universality of the Peregrine Soliton in the Focusing Dynamics of the Cubic Nonlinear Schrödinger Equation”, *Phys. Rev. Lett.* **119**, 033901 (2017).
- [103] J. M. Dudley, G. Genty, A. Mussot, A. Chabchoub, and F. Dias, “Rogue waves and analogies in optics and oceanography”, *Nat. Rev. Phys.* **1**, 675 (2019).
- [104] N. Akhmediev, B. Kibler, F. Baronio, M. Belić, W.-P. Zhong, Y. Zhang, W. Chang, J. M. Soto-Crespo, P. Vouzas, P. Grelu, C. Lecaplain, K. Hammani, S. Rica, A. Picozzi, M. Tlidi, K. Panajotov, A. Mussot, A. Bendahmane, P. Szriftgiser, G. Genty, J. Dudley, A. Kudlinski, A. Demircan, U. Morgner, S. Amiraranashvili, C. Bree, G. Steinmeyer, C. Masoller, N. G. R. Broderick, A. F. J. Runge, M. Erkintalo, S. Residori,

- U. Bortolozzo, F. T. Arecchi, S. Wabnitz, C. G. Tiofack, S. Coulibaly, and M. Taki, “Roadmap on optical rogue waves and extreme events”, *J. Opt.* **18**, 063001 (2016).
- [105] A. Tikan, S. Randoux, G. El, A. Tovbis, F. Copie, and P. Suret, “Local Emergence of Peregrine Solitons: Experiments and Theory”, *Front. Phys.* **8** (2021).
- [106] L. D. Carr and J. Brand, “Spontaneous Soliton Formation and Modulational Instability in Bose-Einstein Condensates”, *Phys. Rev. Lett.* **92**, 040401 (2004).
- [107] Yu. V. Bludov, V. V. Konotop, and N. Akhmediev, “Matter rogue waves”, *Phys. Rev. A* **80**, 033610 (2009).
- [108] P. J. Everitt, M. A. Sooriyabandara, M. Guasoni, P. B. Wigley, C. H. Wei, G. D. McDonald, K. S. Hardman, P. Manju, J. D. Close, C. C. N. Kuhn, S. S. Szigeti, Y. S. Kivshar, and N. P. Robins, “Observation of a modulational instability in Bose-Einstein condensates”, *Phys. Rev. A* **96**, 041601 (2017).
- [109] E. G. Charalampidis, J Cuevas-Maraver, D. J. Frantzeskakis, and P. G. Kevrekidis, “ROGUE WAVES IN ULTRACOLD BOSONIC SEAS”, *Rom. Rep. Phys.* **70**, 504 (2018).
- [110] M. Ruderman, “Freak waves in laboratory and space plasmas”, *Eur. Phys. J. Spec. Top.* **185**, 57 (2010).
- [111] H. Bailung, S. K. Sharma, and Y. Nakamura, “Observation of Peregrine Solitons in a Multicomponent Plasma with Negative Ions”, *Phys. Rev. Lett.* **107**, 255005 (2011).
- [112] R. Sabry, W. M. Moslem, and P. K. Shukla, “Freak waves in white dwarfs and magnetars”, *Phys. Plasmas* **19**, 122903 (2012).
- [113] A. S. Bains, B. Li, and L.-D. Xia, “Kinetic Alfvén solitary and rogue waves in superthermal plasmas”, *Phys. Plasmas* **21**, 032123 (2014).
- [114] R. E. Tolba, W. M. Moslem, N. A. El-Bedwehy, and S. K. El-Labany, “Evolution of rogue waves in dusty plasmas”, *Phys. Plasmas* **22**, 043707 (2015).
- [115] R. Höhmann, U. Kuhl, H.-J. Stöckmann, L. Kaplan, and E. J. Heller, “Freak Waves in the Linear Regime: A Microwave Study”, *Phys. Rev. Lett.* **104**, 093901 (2010).
- [116] E. G. Charalampidis, J. Lee, P. G. Kevrekidis, and C. Chong, “Phononic rogue waves”, *Phys. Rev. E* **98**, 032903 (2018).
- [117] Y. Miyazawa, C. Chong, P. G. Kevrekidis, and J. Yang, “Rogue and solitary waves in coupled phononic crystals”, *Phys. Rev. E* **105**, 034202 (2022).
- [118] A. N. Ganshin, V. B. Efimov, G. V. Kolmakov, L. P. Mezhov-Deglin, and P. V. E. McClintock, “Observation of an Inverse Energy Cascade in Developed Acoustic Turbulence in Superfluid Helium”, *Phys. Rev. Lett.* **101**, 065303 (2008).
- [119] L. Stenflo and M. Marklund, “Rogue waves in the atmosphere”, *J. Plasma Phys.* **76**, 293 (2010).
- [120] Z. Yan, “Financial Rogue Waves”, *Commun. Theor. Phys.* **54**, 947 (2010).
- [121] Z. Yan, “Vector financial rogue waves”, *Phys. Lett. A* **375**, 4274 (2011).

- [122] A. Einstein, “Quantentheorie des einatomigen idealen Gases”, *Sitzungsber. phys.-math. Kl.* **1**, 3 (1925).
- [123] S. N. Bose, “Plancks Gesetz und Lichtquantenhypothese”, *Z. Physik* **26**, 178 (1924).
- [124] W. Greiner, L. Neise, H. Stöcker, and W. Greiner, *Thermodynamics and statistical mechanics*, Fifth Edition, Classical Theoretical Physics (Springer, New York Berlin Heidelberg, 2005).
- [125] F. London, “On the Bose-Einstein Condensation”, *Phys. Rev.* **54**, 947 (1938).
- [126] J. F. Allen and A. D. Misener, “Flow of Liquid Helium II”, *Nature* **141**, 75 (1938).
- [127] P. Kapitza, “Viscosity of Liquid Helium below the λ -Point”, *Nature* **141**, 74 (1938).
- [128] H. F. Hess, “Evaporative cooling of magnetically trapped and compressed spin-polarized hydrogen”, *Phys. Rev. B* **34**, 3476 (1986).
- [129] N. Masuhara, J. M. Doyle, J. C. Sandberg, D. Kleppner, T. J. Greytak, H. F. Hess, and G. P. Kochanski, “Evaporative Cooling of Spin-Polarized Atomic Hydrogen”, *Phys. Rev. Lett.* **61**, 935 (1988).
- [130] W. C. Stwalley and L. H. Nosanow, “Possible “New” Quantum Systems”, *Phys. Rev. Lett.* **36**, 910 (1976).
- [131] E. D. Siggia and A. E. Ruckenstein, “Bose Condensation in Spin-Polarized Atomic Hydrogen”, *Phys. Rev. Lett.* **44**, 1423 (1980).
- [132] S. Chu and C. Wieman, “Laser Cooling and Trapping of Atoms: Introduction”, *J. Opt. Soc. Am. B, JOSAB* **6**, 2020 (1989).
- [133] C. R. Monroe, E. A. Cornell, C. A. Sackett, C. J. Myatt, and C. E. Wieman, “Measurement of Cs-Cs elastic scattering at $T=30 \mu\text{K}$ ”, *Phys. Rev. Lett.* **70**, 414 (1993).
- [134] N. R. Newbury, C. J. Myatt, and C. E. Wieman, “S-wave elastic collisions between cold ground-state ^{87}Rb atoms”, *Phys. Rev. A* **51**, R2680 (1995).
- [135] D. Sesko, T. Walker, C. Monroe, A. Gallagher, and C. Wieman, “Collisional losses from a light-force atom trap”, *Phys. Rev. Lett.* **63**, 961 (1989).
- [136] D. W. Sesko, T. G. Walker, and C. E. Wieman, “Behavior of neutral atoms in a spontaneous force trap”, *J. Opt. Soc. Am. B, JOSAB* **8**, 946 (1991).
- [137] B. G. Levi, “Cornell, Ketterle, and Wieman Share Nobel Prize for Bose–Einstein Condensates”, *Phys. Today* **54**, 14 (2001).
- [138] A. Crubellier, O. Dulieu, F. Masnou-Seeuws, M. Elbs, H. Knöckel, and E. Tiemann, “Simple determination of Na_2 scattering lengths using observed bound levels at the ground state asymptote”, *Eur. Phys. J. D* **6**, 211 (1999).
- [139] N. N. Klausen, J. L. Bohn, and C. H. Greene, “Nature of spinor Bose-Einstein condensates in rubidium”, *Phys. Rev. A* **64**, 053602 (2001).
- [140] K. Henderson, C. Ryu, C. MacCormick, and M. G. Boshier, “Experimental demonstration of painting arbitrary and dynamic potentials for Bose–Einstein condensates”, *New J. Phys.* **11**, 043030 (2009).

- [141] V. Bagnato and D. Kleppner, “Bose-Einstein condensation in low-dimensional traps”, *Phys. Rev. A* **44**, 7439 (1991).
- [142] H. Moritz, T. Stöferle, M. Köhl, and T. Esslinger, “Exciting Collective Oscillations in a Trapped 1D Gas”, *Phys. Rev. Lett.* **91**, 250402 (2003).
- [143] P. Buonsante, P. Kevrekidis, V. Penna, and A. Vezzani, “Ground-state properties of attractive bosons in mesoscopic 1D ring lattices”, *J. Phys. B: At. Mol. Opt. Phys.* **39**, S77 (2006).
- [144] A. D. Jackson and G. M. Kavoulakis, “Bose-Einstein-condensed atoms in toroidal traps”, *Phys. Rev. A* **74**, 065601 (2006).
- [145] S. Basak and H. Pu, “Strongly interacting two-component coupled Bose gas in optical lattices”, *Phys. Rev. A* **104**, 053326 (2021).
- [146] M.-O. Mewes, M. R. Andrews, D. M. Kurn, D. S. Durfee, C. G. Townsend, and W. Ketterle, “Output Coupler for Bose-Einstein Condensed Atoms”, *Phys. Rev. Lett.* **78**, 582 (1997).
- [147] N. P. Robins, P. A. Altin, J. E. Debs, and J. D. Close, “Atom lasers: Production, properties and prospects for precision inertial measurement”, *Phys. Reports* **529**, 265 (2013).
- [148] R. Wynands and S. Weyers, “Atomic fountain clocks”, *Metrologia* **42**, S64 (2005).
- [149] S. Peil, J. L. Hanssen, T. B. Swanson, J. Taylor, and C. R. Ekstrom, “Evaluation of long term performance of continuously running atomic fountains”, *Metrologia* **51**, 263 (2014).
- [150] F. Fang, M. Li, P. Lin, W. Chen, N. Liu, Y. Lin, P. Wang, K. Liu, R. Suo, and T. Li, “NIM5 Cs fountain clock and its evaluation”, *Metrologia* **52**, 454 (2015).
- [151] Y. Shin, M. Saba, T. A. Pasquini, W. Ketterle, D. E. Pritchard, and A. E. Leanhardt, “Atom Interferometry with Bose-Einstein Condensates in a Double-Well Potential”, *Phys. Rev. Lett.* **92**, 050405 (2004).
- [152] M. Albiez, R. Gati, J. Fölling, S. Hunsmann, M. Cristiani, and M. K. Oberthaler, “Direct Observation of Tunneling and Nonlinear Self-Trapping in a Single Bosonic Josephson Junction”, *Phys. Rev. Lett.* **95**, 010402 (2005).
- [153] T. Schumm, S. Hofferberth, L. M. Andersson, S. Wildermuth, S. Groth, I. Bar-Joseph, J. Schmiedmayer, and P. Krüger, “Matter-wave interferometry in a double well on an atom chip”, *Nat. Phys.* **1**, 57 (2005).
- [154] B. V. Hall, S. Whitlock, R. Anderson, P. Hannaford, and A. I. Sidorov, “Condensate Splitting in an Asymmetric Double Well for Atom Chip Based Sensors”, *Phys. Rev. Lett.* **98**, 030402 (2007).
- [155] M. P. G. Robbins, N. Afshordi, A. O. Jamison, and R. B. Mann, “Detection of gravitational waves using parametric resonance in Bose-Einstein condensates”, *Class. Quantum Grav.* **39**, 175009 (2022).

- [156] M. Lu, N. Q. Burdick, S. H. Youn, and B. L. Lev, “Strongly Dipolar Bose-Einstein Condensate of Dysprosium”, *Phys. Rev. Lett.* **107**, 190401 (2011).
- [157] K. Aikawa, A. Frisch, M. Mark, S. Baier, A. Rietzler, R. Grimm, and F. Ferlaino, “Bose-Einstein Condensation of Erbium”, *Phys. Rev. Lett.* **108**, 210401 (2012).
- [158] L. Chomaz, R. M. W. van Bijnen, D. Petter, G. Faraoni, S. Baier, J. H. Becher, M. J. Mark, F. Wächtler, L. Santos, and F. Ferlaino, “Observation of roton mode population in a dipolar quantum gas”, *Nat. Phys.* **14**, 442 (2018).
- [159] S. M. Roccuzzo and F. Ancilotto, “Supersolid behavior of a dipolar Bose-Einstein condensate confined in a tube”, *Phys. Rev. A* **99**, 041601 (2019).
- [160] Y.-C. Zhang, T. Pohl, and F. Maucher, “Phases of supersolids in confined dipolar Bose-Einstein condensates”, *Phys. Rev. A* **104**, 013310 (2021).
- [161] T. Bland, E. Poli, L. A. P. Ardila, L. Santos, F. Ferlaino, and R. N. Bisset, “Alternating-domain supersolids in binary dipolar condensates”, *Phys. Rev. A* **106**, 053322 (2022).
- [162] L. Chomaz, I. Ferrier-Barbut, F. Ferlaino, B. Laburthe-Tolra, B. L. Lev, and T. Pfau, “Dipolar physics: a review of experiments with magnetic quantum gases”, *Rep. Prog. Phys.* **86**, 026401 (2022).
- [163] F. Kh. Abdullaev, A. Gammal, A. M. Kamchatnov, and L. Tomio, “Dynamics of bright matter wave solitons in a bose–einstein condensate”, *Int. J. Mod. Phys. B* **19**, 3415 (2005).
- [164] A. Griffin, D. W. Snoke, and S. Stringari, *Bose-Einstein Condensation* (Cambridge University Press, July 1996).
- [165] N Bogoliubov, “ON THE THEORY OF SUPERFLUIDITY”, *J. Phys.* **11**, 23 (1947).
- [166] F. Dalfovo, S. Giorgini, L. P. Pitaevskii, and S. Stringari, “Theory of Bose-Einstein condensation in trapped gases”, *Rev. Mod. Phys.* **71**, 463 (1999).
- [167] K. Huang and C. N. Yang, “Quantum-Mechanical Many-Body Problem with Hard-Sphere Interaction”, *Phys. Rev.* **105**, 767 (1957).
- [168] C. W. Gardiner and P. Zoller, “Quantum kinetic theory. V. Quantum kinetic master equation for mutual interaction of condensate and noncondensate”, *Phys. Rev. A* **61**, 033601 (2000).
- [169] R. A. Duine and H. T. C. Stoof, “Stochastic dynamics of a trapped Bose-Einstein condensate”, *Phys. Rev. A* **65**, 013603 (2001).
- [170] C. W. Gardiner, J. R. Anglin, and T. I. A. Fudge, “The stochastic Gross-Pitaevskii equation”, *J. Phys. B: At. Mol. Opt. Phys.* **35**, 1555 (2002).
- [171] C. W. Gardiner and M. J. Davis, “The stochastic Gross–Pitaevskii equation: II”, *J. Phys. B: At. Mol. Opt. Phys.* **36**, 4731 (2003).
- [172] N. P. Proukakis and B. Jackson, “Finite-temperature models of Bose–Einstein condensation”, *J. Phys. B: At. Mol. Opt. Phys.* **41**, 203002 (2008).

- [173] N. Proukakis, S. A. Gardiner, M. J. Davis, and M. Szymanska, eds., *Quantum gases: finite temperatures and non-equilibrium dynamics*, Vol. 1, Cold Atoms (Imperial College Press ; Distributed by World Scientific, London : Singapore ; Hackensack, NJ, 2013).
- [174] S. P. Cockburn and N. P. Proukakis, “The stochastic Gross-Pitaevskii equation and some applications”, *Laser Phys.* **19**, 558 (2009).
- [175] H. T. C. Stoof, “Coherent Versus Incoherent Dynamics During Bose-Einstein Condensation in Atomic Gases”, *J. Low Temp. Phys.* **114**, 11 (1999).
- [176] H. T. C. Stoof and M. J. Bijlsma, “Dynamics of Fluctuating Bose–Einstein Condensates”, *J. Low Temp. Phys.* **124**, 431 (2001).
- [177] M. Olshanii, “Atomic Scattering in the Presence of an External Confinement and a Gas of Impenetrable Bosons”, *Phys. Rev. Lett.* **81**, 938 (1998).
- [178] T. D. Lee, K. Huang, and C. N. Yang, “Eigenvalues and Eigenfunctions of a Bose System of Hard Spheres and Its Low-Temperature Properties”, *Phys. Rev.* **106**, 1135 (1957).
- [179] D. S. Petrov, “Quantum Mechanical Stabilization of a Collapsing Bose-Bose Mixture”, *Phys. Rev. Lett.* **115**, 155302 (2015).
- [180] D. S. Petrov and G. E. Astrakharchik, “Ultradilute Low-Dimensional Liquids”, *Phys. Rev. Lett.* **117**, 100401 (2016).
- [181] G. E. Astrakharchik and B. A. Malomed, “Dynamics of one-dimensional quantum droplets”, *Phys. Rev. A* **98**, 013631 (2018).
- [182] P. Cheiney, C. R. Cabrera, J. Sanz, B. Naylor, L. Tanzi, and L. Tarruell, “Bright Soliton to Quantum Droplet Transition in a Mixture of Bose-Einstein Condensates”, *Phys. Rev. Lett.* **120**, 135301 (2018).
- [183] I. Morera, G. E. Astrakharchik, A. Polls, and B. Juliá-Díaz, “Quantum droplets of bosonic mixtures in a one-dimensional optical lattice”, *Phys. Rev. Res.* **2**, 022008 (2020).
- [184] S. I. Mistakidis, T. Mithun, P. G. Kevrekidis, H. R. Sadeghpour, and P. Schmelcher, “Formation and quench of homonuclear and heteronuclear quantum droplets in one dimension”, *Phys. Rev. Res.* **3**, 043128 (2021).
- [185] I. A. Englezos, S. I. Mistakidis, and P. Schmelcher, “Correlated dynamics of collective droplet excitations in a one-dimensional harmonic trap”, *Phys. Rev. A* **107**, 023320 (2023).
- [186] E. H. Lieb, R. Seiringer, and J. Yngvason, “Bosons in a trap: A rigorous derivation of the Gross-Pitaevskii energy functional”, *Phys. Rev. A* **61**, 043602 (2000).
- [187] G. Baym and C. J. Pethick, “Ground-State Properties of Magnetically Trapped Bose-Condensed Rubidium Gas”, *Phys. Rev. Lett.* **76**, 6 (1996).

- [188] L. V. Hau, B. D. Busch, C. Liu, Z. Dutton, M. M. Burns, and J. A. Golovchenko, “Near-resonant spatial images of confined Bose-Einstein condensates in a 4-Dee magnetic bottle”, *Phys. Rev. A* **58**, R54 (1998).
- [189] A. Görlitz, J. M. Vogels, A. E. Leanhardt, C. Raman, T. L. Gustavson, J. R. Abo-Shaeer, A. P. Chikkatur, S. Gupta, S. Inouye, T. Rosenband, and W. Ketterle, “Realization of Bose-Einstein Condensates in Lower Dimensions”, *Phys. Rev. Lett.* **87**, 130402 (2001).
- [190] E. H. Lieb, R. Seiringer, J. P. Solovej, and J. Yngvason, *The Mathematics of the Bose Gas and its Condensation* (Springer Science & Business Media, June 2005).
- [191] A. Muñoz Mateo and V. Delgado, “Ground-state properties of trapped Bose-Einstein condensates: Extension of the Thomas-Fermi approximation”, *Phys. Rev. A* **75**, 063610 (2007).
- [192] A. Muñoz Mateo and V. Delgado, “Effective mean-field equations for cigar-shaped and disk-shaped Bose-Einstein condensates”, *Phys. Rev. A* **77**, 013617 (2008).
- [193] A. Muñoz Mateo and V. Delgado, “Effective one-dimensional dynamics of elongated Bose-Einstein condensates”, *Ann. Phys. (N. Y.)* **324**, 709 (2009).
- [194] H. Moritz, T. Stöferle, K. Günter, M. Köhl, and T. Esslinger, “Confinement Induced Molecules in a 1D Fermi Gas”, *Phys. Rev. Lett.* **94**, 210401 (2005).
- [195] A. J. Leggett, “Bose-Einstein condensation in the alkali gases: Some fundamental concepts”, *Rev. Mod. Phys.* **73**, 307 (2001).
- [196] M. R. Matthews, D. S. Hall, D. S. Jin, J. R. Ensher, C. E. Wieman, E. A. Cornell, F. Dalfovo, C. Minniti, and S. Stringari, “Dynamical Response of a Bose-Einstein Condensate to a Discontinuous Change in Internal State”, *Phys. Rev. Lett.* **81**, 243 (1998).
- [197] M. R. Matthews, B. P. Anderson, P. C. Haljan, D. S. Hall, M. J. Holland, J. E. Williams, C. E. Wieman, and E. A. Cornell, “Watching a Superfluid Untwist Itself: Recurrence of Rabi Oscillations in a Bose-Einstein Condensate”, *Phys. Rev. Lett.* **83**, 3358 (1999).
- [198] E. Nicklas, H. Strobel, T. Zibold, C. Gross, B. A. Malomed, P. G. Kevrekidis, and M. K. Oberthaler, “Rabi Flopping Induces Spatial Demixing Dynamics”, *Phys. Rev. Lett.* **107**, 193001 (2011).
- [199] E. Nicklas, W. Muessel, H. Strobel, P. G. Kevrekidis, and M. K. Oberthaler, “Nonlinear dressed states at the miscibility-immiscibility threshold”, *Phys. Rev. A* **92**, 053614 (2015).
- [200] C. Hamner, Y. Zhang, J. J. Chang, C. Zhang, and P. Engels, “Phase Winding a Two-Component Bose-Einstein Condensate in an Elongated Trap: Experimental Observation of Moving Magnetic Orders and Dark-Bright Solitons”, *Phys. Rev. Lett.* **111**, 264101 (2013).
- [201] V. P. Mineev, “The theory of the solution of two near-ideal Bose gases”, *Sov. Phys. JETP* **40**, 132 (1974).

- [202] T.-L. Ho and V. B. Shenoy, “Binary Mixtures of Bose Condensates of Alkali Atoms”, *Phys. Rev. Lett.* **77**, 3276 (1996).
- [203] B. D. Esry, C. H. Greene, Jr. Burke James P., and J. L. Bohn, “Hartree-Fock Theory for Double Condensates”, *Phys. Rev. Lett.* **78**, 3594 (1997).
- [204] H. Pu and N. P. Bigelow, “Properties of Two-Species Bose Condensates”, *Phys. Rev. Lett.* **80**, 1130 (1998).
- [205] E. Timmermans, “Phase Separation of Bose-Einstein Condensates”, *Phys. Rev. Lett.* **81**, 5718 (1998).
- [206] M. Trippenbach, K. Góral, K. Rzazewski, B. Malomed, and Y. B. Band, “Structure of binary Bose-Einstein condensates”, *J. Phys. B: At. Mol. Opt. Phys.* **33**, 4017 (2000).
- [207] I. M. Merhasin, B. A. Malomed, and R. Driben, “Transition to miscibility in a binary Bose–Einstein condensate induced by linear coupling”, *J. Phys. B: At. Mol. Opt. Phys.* **38**, 877 (2005).
- [208] D. S. Hall, M. R. Matthews, J. R. Ensher, C. E. Wieman, and E. A. Cornell, “Dynamics of Component Separation in a Binary Mixture of Bose-Einstein Condensates”, *Phys. Rev. Lett.* **81**, 1539 (1998).
- [209] H. Pu and N. P. Bigelow, “Collective Excitations, Metastability, and Nonlinear Response of a Trapped Two-Species Bose-Einstein Condensate”, *Phys. Rev. Lett.* **80**, 1134 (1998).
- [210] A. Sinatra, P. O. Fedichev, Y. Castin, J. Dalibard, and G. V. Shlyapnikov, “Dynamics of Two Interacting Bose-Einstein Condensates”, *Phys. Rev. Lett.* **82**, 251 (1999).
- [211] K. M. Mertes, J. W. Merrill, R. Carretero-González, D. J. Frantzeskakis, P. G. Kevrekidis, and D. S. Hall, “Nonequilibrium Dynamics and Superfluid Ring Excitations in Binary Bose-Einstein Condensates”, *Phys. Rev. Lett.* **99**, 190402 (2007).
- [212] S. B. Papp, J. M. Pino, and C. E. Wieman, “Tunable Miscibility in a Dual-Species Bose-Einstein Condensate”, *Phys. Rev. Lett.* **101**, 040402 (2008).
- [213] R. P. Anderson, C. Ticknor, A. I. Sidorov, and B. V. Hall, “Spatially inhomogeneous phase evolution of a two-component Bose-Einstein condensate”, *Phys. Rev. A* **80**, 023603 (2009).
- [214] S. Tojo, Y. Taguchi, Y. Masuyama, T. Hayashi, H. Saito, and T. Hirano, “Controlling phase separation of binary Bose-Einstein condensates via mixed-spin-channel Feshbach resonance”, *Phys. Rev. A* **82**, 033609 (2010).
- [215] M. Egorov, B. Opanchuk, P. Drummond, B. V. Hall, P. Hannaford, and A. I. Sidorov, “Measurement of s -wave scattering lengths in a two-component Bose-Einstein condensate”, *Phys. Rev. A* **87**, 053614 (2013).
- [216] Y. Eto, M. Takahashi, K. Nabeta, R. Okada, M. Kunimi, H. Saito, and T. Hirano, “Bouncing motion and penetration dynamics in multicomponent Bose-Einstein condensates”, *Phys. Rev. A* **93**, 033615 (2016).

- [217] Y. Eto, M. Takahashi, M. Kunimi, H. Saito, and T. Hirano, “Nonequilibrium dynamics induced by miscible–immiscible transition in binary Bose–Einstein condensates”, *New J. Phys.* **18**, 073029 (2016).
- [218] M. A. Cazalilla and A. F. Ho, “Instabilities in Binary Mixtures of One-Dimensional Quantum Degenerate Gases”, *Phys. Rev. Lett* **91**, 150403 (2003).
- [219] T. Sowiński and M. Á. García-March, “One-dimensional mixtures of several ultracold atoms: a review”, *Rep. Prog. Phys.* **82**, 104401 (2019).
- [220] P. Naidon and D. S. Petrov, “Mixed Bubbles in Bose-Bose Mixtures”, *Phys. Rev. Lett.* **126**, 115301 (2021).
- [221] F. Minardi, F. Ancilotto, A. Burchianti, C. D’Errico, C. Fort, and M. Modugno, “Effective expression of the Lee-Huang-Yang energy functional for heteronuclear mixtures”, *Phys. Rev. A* **100**, 063636 (2019).
- [222] S. Li, U. N. Le, and H. Saito, “Long-lifetime supersolid in a two-component dipolar Bose-Einstein condensate”, *Phys. Rev. A* **105**, L061302 (2022).
- [223] C. Politi, A. Trautmann, P. Ilzhöfer, G. Durastante, M. J. Mark, M. Modugno, and F. Ferlaino, “Interspecies interactions in an ultracold dipolar mixture”, *Phys. Rev. A* **105**, 023304 (2022).
- [224] M. Soljačić, K. Steiglitz, S. M. Sears, M. Segev, M. H. Jakubowski, and R. Squier, “Collisions of Two Solitons in an Arbitrary Number of Coupled Nonlinear Schrödinger Equations”, *Phys. Rev. Lett.* **90**, 254102 (2003).
- [225] Y. M. Liu and C. G. Bao, “Analytical solutions of the coupled Gross–Pitaevskii equations for the three-species Bose–Einstein condensates”, *J. Phys. A: Math. Theor.* **50**, 275301 (2017).
- [226] K. Jimbo and H. Saito, “Surfactant behavior in three-component Bose-Einstein condensates”, *Phys. Rev. A* **103**, 063323 (2021).
- [227] E. Blomquist, A. Syrwid, and E. Babaev, “Borromean Supercounterfluidity”, *Phys. Rev. Lett.* **127**, 255303 (2021).
- [228] G. Biondini, D. K. Kraus, and B. Prinari, “The Three-Component Defocusing Non-linear Schrödinger Equation with Nonzero Boundary Conditions”, *Commun. Math. Phys.* **348**, 475 (2016).
- [229] T Kanna, A Annamalar Sheela, and R Babu Mareeswaran, “Spatially modulated two- and three-component Rabi-coupled Gross–Pitaevskii systems”, *J. Phys. A: Math. Theor.* **52**, 375201 (2019).
- [230] S. Lannig, C.-M. Schmied, M. Prüfer, P. Kunkel, R. Strohmaier, H. Strobel, T. Gasenzer, P. G. Kevrekidis, and M. K. Oberthaler, “Collisions of Three-Component Vector Solitons in Bose-Einstein Condensates”, *Phys. Rev. Lett.* **125**, 170401 (2020).
- [231] W. Wang, L.-C. Zhao, E. G. Charalampidis, and P. G. Kevrekidis, “Dark–dark soliton breathing patterns in multi-component Bose–Einstein condensates”, *J. Phys. B: At. Mol. Opt. Phys.* **54**, 055301 (2021).

- [232] L.-C. Zhao and J. Liu, “Rogue-wave solutions of a three-component coupled nonlinear Schrödinger equation”, *Phys. Rev. E* **87**, 013201 (2013).
- [233] K. Manikandan, P. Muruganandam, M. Senthilvelan, and M. Lakshmanan, “Manipulating localized matter waves in multicomponent Bose-Einstein condensates”, *Phys. Rev. E* **93**, 032212 (2016).
- [234] C. Liu, S.-C. Chen, X. Yao, and N. Akhmediev, “Non-degenerate multi-rogue waves and easy ways of their excitation”, *Physica D* **433**, 133192 (2022).
- [235] Y. Kawaguchi and M. Ueda, “Spinor Bose–Einstein condensates”, *Phys. Rep.* **520**, 253 (2012).
- [236] D. M. Stamper-Kurn and M. Ueda, “Spinor Bose gases: Symmetries, magnetism, and quantum dynamics”, *Rev. Mod. Phys.* **85**, 1191 (2013).
- [237] A. Widera, F. Gerbier, S. Fölling, T. Gericke, O. Mandel, and I. Bloch, “Precision measurement of spin-dependent interaction strengths for spin-1 and spin-2 87Rb atoms”, *New J. Phys.* **8**, 152 (2006).
- [238] H. Pu, C. K. Law, S. Raghavan, J. H. Eberly, and N. P. Bigelow, “Spin-mixing dynamics of a spinor Bose-Einstein condensate”, *Phys. Rev. A* **60**, 1463 (1999).
- [239] W. Zhang, D. L. Zhou, M.-S. Chang, M. S. Chapman, and L. You, “Coherent spin mixing dynamics in a spin-1 atomic condensate”, *Phys. Rev. A* **72**, 013602 (2005).
- [240] M.-S. Chang, Q. Qin, W. Zhang, L. You, and M. S. Chapman, “Coherent spinor dynamics in a spin-1 Bose condensate”, *Nat. Phys.* **1**, 111 (2005).
- [241] H. E. Nistazakis, D. J. Frantzeskakis, P. G. Kevrekidis, B. A. Malomed, R. Carretero-González, and A. R. Bishop, “Polarized states and domain walls in spinor Bose-Einstein condensates”, *Phys. Rev. A* **76**, 063603 (2007).
- [242] J.-P. Martikainen, A. Collin, and K.-A. Suominen, “Coreless vortex ground state of the rotating spinor condensate”, *Phys. Rev. A* **66**, 053604 (2002).
- [243] A. E. Leanhardt, Y. Shin, D. Kielpinski, D. E. Pritchard, and W. Ketterle, “Coreless Vortex Formation in a Spinor Bose-Einstein Condensate”, *Phys. Rev. Lett.* **90**, 140403 (2003).
- [244] J. Ieda, T. Miyakawa, and M. Wadati, “Matter-Wave Solitons in an F=1 Spinor Bose–Einstein Condensate”, *J. Phys. Soc. Jpn.* **73**, 2996 (2004).
- [245] J. Ieda, T. Miyakawa, and M. Wadati, “Exact Analysis of Soliton Dynamics in Spinor Bose-Einstein Condensates”, *Phys. Rev. Lett.* **93**, 194102 (2004).
- [246] L. Li, Z. Li, B. A. Malomed, D. Mihalache, and W. M. Liu, “Exact soliton solutions and nonlinear modulation instability in spinor Bose-Einstein condensates”, *Phys. Rev. A* **72**, 033611 (2005).
- [247] W. Zhang, Ö. E. Müstecaplıoğlu, and L. You, “Solitons in a trapped spin-1 atomic condensate”, *Phys. Rev. A* **75**, 043601 (2007).

- [248] M. Uchiyama, J. Ieda, and M. Wadati, “Dark Solitons in F=1 Spinor Bose–Einstein Condensate”, *J. Phys. Soc. Jpn.* **75**, 064002 (2006).
- [249] B. J. Dabrowska-Wüster, E. A. Ostrovskaya, T. J. Alexander, and Y. S. Kivshar, “Multicomponent gap solitons in spinor Bose-Einstein condensates”, *Phys. Rev. A* **75**, 023617 (2007).
- [250] H. E. Nistazakis, D. J. Frantzeskakis, P. G. Kevrekidis, B. A. Malomed, and R. Carretero-González, “Bright-dark soliton complexes in spinor Bose-Einstein condensates”, *Phys. Rev. A* **77**, 033612 (2008).
- [251] G. C. Katsimiga, S. I. Mistakidis, P. Schmelcher, and P. G. Kevrekidis, “Phase diagram, stability and magnetic properties of nonlinear excitations in spinor Bose–Einstein condensates”, *New J. Phys.* **23**, 013015 (2021).
- [252] G. C. Katsimiga, S. I. Mistakidis, K. Mukherjee, P. G. Kevrekidis, and P. Schmelcher, “Stability and dynamics across magnetic phases of vortex-bright type excitations in spinor Bose-Einstein condensates”, *Phys. Rev. A* **107**, 013313 (2023).
- [253] M. Uchiyama, J. Ieda, and M. Wadati, “Multicomponent Bright Solitons in F=2 Spinor Bose–Einstein Condensates”, *J. Phys. Soc. Jpn.* **76**, 074005 (2007).
- [254] C. Qu, L. P. Pitaevskii, and S. Stringari, “Magnetic Solitons in a Binary Bose-Einstein Condensate”, *Phys. Rev. Lett.* **116**, 160402 (2016).
- [255] C. Qu, M. Tylutki, S. Stringari, and L. P. Pitaevskii, “Magnetic solitons in Rabi-coupled Bose-Einstein condensates”, *Phys. Rev. A* **95**, 033614 (2017).
- [256] A. Farolfi, D. Trypogeorgos, C. Mordini, G. Lamporesi, and G. Ferrari, “Observation of Magnetic Solitons in Two-Component Bose-Einstein Condensates”, *Phys. Rev. Lett.* **125**, 030401 (2020).
- [257] X. Chai, D. Lao, K. Fujimoto, R. Hamazaki, M. Ueda, and C. Raman, “Magnetic Solitons in a Spin-1 Bose-Einstein Condensate”, *Phys. Rev. Lett.* **125**, 030402 (2020).
- [258] X. Chai, D. Lao, K. Fujimoto, and C. Raman, “Magnetic soliton: From two to three components with SO(3) symmetry”, *Phys. Rev. Research* **3**, L012003 (2021).
- [259] P. Öhberg and L. Santos, “Dark Solitons in a Two-Component Bose-Einstein Condensate”, *Phys. Rev. Lett.* **86**, 2918 (2001).
- [260] M. A. Hofer, J. J. Chang, C. Hamner, and P. Engels, “Dark-dark solitons and modulational instability in miscible two-component Bose-Einstein condensates”, *Phys. Rev. A* **84**, 041605 (2011).
- [261] D. Yan, J. J. Chang, C. Hamner, M. Hofer, P. G. Kevrekidis, P. Engels, V. Achilleos, D. J. Frantzeskakis, and J. Cuevas, “Beating dark–dark solitons in Bose–Einstein condensates”, *J. Phys. B: At. Mol. Opt. Phys.* **45**, 115301 (2012).
- [262] J. V. Boussinesq, “Théorie de l’intumescence liquide appelée onde solitaire ou de translation se propageant dans un canal rectangulaire”, *C. R. Acad. Sci.* **72**, 755 (1871).

- [263] Rayleigh, “XXXII. *On waves*”, *Phil. Mag., 5th ser.* **1**, 257 (1876).
- [264] D. J. Korteweg and G. De Vries, “XLI. *On the change of form of long waves advancing in a rectangular canal, and on a new type of long stationary waves*”, *Phil. Mag.* **39**, 422 (1895).
- [265] N. J. Zabusky and M. D. Kruskal, “Interaction of “Solitons” in a Collisionless Plasma and the Recurrence of Initial States”, *Phys. Rev. Lett.* **15**, 240 (1965).
- [266] A. S. Fokas and V. E. Zakharov, eds., *Important Developments in Soliton Theory*, Springer Series in Nonlinear Dynamics (Springer Berlin Heidelberg, Berlin, Heidelberg, 1993).
- [267] V. L. Ginzburg and L. D. Landau, “On the theory of superconductivity”, *Sov. Phys. JETP*, 1064 (1950).
- [268] V. L. Ginzburg, “On the macroscopic theory of superconductivity”, *Sov. Phys. JETP* **2**, 589 (1956).
- [269] V. L. Ginzburg and L. P. Pitaevskii, “ON THE THEORY OF SUPERFLUIDITY”, *Sov. Phys. JETP* **34**, 858 (1958).
- [270] R. Y. Chiao, E. Garmire, and C. H. Townes, “Self-Trapping of Optical Beams”, *Phys. Rev. Lett.* **13**, 479 (1964).
- [271] V. I. Talanov, “SELF-FOCUSING OF ELECTROMAGNETIC WAVES IN NON-LINEAR MEDIA”, *Radiophysics* **8**, 254 (1964).
- [272] V. I. Talanov, “Self Focusing of Wave Beams in Nonlinear Media”, *Sov. Phys. JETP* **2**, 138 (1965).
- [273] V. E. Zakharov, “Stability of periodic waves of finite amplitude on the surface of a deep fluid”, *J Appl Mech Tech Phys* **9**, 190 (1968).
- [274] D. J. Benney and G. J. Roskes, “Wave Instabilities”, *Stud. Appl. Math.* **48**, 377 (1969).
- [275] V. E. Zakharov, “Collapse of Langmuir Waves”, *Sov. Phys. JETP* **35**, 908 (1972).
- [276] T. Tsuchida, “N-Soliton Collision in the Manakov Model”, *Prog Theor Phys* **111**, 151 (2004).
- [277] S. V. Manakov, “On the theory of two-dimensional stationary self-focusing of electromagnetic waves”, *Zh. Eksp. Teor. Fiz.* **65**, 505 (1973).
- [278] D. M. Stamper-Kurn and W. Ketterle, “Spinor Condensates and Light Scattering from Bose-Einstein Condensates”, in *Coherent At. Matter Waves*, edited by R. Kaiser, C. Westbrook, and F. David, Les Houches - Ecole d’Ete de Physique Theorique (2001), pp. 139–217.
- [279] I. Morera, A. Muñoz Mateo, A. Polls, and B. Juliá-Díaz, “Dark-dark-soliton dynamics in two density-coupled Bose-Einstein condensates”, *Phys. Rev. A* **97**, 043621 (2018).
- [280] S. Middelkamp, J. Chang, C. Hamner, R. Carretero-González, P. Kevrekidis, V. Achilleos, D. Frantzeskakis, P. Schmelcher, and P. Engels, “Dynamics of dark–bright solitons in cigar-shaped Bose–Einstein condensates”, *Phys. Lett. A* **375**, 642 (2011).

- [281] D. Yan, J. J. Chang, C. Hamner, P. G. Kevrekidis, P. Engels, V. Achilleos, D. J. Frantzeskakis, R. Carretero-González, and P. Schmelcher, “Multiple dark-bright solitons in atomic Bose-Einstein condensates”, *Phys. Rev. A* **84**, 053630 (2011).
- [282] V. Achilleos, P. G. Kevrekidis, V. M. Rothos, and D. J. Frantzeskakis, “Statics and dynamics of atomic dark-bright solitons in the presence of impurities”, *Phys. Rev. A* **84**, 053626 (2011).
- [283] B. Luther-Davies and Y. Xiaoping, “Waveguides and Y junctions formed in bulk media by using dark spatial solitons”, *Opt Lett* **17**, 496 (1992).
- [284] E. A. Ostrovskaya and Y. S. Kivshar, “Nonlinear theory of soliton-induced waveguides”, *Opt. Lett.* **23**, 1268 (1998).
- [285] Y. S. Kivshar and S. K. Turitsyn, “Vector dark solitons”, *Opt. Lett.* **18**, 337 (1993).
- [286] R. Radhakrishnan and M. Lakshmanan, “Bright and dark soliton solutions to coupled nonlinear Schrödinger equations”, *J. Phys. A: Math. Gen.* **28**, 2683 (1995).
- [287] A. V. Buryak, Y. S. Kivshar, and D. F. Parker, “Coupling between dark and bright solitons”, *Phys. Lett. A* **215**, 57 (1996).
- [288] A. P. Sheppard and Y. S. Kivshar, “Polarized dark solitons in isotropic Kerr media”, *Phys. Rev. E* **55**, 4773 (1997).
- [289] Q.-H. Park and H. J. Shin, “Systematic construction of multicomponent optical solitons”, *Phys. Rev. E* **61**, 3093 (2000).
- [290] B. Prinari, F. Vitale, and G. Biondini, “Dark-bright soliton solutions with nontrivial polarization interactions for the three-component defocusing nonlinear Schrödinger equation with nonzero boundary conditions”, *J. Math. Phys.* **56**, 071505 (2015).
- [291] N. Mao and L.-C. Zhao, *Exact analytical soliton solutions of N -component coupled nonlinear Schrödinger equations with arbitrary nonlinear parameters*, Aug. 2022, [arXiv:2208.05696](https://arxiv.org/abs/2208.05696) [cond-mat, physics:math-ph, physics:nlin].
- [292] J. Ieda, T. Miyakawa, and M. Wadati, “Exact soliton solutions of spinor Bose-Einstein condensates”, *Laser Phys.* **16**, 678 (2006).
- [293] T. M. Bersano, V. Gokhroo, M. A. Khamsehchi, J. D’Ambroise, D. J. Frantzeskakis, P. Engels, and P. G. Kevrekidis, “Three-Component Soliton States in Spinor $F = 1$ Bose-Einstein Condensates”, *Phys. Rev. Lett.* **120**, 063202 (2018).
- [294] C.-M. Schmied and P. G. Kevrekidis, “Dark-antidark spinor solitons in spin-1 Bose gases”, *Phys. Rev. A* **102**, 053323 (2020).
- [295] Y.-H. Qin, L.-C. Zhao, Z.-Q. Yang, and L. Ling, “Multivalley dark solitons in multi-component Bose-Einstein condensates with repulsive interactions”, *Phys. Rev. E* **104**, 014201 (2021).
- [296] T. Mithun, A. R. Fritsch, G. N. Koutsokostas, D. J. Frantzeskakis, I. B. Spielman, and P. G. Kevrekidis, *Stationary solitons in $F = 1$ spin-orbit coupled Bose-Einstein condensates*, Dec. 2022, [arXiv:2212.12966](https://arxiv.org/abs/2212.12966) [cond-mat, physics:nlin].

- [297] G. Hegde, S. M. Jose, and R. Nath, “Dynamics of a pair of overlapping polar bright solitons in spin-1 Bose-Einstein condensates”, *Phys. Rev. A* **106**, 043307 (2022).
- [298] V. E. Zakharov and A. M. Rubenchik, “Instability of waveguides and solitons in nonlinear media”, *Sov. Phys. JETP* **38**, 494 (1974).
- [299] D. L. Feder, M. S. Pindzola, L. A. Collins, B. I. Schneider, and C. W. Clark, “Dark-soliton states of Bose-Einstein condensates in anisotropic traps”, *Phys. Rev. A* **62**, 053606 (2000).
- [300] J. Brand and W. P. Reinhardt, “Solitonic vortices and the fundamental modes of the “snake instability”: Possibility of observation in the gaseous Bose-Einstein condensate”, *Phys. Rev. A* **65**, 043612 (2002).
- [301] G. Theocharis, D. J. Frantzeskakis, P. G. Kevrekidis, B. A. Malomed, and Y. S. Kivshar, “Ring Dark Solitons and Vortex Necklaces in Bose-Einstein Condensates”, *Phys. Rev. Lett.* **90**, 120403 (2003).
- [302] I. Shomroni, E. Lahoud, S. Levy, and J. Steinhauer, “Evidence for an oscillating soliton/vortex ring by density engineering of a Bose–Einstein condensate”, *Nat. Phys.* **5**, 193 (2009).
- [303] G. C. Katsimiga, S. I. Mistakidis, G. M. Koutentakis, P. G. Kevrekidis, and P. Schmelcher, “Many-body quantum dynamics in the decay of bent dark solitons of Bose–Einstein condensates”, *New J. Phys.* **19**, 123012 (2017).
- [304] G. Huang, J. Szeftel, and S. Zhu, “Dynamics of dark solitons in quasi-one-dimensional Bose-Einstein condensates”, *Phys. Rev. A* **65**, 053605 (2002).
- [305] N. G. Parker, N. P. Proukakis, and C. S. Adams, “Dark soliton decay due to trap anharmonicity in atomic Bose-Einstein condensates”, *Phys. Rev. A* **81**, 033606 (2010).
- [306] A. E. Muryshev, H. B. van Linden van den Heuvell, and G. V. Shlyapnikov, “Stability of standing matter waves in a trap”, *Phys. Rev. A* **60**, R2665 (1999).
- [307] P. O. Fedichev, A. E. Muryshev, and G. V. Shlyapnikov, “Dissipative dynamics of a kink state in a Bose-condensed gas”, *Phys. Rev. A* **60**, 3220 (1999).
- [308] A. Muryshev, G. V. Shlyapnikov, W. Ertmer, K. Sengstock, and M. Lewenstein, “Dynamics of Dark Solitons in Elongated Bose-Einstein Condensates”, *Phys. Rev. Lett.* **89**, 110401 (2002).
- [309] K. J. Wright and A. S. Bradley, *Stochastic longevity of a dark soliton in a finite-temperature Bose-Einstein condensate*, June 2011, [arXiv:1104.2691](https://arxiv.org/abs/1104.2691) [[cond-mat](#), [physics:quant-ph](#)].
- [310] G. C. Katsimiga, J. Stockhofe, P. G. Kevrekidis, and P. Schmelcher, “Dark-bright soliton interactions beyond the integrable limit”, *Phys. Rev. A* **95**, 013621 (2017).
- [311] G. C. Katsimiga, P. G. Kevrekidis, B. Prinari, G. Biondini, and P. Schmelcher, “Dark-bright soliton pairs: Bifurcations and collisions”, *Phys. Rev. A* **97**, 043623 (2018).

- [312] H. Xu, P. G. Kevrekidis, and T. Kapitula, “Existence, stability, and dynamics of harmonically trapped one-dimensional multi-component solitary waves: The near-linear limit”, *J. Math. Phys.* **58**, 061901 (2017).
- [313] I. Danaïla, M. A. Khamehchi, V. Gokhroo, P. Engels, and P. G. Kevrekidis, “Vector dark-antidark solitary waves in multicomponent Bose-Einstein condensates”, *Phys. Rev. A* **94**, 053617 (2016).
- [314] G. C. Katsimiga, S. I. Mistakidis, T. M. Bersano, M. K. H. Ome, S. M. Mossman, K. Mukherjee, P. Schmelcher, P. Engels, and P. G. Kevrekidis, “Observation and analysis of multiple dark-antidark solitons in two-component Bose-Einstein condensates”, *Phys. Rev. A* **102**, 023301 (2020).
- [315] G. C. Katsimiga, G. M. Koutentakis, S. I. Mistakidis, P. G. Kevrekidis, and P. Schmelcher, “Dark-bright soliton dynamics beyond the mean-field approximation”, *New J. Phys.* **19**, 073004 (2017).
- [316] K. E. Strecker, G. B. Partridge, A. G. Truscott, and R. G. Hulet, “Bright matter wave solitons in Bose–Einstein condensates”, *New J. Phys.* **5**, 73 (2003).
- [317] Th. Busch and J. R. Anglin, “Motion of Dark Solitons in Trapped Bose-Einstein Condensates”, *Phys. Rev. Lett.* **84**, 2298 (2000).
- [318] Th. Busch and J. R. Anglin, “Dark-Bright Solitons in Inhomogeneous Bose-Einstein Condensates”, *Phys. Rev. Lett.* **87**, 010401 (2001).
- [319] C. Becker, S. Stellmer, P. Soltan-Panahi, S. Dörscher, M. Baumert, E.-M. Richter, J. Kronjäger, K. Bongs, and K. Sengstock, “Oscillations and interactions of dark and dark–bright solitons in Bose–Einstein condensates”, *Nat. Phys.* **4**, 496 (2008).
- [320] S. Stellmer, C. Becker, P. Soltan-Panahi, E.-M. Richter, S. Dörscher, M. Baumert, J. Kronjäger, K. Bongs, and K. Sengstock, “Collisions of Dark Solitons in Elongated Bose-Einstein Condensates”, *Phys. Rev. Lett.* **101**, 120406 (2008).
- [321] A. Weller, J. P. Ronzheimer, C. Gross, J. Esteve, M. K. Oberthaler, D. J. Frantzeskakis, G. Theocharis, and P. G. Kevrekidis, “Experimental Observation of Oscillating and Interacting Matter Wave Dark Solitons”, *Phys. Rev. Lett.* **101**, 130401 (2008).
- [322] J. P. Gordon, “Interaction forces among solitons in optical fibers”, *Opt. Lett.*, **OL 8**, 596 (1983).
- [323] F. M. Mitschke and L. F. Mollenauer, “Experimental observation of interaction forces between solitons in optical fibers”, *Opt. Lett.*, **OL 12**, 355 (1987).
- [324] G. Theocharis, A. Weller, J. P. Ronzheimer, C. Gross, M. K. Oberthaler, P. G. Kevrekidis, and D. J. Frantzeskakis, “Multiple atomic dark solitons in cigar-shaped Bose-Einstein condensates”, *Phys. Rev. A* **81**, 063604 (2010).
- [325] U. Al Khawaja, H. T. C. Stoof, R. G. Hulet, K. E. Strecker, and G. B. Partridge, “Bright Soliton Trains of Trapped Bose-Einstein Condensates”, *Phys. Rev. Lett.* **89**, 200404 (2002).

- [326] J. H. V. Nguyen, P. Dyke, D. Luo, B. A. Malomed, and R. G. Hulet, “Collisions of matter-wave solitons”, *Nat. Phys.* **10**, 918 (2014).
- [327] B. J. Dabrowska-Wüster, S. Wüster, and M. J. Davis, “Dynamical formation and interaction of bright solitary waves and solitons in the collapse of Bose–Einstein condensates with attractive interactions”, *New J. Phys.* **11**, 053017 (2009).
- [328] E. A. Ostrovskaya, Y. S. Kivshar, Z. Chen, and M. Segev, “Interaction between vector solitons and solitonic gluons”, *Opt. Lett.* **24**, 327 (1999).
- [329] S Rajendran, P Muruganandam, and M Lakshmanan, “Interaction of dark–bright solitons in two-component Bose–Einstein condensates”, *J. Phys. B: At. Mol. Opt. Phys.* **42**, 145307 (2009).
- [330] C. Anastassiou, M. Segev, K. Steiglitz, J. A. Giordmaine, M. Mitchell, M.-f. Shih, S. Lan, and J. Martin, “Energy-Exchange Interactions between Colliding Vector Solitons”, *Phys. Rev. Lett.* **83**, 2332 (1999).
- [331] G. Dean, T. Klotz, B. Prinari, and F. Vitale, “Dark–dark and dark–bright soliton interactions in the two-component defocusing nonlinear Schrödinger equation”, *Appl. Anal.* **92**, 379 (2013).
- [332] G. Huang, M. G. Velarde, and V. A. Makarov, “Dark solitons and their head-on collisions in Bose-Einstein condensates”, *Phys. Rev. A* **64**, 013617 (2001).
- [333] J. H. V. Nguyen, D. Luo, and R. G. Hulet, “Formation of matter-wave soliton trains by modulational instability”, *Science* **356**, 422 (2017).
- [334] P. Suret, S. Randoux, A. Gelash, D. Agafontsev, B. Doyon, and G. El, *Soliton Gas: Theory, Numerics and Experiments*, Apr. 2023, [arXiv:2304.06541 \[nlin, physics:physics\]](https://arxiv.org/abs/2304.06541).
- [335] L. Draper, “‘Freak’ Ocean Waves”, *Weather* **21**, 2 (1966).
- [336] S. Haver, in *Rogue Waves 2004*, Actes de Colloques - IFREMER (Brest, France, 2004).
- [337] J. Schulz-Stellenfleth and S. Lehner, “Measurement of 2-D sea surface elevation fields using complex synthetic aperture radar data”, *IEEE Trans. Geosci. Remote Sens.* **42**, 1149 (2004).
- [338] T. König, S. Lehner, J. Schulz-Stellenfleth, and B. Schattler, “A new historic ERS wave mode data set for oceanographic applications”, in *IGARSS 2004 2004 IEEE Int. Geosci. Remote Sens. Symp.* Vol. 3 (Sept. 2004), 1888–1891 vol.3.
- [339] X.-M. Li and S. Lehner, “Ocean Wave Measurements in High and Complex Sea State by SAR Wave Mode Data and Numerical Wave Model”, in *SeaSAR 2008*, edited by H. Lacoste and L. Ouwehand, SP-656 (on CD-ROM) (Apr. 2008), pp. 1–5.
- [340] C. Kharif and E. Pelinovsky, “Physical mechanisms of the rogue wave phenomenon”, *Eur. J. Mech. B/Fluids.* **22**, 603 (2003).
- [341] I. I. Didenkulova, A. V. Slunyaev, E. N. Pelinovsky, and C. Kharif, “Freak waves in 2005”, *Nat. Hazards Earth Syst. Sci.* **6**, 1007 (2006).

- [342] E. Didenkulova, I. Didenkulova, and I. Medvedev, “Freak wave events in 2005–2021: statistics and analysis of favourable wave and wind conditions”, *Nat. Hazards Earth Syst. Sci.* **23**, 1653 (2023).
- [343] N. Akhmediev and E. Pelinovsky, “Editorial – Introductory remarks on “Discussion & Debate: Rogue Waves – Towards a Unifying Concept?””, *Eur. Phys. J. Spec. Top.* **185**, 1 (2010).
- [344] S. Haver and O. J. Andersen, “Freak Waves: Rare Realizations of a Typical Population Or Typical Realizations of a Rare Population?”, in The Tenth International Offshore and Polar Engineering Conference (May 2000).
- [345] K. Henderson, D. Peregrine, and J. Dold, “Unsteady water wave modulations: fully nonlinear solutions and comparison with the nonlinear Schrödinger equation”, *Wave Motion* **29**, 341 (1999).
- [346] K. B. Dysthe and K. Trulsen, “Note on Breather Type Solutions of the NLS as Models for Freak-Waves”, *Phys. Scr.* **1999**, 48 (1999).
- [347] C. Sulem and P. L. Sulem, *The nonlinear Schrödinger equation: self-focusing and wave collapse*, Applied Mathematical Sciences 139 (Springer, New York, 1999).
- [348] N. Akhmediev, J. M. Soto-Crespo, and A. Ankiewicz, “Extreme waves that appear from nowhere: On the nature of rogue waves”, *Phys. Lett. A* **373**, 2137 (2009).
- [349] N. Akhmediev, J. M. Soto-Crespo, and A. Ankiewicz, “Could rogue waves be used as efficient weapons against enemy ships?”, *Eur. Phys. J. Spec. Top.* **185**, 259 (2010).
- [350] N. K. Vitanov, A. Chabchoub, and N. Hoffmann, “Deep-Water Waves: on the Nonlinear Schrödinger Equation and its Solutions”, *JTMA* **43**, 43 (2013).
- [351] C. B. Ward and P. G. Kevrekidis, “Rogue Waves as Self-Similar Solutions on a Background: A Direct Calculation”, ArXiv190205494 Nlin (2019), [arXiv:1902.05494 \[nlin\]](https://arxiv.org/abs/1902.05494).
- [352] A. Ankiewicz, J. M. Soto-Crespo, and N. Akhmediev, “Rogue waves and rational solutions of the Hirota equation”, *Phys. Rev. E* **81**, 046602 (2010).
- [353] N. Akhmediev and A. Ankiewicz, “Modulation instability, Fermi-Pasta-Ulam recurrence, rogue waves, nonlinear phase shift, and exact solutions of the Ablowitz-Ladik equation”, *Phys. Rev. E* **83**, 046603 (2011).
- [354] Z. Yan, “Rogue waves in nonlinear science”, *J. Phys.: Conf. Ser.* **400**, 012084 (2012).
- [355] A. Chowdury, A. Ankiewicz, and N. Akhmediev, “Moving breathers and breather-to-soliton conversions for the Hirota equation”, *Proc. R. Soc. Math. Phys. Eng. Sci.* **471**, 20150130 (2015).
- [356] D. Kraus, G. Biondini, and G. Kovačič, “The focusing Manakov system with nonzero boundary conditions”, *Nonlinearity* **28**, 3101 (2015).
- [357] A. R. Osborne, *Nonlinear ocean waves and the inverse scattering transform*, International Geophysics Series 97 (Academic Press Elsevier, Burlington, MA, 2010).

- [358] M. Tajiri and Y. Watanabe, “Breather solutions to the focusing nonlinear Schrödinger equation”, *Phys. Rev. E* **57**, 3510 (1998).
- [359] V. I. Bespalov and V. I. Talanov, “Filamentary Structure of Light Beams in Nonlinear Liquids”, *Sov. J. Exp. Theor. Phys. Lett.* **3**, 307 (1966).
- [360] W. Królikowski, O. Bang, N. I. Nikolov, D. Neshev, J. Wyller, J. J. Rasmussen, and D. Edmundson, “Modulational instability, solitons and beam propagation in spatially nonlocal nonlinear media”, *J. Opt. B: Quantum Semiclass. Opt.* **6**, S288 (2004).
- [361] A. E. Kraych, P. Suret, G. El, and S. Randoux, “Nonlinear Evolution of the Locally Induced Modulational Instability in Fiber Optics”, *Phys. Rev. Lett.* **122**, 054101 (2019).
- [362] T. Mithun and K. Kasamatsu, “Modulation instability associated nonlinear dynamics of spin-orbit coupled Bose-Einstein condensates”, *J. Phys. B: At. Mol. Opt. Phys.* **52**, 045301 (2019).
- [363] P. A. E. M. Janssen, “Nonlinear Four-Wave Interactions and Freak Waves”, *J. Phys. Oceanogr.* **33**, 863 (2003).
- [364] M. Onorato, A. R. Osborne, and M. Serio, “Modulational Instability in Crossing Sea States: A Possible Mechanism for the Formation of Freak Waves”, *Phys. Rev. Lett.* **96**, 014503 (2006).
- [365] K. Trulsen, in *The Ocean in Motion: Circulation, Waves, Polar Oceanography*, edited by M. G. Velarde, R. Y. Tarakanov, and A. V. Marchenko, Springer Oceanography (Springer International Publishing, Cham, 2018), pp. 239–247.
- [366] Y.-C. Ma, “The Perturbed Plane-Wave Solutions of the Cubic Schrödinger Equation”, *Stud. Appl. Math.* **60**, 43 (1979).
- [367] E. A. Kuznetsov, “Solitons in a parametrically unstable plasma”, *Dokl. Akad. Nauk SSSR* **236**, 575 (1977).
- [368] D. H. Peregrine, “Water waves, nonlinear Schrödinger equations and their solutions”, *J. Aust. Math. Soc. Series B, Appl. Math.* **25**, 16 (1983).
- [369] N. N. Akhmediev and V. I. Korneev, “Modulation instability and periodic solutions of the nonlinear Schrödinger equation”, *Theor Math Phys* **69**, 1089 (1986).
- [370] N. Karjanto, “Peregrine Soliton as a Limiting Behavior of the Kuznetsov-Ma and Akhmediev Breathers”, *Front. Phys.* **9**, 599767 (2021).
- [371] V. I. Shrira and V. V. Geogjaev, “What makes the Peregrine soliton so special as a prototype of freak waves?”, *J. Eng. Math.* **67**, 11 (2010).
- [372] J. M. Dudley, G. Genty, F. Dias, B. Kibler, and N. Akhmediev, “Modulation instability, Akhmediev Breathers and continuous wave supercontinuum generation”, *Opt. Express, OE* **17**, 21497 (2009).
- [373] E. M. Dianov, Z. S. Nikonova, A. M. Prokhorov, and V. N. Serkin, “Optimal compression of multisoliton pulses in fiber-optic waveguides”, *Pisma V Zhurnal Tekhnicheskoi Fiz.* **12**, 756 (1986).

- [374] N. N. Akhmediev, L. L. Betina, V. M. Eleonskiĭ, N. E. Kulagin, N. V. Ostrovskaya, and É. A. Poltoratskiĭ, “Optimal self-compression of multisoliton pulses in an optical fiber”, *Sov. J. Quantum Electron.* **19**, 1240 (1989).
- [375] A. Chabchoub, N. P. Hoffmann, and N. Akhmediev, “Rogue Wave Observation in a Water Wave Tank”, *Phys. Rev. Lett.* **106**, 204502 (2011).
- [376] A. Chabchoub, N. Hoffmann, M. Onorato, and N. Akhmediev, “Super Rogue Waves: Observation of a Higher-Order Breather in Water Waves”, *Phys. Rev. X* **2**, 011015 (2012).
- [377] A. Chabchoub and M. Fink, “Time-Reversal Generation of Rogue Waves”, *Phys. Rev. Lett.* **112**, 124101 (2014).
- [378] A. Chabchoub, “Tracking Breather Dynamics in Irregular Sea State Conditions”, *Phys. Rev. Lett.* **117**, 144103 (2016).
- [379] G. Xu, A. Chabchoub, D. E. Pelinovsky, and B. Kibler, “Observation of modulation instability and rogue breathers on stationary periodic waves”, *Phys. Rev. Res.* **2**, 033528 (2020).
- [380] A. Tikan, F. Bonnefoy, G. Roberti, G. El, A. Tovbis, G. Ducrozet, A. Cazaubiel, G. Prabhudesai, G. Michel, F. Copie, E. Falcon, S. Randoux, and P. Suret, “Prediction and manipulation of hydrodynamic rogue waves via nonlinear spectral engineering”, *Phys. Rev. Fluids* **7**, 054401 (2022).
- [381] C. Kharif, E. Pelinovsky, and A. Slunyaev, *Rogue Waves in the Ocean*, Advances in Geophysical and Environmental Mechanics and Mathematics (Springer-Verlag, Berlin Heidelberg, 2009).
- [382] B. S. White and B. Fornberg, “On the chance of freak waves at sea”, *J. Fluid Mech.* **355**, 113 (1998).
- [383] M. G. Brown, “Space–time surface gravity wave caustics: structurally stable extreme wave events”, *Wave Motion* **33**, 117 (2001).
- [384] B. Kinsman, *Wind Waves: Their Generation and Propagation on the Ocean Surface* (Courier Corporation, Jan. 1984).
- [385] M. Onorato, A. R. Osborne, M. Serio, and S. Bertone, “Freak Waves in Random Oceanic Sea States”, *Phys. Rev. Lett.* **86**, 5831 (2001).
- [386] A. Calini and C. M. Schober, “Homoclinic chaos increases the likelihood of rogue wave formation”, *Phys. Lett. A* **298**, 335 (2002).
- [387] T. B. Benjamin and J. E. Feir, “The disintegration of wave trains on deep water Part 1. Theory”, *J. Fluid Mech.* **27**, 417 (1967).
- [388] T. B. Benjamin, K. Hasselmann, and M. J. Lighthill, “Instability of periodic wavetrains in nonlinear dispersive systems”, *Proc. R. Soc. Lond. Ser. Math. Phys. Sci.* **299**, 59 (1967).
- [389] V. Zakharov and L. Ostrovsky, “Modulation instability: The beginning”, *Physica D: Nonlinear Phenomena* **238**, 540 (2009).

- [390] G. Biondini and E. Fagerstrom, “The Integrable Nature of Modulational Instability”, *SIAM J. Appl. Math.* **75**, 136 (2015).
- [391] G. Biondini and D. Mantzavinos, “Universal Nature of the Nonlinear Stage of Modulational Instability”, *Phys. Rev. Lett.* **116**, 043902 (2016).
- [392] G. Biondini, S. Li, D. Mantzavinos, and S. Trillo, “Universal Behavior of Modulationally Unstable Media”, *SIAM Rev.* **60**, 888 (2018).
- [393] P. G. Kevrekidis and D. J. Frantzeskakis, “Pattern forming dynamical instabilities of bose–einstein condensates”, *Mod. Phys. Lett. B* **18**, 173 (2004).
- [394] C. Garrett and J. Gemmrich, “Rogue waves”, *Phys. Today* **62**, 62 (2009).
- [395] M. Onorato, T. Waseda, A. Toffoli, L. Cavaleri, O. Gramstad, P. A. E. M. Janssen, T. Kinoshita, J. Monbaliu, N. Mori, A. R. Osborne, M. Serio, C. T. Stansberg, H. Tamura, and K. Trulsen, “Statistical Properties of Directional Ocean Waves: The Role of the Modulational Instability in the Formation of Extreme Events”, *Phys. Rev. Lett.* **102**, 114502 (2009).
- [396] V. E. Zakharov and A. A. Gelash, “Nonlinear Stage of Modulation Instability”, *Phys. Rev. Lett.* **111**, 054101 (2013).
- [397] A. A. Gelash and V. E. Zakharov, “Superregular solitonic solutions: a novel scenario for the nonlinear stage of modulation instability”, *Nonlinearity* **27**, R1 (2014).
- [398] S. L. Cornish, S. T. Thompson, and C. E. Wieman, “Formation of Bright Matter-Wave Solitons during the Collapse of Attractive Bose-Einstein Condensates”, *Phys. Rev. Lett.* **96**, 170401 (2006).
- [399] D. Luo, Y. Jin, J. H. V. Nguyen, B. A. Malomed, O. V. Marchukov, V. A. Yurovsky, V. Dunjko, M. Olshanii, and R. G. Hulet, “Creation and Characterization of Matter-Wave Breathers”, *Phys. Rev. Lett.* **125**, 183902 (2020).
- [400] P. Medley, M. A. Minar, N. C. Cizek, D. Berryrieser, and M. A. Kasevich, “Evaporative Production of Bright Atomic Solitons”, *Phys. Rev. Lett.* **112**, 060401 (2014).
- [401] A. L. Marchant, T. P. Billam, T. P. Wiles, M. M. H. Yu, S. A. Gardiner, and S. L. Cornish, “Controlled formation and reflection of a bright solitary matter-wave”, *Nature Communications* **4**, 1865 (2013).
- [402] M. R. Andrews, C. G. Townsend, H.-J. Miesner, D. S. Durfee, D. M. Kurn, and W. Ketterle, “Observation of Interference Between Two Bose Condensates”, *Science* **275**, 637 (1997).
- [403] W. P. Reinhardt and C. W. Clark, “Soliton dynamics in the collisions of Bose - Einstein condensates: an analogue of the Josephson effect”, *J. Phys. B: At. Mol. Opt. Phys.* **30**, 785 (1997).
- [404] T. F. Scott, R. J. Ballagh, and K. Burnett, “Formation of fundamental structures in Bose - Einstein condensates”, *J. Phys. B: At. Mol. Opt. Phys.* **31**, 329 (1998).
- [405] M. Hofer, P. Engels, and J. Chang, “Matter–wave interference in Bose–Einstein condensates: A dispersive hydrodynamic perspective”, *Physica D* **238**, 1311 (2009).

- [406] P. Engels and C. Atherton, “Stationary and Nonstationary Fluid Flow of a Bose-Einstein Condensate Through a Penetrable Barrier”, *Phys. Rev. Lett.* **99**, 160405 (2007).
- [407] L. D. Carr, J. Brand, S. Burger, and A. Sanpera, “Dark-soliton creation in Bose-Einstein condensates”, *Phys. Rev. A* **63**, 051601 (2001).
- [408] A. M. Kamchatnov, R. A. Kraenkel, and B. A. Umarov, “Asymptotic soliton train solutions of the defocusing nonlinear Schrödinger equation”, *Phys. Rev. E* **66**, 036609 (2002).
- [409] V. A. Brazhnyi and A. M. Kamchatnov, “Creation and evolution of trains of dark solitons in a trapped one-dimensional Bose-Einstein condensate”, *Phys. Rev. A* **68**, 043614 (2003).
- [410] C. Hamner, J. J. Chang, P. Engels, and M. A. Hoefer, “Generation of Dark-Bright Soliton Trains in Superfluid-Superfluid Counterflow”, *Phys. Rev. Lett.* **106**, 065302 (2011).
- [411] N. I. Nikolov, D. Neshev, W. Królikowski, O. Bang, J. J. Rasmussen, and P. L. Christiansen, “Attraction of nonlocal dark optical solitons”, *Opt. Lett.* **29**, 286 (2004).
- [412] B. Wu, J. Liu, and Q. Niu, “Controlled Generation of Dark Solitons with Phase Imprinting”, *Phys. Rev. Lett.* **88**, 034101 (2002).
- [413] T. Kurosaki and M. Wadati, “Matter-Wave Bright Solitons with a Finite Background in Spinor Bose–Einstein Condensates”, *J. Phys. Soc. Jpn.* **76**, 084002 (2007).
- [414] J. A. Espínola-Rocha and P. Kevrekidis, “Thresholds for soliton creation in the Ablowitz–Ladik lattice”, *Math. Comput. Simul.* **80**, 693 (2009).
- [415] M. Toda and M. A. Breazale, “Theory of Nonlinear Lattices (second, enlarged edition)”, *J. Acoust. Soc. Am.* **87**, 461 (1990).
- [416] M. Ma, R. Navarro, and R. Carretero-González, “Solitons riding on solitons and the quantum Newton’s cradle”, *Phys. Rev. E* **93**, 022202 (2016).
- [417] V. E. Zakharov, A. N. Pushkarev, V. F. Shvets, and V. V. Yan’kov, “Soliton turbulence”, *Sov. Phys. JETP* **48**, 83 (1988).
- [418] S. Nazarenko, *Wave Turbulence*, Vol. 825, Lecture Notes in Physics (Springer Berlin Heidelberg, Berlin, Heidelberg, 2011).
- [419] D. Kachulin, A. Dyachenko, and V. Zakharov, “Soliton Turbulence in Approximate and Exact Models for Deep Water Waves”, *Fluids* **5**, 67 (2020).
- [420] V. E. Zakharov, “Kinetic Equation for Solitons”, *Sov. Phys. JETP* **33**, 538 (1971).
- [421] M.-M. Shen and D. R. Nicholson, “Numerical comparison of strong Langmuir turbulence models”, *Phys. Fluids* **30**, 1096 (1987).
- [422] H. Büttner and F. G. Mertens, “Toda lattice: Statistical mechanics and solitons”, *Solid State Commun.* **29**, 663 (1979).

- [423] S. E. Nagler, W. J. L. Buyers, R. L. Armstrong, and B. Briat, “Solitons in the one-dimensional antiferromagnet CsCoBr₃”, *Phys. Rev. B* **28**, 3873 (1983).
- [424] B. A. Malomed, “Interactions between Solitons in a Monomode Fiber”, in *Nonlinear Guid.-Wave Phenom. 1991 Pap. MF3* (Sept. 1991), MF3.
- [425] B. A. Malomed, “Bound States in a Gas of Solitons Supported by a Randomly Fluctuating Force”, *EPL* **30**, 507 (1995).
- [426] A. Schwache and F. Mitschke, “Properties of an optical soliton gas”, *Phys. Rev. E* **55**, 7720 (1997).
- [427] H. Flaschka, M. G. Forest, and D. W. McLaughlin, “Multiphase averaging and the inverse spectral solution of the Korteweg—de Vries equation”, *Commun. Pure Appl. Math.* **33**, 739 (1980).
- [428] G. A. El, “The thermodynamic limit of the Whitham equations”, *Physics Letters A* **311**, 374 (2003).
- [429] G. A. El and A. M. Kamchatnov, “Kinetic Equation for a Dense Soliton Gas”, *Phys. Rev. Lett.* **95**, 204101 (2005).
- [430] G. A. El, “Soliton gas in integrable dispersive hydrodynamics”, *J. Stat. Mech.* **2021**, 114001 (2021).
- [431] B. Doyon, T. Yoshimura, and J.-S. Caux, “Soliton Gases and Generalized Hydrodynamics”, *Phys. Rev. Lett.* **120**, 045301 (2018).
- [432] I. Redor, E. Barthélemy, H. Michallet, M. Onorato, and N. Mordant, “Experimental Evidence of a Hydrodynamic Soliton Gas”, *Phys. Rev. Lett.* **122**, 214502 (2019).
- [433] P. Suret, A. Tikan, F. Bonnefoy, F. Copie, G. Ducrozet, A. Gelash, G. Prabhudesai, G. Michel, A. Cazaubiel, E. Falcon, G. El, and S. Randoux, “Nonlinear Spectral Synthesis of Soliton Gas in Deep-Water Surface Gravity Waves”, *Phys. Rev. Lett.* **125**, 264101 (2020).
- [434] A. Costa, A. R. Osborne, D. T. Resio, S. Alessio, E. Chirivì, E. Saggese, K. Bellomo, and C. E. Long, “Soliton Turbulence in Shallow Water Ocean Surface Waves”, *Phys. Rev. Lett.* **113**, 108501 (2014).
- [435] A. R. Osborne, D. T. Resio, A. Costa, S. Ponce de León, and E. Chirivì, “Highly nonlinear wind waves in Currituck Sound: dense breather turbulence in random ocean waves”, *Ocean Dyn.* **69**, 187 (2019).
- [436] A. Slunyaev, “Persistence of hydrodynamic envelope solitons: Detection and rogue wave occurrence”, *Phys. Fluids* **33**, 036606 (2021).
- [437] G. El and A. Tovbis, “Spectral theory of soliton and breather gases for the focusing nonlinear Schrödinger equation”, *Phys. Rev. E* **101**, 052207 (2020).
- [438] G. A. El and M. A. Hofer, “Dispersive shock waves and modulation theory”, *Physica D* **333**, 11 (2016).

- [439] A. A. Gelash and D. S. Agafontsev, “Strongly interacting soliton gas and formation of rogue waves”, *Phys. Rev. E* **98**, 042210 (2018).
- [440] H. Chaachoua Sameut, S. Pattu, U. Al Khawaja, M. Benarous, and H. Belkroukra, “Peregrine Soliton Management of Breathers in Two Coupled Gross–Pitaevskii Equations with External Potential”, *Phys. Wave Phen.* **28**, 305 (2020).
- [441] P. A. Ruprecht, M. J. Holland, K. Burnett, and M. Edwards, “Time-dependent solution of the nonlinear Schrödinger equation for Bose-condensed trapped neutral atoms”, *Phys. Rev. A* **51**, 4704 (1995).
- [442] C. C. Bradley, C. A. Sackett, and R. G. Hulet, “Bose-Einstein Condensation of Lithium: Observation of Limited Condensate Number”, *Phys. Rev. Lett.* **78**, 985 (1997).
- [443] C. A. Sackett, J. M. Gerton, M. Welling, and R. G. Hulet, “Measurements of Collective Collapse in a Bose-Einstein Condensate with Attractive Interactions”, *Phys. Rev. Lett.* **82**, 876 (1999).
- [444] J. M. Gerton, D. Strekalov, I. Prodan, and R. G. Hulet, “Direct observation of growth and collapse of a Bose–Einstein condensate with attractive interactions”, *Nature* **408**, 692 (2000).
- [445] E. A. Donley, N. R. Claussen, S. L. Cornish, J. L. Roberts, E. A. Cornell, and C. E. Wieman, “Dynamics of collapsing and exploding Bose–Einstein condensates”, *Nature* **412**, 295 (2001).
- [446] Z. Dutton and C. W. Clark, “Effective one-component description of two-component Bose-Einstein condensate dynamics”, *Phys. Rev. A* **71**, 063618 (2005).
- [447] B. Bakkali-Hassani, C. Maury, Y.-Q. Zou, É. Le Cerf, R. Saint-Jalm, P. C. M. Castilho, S. Nascimbene, J. Dalibard, and J. Beugnon, “Realization of a Townes Soliton in a Two-Component Planar Bose Gas”, *Phys. Rev. Lett.* **127**, 023603 (2021).
- [448] M. Bertola and A. Tovbis, “Universality for the Focusing Nonlinear Schrödinger Equation at the Gradient Catastrophe Point: Rational Breathers and Poles of the Tritronquée Solution to Painlevé I”, *Commun. Pure Appl. Math.* **66**, 678 (2013).
- [449] M. J. Ablowitz and J. T. Cole, “Transverse Instability of Rogue Waves”, *Phys. Rev. Lett.* **127**, 104101 (2021).
- [450] Z. Yan, V. V. Konotop, and N. Akhmediev, “Three-dimensional rogue waves in nonstationary parabolic potentials”, *Phys. Rev. E* **82**, 036610 (2010).
- [451] D. Mihalache, “Multidimensional localized structures in optical and matter-wave media: A topical survey of recent literature”, *Rom. Rep. Phys.* **69**, 403 (2017).
- [452] G. Zhang, L. Ling, and Z. Yan, “Multi-component Nonlinear Schrödinger Equations with Nonzero Boundary Conditions: Higher-Order Vector Peregrine Solitons and Asymptotic Estimates”, *J. Nonlinear Sci.* **31**, 81 (2021).
- [453] R. H. J. Grimshaw and A. Tovbis, “Rogue waves: analytical predictions”, *Proc. R. Soc. Math. Phys. Eng. Sci.* **469**, 20130094 (2013).

- [454] P. Blanco-Mas and C. E. Creffield, “Generating soliton trains through Floquet engineering”, [Phys. Rev. A **107**, 043310 \(2023\)](#).

Acknowledgements

First and foremost, I would like to thank my thesis supervisor, Prof. Peter Schmelcher, for giving me the opportunity to pursue a Ph.D. in his group, for our discussions, inside and outside the office, and for his support throughout these years.

I also acknowledge the financial support by the by the Deutsche Forschungsgemeinschaft (DFG) in the framework of the SFB 925 “Light induced dynamics and control of correlated quantum systems”.

Special thank you to my collaborators, Lia, Panos, Barbara, Gino, Simos, Sean and Peter E., for all what I have learned from them, and with them, and for our projects together *across the pond*.

During my time at the ZOQ, I met a lot of fantastic people with whom I had the chance to discuss and laugh about life and science, in particular Maxim, Frederic, Ansgar, Friethjof, Jie, Dimitris, Kevin, Malte, Dan, Fabian, Lia, George, Giorgis, Simos, Martin, Kapil, Felipe, Zeki, Rohan, Rick, André, Ilias, Christian M., Christian F., Aritra, Andrea, Alexandra, Samir, Iqra and Jan. Thanks also to Anja, for helping me with all the administrative stuff; thanks to my student, Fanis; thanks again to Geroge, for keeping the tea business in the office alive; and thanks again to those who took the time to have a look at an earlier version of this thesis: Maxim, Dimitris, Lia, Friethjof, Dan, Ansgar, Zeki, and Aitor.

Mens sana in corpore sano. For that, I’m gratefully thankful to my *Sensei*, Thomas Volkmann, and the karatekas at Kyodo Dojo for accepting me as a member of their karate family, for teaching me the ways of the Shotokan Karate, and for awarding me with the *Kuro-Obi*. Oss. Not to mention my McFit buddies, Maxim, Jie, Dimitris and Agustín, as well as the runners, Jie, André, Peter S. and Jose.

I would also like to thank Ulj and Masha, for making me feel at home; Daisuke, for his commitment at organizing the monthly Japanese-German tandems; Malte, for organizing the awesome games of *Twilight Imperium IV*; Jenny and Connor, for organizing *funtastic* board-game nights; and Andreas, for showing me the world of *Dungeons and Dragons*. Thanks to Joan and Rocha for all the adventures we had playing and exploring fantasy worlds from sunset to sunrise, and Aitor, for those moments in Jülich and in the *Summoner’s Rift*.

Last, an immense heartfelt thank you to my family, specially my parents and my sister, for being so close despite being so far, and Cris, my partner during this adventure that has been living in Hamburg¹.

¹Due to the lack of sunlight in Hamburg, the author’s mind may have been dulled, and he apologizes if he has forgotten to thank You.

Eidesstattliche Versicherung / Declaration of oath

Hiermit versichere ich an Eides statt, die vorliegende Dissertationsschrift selbst verfasst und keine anderen als die angegebenen Hilfsmittel und Quellen benutzt zu haben.

Die eingereichte schriftliche Fassung entspricht der auf dem elektronischen Speichermedium.

Die Dissertation wurde in der vorgelegten oder einer ähnlichen Form nicht schon einmal in einem früheren Promotionsverfahren angenommen oder als ungenügend beurteilt.

Hamburg, den 25.10.2023

A handwritten signature in black ink, appearing to read 'Alejandro', with a long horizontal stroke extending to the right.

Alejandro ROMERO Ros

